

THERMO-FLUID AND MECHANICAL DESIGN AND OPTIMIZATION OF AN
ADVANCED PRINTED CIRCUIT HEAT EXCHANGER FOR SUPERCRITICAL CO₂
BRAYTON CYCLES

by

Javad Khalesi

A dissertation submitted to the faculty of
The University of North Carolina at Charlotte
in partial fulfillment of the requirements
for the degree of Doctor of Philosophy in
Mechanical Engineering

Charlotte

2021

Approved by:

Dr. Nenad Sarunac

Dr. Harish Cherukuri

Dr. Russell Keanini

Dr. Yuri Godin

Dr. Wesley Williams

ABSTRACT

JAVAD KHALESI. Thermo-fluid and Mechanical Design of an Advanced Printed Circuit Heat Exchanger for Supercritical CO₂ Brayton Cycles. (Under the direction of DR. NENAD SARUNAC)

A supercritical carbon dioxide (sCO₂) Brayton power cycle is considered as one of the promising energy conversion systems for a number of applications such as advanced nuclear reactors, advanced fossil, and Concentrated Solar Power (CSP) plants due to its high thermodynamic efficiency and small equipment size (heat exchangers and turbomachinery). The compact heat exchangers such as Printed Circuit Heat Exchangers (PCHEs) with micro-channel geometry are suitable for coupling different heat sources such as nuclear reactor to a sCO₂ Brayton power cycle. PCHEs offer very high specific heat transfer area and pressure containment and are typically fabricated using chemical etching and diffusion bonding process [1].

Conventional semi-circular micro-channel PCHEs are used for recuperators and general use heat exchangers. The objective of this study is to design and optimize an advanced PCHE micro-channel geometry and topology for a sCO₂ Brayton cycle. This work is concerned with the design where both sides of the plate are etched forming a double-etched micro-channel design configuration. In this advanced micro-channel topology, shim plates are needed to construct a PCHE stack using diffusion bonding. The design goals are to maximize heat transfer, minimize pressure drop, improve thermal performance and reduce the size, while maintaining mechanical integrity of a PCHE.

Thermo-hydraulic performance of semi-circular micro-channel and advanced semi-circular and circular double-etched micro-channel geometries, i.e., the Nusselt number and Fanning Friction Factor (friction coefficient) and the overall heat transfer coefficient U

between the hot and cold channels, pressure drop, and maximum stress, were determined and are reported in this work. The results obtained for the advanced double-etched microchannel geometry were compared to the “conventional” semi-circular single-etched (single-side etched) micro-channel design for the counter-flow arrangement.

Using ANSYS-Workbench, a multi-objective optimization algorithm employing NSGA-II and Response Surface Approximation (RSA) as a surrogate model was used for design and optimization of the advanced double-etched micro-channel PCHE geometry. The channel fin, the channel pitch, and shim plate thickness were the parameters used in optimization. Alloys 617 and 230 were used as materials of construction.

ACKNOWLEDGEMENTS

I would like to express my appreciation and gratitude to my advisor Dr. Nenad Sarunac for his continuous help and support during this challenging research project. It is undeniable that I would not be able to reach this stage without his valuable guidance. I am thankful for providing the opportunity to collaborate with him during my PhD studies at the University of North Carolina at Charlotte.

I would like to express my gratitude to Dr. Harish Cherukuri, the Chair of Mechanical Engineering and Engineering Science department, for his help, time, and advice during my research project.

I would like to thank Dr. Russell Keanini, Dr. Yuri Godin, and Dr. Wesley Williams for accepting to be in my doctoral committee and for sharing their valuable knowledge.

I would like to give thanks to the graduate school at UNC Charlotte for supporting me by tuition and health insurance (GASP) during my PhD program.

I am thankful to my friends Dr. Sina Modaresahmadi for helping with design and Finite Element modeling and simulation with ANSYS-Mechanical module, and Dr. Neda Pouraskari for supporting me during my PhD study.

DEDICATION

To my parents and siblings who have always supported me.

TABLE OF CONTENTS

LIST OF FIGURES	xi
LIST OF TABLES	xviii
NOMENCLATURE	xxii
CHAPTER 1: INTRODUCTION AND PROBLEM STATEMENT	1
1.1 Overview	1
1.2 Motivation and objectives	2
1.3 Printed Circuit Heat Exchangers (PCHEs)	9
1.4 Significance and novelty of the project	14
1.5 Previous works	18
1.6 Overall PCHE performance, effectiveness-NTU theory	25
1.7 Outline of the study	28
CHAPTER 2: GOVERNING EQUATIONS AND CONJUGATE HEAT TRANSFER PROBLEM	32
2.1 Overview	32
2.2 Conjugate heat transfer problem	32
2.2.1 Axial conduction in the conjugate heat transfer	34
2.3 Simultaneously developing laminar flow and heat transfer	35
2.4 CFD analysis and solver choice	37
2.5 Grid sensitivity analysis for studied geometries	39
2.6 Simulation of the conjugate heat transfer in a square micro-channel	41
2.6.1 Physical model	42
2.6.2 Axial variation of the friction coefficient and Nusselt number	46
CHAPTER 3: SUPERCRITICAL CO ₂	50
3.1 Overview	50
3.2 SCO ₂ characteristics	50
3.3 Conjugate heat transfer and sCO ₂ flow through the PCHE micro-channels	54
3.4 System description	55
3.4.1 Geometry and computational domain	55
3.5 Results and discussion	57
3.5.1 Variation of bulk fluid temperature and wall heat flux along the channel length	57

3.5.2 Thermo-physical properties of supercritical CO ₂	60
3.5.3 Hydraulic analysis	61
3.5.4 Thermal analysis	69
CHAPTER 4: VALIDATION OF NUMERICAL MODEL	77
4.1 Overview	77
4.2 Physical model	77
4.3 Semi-circular (Base model) and semi-circular staggered double-etched geometry – Validation of results	83
4.4 Circular channel geometry -Validation of results	84
CHAPTER 5: FINITE ELEMENT ANALYSIS - BOUNDARY CONDITIONS FOR STRESS CALCULATIONS	86
5.1 Overview	86
5.2 System description	88
5.2.1 Thermal analysis	88
5.2.2 Numerical modeling and validation	90
5.2.3 Temperature field	92
5.3 Structural analysis	94
5.3.1 Finite Element modeling	95
5.3.2 Generalized Plane Strain	97
5.3 Stress field for the generalized plane strain model	99
5.3.1 Thermal stress: 2D generalized plane strain versus 3D stress at different locations	104
5.4 The effect of mechanical boundary conditions on thermal and mechanical stresses	106
5.4.1 Physical model	106
5.4.2 Gird independence study	109
5.4.3 Validation of the numerical model	110
5.4.4 Stress field for different models with different boundary conditions	114
5.5 Effective and realistic boundary conditions for the PCHE core	123
5.5.1 Mechanical boundary conditions on top/bottom walls	126
5.5.2 Temperature field	128
5.5.3 Stress field	130
5.5.4 The effect of the right/left wall B.C.s and spring stiffness on stress distribution	138

CHAPTER 6: ADVANCED MICRO-CHANNEL GEOMETRY AND TOPOLOGY-DOUBLE-ETCHED STAGGERED GEOMETRY	142
6.1 Overview	142
6.2 System description, operating pressure and temperature	143
6.3 Thermal and hydraulic performance of studied PCHEs	146
6.3.1 Boundary conditions for the Base and Staggered double-etched models	146
6.3.2 CFD results for the Base and Staggered double-etched geometries	147
6.4 The effect of channel fin thickness on the channel wall temperature	148
6.5 Temperature distribution in channel walls	151
6.6 Structural analysis	153
6.6.1 ANSYS modeling	154
6.6.2 Mesh independence study for stress calculation	157
6.6.3 Optimization of staggered double-etched geometry	159
6.7 Thermal and hydraulic performance of the optimized staggered double-etched (SDE) geometry	166
6.8 Overall heat transfer coefficient (U)	169
6.8.1 LMTD method	169
6.8.2 Integration method	170
6.8.3 Effectiveness-NTU (ϵ -NTU) method	172
CHAPTER 7: ADVANCED MICRO-CHANNEL GEOMETRY AND TOPOLOGY-STAGGERED DOUBLE-BANKING CIRCULAR GEOMETRY	178
7.1 Overview	178
7.2 System description, operating pressure and temperature	178
7.3 Thermal and hydraulic performance of studied PCHEs	182
7.3.1 Boundary conditions for the BM and circular SDE geometries for the 1 st scenario	184
7.3.2 Thermal and hydraulic performance of the Base and circular SDE geometries for the 1 st scenario	187
7.4 Temperature distribution in channel walls	194
7.5 Potential candidate materials for IHX	196
7.6 Structural analysis	199
7.6.1 ANSYS modeling	200

7.6.2 Stress calculation and optimization of the circular staggered double-etched geometry	201
7.7 Thermal and hydraulic performance of the optimized geometry, 1 st scenario	208
7.8 IHX thermal performance	210
7.8.1 Overall heat transfer coefficient (U)	210
7.8.2 Effectiveness-NTU (ϵ -NTU) method	211
7.9 Optimized circular staggered geometry for Alloy 230	216
7.10 Thermal and hydraulic performance of studied IHX, 2 nd scenario	220
7.10.1 Geometry and boundary conditions	220
7.10.2 Thermal and hydraulic performance, 2 nd scenario	221
7.10.3 Heat exchanger thermal duty and effectiveness	225
CHAPTER 8: CONCLUSIONS AND RECOMMENDATIONS FOR FUTURE RESEARCH	228
8.1 Overview	228
8.2 Research contributions	228
8.2.1 The effect of large variation of thermo-physical properties of sCO ₂ and liquid sodium on thermal and hydraulic performance of microchannel PCHE	228
8.2.2 Design and optimization of advanced double-etched micro-channel PCHE geometries	229
8.3 Challenges associated with the design and optimization	231
8.4 Recommendations for future research	231
REFERENCES	233

LIST OF FIGURES

Figure 1. 1 (a) Simple Rankine cycle with recuperation, (b) Simple Brayton cycle with recuperation, (c) T-s diagram of Brayton and Rankine cycles [4, 7].....	4
Figure 1. 2. Schematic of (a) sCO ₂ recompression cycle arrangement with heat source (b) operating pressures and temperatures of IHX and HTR, HTR and LTR refer to High and Low Temperature recuperators [8].....	6
Figure 1. 3. P-T diagram of CO ₂	7
Figure 1. 4. PCHE block and components	10
Figure 1. 5. Micrographs of bonded section showing complete recrystallization	10
Figure 1. 6. General overview of a semi-circular micro-channel PCHE [15]	13
Figure 1. 7. General overview of a rectangular micro channel PCHE	14
Figure 1. 8. Schematic of semi-circular staggered double-etched, double banking geometry	17
Figure 1. 9. Schematic of circular staggered double-banking pattern	17
Figure 2. 1. Solid-fluid interface in conjugate heat transfer	34
Figure 2. 2. Hot and cold side interfaces in a heat exchanger	34
Figure 2. 3. (a) Schematic of the square duct and computational domain, (b) Computational grid close to the channel wall [25]	43
Figure 2. 4. Axial variation of peripherally-averaged Nusselt number for water, Pr=6.9	46
Figure 2. 5. Variation of friction coefficient along the channel for studied fluids	47
Figure 2. 6. Variation of the Nusselt number along the channel for studied fluids (top), Nusselt number illustrated in smaller range (bottom).....	48
Figure 3. 1. Continued, (c) dynamic viscosity and (d) density [66] over a range of pressure; T _{pc} is the pseudo-critical temperature.....	52
Figure 3. 2. (a) T-s diagram of CO ₂ over a range of pressure, (b) Compression work for different compressor inlet pressure [66]	53
Figure 3. 3. T-s diagram of the Regenerative Brayton cycle with recompression [66]	54

Figure 3. 4. (a) Schematic of the two micro-channel configuration, boundary conditions and details of computational domain, (b) Numerical grid	56
Figure 3. 5. Parallel Flow: (a) Variation of bulk temperature of the liquid sodium and sCO ₂ and (b) heat flux over a range of pressure	59
Figure 3. 6. Counter Flow: (a) Variation of bulk temperature of the liquid sodium and aCO ₂ and (b) heat flux over a range of pressure	59
Figure 3. 7. Variation of thermo-physical properties with temperature of the working fluid (sCO ₂)	61
Figure 3. 8. Cold (sCO ₂) micro-channel: Variation of (a) Bulk velocity, (b) Friction coefficient for parallel and counter-flow arrangements	63
Figure 3. 9. Hot (liquid sodium) micro-channel: (a) Bulk temperature and velocity variation along the duct, (b) Normalized velocity contours at $Z/D_h=200$ in a fully-developed flow for the counter-flow arrangement	65
Figure 3. 10. Variation of friction coefficient along the channel length: liquid sodium	66
Figure 3. 11. X-Y cross-section at $Z/D_h=200$ for the local shear stress analysis.....	67
Figure 3. 12. Cold (sCO ₂) micro-channel: Variation of local wall velocity gradient along the A-B line with pressure for the Parallel-flow and Counter-flow	68
Figure 3. 13. Cold (sCO ₂) micro-channel: Axial variation of Nusselt number over a range of pressure	70
Figure 3. 14. Temperature contours for two micro-channel configurations at a $Z/D_h=125$ and 10 MPa, (a) Parallel flow, (b) Counter-flow	71
Figure 3. 15. Axial variation of Nusselt number for the liquid sodium in parallel- and counter-flow arrangements for operating pressures of 8, 10, and 30 MPa	72
Figure 3. 16. Cold (sCO ₂) micro-channel: Variation of local (a) heat flux (b) wall temperature gradient (c) heat transfer coefficient along the A- B line over a range of pressure and parallel- and counter-flow arrangements.....	76

Figure 4. 1. Schematic of a semi-circle channel cross section selected as a Base model from the literature [70, 71]	79
Figure 4. 2. Schematic of a circular micro-channel cross section geometry	80
Figure 4. 3. The schematic of semi-circular staggered double-etched cross section geometry and topology	80
Figure 4. 4. Computational grid for the Base model, circular and semi-circular staggered double-etched micro-channel geometries	81
Figure 5. 1. The schematic of sCO ₂ Brayton cycle integrated with CSP [74].....	88
Figure 5. 2. (a) Schematic of the micro-channel arrangement, (b) computational domain, (c) discretization grid.....	89
Figure 5. 3. (a) 3D temperature contour, (b) temperature distribution along the channel	93
Figure 5. 4. Temperature (°C) contours (a) mid-plane, (b) Z=0.025 m, (c) Z=0.175 m.	94
Figure 5. 5. FE model (a) geometry and B. Cs, (b) grid.	95
Figure 5. 6. Thermal stress field (a) 3D model, (b) 2D plane strain, (c) 2D generalized plane strain, (d) 3D mid-plane	101
Figure 5. 7. 2D generalized plane strain (a) Total stress, (b) Mechanical stress only	102
Figure 5. 8. Axial direction thermal stress component contour, periodic BC (a) Plane strain, (b) 2D generalized plane strain, (c) 3-D mid plane	103
Figure 5. 9. Thermal stress contour at cold inlet (z=0.025 m) (a) 2D Generalized plane strain, (b) 3D models	105
Figure 5. 10. Thermal stress contours (a) 2D Generalized plane strain, (b) at hot inlet (z=0.175 m) in 3D models.....	106
Figure 5. 11. Schematic of studied geometries by Lee and Lee [18] and boundary conditions.	108
Figure 5. 12. Maximum stress intensity value at the channel corner for different number of grid elements and fillet size.....	109
Figure 5. 13. Numerical grid used for the 4×4 PCHE core simulation.....	110

Figure 5. 14. The temperature contours in 4×4 PCHE model	111
Figure 5. 15. The stress intensity along the hot and cold wall periphery compared to values reported in Lee and Lee [18].....	112
Figure 5. 16. (a) mechanical stresses (b) mechanical stress	113
Figure 5. 17. Schematics of the PCHE models used in the boundary conditions sensitivity analysis (a) 2×1, (b) 8×1 PCHEs.....	115
Figure 5. 18. The location where stress is reported	116
Figure 5. 19. Stress intensity distribution along the channel hot/cold wall for 2×1 PCHE and 8×1 PCHE	118
Figure 5. 20. Total stress intensity along the channel wall for 8×1 PCHE in current study and 8×8 PCHE from Lee and Lee.....	120
Figure 5. 21. Stress intensity distribution along the channel hot/cold wall in 4×4 PCHE model	122
Figure 5. 22. (a) 3D PCHE lab-scale prototype [78], (b) schematic of PCHE and spring elements	125
Figure 5. 23. (a) 2-spring model, (b) 1-spring-fixed model, (c) 1-spring-zero y-displacement model, (d) paths	127
Figure 5. 24. Cross-section of the CFD model	128
Figure 5. 25. (a) mid-plane solid temperature distribution, (b) hot and cold local wall channel temperature	129
Figure 5. 26. The schematic of 3D lab-scale PCHE by Song [78]	130
Figure 5. 27. Case 1: (a) stress field corresponding to Song's B.C.s.....	131
Figure 5. 28. Case 2: (a) stress field corresponding to 1-spring-fixed support B.C.s,.....	133
Figure 5. 29. Case 3: (a-b) stress field for 1-spring- zero y-displacement B.C.s.....	135
Figure 5. 30. (a-c) stress distribution along the paths (d) paths.....	138

Figure 5. 31. The equivalent stress distribution on (a) F-E path (b) I-K path for different right/left wall B.C.s, (c) F-E path over a range of spring stiffness	140
Figure 6. 1. The flowchart of calculations and analyses performed in Chapter 6	143
Figure 6. 2. The sCO ₂ recompression Brayton cycle arrangement.....	144
Figure 6. 3. The optimized sCO ₂ Brayton cycle with recompression [8]	144
Figure 6. 4. The operating temperature and pressure determined by Floyd et al. [8] for HTR ..	145
Figure 6. 5. The Base and semi-circular staggered double-etched models.....	146
Figure 6. 6. Hollow cylinder with different convection surface boundary conditions [51].....	150
Figure 6. 7. (a) temperature contours, (b) cold side channel wall temperature distribution.....	152
Figure 6. 8. (a) Staggered double-etched geometry used in stress calculation, (b) Locations of the maximum stress	155
Figure 6. 9. (a) the maximum allowable stress for different high temperature materials [79], mechanical properties of as-received Alloys 617 from the French VHTR program (b) Yield Stress vs. Temperature [80]	157
Figure 6. 10. Mesh illustration for stress calculations	158
Figure 6. 11. The stress variation along the A-B path	158
Figure 6. 12. Stress contours (a) full PCHE model, (b) details of stress contours for the optimized geometry (channel fin thickness=0.294 mm)	163
Figure 6. 13. Stress distribution along the A-B and C-D paths of the optimized geometry.	164
Figure 6. 14. Stresses in channel fin and shim plate over a range of (a) shim plate thickness, (b) channel fin thickness.....	165
Figure 6. 15. Stresses in the channel fin and shim plate plotted over a range of channel fin thickness for shim plate thickness of 0.448	166
Figure 6. 16. The wall heat flux (a) cold side, (b) hot side, for both geometries.....	168
Figure 6. 17. Variation of bulk temperature along the channel for (a) Optimized geometry, (b) Base model.....	169

Figure 6. 18. The variation of (a) the wall heat flux cold side, (b) overall heat transfer coefficient	172
Figure 6. 19. An illustration of both Base model and the optimized staggered geometries	175
Figure 7. 1. The sCO ₂ recompression Brayton cycle arrangement [8]	179
Figure 7. 2. The optimized sCO ₂ Brayton cycle with recompression [8]	179
Figure 7. 3. The operating temperature and pressure determined by Floyd et al.[8] for HTR ...	180
Figure 7. 4. The Base and circular staggered double-etched geometry	181
Figure 7. 5. Variation of (a) Nusselt number, (b) wall heat flux, along the channel length for the Base model.....	189
Figure 7. 6. Variation of (a) Nusselt number, (b) wall heat flux, along the channel length for the circular staggered doubled-etched geometry	190
Figure 7. 7. Variation of local wall heat flux at $Z/D_h=110$ (a) Base model cold side, (b) Base model hot side, (c) circular staggered model, hot and cold sides	192
Figure 7. 8. Friction coefficient along the channel length, (a) The Base model, (b) the circular staggered model	193
Figure 7. 9. Variation of (a) wall shear stress, Left: sCO ₂ channel, Right: liquid sodium channel (b) dynamic viscosity, (c) density, along the channel length in the Base model and the circular SDE geometry	194
Figure 7. 10. Contour of solid domain temperature at mid-plane section	195
Figure 7. 11. Variation of (a) maximum allowable stress [79], mechanical properties of as-received Alloys 617 and 230 from the French VHTR program (b) Yield Stress vs. Temperature and (c) UTS vs. Temperature [19, 80]	198
Figure 7. 12. (a) the circular staggered double-etched geometry used in stress calculation, (b) the locations (hot side and cold side paths) where stresses in channel walls are reported	201
Figure 7. 13. The stress contours for the optimized geometry (channel fin thickness=0.428 mm)	204
Figure 7. 14. The stress distribution along the hot path.....	205

Figure 7. 15. The stress distribution along the cold path.	206
Figure 7. 16. Variation of maximum total stress over a range of channel fin thickness.....	207
Figure 7. 17. Hot and cold channel walls maximum stress values over a range of channel fin thickness.....	207
Figure 7. 18. The peripherally-averaged wall heat flux (a) cold channel, (b) hot channel, for both geometries, 1 st scenario	209
Figure 7. 19. The frontal view in the optimized circular SDE staggered geometry	214
Figure 7. 20. The variation of maximum total stress over a range of channel fin thickness using Alloy 617 and Alloy 230 as solid materials.....	219
Figure 7. 21. Friction coefficient C_f and wall shear stress for both scenarios	225

LIST OF TABLES

Table 1. 1. Primary cycle operating condition for different applications (IHX)	8
Table 1. 2. Operating conditions for the recuperated Brayton cycle with recompression.....	8
Table 1. 3. Micro-channel configurations.....	11
Table 1. 4. Thermal and hydraulic performance of PCHE channel types	12
Table 2. 1. Details of the grid independence study results for the square channel.....	40
Table 2. 2. Details of the grid independence study results for the semi-circular channel	41
Table 2. 3. The details of grid independence study results for the circle channel.....	41
Table 2. 4. Thermo-physical properties of studied fluids	42
Table 2. 5. Dimensions of the micro-channel and surrounding walls (mm).....	43
Table 2. 6. Boundary conditions	44
Table 2. 7. The predicted numerical results for water in the validation study and calculated error [25].....	45
Table 3. 1. Dimensions of the liquid sodium-cooled micro-channel configuration analyzed in this study, dimensions in mm	56
Table 3. 2. Boundary conditions.....	57
Table 3. 3. Operating conditions.....	57
Table 3. 4. Bulk fluid temperature, local wall temperature, viscosity, velocity gradient, and shear stress as functions of pressure for the parallel- and counter-flow arrangements.....	68
Table 3. 5. Bulk fluid temperature, local wall temperature, wall temperature gradient, wall heat flux, and heat transfer coefficient as functions of pressure for the parallel- and counter-flow arrangements	73
Table 4. 1. Dimensions of the micro-channel and surrounding walls for analyzed geometries ...	82
Table 4. 2. The Boundary conditions for studied models	82
Table 4. 3. The $C_f Re$ and Nusselt number values obtained in this study for semi-circular geometry. The error was calculated with respect to values reported by Shah and London [53]..	84

Table 4. 4. The C_f , Re and Nusselt number values obtained in this study for a circular geometry	85
Table 5. 1. The domain parameters.....	89
Table 5. 2. Boundary conditions for pressure and temperature used in thermal analysis.....	90
Table 5. 3. The temperature-dependent thermo-physical and mechanical properties of SS316L	91
Table 5. 4. The Nusselt number and friction coefficient comparison.....	92
Table 5. 5. The Nusselt number and friction coefficient comparison with literature for sCO_2	92
Table 5. 6. The domain parameters.....	107
Table 5. 7. Material properties of stainless steel 316 [18]	108
Table 5. 8. Stress intensity for studied locations A to D.....	119
Table 5. 9. The equivalent stress for studied locations A to D	119
Table 5. 10. Stress intensity and equivalent stress for locations A to D for the 4×4 PCHE model	123
Table 5. 11. Thermal and mechanical properties of Alloy 617 at 360 °C.....	129
Table 6. 1. The Boundary conditions for studied PCHE models.....	147
Table 6. 2. Thermal and hydraulic performance of studied PCHEs	147
Table 6. 3. Hot and cold channel wall temperature for different fin thickness.....	150
Table 6. 4. Physical and mechanical properties of Alloy 617	156
Table 6. 5. The grid size and number of elements used in the grid independence study.....	159
Table 6. 6. Three candidate geometries selected in the design optimization.....	160
Table 6. 7. PCHE improvement in optimization design	161
Table 6. 8. Thermal and hydraulic performance of the Base model (BM) and optimized staggered double-etched (SDE) geometries	167
Table 6. 9. The overall heat transfer coefficient U by LMTD method.....	170
Table 6. 10. Overall heat transfer coefficient obtained by using the Integration method.....	171

Table 6. 11. The NTU and effectiveness calculated for the optimized staggered double-etched (SDE) and Base model (BM).....	173
Table 6. 12. PCHE unit weight and dimensions for BM and optimized SDE geometries	175
Table 6. 13. Heat transfer per volume and the heat exchanger compactness for Base model (BM) and optimized staggered double-etched (SDE) geometries	177
Table 7. 1. Boundary conditions for the Base model.....	185
Table 7. 2. Details of channel length calculations for the BM (LMDT method, hot and cold fluids)	185
Table 7. 3. Boundary conditions for the circular staggered double-etched model, 1 st scenario .	186
Table 7. 4. Details of channel length calculations for circular staggered geometry (LMDT method, hot (liquid sodium) and cold (sCO ₂) fluids)	186
Table 7. 5. Details of the PCHE geometries used in this study	187
Table 7. 6. Thermal and hydraulic performance of studied PCHEs	188
Table 7. 7. Physical and mechanical properties of Alloys 617 and 230	199
Table 7. 8. First three candidates for optimal geometry in the design optimization.....	202
Table 7. 9. Reduction of PCHE size in optimization design for Alloy 617.....	203
Table 7. 10. Thermal and hydraulic performance of the optimized circular staggered geometry and circular staggered geometry, 1 st scenario, Re=1000 for the cold side inlet	208
Table 7. 11. Heat transfer coefficient for studied geometries.....	210
Table 7. 12. NTU and effectiveness of the optimized circular staggered double-etched, circular staggered, and Base model geometry.....	213
Table 7. 13. PCHE unit weight and dimensions of the circular staggered and optimized circular staggered geometries.....	214
Table 7. 14. Heat transfer per volume and the heat exchanger compactness for circular staggered geometries	215
Table 7. 15. Three candidates for the design optimization using Alloy 230	217

Table 7. 16. Comparison of optimized circular geometries for Alloys 617 and 230.....	218
Table 7. 17. Comparison of the IHX size for Alloys 617 and 230 - optimized circular staggered geometries	220
Table 7. 18. Boundary conditions and mass flows of working fluids for the 2 nd scenario	221
Table 7. 19. Thermal and hydraulic performance for studied scenarios.....	222
Table 7. 20. The overall heat transfer coefficient for studied scenarios	224
Table 7. 21. Heat transfer performance of a heat exchanger for investigated scenarios	226
Table 7. 22. The bulk temperature at the hot and cold channel inlet and exit	227

NOMENCLATURE

A	Area, m^2
C	Heat capacity rate, $J/K.s$
C_f	Friction coefficient
C_p	Specific heat at constant pressure, $J/kg.K$
D_h	Hydraulic diameter, m
f	Body force, N
h	Heat transfer coefficient, $W/m^2.K$
k	Thermal conductivity, $W/m.K$
L	Channel length, m
\dot{m}	Mass flow rate, kg/s
Nu	Nusselt number (hD/k)
Pr	Prandtl number ($\mu c_p/k$)
ΔP	Pressure drop
Q	Heat rate, W
q''	Wall heat flux, W/m^2
Re	Reynolds number ($\rho u D/\mu$)
T	Temperature, K
ΔT_{LMTD}	Log mean temperature difference
θ	Dimensionless temperature
U	Overall heat transfer coefficient, $W/m^2.K$
\bar{U}	Average overall heat transfer coefficient, $W/m^2.K$
u	Bulk velocity, m/s
u_{max}	Maximum velocity in the channel, m/s

x, y Transverse coordinate, m

z Axial coordinate, m

Greek symbols

α Coefficient of thermal expansion, $1/^\circ\text{C}$

ε Effectiveness

ε Strain

γ Shear strain,

τ Peripherally-averaged shear stress, Pa

τ_w Wall shear stress, Pa

σ Stress, MPa

z Axial coordinate, m

μ Dynamic viscosity, Pa s

ρ Density, kg/m^3

Subscripts

b Bulk (mass-weighted average)

c Cold

c Conduction

c Cross section

Cr Critical

f Fluid

e Equivalent

h Convection

h Hot

I	Intensity
i	Inlet
l	Peripherally-averaged
max	Maximum
o	Outlet
s	Surface
t	Total
w	Wall
O	Total

CHAPTER 1: INTRODUCTION AND PROBLEM STATEMENT

1.1 Overview

This study focuses on the design, analysis and optimization of a Printed Circuit Heat Exchanger (PCHE) core for the Brayton cycle for the advanced fossil, nuclear, or Concentrated Solar Power (CSP) power plants which use supercritical CO₂ as a working fluid in the power cycle. A detailed analysis of variation of supercritical CO₂ (sCO₂) thermo-physical and transport properties under a range of operating conditions covering pressures very close to the Critical Point (CP) and pseudo-critical region was performed. Thermo-physical properties of sCO₂ were determined using the REFPROP NIST database [2]. The results of this study were used to determine the desired operating pressure for an advanced PCHE. The design analysis (thermal and hydraulic) and optimization of the micro-channel geometry and topology were performed using the ANSYS software package. The Computational Fluid Dynamics (CFD) was employed to design, optimize, and analyze thermal and hydraulic performance of a PCHE used as a high temperature recuperator (HTR) and as an Intermediate Heat Exchanger (IHX) in an advanced high-efficiency (42.2% net) 650 MW power plant. The PCHE design was developed for an IHX operating at a high pressure (25.1 MPa) and outlet temperature (515 °C) where IHX is coupled to the sCO₂ Brayton cycle with recompression, Figure 1. 2a. As shown in Figure 1. 2b, the HTR operates with a lower pressure compared to the IHX, 8.6 MPa on the recuperator hot side.

Also, as the Figure 1. 2b shows, the IHX is operating with liquid sodium as a hot side fluid and sCO₂ as the cold side fluid, while sCO₂ is used as the working fluid on both sides of the recuperator. This combination of working fluids and operating conditions represents a significant challenge for the PCHE design. Due to the difference in operating conditions,

optimization of the PCHE design and its topology (arrangement of the hot and cold channels and their geometry) was performed in this work for both the IHX and recuperator applications using the Multi Objective Genetic Algorithm (MOGA). The optimization process employed is based on the American Society of Mechanical Engineering (ASME) Boiler and Pressure Vessel Code (BPVC) section III rules for the recuperator and IHX design and construction. Alloys 617 and 230 were considered as potential materials of construction for the HTR and IHX and their mechanical properties were used in the design and optimization process.

1.2 Motivation and objectives

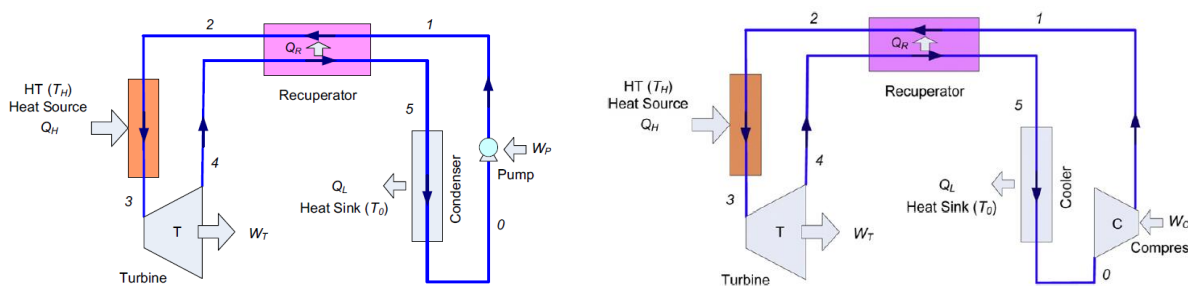
The supercritical carbon dioxide (sCO_2) Brayton power cycle is considered as one of the promising energy conversion systems for a number of applications such as advanced nuclear reactors, advanced fossil, and Concentrated Solar Power (CSP) plants due to its high thermodynamic efficiency and small equipment size (heat exchangers and turbomachinery). In nuclear application, the highest efficiency can be achieved by using Helium as a working fluid in the Brayton cycle, high maximum temperature is needed. At the maximum temperature of 900°C , the Helium Brayton cycle can achieve net efficiency in the 45-48% range [3]. However, the high temperature environment can be challenging to the structural materials. The sCO_2 power cycle achieves high efficiencies in the temperature range of $500\text{-}700^\circ\text{C}$. This temperature range is suitable for a range of applications such as Concentrated Solar Power (CSP).

In the CSP application, using traditional molten salt and steam Rankine cycle (subcritical /supercritical) with high turbine inlet temperature (565°C - 620°C) gives high efficiency of 40-45% [3, 4]. However, the use of high temperature materials for turbomachinery and heat exchangers increases capital cost of the CSP plants. Although the use

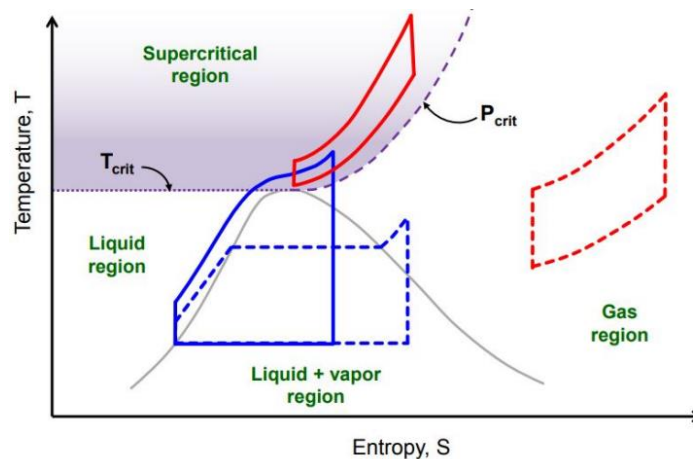
of novel heat transfer/storage and working fluids, such as molten nitrate salt, with high temperature limit of 600°C would increase efficiency of a CSP plant, it also increases the potential for chemical corrosion of CSP components. The next generation of CSP is being designed to provide heat to a supercritical CO_2 power cycle with maximum temperature higher than 700°C for high power plant efficiency and lower costs. It should be mentioned that the heat rejection in a supercritical CO_2 power plant can be accomplished by using dry-cooling which is highly beneficial and important for the CSP plants built in arid areas [4].

Feher [5] proposed a supercritical CO_2 Brayton cycle that operates above the critical pressure of carbon dioxide allowing expansion and compression to occur in the gas-like (low density) and liquid-like (high density) regions to maximize the turbine power output and minimize the pump work input, respectively. Feher [5] and Angelino [6] reported that the power cycle operating at the supercritical state has higher power output compared to a transcritical CO_2 power cycle. Feher [5] also investigated the effect of different working fluids at a supercritical state on the Brayton cycle power output and demonstrated limitations of the Rankine cycle over the Brayton cycle. Similar to the Brayton cycle, supercritical CO_2 Brayton cycle has the potential for high degree of recuperation. Figure 1. 1 shows the process flow diagrams of the simple Rankine cycle, and sCO_2 Brayton cycle with recuperation, and T-s diagram for both power cycles. As Figure 1. 1c shows, the Rankine cycle operates across the liquid-vapor region under the dome while the Brayton cycle operates in the gas region. Due to the nature of the working fluid in the Rankine cycle, heat recuperation is not possible and practical with a simple recuperator, while the high-pressure ratio (typically 3000 to 1) requires multiple turbine stages. The Brayton cycle avoids these issues, but the compression work needed to compress air to the turbine inlet pressure (typical pressure ratio less than 30) is very

high, reducing the net power output and efficiency of the Brayton cycle. Using a supercritical power cycle, the issues associated with the Rankine and Brayton cycles are avoided. It should be noted that similar to the Brayton cycle, a large heat transfer surface area is needed for a supercritical power cycle. Feher [5] selected CO_2 as the working fluid due to moderate critical conditions (pressure and temperature) of the CO_2 . The low critical temperature of CO_2 allows heat rejection at a very low temperature. Thus, temperature difference between the high and low temperature in the power cycle increases resulting in an increase in the power output. There are other gases, including monatomic gases that have even lower critical temperature, but a very low critical temperature makes it difficult to reject heat to the environment.



(a) Simple Rankine cycle with recuperation (b) Simple Brayton cycle with recuperation



(c) T-s diagram for different power cycles

Figure 1. 1 (a) Simple Rankine cycle with recuperation, (b) Simple Brayton cycle with recuperation, (c) T-s diagram of Brayton and Rankine cycles [4, 7]

Feher [5] and Angelino [6] discussed issues concerned with irreversibility of the heat transfer in the recuperator in a sCO_2 power cycle (also called pinch-point problem [3]), and have proposed a recompression cycle to avoid the low pinch-point issue in the recuperated sCO_2 Brayton power cycle. In a recompression cycle, the low and high temperature recuperators (LTR and HTR) divide heat recuperation into two sections with different mass flow rates. A closed sCO_2 Brayton cycle with recompression, also known as a Feher power cycle, is presented in Figure 1. 2a where heat source is an advanced sodium cooled fast nuclear reactor (SFR) or a CSP plant. As shown in Figure 1. 2a, a fraction of the sCO_2 fluid flow is bypassed to the recompression compressor before a precoolers and the pressurized sCO_2 fluid flow is merged with the main flow upstream of the high temperature recuperator.

Due to the high thermal input to a sCO_2 cycle, large amount of recuperation is occurring in the HTR and LTR. These two heat exchangers account for more than 30% of the power cycle cost [4]. Thus, the use of novel highly efficient compact heat exchangers based on diffusion bounded microchannel technology, which offers low terminal temperature difference and pinch point, will increase power cycle efficiency, reduce heat exchanger size and cost, and total cost of the power cycle [3].

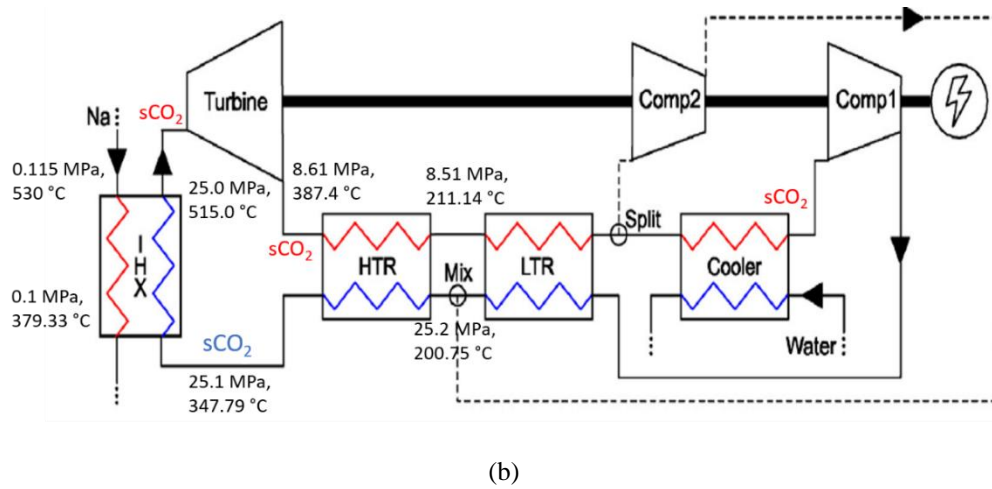
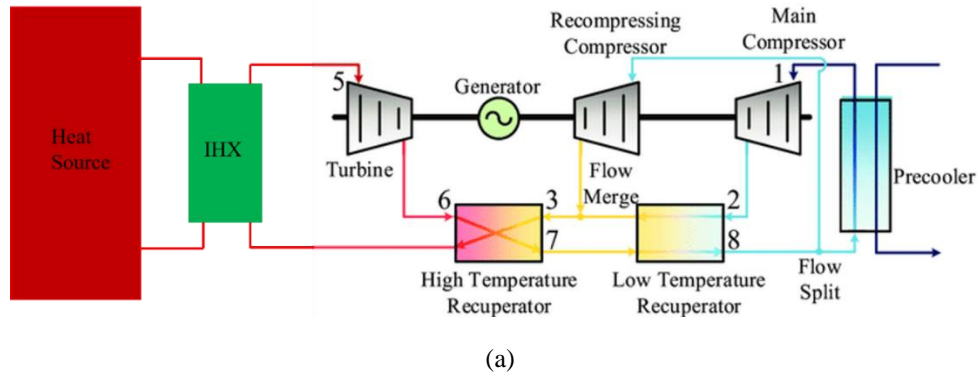


Figure 1. 2. Schematic of (a) $s\text{CO}_2$ recompression cycle arrangement with heat source (b) operating pressures and temperatures of IHX and HTR, HTR and LTR refer to High and Low Temperature recuperators [8]

In a nuclear application, generated heat is transferred from the reactor core by the coolant to the primary loop via the primary heat exchanger placed inside reactor vessel. An intermediate heat exchanger (IHX) transfers this heat to the work cycle, as presented in Figure 1. 2a, or for safety reasons to the secondary or isolation loop (not shown in Figure 1. 2a). Thus, the heat may be transferred between the following combinations of fluids: liquid metal-to-liquid metal (for example, sodium-sodium) and liquid metal-to $s\text{CO}_2$ in a sodium-cooled fast reactor (SFR), or gas-to-gas (helium-to-helium or helium-to- $s\text{CO}_2$) in a Very High Temperature Reactor (VHTR). In a CSP application, the heat transfer circuit is simpler; heat

supplied by the solar tower is transferred by the heat transfer fluid (liquid sodium or solar salt) to the working fluid (sCO_2) via an IHX since the secondary (isolation) loop is not needed.

For all advantages mentioned above, the sCO_2 Brayton cycle is the primary candidate for several missions. In the sCO_2 Brayton cycle, CO_2 is kept at a supercritical state (above the critical pressure and temperature) which provides a single phase¹ working medium throughout the entire cycle. A sCO_2 is considered as a unique working fluid because of its thermo-physical properties. Also, it is inexpensive, non-toxic and non-flammable and reaches critical state at a relatively low temperature and pressure (304.25 K/73.8 bar) [9-11]. Figure 1. 3 shows the critical point (CP) and CO_2 states, including supercritical fluid state, over the pressure and temperature range. Similar diagrams can be constructed for other working fluids.

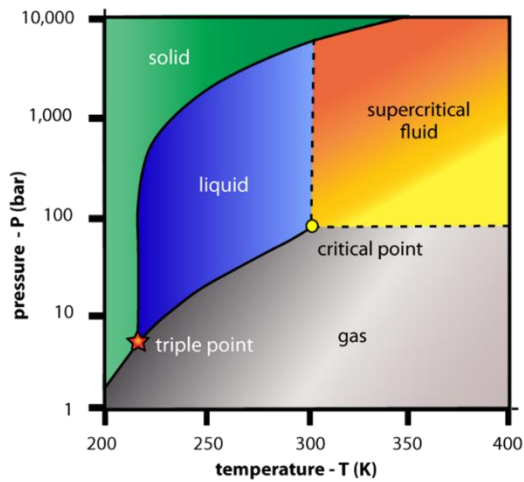


Figure 1. 3. P-T diagram of CO_2

Table 1. 1 lists the primary cycle operating pressure and temperature for different applications, while Table 1. 2 shows operating conditions for a recuperated sCO_2 Brayton power cycle with recompression.

¹ Strictly speaking, there are no phases in a supercritical fluid, just relatively homogeneous supercritical fluid state.

Table 1. 1. Primary cycle operating condition for different applications (IHX)

System	Max. Temperature [°C]	Primary Fluid	Pressure [MPa]	Secondary Fluid	Pressure [MPa]
Nuclear	~ 550	Sodium	0.1	sCO ₂	20-30 or higher
Nuclear	750 to 950	Helium	7	sCO ₂	10-20
Solar	750	Solar salt	0.1	sCO ₂	20-30 or higher

Table 1. 2. Operating conditions for the recuperated Brayton cycle with recompression

System	Max. Temperature [°C]	Primary Fluid	Pressure [MPa]	Secondary Fluid	Pressure [MPa]
HT	~730	sCO ₂	8-9	sCO ₂	20-30
LT	~630	sCO ₂	8-9	sCO ₂	20-30

The compact heat exchangers with mini/micro channel geometry are suitable for coupling different heat sources such as nuclear reactor to a sCO₂ Brayton cycle. Compact heat exchangers operate at high temperature and pressure conditions, where traditional heat exchangers such as shell and tube heat exchangers and plate-frame heat exchangers are unsuitable. Having very high specific heat transfer area and pressure containment, a Printed Circuit Heat Exchanger (PCHE) is a good choice for a sCO₂ Brayton cycle in different applications. PCHEs are generally used for working fluids with moderate heat capacity gas or for supercritical fluids [12, 13]. The PCHE units are typically fabricated using chemical etching and diffusion bonding process.

1.3 Printed Circuit Heat Exchangers (PCHEs)

Advanced heat exchangers, Printed Circuit Heat Exchangers (PCHEs) are compact heat exchangers providing very large specific heat transfer area ($4,000 \text{ m}^2/\text{m}^3$ or higher) and high pressure containment. The very high effectiveness and low terminal temperature difference (2 to 3°C) make a PCHE a competitive candidate for a wide range of applications [13].

Typically, a PCHE is fabricated from a large number of thin substrate plates with chemically etched micro-channels. To form a PCHE block with very high mechanical strength, the plates are diffusion-bonded at high temperature and pressure. Figure 1. 4 shows a formed PCHE block and etched plates, while micrographs of the bonded section showing a complete recrystallization after diffusion bonding process are presented in Figure 1. 5. Development of a diffusion bonding technology has facilitated development of a highly effective and efficient (high rate of heat exchange per unit volume) printed circuit heat exchanger designs with very high heat transfer surface-to-volume ratios [13, 14]. Once bonded, the heat exchanger becomes a monolithic block of metal since the weld fusion line between plates disappears as the grain structure recrystallizes during the diffusion process.

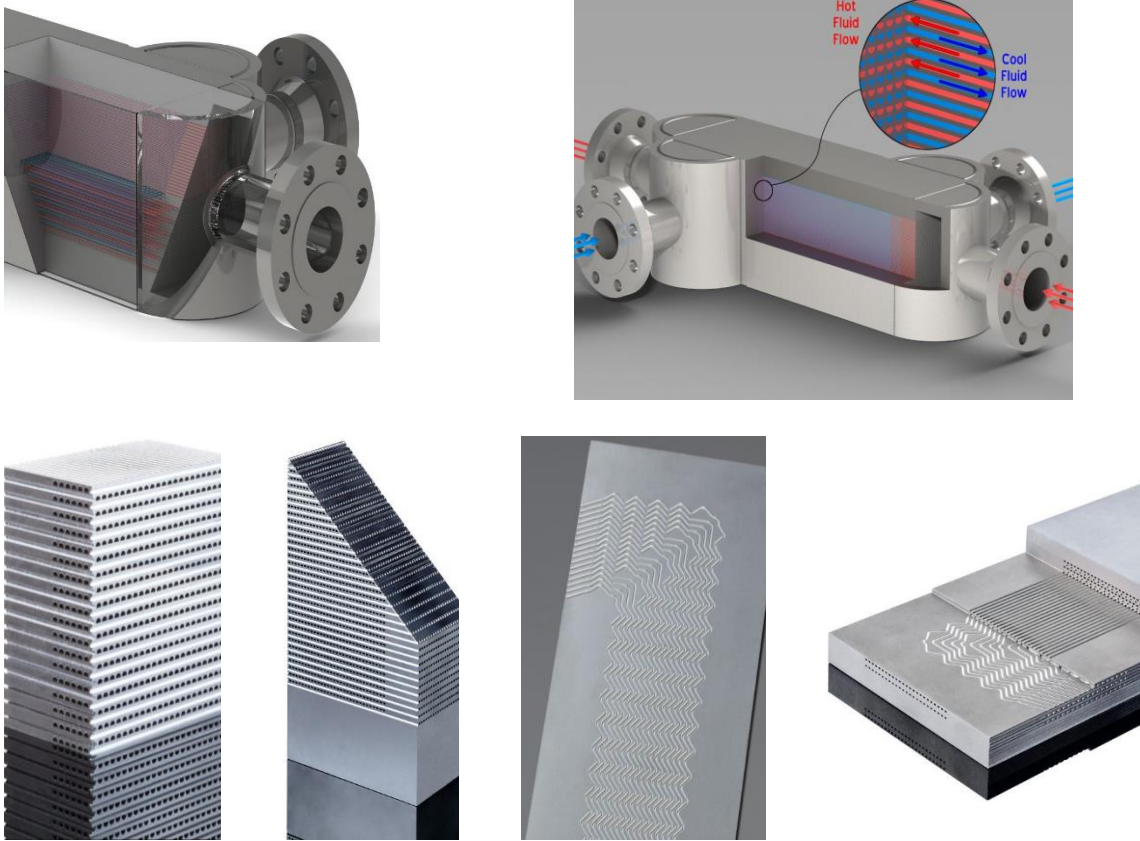


Figure 1. 4. PCHE block and components

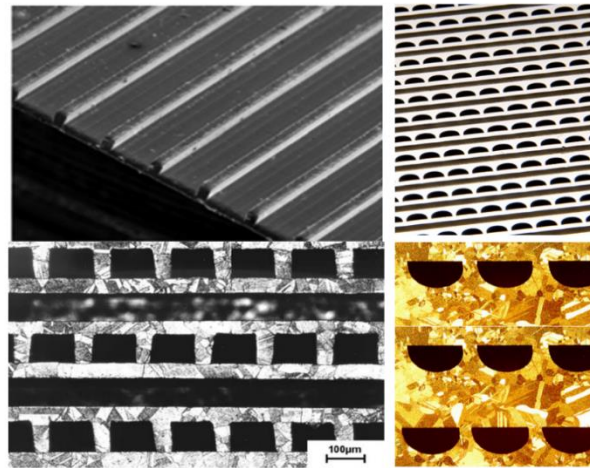

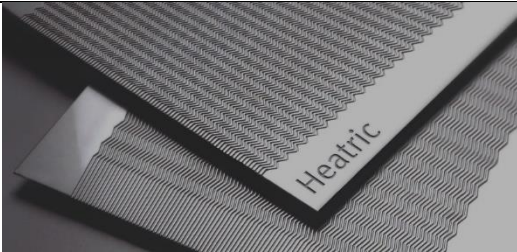
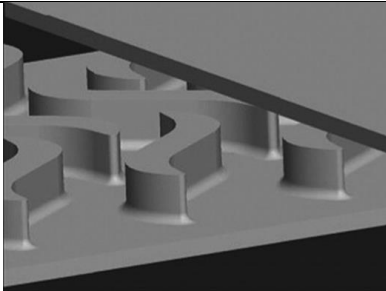
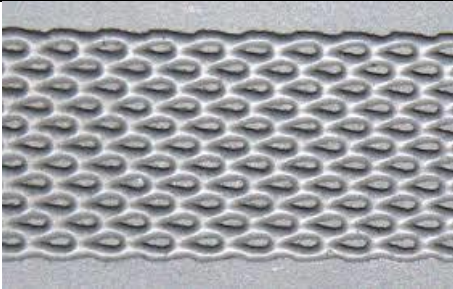


Figure 1. 5. Micrographs of bonded section showing complete recrystallization

The overall performance of a PCHE strongly depends on the geometry of the flow passage (micro-channel) etched in the plates, such as: hydraulic diameter, micro-channel angle, and spacing. Different micro-channel configuration such as straight, zigzag, and sinusoidal

channels and S-shape fin and airfoil fin have been investigated for the PCHE design. Table 1. 3 presents different types of micro-channel configurations and their manufacturers.

Table 1. 3. Micro-channel configurations

Channel type	Developer	Schematic
Straight	Heatric (1985)	
Zigzag	Heatric	
S-shaped fin	Tokyo Institute of Technology (Tsuzuki et al. 2007)	
Airfoil fin	POSTECH (Kim et al., 2008).	

The straight and zigzag channels are most often used by Heatric, the commercial company manufacturing PCHEs. The S-shaped and airfoil fin PCHEs were first developed by the Tokyo Institute of Technology (Tsuzuki et al. 2007) and POSTECH (Kim et al., 2008),

respectively. For typical applications these micro-channel patterns are manufactured with uniform cross-section profile through the entire channel featuring a semi-circular profile. Zigzag channels are more difficult to manufacture and difficult to analyze numerically due to the effect of certain geometric parameters, such as rounding at the channel bends and resulting in flow separation and turbulence generation.

Thermo-hydraulic performance of straight and zigzag micro-channels has been investigated numerically and experimentally over a range of geometric parameters for sCO₂ and s-Helium as working fluids. Each channel type has certain advantages and disadvantages. Table 1. 4 lists thermal and hydraulic performance of different micro-channel designs compared to the straight channel design.

Table 1. 4. Thermal and hydraulic performance of PCHE channel types

Channel Type	Pressure drop	Heat transfer	Cost
Straight	Low	Good	reasonable
Zigzag	Very high	high	high
Sinusoidal	medium	Medium	high
S-shape fin	Low	Medium	high
Airfoil fin	Low	Medium	high

PCHEs may have different specifications and cross-section channel shapes, such as semi-circular, rectangular, circular, and trapezoidal. Figure 1. 6 shows a conventional semi-circular geometry of the PCHE core employing straight micro-channels and a counter-flow arrangement. Figure 1. 7 illustrates rectangular micro-channels. It should be noted that the channel size and shape depend on the application. Micro-sized semi-circular channels are

widely used for recuperators and general use heat exchangers. To simulate performance of a PCHE core, a representative section of the core is selected for the analysis.

The channel size also affects the flow regime, which could be laminar, turbulent, or transitional depending on the channel size (hydraulic diameter) and mass flow rate of working fluid(s). Very small hydraulic diameter (micro-channel size) compared to its length makes the flow laminar fully developed resulting in higher effectiveness and lower axial conduction compared to the mini-sized channels. As the channel hydraulic diameter increases, the flow regime transitions to turbulent.

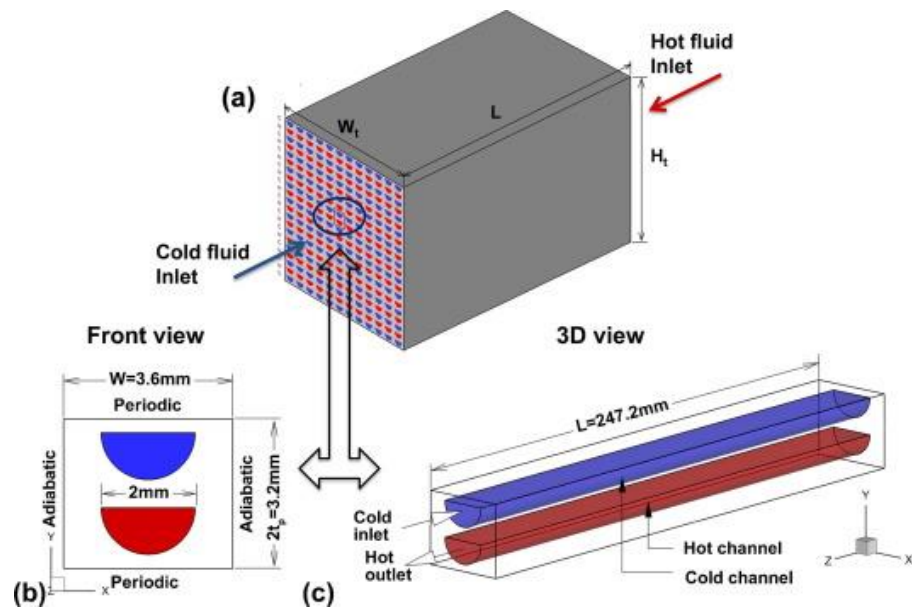


Figure 1. 6. General overview of a semi-circular micro-channel PCHE [15]

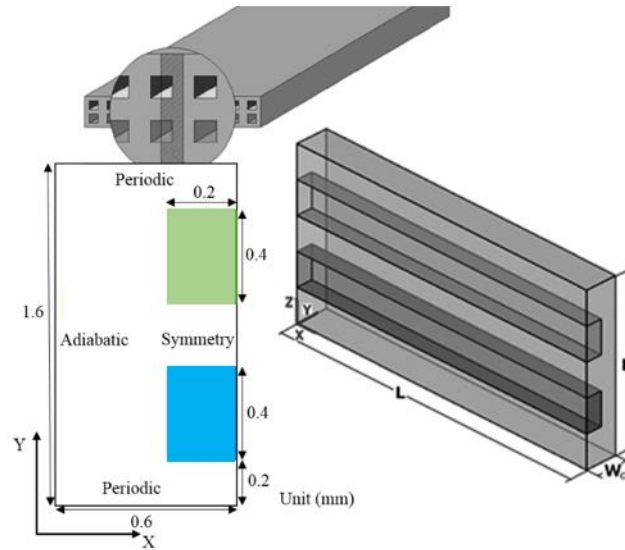


Figure 1. 7. General overview of a rectangular micro channel PCHE

The three important PCHE parameters include: heat transfer, pressure drop, and mechanical integrity. The design goals are to maximize heat transfer, minimize pressure drop, improve thermal performance and reduce the size, while maintaining mechanical integrity of a PCHE.

1.4 Significance and novelty of the project

In a conventional PCHE design, micro-channels are etched on one side of the plate. This work is concerned with the design where both sides of the plate are etched forming the double-etched micro-channel design configuration. In this advanced micro-channel topology, sometimes referred to as double-banking micro-channel design, shim plates are needed to construct a PCHE stack using diffusion bonding, as presented in Figure 1. 8. The straight channels of a semi-circular cross sectional shape are etched on both sides of the plate in a staggered arrangement to increase the heat transfer area per unit volume, minimize PCHE size, improve metal utilization and reduce the cost, and minimize pressure loss and pumping requirements (parasitic power requirements). However, as thermal performance of a PCHE is

increased by increasing the complexity of the PCHE design and channel geometry, e.g., zigzag channels, pressure drop of the working fluid flowing through the PCHE increases. Double-etched configuration offers several advantages such as higher heat transfer surface area, increased volume flow rate of the hot and cold fluids, and lower pressure drop compared to the conventional single side etching design. Double-etching and double-banking investigated in this study are novel concepts not studied previously even by the leading developers of the PCHE technology such as Sandia National Laboratory, University of Wisconsin at Madison, or Heatric (UK PCHE manufacturer).

The objective of this study is to apply numerical analysis and genetic optimization algorithm to design a very compact core of a PCHE for a $s\text{CO}_2$ Brayton power cycle employing advanced micro-channel geometry and topology.

The main objectives of this work are the following:

- Examine the design and operating conditions and perform a parametric sensitivity analysis to determine the effect of working fluid properties on thermal and hydraulic performance of a PCHE.
- Investigate a simultaneously developing and hydro-dynamically fully-developed flow and conjugate heat transfer in a semi-circle micro-channel for $s\text{CO}_2$ and liquid sodium as working fluids and laminar flow regime.
- Provide a design methodology and a CFD-based approach for PCHE design engineering and analysis by developing a design-by-analysis method for design optimization.
- Understand and develop the design optimization process and methodology.

- Combine the design optimization and CFD design tools for advanced power plant thermodynamic components.
- Design a counter-current flow arrangement PCHE with straight micro-channels for high-temperature and moderate operating pressure conditions using Alloy 617 and Alloy 230.

Two new micro-channel designs and arrangements (topologies); staggered semi-circle and double banking shown in Figure 1. 8, and staggered double-banking circle channels shown in Figure 1. 9 photo-chemically etched on both sides of the plate (double-etched) were designed in this research study. Their thermo-hydraulic performance was determined and compared to the conventional semi-circle micro-channel design.

Three-dimensional Navier-Stokes and energy equations describing simultaneously developing flow and conjugate heat transfer in the PCHE micro-channels in the counter-flow arrangement were solved numerically using the Fluent code, computational fluid dynamics (CFD) software ANSYS. Thermo-physical properties of the working fluid (sCO_2) were determined using REFPROP NIST database coupled to Fluent. Accurate determination of thermo-physical properties of sCO_2 is very important since those vary significantly around the critical point. Thermo-elastic analysis of the PCHE core to determine stresses was performed using the Finite Element Method (FEM).

Schematic of the staggered double-etched pattern for the sCO_2 - sCO_2 application (recuperator) is presented in Figure 1. 8. The advantage of the novel double-etched and double-banking geometry is a considerably better utilization of the metal and, hence larger specific heat transfer area (heat transfer area per volume of the heat exchanger), more compact design, and lower weight and cost, compared to the conventional single-side etching. The channel

geometry: hydraulic diameter, width, spacing, and channel offset were determined based on the allowable stresses with the goal of maximizing the specific heat transfer area and overall heat transfer rate between the hot and cold fluid channels, while minimizing heat exchanger volume. Thermo-hydraulic performance of the novel PCHE geometries was investigated for the laminar flow regime.

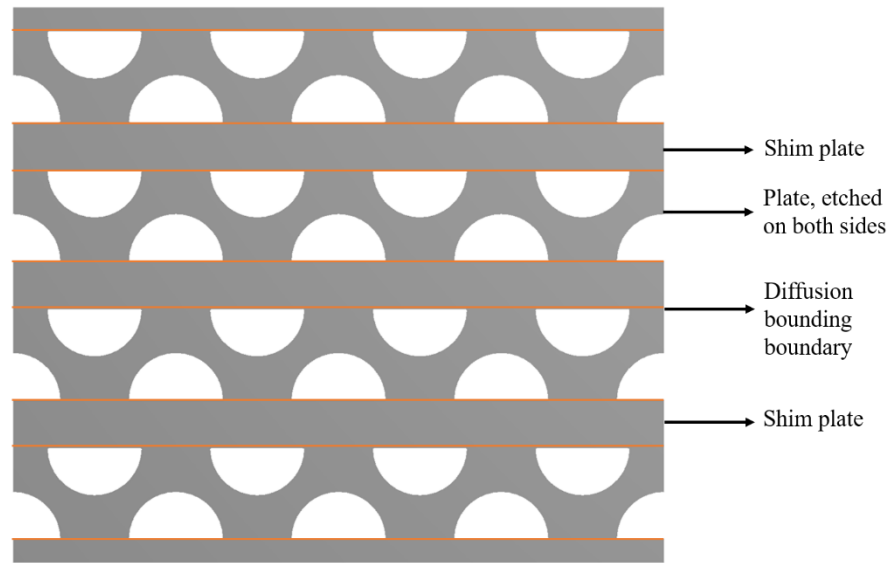


Figure 1. 8. Schematic of semi-circular staggered double-etched, double banking geometry

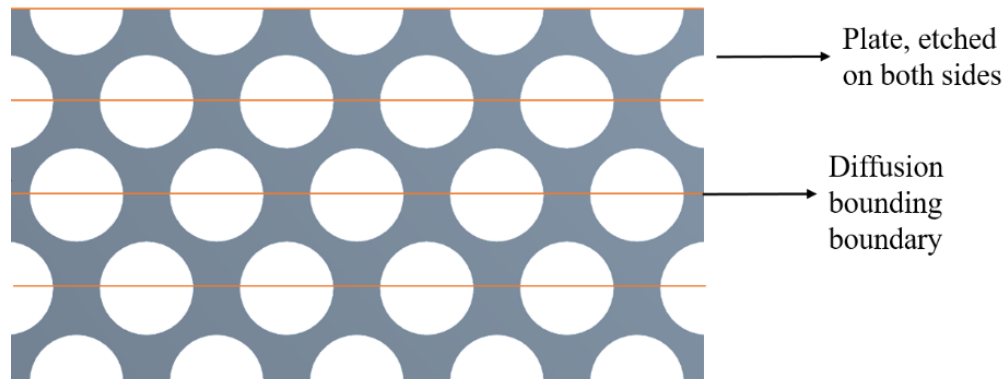


Figure 1. 9. Schematic of circular staggered double-banking pattern

The main advantage of the novel staggered double-banking circular design involves circular geometry of the micro-channels where corners as stress concentration points and

regions of very low local heat transfer coefficient are avoided, as shown in Figure 1. 9. This channel design and topology was applied to the IHX operating with the liquid metal and $s\text{CO}_2$ as the hot and cold working fluids (the liquid metal- $s\text{CO}_2$ configuration), and to the recuperator operating with $s\text{CO}_2$ as both the hot and cold working fluid (the $s\text{CO}_2$ - $s\text{CO}_2$ configuration).

Thermo-hydraulic performance of both geometries, i.e., the Nusselt number, Fanning Friction Factor (friction coefficient) and the overall heat transfer coefficient U between the hot and cold channels, pressure drop, and maximum stress, were determined and are reported in this work. The results obtained for the novel design configurations were compared to the “conventional” semi-circular single-etched (single side etched) micro-channel design for the counter-flow arrangement. The counter-flow arrangement was selected for the analysis due to its better thermal performance compared to the parallel-flow arrangement.

A PCHE used in the above-mentioned applications is envisioned to operate at very high temperature and pressure, or high pressure difference between the hot and cold fluids and will be subject to high stresses, thus it needs to be manufactured of very expensive high Nickel alloys. Since the proposed novel designs offer a better utilization of metal and higher heat transfer coefficient, the benefits of the advanced design include a more compact (smaller) and lighter heat exchanger, and thus lower and more competitive cost compared to the conventional design.

1.5 Previous works

The channel size, shape, and configuration of various PCHE designs have been widely studied, however the optimum configuration has to be determined for a specific application. It should be noted that the enhancement of thermal performance of a PCHE that could be achieved by changing the channel size and configuration (topology) can be challenging since

thermal performance and structural integrity of the heat exchanger have to be evaluated concurrently.

Hesselgreaves [16] studied heat transfer and pressure drop in compact heat exchangers and improved corresponding correlations for different configurations. Dostal et al. [3] performed a design analysis of a PCHE intermediate heat exchanger for a supercritical CO₂ Brayton cycle and has performed the cost and the weight analyses for the next generation nuclear power plant. A Heatric PCHE was selected as a base model and a simplified stress analysis was performed to adjust the plate thickness and plate pitch for specific operating pressure used in the sCO₂ Brayton power cycle loop. The optimum operating condition was found to render the lowest cost, as well as the reduction in maximum stresses in the PCHE that the structural material can withstand. Pra et al. [17] performed an experiment using an air test loop to determine temperature field and the thermal and mechanical stress variation of a mock-up PCHE used as a recuperator in the High Temperature Reactor during thermal shock. Computational Fluid Dynamics (CFD) and Finite Element analyses were carried out to understand variation of thermal stresses in the walls of hot and cold channels and identify critical locations with severe thermal strains. The analysis at steady-state conditions was also performed to obtain pressure loss and thermal duty of the recuperator. The authors pointed out that the most critical locations of thermo-mechanical stresses are the core-header connections, and it is impossible to measure the values of thermal strain and deformations at these locations. Lee and Lee [18] numerically investigated thermal and mechanical stresses in an IHX for a sCO₂ Brayton cycle under the steady-state operating conditions. The temperature distribution was determined using FLUENT and imported into the ANSYS-mechanical to determine thermal and mechanical stresses. The Plane strain model was utilized to calculate stresses for

a PCHE representative unit cell. The authors applied unconstrained boundary conditions to the model sides for the stress analyses and assumed that ANSYS-mechanical adds a weak spring to the sides to restrain the rigid body motion. The effect of the number of micro-channels in each row and column in the PCHE unit on the thermal and mechanical stresses was also studied. The departure from the linear elasticity at the channel corners was depicted. They noted that the simplified stress calculation method, based on a thick cylinder assumption, may underestimate numerically predicted stresses due to not considering the periodic and thermal stresses in the model. Natesan et al. [19] investigated issues associated with a PCHE IHX for the high temperature power generation system using helium as the working fluid in the primary heat transfer loop. The hot fluid temperature at the IHX outlet (gas turbine inlet) was about 850-900 °C. Numerical analysis of the hydraulic-thermal performance of the PCHE was performed to obtain the pressure losses and temperature distribution at the steady-state operating conditions. The temperature distribution in the solid domain was used to calculate thermal stresses in the solid domain. Alloy 617 was chosen as the structural material with the temperature-dependent mechanical properties. In the analysis of the thermal and mechanical stresses, axial deformation of zero and generalized plane strain deformations (constant displacement) were assumed for the hot and cold ends, respectively. The allowable design life for Alloy 617 was assessed based upon the IHX operating pressure and temperature.

Many researchers performed numerical studies of the flow and heat transfer performance of PCHEs [1, 20-25]. Shi et al. [26] numerically investigated the friction coefficient and heat transfer for the sCO₂ and molten salt as working fluids flowing in a rectangular-airfoil fin PCHE. The effect of mass flux and inlet temperature on the heat transfer and pressure drop was studied. The results obtained for this type of PCHE were compared to

those of straight and zig-zag channel PCHEs. It was found that increasing the inlet temperature of molten salt results in a decrease in the sCO_2 heat transfer performance but an increase in the molten salt heat transfer performance. Also, it was reported that the airfoil PCHE provides the best heat transfer performance, compared to the straight and zigzag PCHE types. Kim et al. [9] established a mathematical expression for predicting thermal performance of a PCHE with semi-circular micro-channels considering parallel-, counter-, and cross-flow arrangements. They studied the effect of channel size and length on thermal performance of PCHEs. It was determined that thermal performance of a PCHE depends on geometric parameters (micro-channel topology), material properties, and flow arrangement. Marchionni et al. [27] performed a numerical investigation to obtain an off-design performance map of a 630 kW PCHE for a sCO_2 energy conversion system (power cycle). The developed map provides a visualization of the effect of variation in thermo-physical properties of sCO_2 on the flow and heat transfer performance of the PCHE. Guo and Huai [28] studied the behavior of CO_2 under supercritical operating conditions in a recuperator, investigated thermal performance of the recuperator under sudden changes in specific heat and density of sCO_2 , and adopted a methodology to deal with this challenge. Also, the effect of heat capacity rate on the frictional entropy generation, and thermal conductivity and wall thickness on the axial conduction were explored. Li et al. [29] developed a semi-empirical correlation, based on the numerical and experimental approaches, for a turbulent flow using sCO_2 as a working fluid in a semi-circular PCHE micro-channel. Researchers [15, 30-32] have studied different PCHE's configurations and channel arrangements and their results concerning thermal and hydraulic performance were compared to the straight channel PCHEs.

PCHEs with different channel geometries such airfoil fin (AFF), S-shape and sinusoidal (in the axial direction) were investigated by a number of researchers [10, 33, 34]. Chu et al. [35] considered a NACA four-digit airfoil fin PCHE to investigate its thermo-hydraulic performance as a recuperator in a sCO₂ Brayton cycle. Different airfoil profile and layout configurations were selected, and the flow and heat transfer results were compared. It was determined that on average AFFs may improve the heat transfer performance, accompanied by a pressure drop increase. Li et al. [36] numerically studied flow characteristics of an AFF PCHE used in a sCO₂ Brayton cycle and proposed two AFF PCHE types to reduce the effect of the impact area on the local flow resistance. The flow drag reduction was used in analysis of hydraulic performance.

A number of experimental research studies have been conducted to explore and characterize hydraulic and thermal performance of PCHEs. Cheng et al. [37] experimentally investigated thermal and hydraulic performance of a PCHE using sCO₂ as a working fluid in a pre-cooler in a supercritical Brayton cycle. They studied the effect of mass flow rate and temperature on the effectiveness of the selected PCHE and the pressure drop. Zhou et al. [38] constructed a test platform and conducted experiments to explore thermal and hydraulic performance of a PCHE recuperator. The aim of the study was to verify if the recuperator prototype meets the heat transfer effectiveness and pressure drop requirements as a parallel module. It was found that the PCHE recuperator heat transfer effectiveness of >92% and pressure drop of <250 kPa meet the requirements of a full-scale PCHE recuperator in a MW-class sCO₂ Brayton cycle. An IHX PCHE was selected to investigate functionality of the PCHE in the molten salt/liquid sodium-sCO₂ arrangement by Aakre and Anderson [39] in the test loop at the University of Wisconsin. The purpose of this study was to compare measured values

of terminal temperatures and pressure drop with those calculated by using the existing heat transfer and flow correlations. The experiments were performed for a range of mass flow rate and temperatures under steady state flow conditions. Pidaparti et al. [40] experimentally investigated thermal-hydraulic performance of the rectangular and airfoil fin PCHEs and compared to those of zig-zag PCHE for the sCO₂ power cycles. It was found that the Nusselt number in the rectangular fin PCHE is higher compared to the zig-zag PCHE. Also, the size of PCHE can be reduced up to 25% using fin-type PCHEs. To determine the heat transfer and pressure drop characteristics of sCO₂ in proximity of the Critical Point (CP), Bae et al. [41] conducted an experiment using a diffusion-bounded PCHE in a sCO₂ test loop at KAIST. They studied the multi-phase pressure drop and heat transfer of CO₂ near the CP and a set of correlations was reported for two-phase CO₂ flow. Measurement of a heat transfer coefficient for a supercritical CO₂ was performed by Jajja et al. [42] in a micro-channel channel subjected to the non-uniform heat flux. The effect of variation of thermo-physical properties of CO₂ near the CP on the pressure drop and heat transfer was studied. They also determined the effect of mass flow, variable heat flux, temperature, and variable reduced pressure ($P_r = P/P_c$, where P_c is the critical pressure) on the heat transfer coefficient. A set of correlations was developed for buoyancy and flow acceleration, and the results were compared to the available correlations. Baek et al. [43] experimentally studied hydro-thermal performance of a cryogenic PCHE and determined its pressure drop and thermal effectiveness. They also determined that for low Reynolds numbers the axial conduction plays important role in heat transfer. Thermal-hydraulic performance of a rectangular microchannel PCHE was studied experimentally for waste heat recovery by J. Yih and H. Wang [44]. A two-pass cross-flow micro-channel PCHE was selected. The heat transfer effectiveness for different working fluids under variation of

flow temperature was reported. The effectiveness of 88–98% was calculated for the rectangular cross-flow PCHE.

The optimization techniques have been widely employed in design engineering to reduce the computational design time and costs and develop the optimal geometry configurations. Generally, optimization techniques involve multiple disciplines and objectives. Multiple tasks and objectives are simultaneously considered in a multi-objective optimization. Deb et al. [45] developed a Non-dominated Sorting Genetic Algorithm (NSGA-II) and performed a multi-objective optimization to obtain Pareto-optimal solutions. Goel et al. [46] performed a multi-objective optimization with NSGA-II using Response Surface Approximation (RSA) as a surrogate model. Husain and Kin [47] conducted a CFD simulation for rectangular micro-channel heat sink in laminar flow regime to explore the effect of micro-channel geometry on thermal resistance and power pumping. A multi-objective optimization was performed to determine optimum geometry of the micro-channel heat sink using a surrogate model in combination with the local search strategy with temperature-dependent thermo-physical properties of the material. Li and Kim [48] optimized the geometry of a pin-fin arrays micro-channel using local search strategy and NSGA-II. The NSGA-II was coupled with RANS flow and heat transfer in a 3D channel. Lee and Kim [49, 50] optimized a conventional zigzag PCHE with the single- and double faced channels using multi-objective genetic algorithm.

A hybrid multi-objective algorithm coupled with RSA in a RANS flow and heat transfer was employed in this work to determine the optimal topology of the hot and cold channels and investigate interaction between the thermal and hydraulic performance.

1.6 Overall PCHE performance, effectiveness-NTU theory

The heat exchanger sizing and heat transfer rate are used to quantify thermal design and thermal performance of a PCHE. The total heat transfer rate Q , heat transfer surface area A_s , heat capacity rate C , fluid terminal temperatures, and overall heat transfer coefficient U are determined to evaluate thermal performance of a heat exchanger.

In the numerical analysis, the mass flow rate of the hot and cold fluids and temperatures at the hot and cold side inlets a PCHE are known. The computational fluid dynamics is used to numerically determine pressure drop, and hot and cold temperatures at the heat exchanger exit. The heat transfer performance characteristics such as overall heat transfer coefficient U , number of transfer units NTU and PCHE effectiveness ε can be obtained by using pressure drop and heat transfer performance characteristics. The overall heat transfer coefficient U indicates the overall heat transfer resistance of the system. The overall heat transfer coefficient can be calculated using the log mean temperature difference method (ΔT_{LMTD}) [51].

$$U = \frac{Q}{A_s \Delta T_{LMTD}} \quad (1.1)$$

The heat load Q of a PCHE is given as:

$$Q = \dot{m} c_p (T_i - T_o) \quad (1.2)$$

Where \dot{m} is the mass flow rate of the working fluid, c_p is specific heat, and T_i and T_o are the inlet and exit fluid temperatures. For the counter-flow arrangement, ΔT_{LMTD} is given as:

$$\Delta T_{LMTD} = \frac{(T_{hi} - T_{co}) - (T_{ho} - T_{ci})}{\ln\left(\frac{T_{hi} - T_{co}}{T_{ho} - T_{ci}}\right)} \quad (1.3)$$

Where T_{ci} , T_{co} , T_{hi} , and T_{ho} are mass-weighted average temperature at the cold and hot inlets and exits, respectively.

The overall heat transfer coefficient U may be written in terms of total thermal resistance R_t .

$$U = \frac{1}{A_s R_t} \quad (1.4)$$

For a pair of the hot and cold channels, the total thermal resistance is given as:

$$R_t = \frac{1}{h_h A_s} + \frac{1}{h_c A_s} + R_c \quad (1.5)$$

Where quantities R_c , h_h and h_c are thermal resistances to conduction and convection on the hot and cold sides, respectively. Thermal resistance to conduction is dependent upon the solid material and wall thickness between the hot and cold channels (fin thickness) while thermal resistance to convection is strongly dependent on the mass flow rate (Reynolds number or flow regime), channel geometry, and its size (hydraulic diameter).

The number of transfer units NTU is a well-known dimensionless number used to determine the required heat exchanger unit size in the heat exchanger design i.e., the heat exchanger duty when exit temperatures of cold and hot working fluids are not known. NTU is calculated as:

$$NTU = \frac{UA_s}{C_{\min}} \quad (1.6)$$

Where C_{\min} is the minimum of the heat capacity rates of the hot and cold channel fluids. The capacity rate is a product of the mass flow rate and specific heat of a fluid stream. Since the specific heat of sCO_2 is a function of pressure and temperature in the channel, and the ε -

NTU method assumes constant fluid properties, the average specific heat has to be calculated along the channel length.

In the steady-state operation, the conservation of energy states in the absence of heat losses, the heat transfer rates for the hot and cold channels exchanging heat are equal. As Equation (1.7) shows, the maximum temperature change is associated with the stream having a minimum heat capacity rate C_{\min} . The maximum heat transfer capability of a heat exchanger is given as:

$$Q_{\max} = C_{\min} (T_{hi} - T_{ci}) \quad (1.7)$$

The heat exchanger effectiveness ε is defined as:

$$\varepsilon = \frac{Q}{Q_{\max}} \quad (1.8)$$

The heat rate Q can be either the hot or cold side heat rate [51]. The effectiveness of a heat exchanger can be determined from the heat capacity rate and terminal temperatures. The LMTD and ε -NTU approaches are widely accepted in the calculation of heat exchanger performance. The overall heat transfer coefficient is calculated using the LMTD method based on the values of inlet and outlet bulk fluid temperatures and mass flow rates. The ε -NTU method is employed if the values of fluid temperature at the heat exchanger outlet are unknown. Using the LMTD method in this case requires solving a nonlinear system of two equations, Equation (1.1) and Equation (1.3). It should be noted that for a constant heat transfer area and heat transfer coefficient, the larger LMTD means higher heat transfer rate. However, the use of LMTD method is limited by the requirement of constant flow rate and constant thermal properties of the working fluids [52]. In the LMTD method, it is assumed that specific heat in particular, does not change and the overall heat transfer coefficient is constant and is not a

function of temperature. It is further assumed no phase change occurs and change in kinetic and potential energies is negligible [51].

The ϵ -NTU method is used to determine outlet temperatures of the working fluids without solving a nonlinear system of two equations. The ϵ -NTU method can be used for various flow arrangements, such as parallel and counter-current flows. Effectiveness ϵ is a function of NTU where NTU is calculated using the minimum heat capacity rate C_{\min} and overall heat transfer coefficient U . The ϵ -NTU method assumes that the specific heat is constant, which makes this method unsuitable for thermal analysis of a heat exchanger using $s\text{CO}_2$ as working fluid, especially for operating conditions close to the CP. A suitable method of calculating the overall heat transfer coefficient, Nusselt number, and friction coefficient in cases where there is a significant variation in thermal properties through the heat exchanger is the Integration method described in Section 6.8.2 of Chapter 6.

1.7 Outline of the study

A brief outline of the study is presented in this section. Chapter 1 (Introduction and Problem Statement) briefly describes research objectives, scope of the research project, specific objectives and expected outcomes, a review of previous work on PCHEs done by others and heat exchanger performance and parameters affecting it. A short description of the heat exchanger design/analysis theories and methods (LMTD and effectiveness-NTU) is also provided.

In Chapter 2 (Governing Equations and model validation), the governing equations for the simultaneously developing flow and conjugate heat transfer problem are described. The solver for the numerical analysis was chosen and used for water with constant thermo-physical properties. The results were validated against the exact (analytical) solution reported by Shah

and London [53]. The axial conduction phenomenon in the conjugate heat transfer is presented and the results obtained for the conjugate heat transfer problem and pure convection heat transfer problem were compared for the high and low Prandtl number fluids.

In Chapter 3 (Supercritical CO₂), thermo-physical properties of a supercritical CO₂ and definitions of dimensionless parameters such as Nusselt number and friction coefficient are presented. The effects of sCO₂ properties on heat transfer and pressure drop were determined and analyzed for a specific channel geometry.

In Chapter 4, (Validation of numerical model) thermo-physical properties of liquid sodium are presented, and the heat transfer characteristics and axial conduction for low Prandtl number fluid (liquid sodium) were determined and compared to the values reported by Shah and London [53]. The liquid sodium and sCO₂ were used as hot and cold working fluids in a PCHE, respectively and the analysis was performed to determine the effect of large variation of thermo-physical properties of sCO₂ with pressure in the vicinity of CP on thermal performance of a PCHE for both the parallel and counter-flow arrangements.

In Chapter 5 (Finite Element Analysis-boundary conditions for stress calculations), the applicability of the Finite Element Method (FEM) for predicting stresses in a micro-channel PCHE geometry was studied. A section of the PCHE, representing PCHE core, including a pair of hot and cold semi-circular micro-channels was selected for structural assessment for conditions corresponding to the steady-state operation. A sensitivity analysis was performed to determine the appropriate boundary conditions for the stress integrity evaluation of the novel PCHE topology.

In Chapter 6 (Advanced Micro-channel geometry and Topology-Double-etched staggered geometry), the operating pressure and temperature corresponding to a High

Temperature Recuperator (HTR) used in a $s\text{CO}_2$ recompression Brayton cycle were considered for a $s\text{CO}_2$ - $s\text{CO}_2$ PCHE recuperator. An optimization of fin and shim plate thicknesses for the staggered double-etched and double banking topologies of the semi-circular channels subject to the constraint of maximum allowable stress was performed. The Multi-Objective Genetic Algorithm (MOGA) in ANSYS was used to determine the optimized PCHE core topology such as the channel pitch and fin and the shim plate thicknesses. Thermal and hydraulic performance of the optimized geometry was obtained and CFD results were compared to those obtained for the semi-circular conventional geometry for the same working fluids. Also, an analysis of the heat exchanger performance employing the optimized geometry was performed using the effectiveness-NTU theory of heat exchangers.

In Chapter 7 (Advanced Micro-channel geometry and Topology- staggered double-banked circular geometry), the operating conditions of an IHX used in a $s\text{CO}_2$ recompression Brayton cycle were considered as the cold and hot working fluids in a $s\text{CO}_2$ -liquid sodium IHX. The MOGA was employed to optimize the IHX topology by obtaining the optimum fin thickness between the hot and cold channels subject to the constraint of the maximum allowable stress. A CFD simulation was performed to determine thermal and hydraulic performance of the optimized IHX geometry for the selected pressure and temperature conditions. CFD results obtained for the optimized geometry were compared to the results obtained for the conventional IHX geometry. The effectiveness-NTU theory of heat exchangers was applied to calculate thermal performance of the analyzed IHX. Alloys 617 and 230 were considered as candidate materials of construction of the IHX and structural analysis was performed for both alloys. Structural analysis and optimization of the IHX geometry were conducted for Alloy 617 first and then repeated for Alloy 230. Since the maximum allowable

stress for Alloy 230 is considerably higher compared to Alloy 617, the use of this alloy allows the size of the IHX to be reduced.

Chapter 8 (Conclusions and recommendations for future research) summarizes major contributions to the state-of-the-art of the PCHE channel geometry and topology, accomplishments of this research work, conclusions, and recommendations for further work.

CHAPTER 2: GOVERNING EQUATIONS AND CONJUGATE HEAT TRANSFER PROBLEM

2.1 Overview

The conjugate heat transfer and pure convection heat transfer problems are described in this section. The governing equations for solving a simultaneously developing flow and conjugate heat transfer problem in a duct (channel) and conduction heat transfer in a solid domain (channel walls) for steady-state conditions are presented. The numerical solver used in this research work is also presented. The grid independence study was performed for different channel cross-section geometries including square, semi-circle and circle geometries used in this research work. The dimensionless parameters used in the data reduction analysis are presented in Section 2.4.

To better understand and explain the heat transfer mechanisms and conjugate heat transfer problem in an elemental micro-channel heat exchanger, a numerical model for a 3D square-shaped micro-channel was developed to study the conjugate heat transfer in a micro-size channel for different working fluids [1, 25]. The physical model, boundary conditions and modeling assumptions used in the numerical model are described. The Nusselt number and friction coefficient obtained in CFD simulations performed for a number of working fluids including liquid sodium, air, supercritical CO₂, water and engine oil (SEA 30) covering a wide range of Prandtl number values were compared to the values reported in the literature. Thermo-physical properties of the working fluids were assumed constant in these calculations.

2.2 Conjugate heat transfer problem

Convection and conduction are major heat transfer modes in the fluids and solid materials. In a pure convection, heat is transferred between the surface and a fluid moving over the surface due to bulk momentum of flow molecules or significant diffusion of matter, while

in a pure heat conduction, thermal energy is transferred by the microscopic motion, vibration and collision of solid particles in the presence of temperature gradient [51]. The conjugate heat transfer is important when the convection heat transfer coefficient h needs to be calculated at the solid-fluid interface in the presence of not-negligible axial conduction in a fluid and solid wall. Since there is no theoretical approach for calculating the convection heat transfer coefficient, this quantity is determined through experiments. In the last decades, with the development of computational fluid dynamics (CFD), empirical correlations for convection heat transfer coefficient were replaced by the conjugate heat transfer analysis. The conjugate heat transfer analysis describes heat transfer between the solid body submerged in a fluid flow. In the conjugate heat transfer analysis, the heat conduction equation, Navier Stokes equations, and energy equation are solved separately for the fluid and solid subdomains. The values of wall heat flux and temperature are matched at the solid-fluid interface. Figure 2. 1 shows the fluid and solid subdomains and the fluid-solid interface. In a conjugate heat transfer problem, the wall heat flux and temperature at the solid-fluid interface are unknown and depend on thermal properties of the solid material and the fluid, the flow regime, and geometry of the solid subdomain such as hydraulic diameter for the internal flow. Considering an analytical solution for the boundary layer in the fluid subdomain and solving a heat conduction equation in the solid subdomain, one can obtain $q_{wf} = f_1(T_{wf})$ and $q_{ws} = f_2(T_{ws})$ where q_{wf} and q_{ws} are wall heat fluxes at the fluid subdomain and solid subdomain interface. Since $q_{wf} = q_{ws}$ at the solid-fluid interface, an equation for determining wall temperature field can be developed.

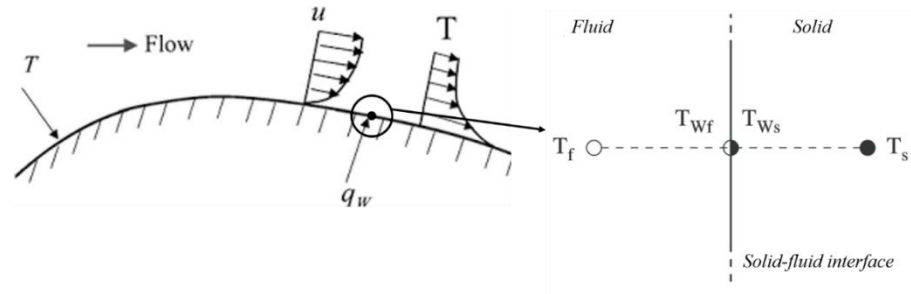


Figure 2. 1. Solid-fluid interface in conjugate heat transfer

As shown in Figure 2. 2, there are two solid-fluid interfaces in heat exchangers, the hot side interface and the cold side interface. Temperature field within the solid wall and the wall temperatures at both hot and cold side interfaces can be determined accurately by the numerical analysis of the conjugate heat transfer problem, thus allowing for the accurate determination of the convection heat transfer coefficient.

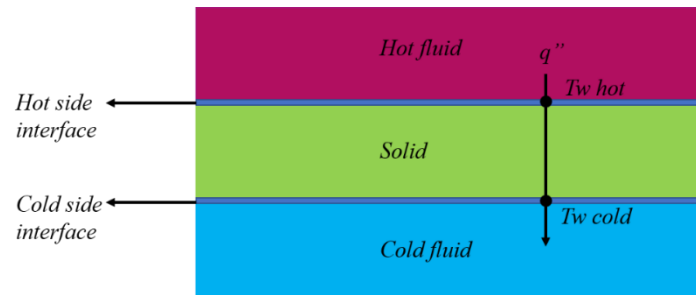


Figure 2. 2. Hot and cold side interfaces in a heat exchanger

2.2.1 Axial conduction in the conjugate heat transfer

In the conjugate heat transfer problems, the convection heat transfer mode dominates conduction heat transfer in the macro-size channels and axial heat conduction in the channel wall may be neglected because the channel wall thickness is small compared to the channel hydraulic diameter. However, in the micro-size channels the effect of axial conduction cannot be neglected since the cross-section area of the solid wall is comparable to the cross-section area of the channel [54]. Thus, axial heat conduction in channel walls affects heat transfer in micro-channels [25]. Therefore, the heat transfer values reported in the literature for the micro-

channels deviate from the values obtained from established heat transfer correlations. Figure 2. 6 shows the Nusselt number values obtained in this study. The results show that the Nusselt number decreases at the channel exit because axial conduction decreases wall heat flux at the channel exit [1, 25]. In summary, the axial heat conduction is affecting the value of heat flux along the channel wall. The effect is more pronounced with variation of Peclet number ($Pe=Re.Pr$) where Pr is Prandtl number. For high values of Pe number, axial heat conduction can be neglected [55]. The axial heat conduction is also affected by the hydraulic diameter and channel wall thickness (solid substrate), and thermal conductivity of the channel wall material.

The results obtained in the current study and reported in the literature [56-58] show that the value of Nusselt number in the fully developed flow is smaller for low Prandtl number ($Pr < 0.1$) compared to “regular fluids” such as water and air when thermal conductivity of the fluid is high compared to the solid substrate. This can be explained by higher conduction resistance in channel wall along the channel for low Pr number flows.

2.3 Simultaneously developing laminar flow and heat transfer

The simultaneously developing flow and heat transfer occurs in the presence of heating/cooling at channel walls and coincides with the fluid flow at a micro-channel inlet. Depending on the Prandtl number, thermal boundary layer development can be faster or slower compared to the hydraulic (velocity) boundary layer. For most gases, the Prandtl number is about 1 thus, thermal and hydraulic boundary layers develop simultaneously with approximately the same rate and have approximately the same thickness.

For liquid metals such as liquid sodium, thermal conductivity is significantly higher compared to most gases, resulting in a very low value of Pr number ($Pr \ll 1$, $Pr = \mu C_p / k$) where μ , C_p and k are dynamic viscosity, specific heat and thermal conductivity, respectively. For

high Prandtl number fluids ($Pr \gg 1$), such as engine oil, thickness of the velocity boundary layer is much larger compared to the thermal boundary layer, thus thermal boundary layer develops in a presence of a fully-developed velocity boundary region. Thermo-hydraulic characteristics of low Prandtl number fluids, such as liquid metals, liquid sodium in this example, are different compared to “regular fluids”. For liquid sodium, high thermal conductivity results in a much thicker thermal boundary layer, compared to the velocity boundary layer, thus velocity boundary layer develops in the presence of much thicker thermal boundary layer, and heat transfer is dominated by conduction [59].

Many researchers have studied simultaneously developing flow and heat transfer for different fluids for a variety of channel cross-section shapes for straight ducts [1, 25]. Shah and London [53, 60] and Bhatti and Savary [61, 62] have reviewed a number of analytical and numerical solutions for different duct geometries in a fully developed laminar flow. Shah and London [53] was selected as the reference literature for validation of the numerical model used in this research work.

The conservation equations (momentum and continuity) and energy equation for a 3D steady-state laminar incompressible fluid flow and Laplace equation for the steady-state heat conduction in solid walls are given as [1, 25]:

$$\frac{\partial(\rho u_j)}{\partial x_j} = 0 \quad (2.1)$$

$$\frac{\partial(\rho u_i u_j)}{\partial x_j} = \frac{\partial(P_i)}{\partial x_i} + \frac{\partial}{\partial x_j} \left(\mu \left(\frac{\partial u_i}{\partial x_j} + \frac{\partial u_j}{\partial x_i} \right) \right) \quad (2.2)$$

$$\frac{\partial}{\partial x_j} \left[u_j (\rho E + P) \right] = \frac{\partial}{\partial x_j} \left[k_f \frac{\partial T}{\partial x_j} \right] \quad (2.3)$$

$$\frac{\partial}{\partial x_j} \left(k_s \frac{\partial T}{\partial x_j} \right) = 0 \quad (2.4)$$

The value of index i represents x , y , and z directions, respectively and varies 1 to 3. Index j is the summation index which also varies from 1 to 3.

2.4 CFD analysis and solver choice

The momentum, continuity and energy equations for a 3D steady-state laminar incompressible fluid flow and Laplace equation for the steady-state heat conduction in solid walls of the channel were solved numerically by the Fluent code. Fluent is a computational fluid dynamics software and is available for academic use in Ansys software package [63] .

Fluent code utilizes the Finite Volume Method to discretize the momentum and energy equations. The second order upwind scheme and Quick scheme were used for discretization of advection terms, while the SIMPLE algorithm was used for coupling the velocity and pressure in the numerical solution procedure [1, 25]. An implicit method, the least squares approach was used for solving a system of governing equations. The RMS residuals level of 10^{-6} was set as a convergence criterion for all governing equations. The local velocity gradient and mass flow rate at the channel outlet were monitored to make sure that the solution has reached convergence.

Thermo-physical properties of different fluids and their variation with temperature were obtained from REFPROP [2]. Dynamic viscosity, density, specific heat and thermal conductivity of sCO_2 and liquid sodium were considered as temperature-dependent [1, 25]. Fluent was coupled to the NIST REFPROP 9.0 to obtain accurate fluid properties for sCO_2 . Thermo-physical properties of liquid sodium change monotonically with temperature and were

calculated by using correlations from the literature [64] given below. The specific heat of liquid sodium was taken constant ($C_p=1,380$ J/kg.K) [1, 51].

$$k(T) = 124.67 - 0.11381T + 5.5226e - 5T^2 - 1.1842e - 8T^3, \frac{W}{m.K} \quad (2.5)$$

$$\mu(T) = e^{-6.4406 - 0.395 \ln T + \frac{556.835}{T}}, Pa.s \quad (2.6)$$

$$\rho(T) = 219 + 275.32(1 - \frac{T}{2505}) + 511.58(1 - \frac{T}{2505}), \frac{kg}{m^3} \quad (2.7)$$

Where T is temperature in Kelvin.

Dimensionless parameters such as Nusselt number and friction coefficient were used in the data reduction analysis. The friction coefficient C_f , dimensionless friction coefficient ($C_f Re_D$), and Nusselt number (Nu) are defined as:

$$C_f = \frac{\tau}{\frac{1}{2} \rho u^2} \quad (2.8)$$

$$C_f . Re_{D_h} = \frac{\tau . D_h}{\frac{1}{2} \rho u^2} \quad (2.9)$$

$$Nu = \frac{h D_h}{k_f} = \left(\frac{q_l''}{T_l - T_b} \right) \frac{D_h}{k_f} \quad (2.10)$$

Mass-weighted average bulk velocity and temperature and peripherally-averaged wall shear stress, wall heat flux and wall temperature were used to calculate Nusselt number (2.10) and friction coefficient (2.8) [1, 25].

$$h = \frac{q_l''|_{y=0}}{T_w - T_b} \quad (2.11)$$

$$\theta = \frac{T - T_{bi}}{T_{bo} - T_{bi}} \quad (2.12)$$

The local values of wall heat flux and wall temperature, and inlet and outlet bulk temperature are denoted as $q''|_{y=0}$, T_w , T_{bi} , and T_{bo} , respectively [1, 25, 51] .

The local temperature gradient and the local velocity gradient at the boundary and pressure drop ΔP per unit channel length are determined as follows [1]:

$$\frac{\partial T}{\partial y} \Big|_{y=0} = \frac{q''|_{y=0}}{k_f} \quad (2.13)$$

$$\frac{\partial u_z}{\partial y} \Big|_{y=0} = \frac{\tau_w}{\mu} \quad (2.14)$$

$$\frac{\Delta P}{L} = \frac{4\tau}{D_h} \quad (2.15)$$

Where τ_w denotes the local wall shear stress [1, 25].

2.5 Grid sensitivity analysis for studied geometries

Grid fineness plays an important role in numerical analysis, affecting accuracy, computational time, and cost of CFD, with finer grids giving better accuracy but resulting in longer computational time and higher cost. Therefore, it is very important to examine the grid size (fineness) and the number of grid points in the computational domain, especially at the fluid-solid interface, to make sure the results of numerical analysis are independent of the grid size and structure. Thus, a grid independency analysis was performed for all micro-channel geometries studied in this work to obtain the grid fineness resulting in a grid-independent solution. Ansys meshing module was used to generate a fully-structured grid with hexahedral elements for the entire computation domain. An initial grid size was selected for the computational domain, the convergence criteria was monitored, and the grid was further

refined until the minimum residual error of 10^{-6} was reached. In the grid refinement process, the height of the first layer of the grid on the solid-fluid interface and the number of grid points were changed and the numerical results were monitored until a grid-independent solution was obtained.

Water with constant thermo-physical properties was used as a working fluid in different micro-channel geometries and the values of $C_f.Re$ and Nu number obtained in a fully developed flow region for constant and uniform heat flux boundary condition were monitored as grid fineness was varied. The values of $C_f.Re$ and Nu number obtained in each individual run were compared to the values of $C_f.Re$ and Nu number reported in Shah and London [53]. For the constant and uniform heat flux boundary condition, the values of $C_f.Re$ and Nu number reported by Shah and London for the square, semi-circular and circular channels are 14.22/3.091, 15.767/2.923, and 16/4.364, respectively.

Summary of the grid independency study results obtained for the square, semi-circle and circle micro-channel geometries studied in this work is given in Table 2. 1, Table 2. 2, and Table 2. 3. Quantity Y_0 is the height of the first layer grid element.

Table 2. 1. Details of the grid independence study results for the square channel

Geometry	Case	Number of grid points ($\times 10^6$)	Y_0 (mm)	Number of prismatic layers	$C_f.Re$	$C_f.Re$ Error%	Nu	Nu Error%
Square ($D_h=0.4$ mm)	Grid 1	0.88	0.1	4	15.67	10.20	3.43	10.96
	Grid 2	1.01	0.05	8	14.84	4.36	3.40	10
	Grid 3	1.22	0.08	10	14.33	0.77	3.12	0.94
	Grid 4	1.43	0.001	12	14.33	0.77	3.12	0.94
	Grid 5	1.46	0.001	14	14.28	0.42	3.10	0.29
	Grid 6	1.61	0.001	16	14.21	0.07	3.10	0.29

To calculate the error for Nu number and $C_f Re$, the relative difference with respect to the original value was calculated using the expression $\frac{\Phi - \Phi_{ref}}{\Phi_{ref}} \times 100$ where Φ is any parameter of interest. The original values are those reported in reference [53].

Table 2. 2. Details of the grid independence study results for the semi-circular channel

Geometry	Case	Number of grid points ($\times 10^6$)	Y_0 (mm)	Number of prismatic layers	$C_f Re$	$C_f Re$ Error%	Nu	Nu Error%
Semi-circle ($D_h=0.922$ mm)	Grid 1	0.45	0.004	16	15.7536	0.084	2.95	1.25
	Grid 2	0.63	0.004	16	15.7537	0.083	2.87	1.63
	Grid 3	0.89	0.004	16	15.756	0.069	2.9	0.69

Table 2. 3. The details of grid independence study results for the circle channel

Geometry	Case	Number of grid points ($\times 10^6$)	Y_0 (mm)	Number of prismatic layers	$C_f Re$	$C_f Re$ Error%	Nu	Nu Error%
Circle ($D_h=1.51$ mm)	Grid 1	0.43	0.01	6	15.96	0.25	4.55	4.36
	Grid 2	0.66	0.01	8	15.98	0.125	4.51	3.44
	Grid 3	0.86	0.01	10	15.989	0.06	4.29	1.6

2.6 Simulation of the conjugate heat transfer in a square micro-channel

The analysis of a conjugate heat transfer problem in a square micro-channel is described in this section for different working fluids covering a range of Prandtl number values. The Nusselt number and friction coefficient were obtained and compared to the values reported by Shah and London [53]. Liquid sodium, air, supercritical CO_2 (sCO_2) at 10 MPa, water,

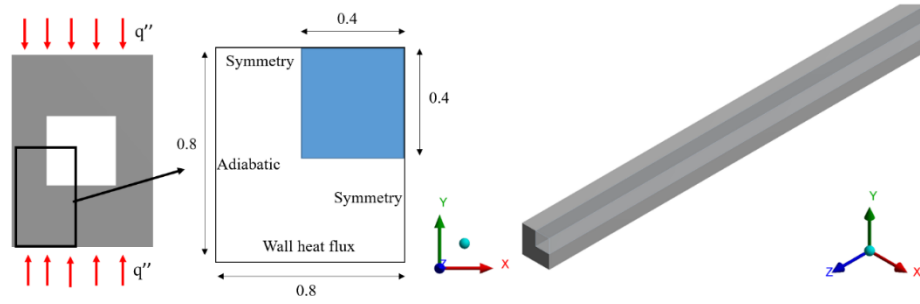
engine Oil (SAE 30 at 200°C) were selected as working fluids for the simultaneously developing flow and conjugate heat transfer problem in a square micro-channel. Table 2. 4 lists thermo-physical properties of the studied fluids at specific values of pressure and temperature.

Table 2. 4. Thermo-physical properties of studied fluids

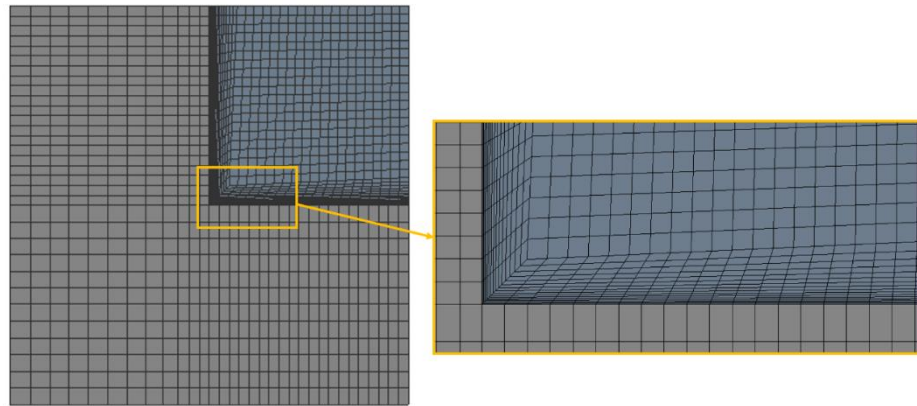
Fluid	Temp. °C	Thermal conductivity W/m K	Viscosity mPa s	Heat capacity J/kg K	Density kg/m ³	Prandtl number
Liquid Sodium	100	89.29	0.6813	1380	925.23	0.0105
Air	30	0.026	0.019	1.01	1.225	0.73
SCO ₂ ,10 MPa	30	0.08494	0.0663	3245.1	773.03	2.53
Water	30	0.607	1.002	4182	998	6.9
Engine Oil, SAE 30	200	0.13	12.15	2093	810	190

2.6.1 Physical model

The schematic of the geometry, a 3D straight square cross section micro-channel analyzed for the conjugate heat transfer for different fluid Prandtl numbers, is illustrated in Figure 2. 3a. Table 2. 5 and Table 2. 6 list the geometry and boundary conditions.



(a)



(b)

Figure 2. 3. (a) Schematic of the square duct and computational domain, (b) Computational grid close to the channel wall [25]

Table 2. 5. Dimensions of the micro-channel and surrounding walls (mm)

Material	Stainless Steel
Thickness	0.8
Pitch	0.4
Width	0.8
Channel width/depth	0.4
Heat transfer area (mm ²)	960
Length	300

Table 2. 6. Boundary conditions

Boundary	Boundary Conditions
Inlet	Velocity inlet
Outlet	Pressure outlet
Top wall	Symmetry
Bottom wall	Wall heat flux
Side walls	Adiabatic/symmetry
Front wall	Adiabatic
Back wall	Adiabatic

Figure 2. 3a shows boundary conditions used in this study. The symmetry boundary condition was applied along the vertical (Y) axis, allowing only one half of the micro-channel to be modeled. A uniform heat flux of $1,000 \text{ W/m}^2$ was imposed on the bottom wall, and all other boundaries were assumed to be perfectly insulated (i.e., adiabatic), as presented in Table 2. 6. The uniform flow velocity was set at the inlet as the flow B.C. corresponding to $Re=100$ and studied operating pressure of CO_2 of 100 bar. The uniform temperature of 30°C was selected for water, air and sCO_2 while temperatures of 200°C and 100°C were chosen for SAE30 oil and liquid sodium, respectively. These inlet temperatures were used to determine transport properties of each working fluid.

Thermo-physical properties of the studied working fluids were assumed to be independent of temperature. The obtained CFD results were analyzed to determine dimensionless parameters such as $C_f Re$ and Nusselt number Nu . The results were compared to the analytical solutions reported in the literature (Shah and London [53] and Lundgren [65]). Shah and London [53] reported the values for $C_f Re$ and Nusselt number (Nu of 14.22 and 3.60795, respectively for the fully-developed laminar flow, constant wall heat flux in the axial direction, and constant peripherally-averaged wall temperature. The values of $C_f Re$ and Nusselt number obtained in this study for water as a working fluid are compared to the

analytical results by Shah and London in Table 2. 7. As the results show, there is an excellent agreement between the results obtained in this study and analytical solutions obtained by Shah and London [53].

Table 2. 7. The predicted numerical results for water in the validation study and calculated error [25]

Selected Parameters	Shah and London [53], Lundgren [65]	Current study (water)	Error %
$C_f \cdot Re$	14.227	14.218	0.06%
Nusselt number	3.6079	3.6073	0.02%

The results presented in Figure 2. 4 show that the predicted peripherally-averaged value of the Nusselt number of 3.6073 for the fully developed flow and heat transfer is in the excellent agreement with the fully-developed Nusselt number value of 3.6079 given by Shah and London [53]. A decrease in the Nusselt number near the channel outlet, predicted in this study, caused by the axial conduction in the channel wall, illustrates the nature of the conjugate heat transfer problem. It has to be noted that this effect is absent in the case of pure convection [1, 25].

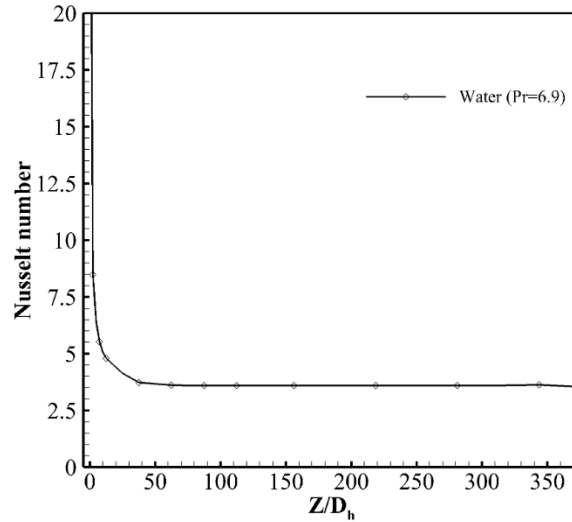


Figure 2. 4. Axial variation of peripherally-averaged Nusselt number for water, $Pr=6.9$

2.6.2 Axial variation of the friction coefficient and Nusselt number

The results of the analysis of a simultaneously developing flow and heat transfer in a square micro-channel are presented and analyzed in this section. In the developing flow region, pressure drop is a result of a wall shear stress and development of the velocity profile due to the change in momentum. If the heat flux at the wall is invariant both axially and peripherally, change in the momentum is the only factor affecting development of the velocity profile. However, if the wall heat flux is not constant, velocity gradient i.e., the wall shear stress is also affected by the variation of the heat flux along the channel wall. Since in the analyzed case the wall heat flux is invariant along the channel length (except at the channel exit due to the effect of axial conduction) thermo-physical properties of the working fluids are assumed independent of temperature, the velocity profile stays unchanged in the flow direction. The friction coefficient C_f , representing the dimensionless wall shear stress, was calculated from Eqn. 2.8.

Figure 2. 5 shows variation of the friction coefficient along the channel (in the flow direction) for different analyzed fluids covering a range of Prandtl number values. The friction coefficient rapidly decreases in the entrance region where the hydraulic boundary layer is

developing and reaches constant value of 0.0749 in the fully developed flow because velocity profile is invariant in the fully-developed flow. The results show that the friction coefficient does not change in the fully developed laminar flow for fluids having different Pr numbers.

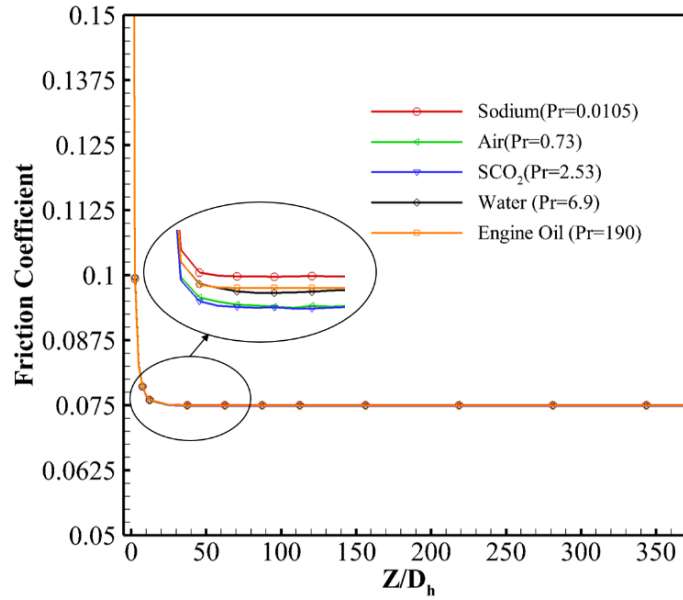


Figure 2. 5. Variation of friction coefficient along the channel for studied fluids

For engine oil (SAE 30) having Pr number of 190 at 200 °C, thermal diffusion is very low compared to liquid sodium with low Pr number of 0.0105. Thus, as discussed earlier, velocity boundary layer is much thicker compared to the thermal boundary layer. Also, thermal diffusivity of liquid sodium is considerably higher compared to air and water, thus thermal boundary layer develops faster, and thermal entrance region is short.

Figure 2. 6 illustrates variation of the Nusselt number along the channel length (in the flow direction) for different analyzed fluids covering a range of Pr number values. The results show that the Nusselt number for air, sCO₂, and water having Pr number values of 0.72, 2.53, and 6.9, respectively reaches the value of 3.607 in the fully-developed region after a rapid decrease in the entrance region. As presented in Figure 2.6, due to the effect of axial conduction

the value of Nusselt number decrease at the channel exit to 3.06 for air, 3.175 for sCO₂ and 3.54 for water.

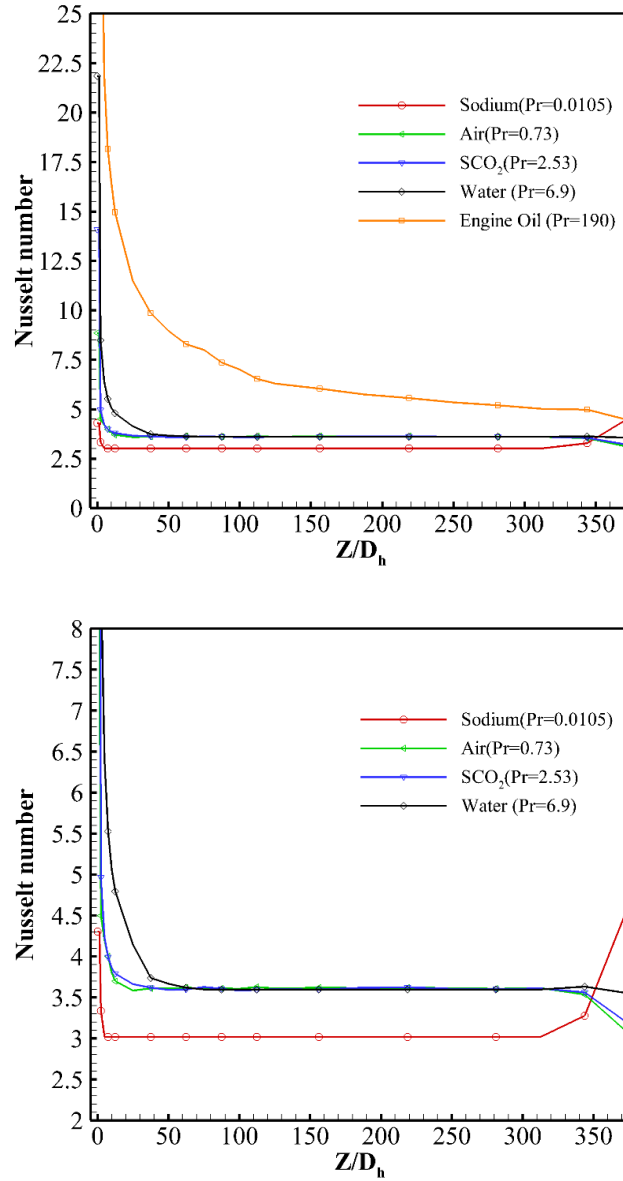


Figure 2. 6. Variation of the Nusselt number along the channel for studied fluids (top),
Nusselt number illustrated in smaller range (bottom)

The values of Nusselt number in the fully developed flow for fluids with Pr numbers of the same order of magnitude such as air, sCO₂, and water approach 3.607. However, the Nusselt number for liquid sodium, and Engine oil reach different values. As shown in Figure

2. 6, for the analyzed channel geometry, the flow does not become fully developed for the Engine oil since thermal diffusivity of the engine oil is small compared to water. A longer channel length is needed to reach thermally fully developed flow for Engine oil. The effect of axial conduction at the channel exit for the Engine oil can be seen in Figure 2. 6.

Thermal conductivity of liquid sodium is significantly higher compared to that of the channel solid substrate (wall) causing an increase in contribution of conduction to heat transfer along the channel. High thermal conductivity of liquid sodium decreases the value of Nusselt number in the fully developed flow. High thermal conductivity i.e., low Prandtl number increases resistance to heat conduction resistance in the channel wall, while thermal diffusion and axial conduction i.e., wall heat flux increase along the channel length.

For liquid sodium and fully developed flow, the value of the Nusselt number is approaching 3.018, which is lower compared to the values for water and air (referred to as “regular fluids”). Due to effects of thermal conductivity and diffusivity on heat transfer, for liquid sodium, wall temperature is constant along the periphery of channel wall. The value of the Nu number for liquid sodium obtained in this work of 3.018 is comparable to the Nu number of 2.976 reported by Shah and London [53]. It should be noted that despite the low value of Nu number, the heat transfer coefficient at the channel wall for liquid sodium is very high compared to other working fluids, such as water and air, analyzed in this work, and as a result, the value of bulk fluid temperature is approaching wall temperature.

CHAPTER 3: SUPERCRITICAL CO₂

3.1 Overview

In this section, thermo-physical properties of supercritical CO₂ and their effects on thermal and hydraulic performance in a micro-channel heat exchanger are presented. A physical model representing a square micro-channel PCHE was used to numerically determine and explore the effect of sCO₂ properties on hydraulic and thermal performance of the heat exchanger. Two straight square cross-section micro-channels comprising an elemental heat exchanger were modeled, where sCO₂ and liquid sodium were used as working fluids in the cold and hot channels. The variation in density, thermal conductivity, dynamic viscosity and specific heat with operating pressure and temperature on flow and heat transfer is presented for the studied geometry [1].

3.2 sCO₂ characteristics

The advanced power generation technology, the state-of-the-art technology, is being developed to achieve the highest cycle efficiency with the lowest capital cost. The sCO₂ Brayton cycle has been introduced as an outstanding candidate for replacing the conventional power cycles owing to its high cycle efficiency, compact power cycle equipment, and simple and small turbomachinery. Single phase heat rejection, high power output, single stage pumps or compressors and a turbine (expander), and low compression power input are other advantages of the sCO₂ power cycles.

sCO₂ is a distinctive working fluid thanks to its variable transport and thermo-physical properties. CO₂ reaches the supercritical state above the Critical Point CP, i.e., above the relatively low critical temperature T_{cr} and pressure P_{cr} of 304.25K and 73.8 bar, respectively and, in general, behaves like a gas in terms of viscosity with a density similar to the liquid [1].

The properties of sCO₂ vary between the states of gas and liquid depending on the operating temperature and pressure. The largest change in thermo-physical properties occurs at the CP or near the pseudo-critical line. Figure 3. 1 shows variation of thermo-physical properties of CO₂ for different pressures near the CP. As shown in this figure, there is a large variation in CO₂ properties near the CP. The Specific heat at CP is theoretically infinite since there is no phase change. Also, thermal conductivity reaches its maximum value at CP. As the data presented in Figure 3. 1d show, large variation in density occurs near the CP and along the pseudo-critical line. Above the pseudo critical line, CO₂ density is high and approaches density of the liquid, thus this region is called the “liquid-like” region. Below the pseudo-critical line, CO₂ density is low, approaching density of the gas. Therefore, this region is referred to as the “gas-like” region [66].

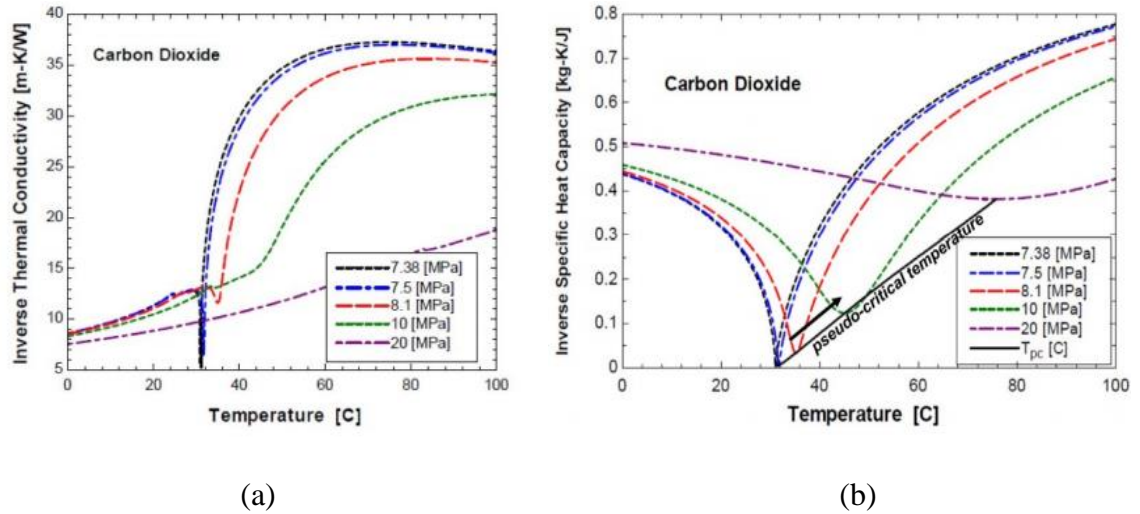


Figure 1.3. (a) thermal conductivity (inverse), (b) specific heat at constant pressure (inverse),

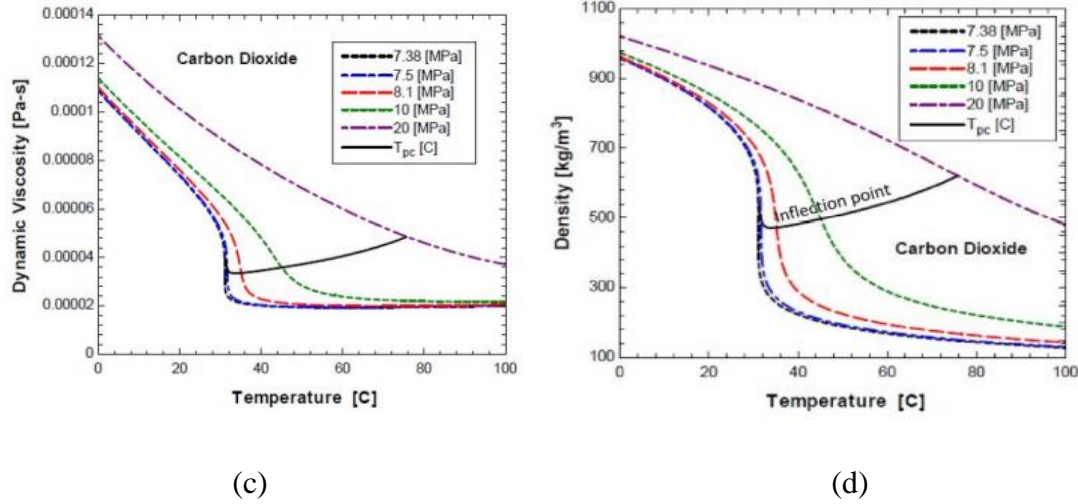


Figure 3. 1. Continued, (c) dynamic viscosity and (d) density [66] over a range of pressure; T_{pc} is the pseudo-critical temperature

Figure 3. 2a shows the T-s diagram for CO₂ and state points associated with compression in a recompression sCO₂ Brayton cycle investigated by the Sandia National Lab [67]. The green dotted lines show the heat rejection and compression part of the cycle, while the red lines show compression process (compressor inlet and outlet) for different operating conditions (pressure and temperature) at the compressor inlet. The dark blue line shows the pseudo-critical line. The “liquid-like” region is located to the left of the pseudo critical line, while the “gas-like” region is to the right of the pseudo-critical line. As discussed above, CO₂ density in the “liquid-like” region is high (65 to 80% of water density), while in the “gas-like” region density is low (15-30% of water). This large difference in CO₂ density results in a significant difference in the compression work, which is considerably lower in the liquid-like region compared to the gas-like region, as presented in Figure 3. 2b. Thus, in a sCO₂ cycle, CO₂ is compressed in the liquid-like region to minimize compression work (power) and is expanded in the vapor-like region to maximize expansion work (power). This results in an increase in net power output and efficiency of a sCO₂ Brayton cycle, as investigated and reported by Javanshir [66] and presented in Figure 3. 3. As the figure shows, the net power

output of a supercritical sCO₂ Brayton cycle operating above the critical pressure at maximum pressure of 30 MPa is higher compared to a trans-critical sCO₂ cycle operating at maximum pressure of 10 MPa.

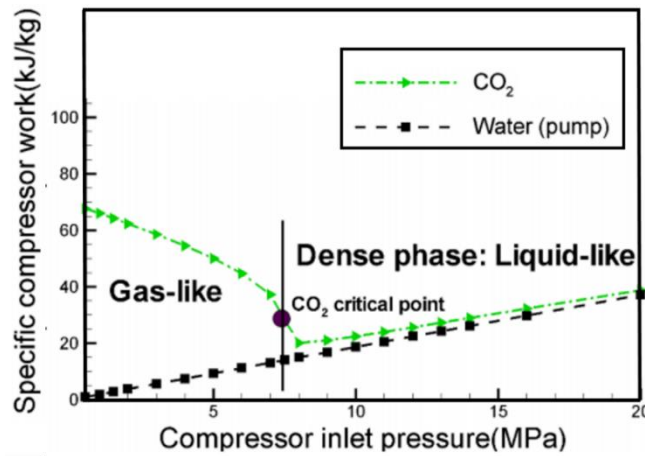
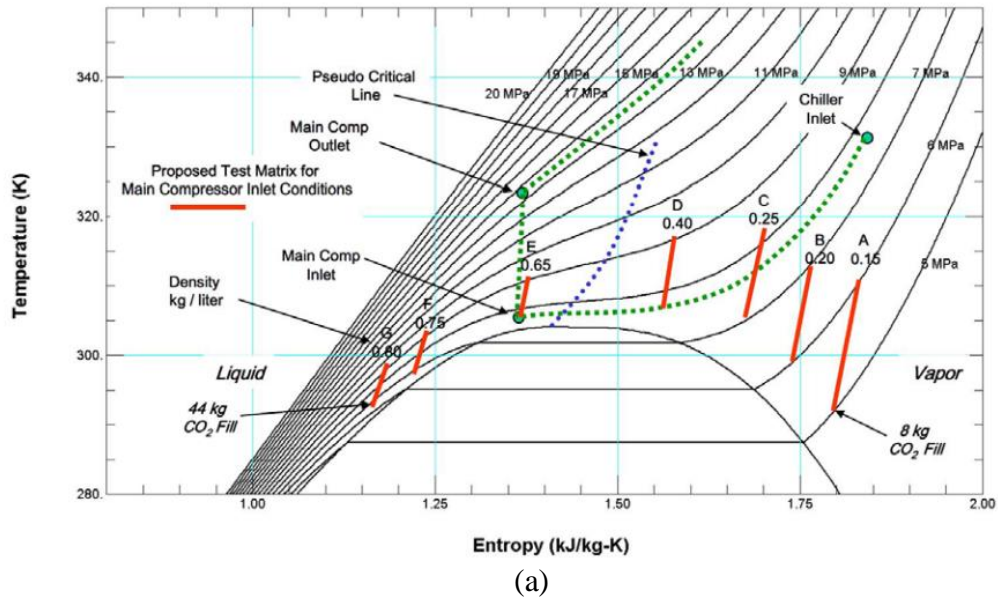


Figure 3. 2. (a) T-s diagram of CO₂ over a range of pressure, (b) Compression work for different compressor inlet pressure [66]

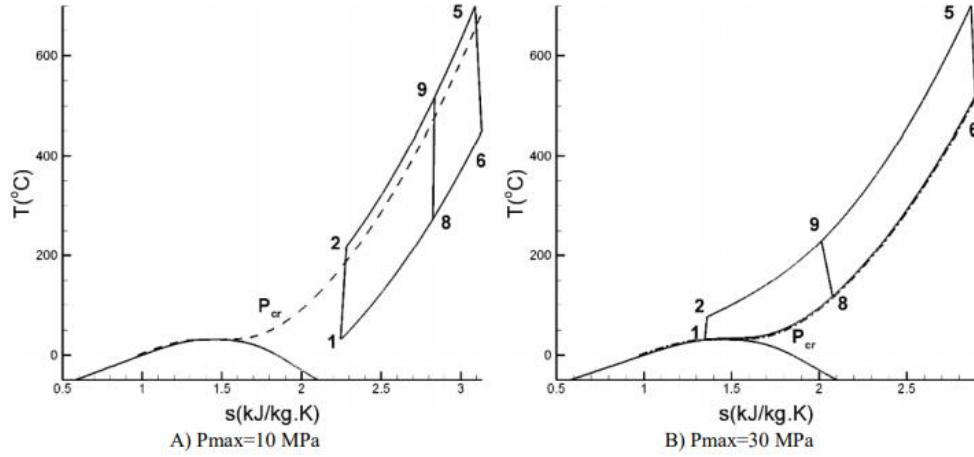


Figure 3. 3. T-s diagram of the Regenerative Brayton cycle with recompression [66]

3.3 Conjugate heat transfer and sCO₂ flow through the PCHE micro-channels

For a proper design of a compact heat exchanger, it is important to understand and predict the conjugate heat transfer and sCO₂ flow through the micro-channels of a PCHE [1]. The design of a PCHE operating near the CP and in the pseudo-critical region is challenging and complicated because of the large variation in thermo-physical and transport properties of sCO₂. As mentioned in Chapter 2, the conventional design approaches such as Logarithmic Mean Temperature Difference (LMTD) or ϵ -NTU methods are impractical due to underlying assumption of constant properties² of the working fluid(s). Due to a large variation in sCO₂ properties with operating temperature and pressure, the computer-aided analysis and numerical modeling are difficult and challenging [25].

Numerical analysis of the local and overall flow and heat transfer in a 3-D square-shaped micro-channel was performed for the laminar flow regime and constant value of Reynolds number to investigate the effect of axial heat conduction for simultaneously developing laminar flow and heat transfer. The analysis was conducted for the liquid sodium

² Thermo-physical and transport properties of working fluids are assumed constant to allow integration of the governing differential equations and obtain a closed form solution.

and sCO₂ as working fluids in the hot and cold channels of the heat exchanger. The study provides a detailed insight into the sCO₂ flow and conjugate heat transfer within individual micro-channels. The heat transfer performance due to flow acceleration caused by the heat flux imposed along the channel length, non-uniform flow distribution along the channel due to large variation in thermo-physical properties of sCO₂, and local characterization of flow and heat transfer require a detailed numerical analysis [1].

The operating pressure in the cold sCO₂ micro-channel was varied in the 8 to 30 MPa range (corresponding to the conditions near to and far from the CP) to determine the effect of variation in thermo-physical properties on thermo-hydraulic performance of PCHEs, such as recuperators and other heat exchangers used in a sCO₂ Brayton cycle. The results (Nusselt number Nu and Fanning friction factor (friction coefficient C_f)) were compared to the analytical and numerical solutions from the literature. The results concerning variation of the Fanning friction factor and Nusselt number along the channel length show that for the parallel flow arrangement axial heat conduction in the channel wall has a significant effect on the heat transfer coefficient near the channel outlet. For the counter-flow arrangement, heat transfer at both the channel inlet and outlet is affected. For sCO₂ as a working fluid, large variations in its viscosity and thermal conductivity around the CP have a large effect on pressure drop and heat transfer.

3.4 System description

3.4.1 Geometry and computational domain

The schematic representation of a micro-channel PCHE geometry analyzed in this study is given in Figure 3. 4a. Two straight rectangular cross-section micro-channels, each having the inner hydraulic diameter of 0.4 mm, comprising an elemental heat exchanger were

modeled. The channel geometry and boundary conditions are listed in Table 3. 1 and Table 3. 2, while the operating conditions used in the analysis are given in Table 3. 3 [1].

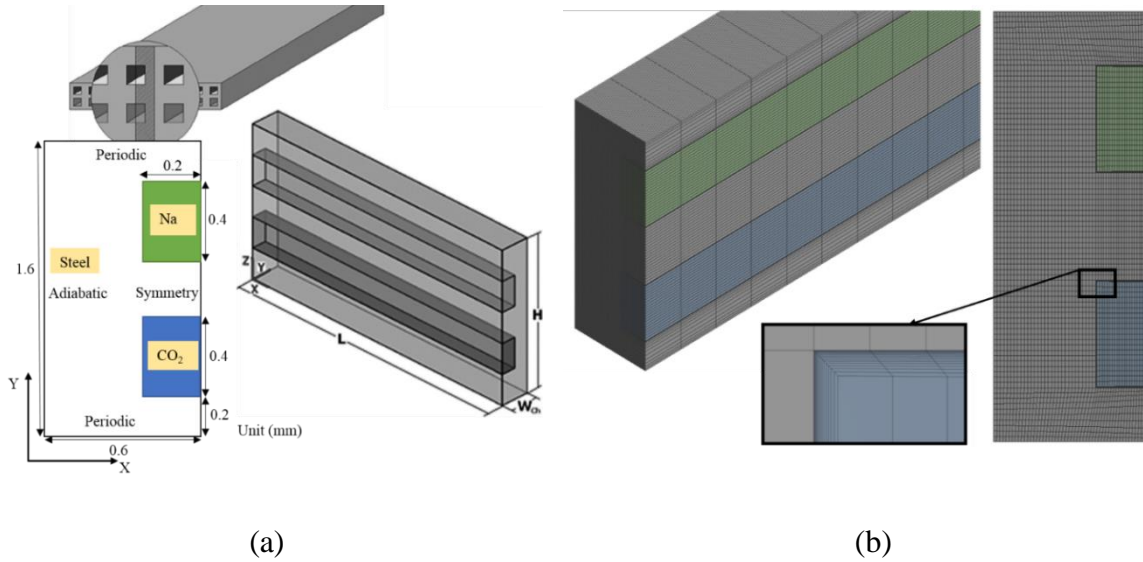


Figure 3. 4. (a) Schematic of the two micro-channel configuration, boundary conditions and details of computational domain, (b) Numerical grid

Table 3. 1. Dimensions of the liquid sodium-cooled micro-channel configuration analyzed in this study, dimensions in mm

Parameter	Cold and Hot Side
Plate material	SS316L
Plate thickness	0.8
Horizontal pitch	0.4
Wall width	0.6
Channel width	0.4
Channel depth	0.4
Hydraulic diameter	0.4
Channel length	120

To reduce computational time and effort, the symmetry boundary condition was specified on the right-hand side of the computational domain, as presented in Figure 3. 4a. Periodic boundary conditions were specified at the top and bottom walls to model multiple layers of micro-channels etched in thin substrate plates. The left wall was assumed to be

adiabatic. The velocity inlet and pressure outlet boundary conditions were specified at the inlet and outlet of the micro-channels. The details of numerical setup can be found in Chapter 2, Section 2.4.

Table 3. 2. Boundary conditions

Boundary	B.C.'s
Fluid inlets	Velocity inlet
Fluid outlets	Pressure outlet
Top and Bottom walls	Periodic
Side walls	Adiabatic-symmetry
Front and Back walls	Adiabatic

Table 3. 3. Operating conditions

Property	Cold Side (s-CO ₂)			Hot Side (Liquid Sodium)		
	Inlet	Outlet	Velocity (m/s)	Inlet	Outlet	Velocity (m/s)
P (MPa)	-	8	0.021	-	0.1	0.1879
	-	10	0.0225	-		
	-	30	0.028	-		
T (K)	300	-	-	366	-	-

3.5 Results and discussion

3.5.1 Variation of bulk fluid temperature and wall heat flux along the channel length

Variation in the bulk fluid temperature and peripherally-averaged wall heat flux along the channel length, i.e., in the axial (flow) direction is presented in Figure 3. 5 for the parallel-flow arrangement, and in Figure 3. 6 for the counter-flow arrangement. The analysis was performed for two working fluids: liquid sodium as the hot fluid and sCO₂ as the cold fluid.

Variation in the bulk temperature of the hot and cold fluids with channel length presented in Figure 3. 5a shows that temperature of the hot fluid decreases from its initial value

of 366 K, while temperature of the cold fluid increases from the initial value of 300 K. Temperatures of both fluids reach a constant value for $Z/D_h \geq 150$, and due to the high thermal conductivity of the substrate metal are approximately the same, with the hot fluid temperature being approximately 0.5 K higher. Due to the variation in thermo-physical properties of $s\text{CO}_2$ with pressure, bulk temperature of the $s\text{CO}_2$ depends on the operating pressure. Although thermo-physical properties of the liquid sodium are independent of pressure, variation of its bulk temperature, shown in Figure 3. 5, is caused by the variation in thermo-physical properties of $s\text{CO}_2$, which affect heat transfer in the cold micro-channel, heat transfer between the hot and cold micro-channels, and, consequently, heat transfer in the hot micro-channel.

Variation of the wall heat flux $q''|_{y=0}$ along the micro-channel length presented in Figure 3. 5b shows very high values of the wall heat flux in the inlet region of the micro-channel, followed by the rapid decrease as bulk temperatures of the hot and cold fluids approach each other. For $Z/D_h \geq 150$ the wall heat flux, representing heat transfer between the cold and hot channels is approximately equal to 150 kW/m^2 .

The results for the counter-flow configuration are presented in Figure 3. 6. While the variation in bulk temperature of the hot and cold fluids differs from the parallel-flow configuration, as shown in Figure 3. 6b variation in the wall heat flux along channel length is approximately the same as for the parallel-flow. Results for the counter-flow arrangement presented in Figure 3. 6a show that the cold fluid bulk temperature increases as flow progresses through the channel from left to right, and for $Z/D_h \geq 150$ to 200 it approaches the value of the hot fluid temperature. The bulk temperature of the hot fluid flowing in the hot channel from left to right is initially approximately constant, and for $Z/D_h \leq 150$ to 200 begins to decrease reaching its final value in the 350 to 360 K range at the cold end of the channel. The operating

pressure in the cold channel has a significant effect on the axial temperature variation; the increase in the bulk temperature of the cold fluid (sCO₂) and decrease in the bulk temperature of the hot fluid (liquid sodium) are larger for the sCO₂ pressure much higher than the critical pressure. Similar to the parallel-flow configuration, changes in the operating pressure in the cold channel propagate to the hot channel via changes in the wall heat flux (representing local heat transfer between the two micro-channels).

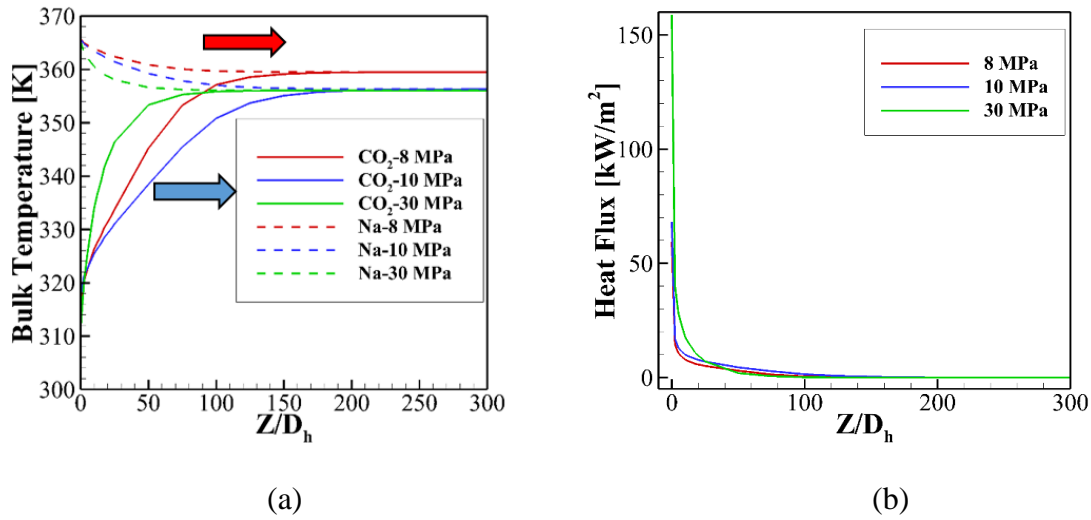


Figure 3. 5. Parallel Flow: (a) Variation of bulk temperature of the liquid sodium and sCO₂ and (b) heat flux over a range of pressure

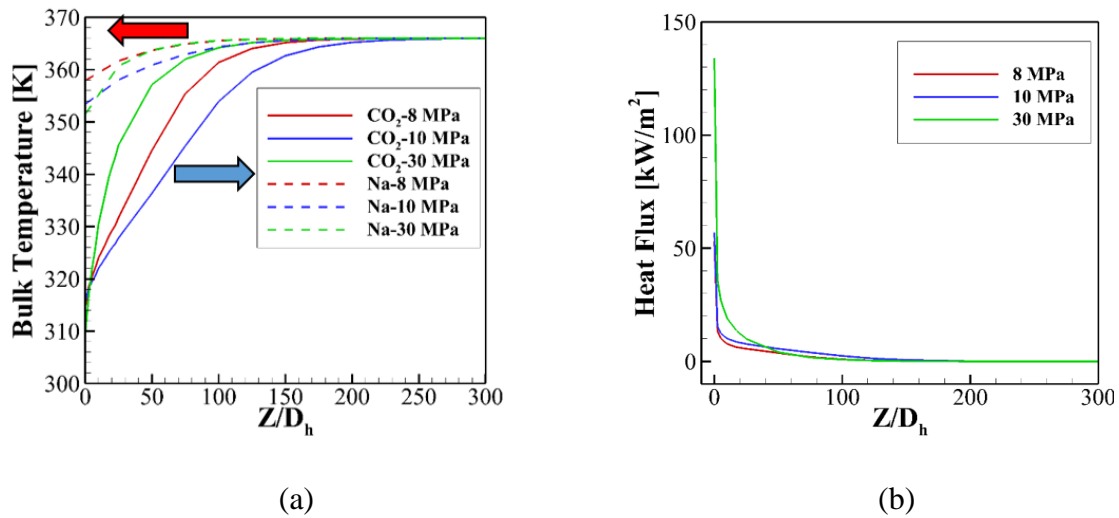


Figure 3. 6. Counter Flow: (a) Variation of bulk temperature of the liquid sodium and aCO₂ and (b) heat flux over a range of pressure

3.5.2 Thermo-physical properties of supercritical CO₂

Properties of CO₂ were discussed in detail in Chapter 2. In the supercritical region, there is no distinction between the liquid and vapor phases, and a supercritical fluid is considered homogeneous since phase boundaries vanish. In the vicinity of CP, representing the end point of a phase equilibrium curve, and along the pseudo-critical line, thermo-physical properties of a supercritical fluid undergo large changes. These large variations in fluid properties gradually disappear as operating pressure and temperature are increased from the critical values.

Variation in density, specific heat, dynamic viscosity, and thermal conductivity of CO₂ with temperature and pressure corresponding to the operating conditions analyzed in this study for a pair of the square-shaped micro-channels is presented in Figure 3. 7. As the results show, variation in thermo-physical properties of sCO₂ (cold fluid) shows a peak near the CP. However, as the fluid temperature and pressure increase above the critical values, variation in fluid properties becomes smooth and monotonic. This variation in CO₂ properties has a large effect on hydraulic and thermal performance of a micro-channel. The axial locations in the cold channel, where large variations in thermo-physical properties occur, and corresponding fluid temperatures are shown in Figure 3. 7. For operating pressures of 8, 10 and 30 MPa, large variations in thermo-physical properties occur at $Z/D_h = 18, 42,$ and 77.55 and corresponding temperatures of 307.803 K, 318.154 K, and 360.204 K, respectively.

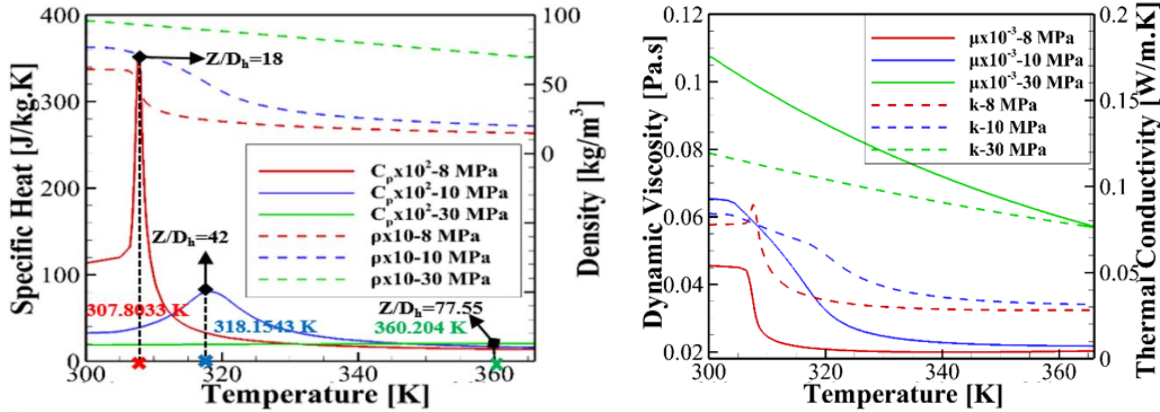


Figure 3. 7. Variation of thermo-physical properties with temperature of the working fluid (sCO₂)

The maximum values of specific heat and density are at the channel centerline where the fluid temperature is lower compared to the near-wall region. For operating pressures of 8, 10 and 30 MPa, peak values of specific heat are 33.339, 7.590, and 2.0616 kJ/kg-K, respectively. The corresponding values of density are 443.22, 482, and 714 kg/m³, respectively. Variations in density and thermal conductivity of sCO₂ caused by changes in pressure affect velocity and temperature distributions within the cold micro-channel, velocity and temperature gradients at the channel wall, and thus wall shear stress, friction coefficient, wall heat flux, and convection heat transfer coefficient.

3.5.3 Hydraulic analysis

3.5.3.1 Friction coefficient for supercritical CO₂

The friction coefficient given by Eqn. 2.8 represents dimensionless pressure drop in a micro-channel. In this study, the friction coefficient was evaluated for a simultaneously developing flow and heat transfer in both the hot and cold channels. Based on the results presented in Reference [68], where the friction coefficient C_f was determined for the semi-circular micro-channel geometry and the laminar flow regime, the dimensionless form of the friction coefficient, expressed as a $C_f \text{ Re}$ product, does not change appreciably with the

Reynolds number. The friction coefficient is, however, strongly dependent on the wall temperature and heat flux due to their effect on the wall temperature gradient and local fluid properties.

Variation in bulk flow velocity along length of the cold micro-channel (expressed in dimensionless form as Z/D_h) predicted in this study for the inlet sCO₂ pressure in the 8 to 30 MPa range is presented in Figure 3. 8a. The dotted lines correspond to the parallel-flow arrangement, while the solid lines denote the counter-flow arrangement. As the results show, development of bulk velocity for both flow arrangements is similar; the velocity increases and flow accelerates due to the increase in bulk fluid temperature reaching constant value for $Z/D_h \geq 150$, corresponding to the axial location where the bulk fluid temperature and heat flux reach constant values, as shown in Figure 3. 5 and Figure 3. 6. The results also show that development of the bulk flow velocity depends strongly on fluid pressure; with higher velocities corresponding to lower pressure. For the range of investigated pressures, bulk velocity is highest for operating pressures close to the critical pressure P_{cr} . Flow acceleration decreases as inlet pressure is increased due to the increase in fluid density as shown in Figure 3. 7.

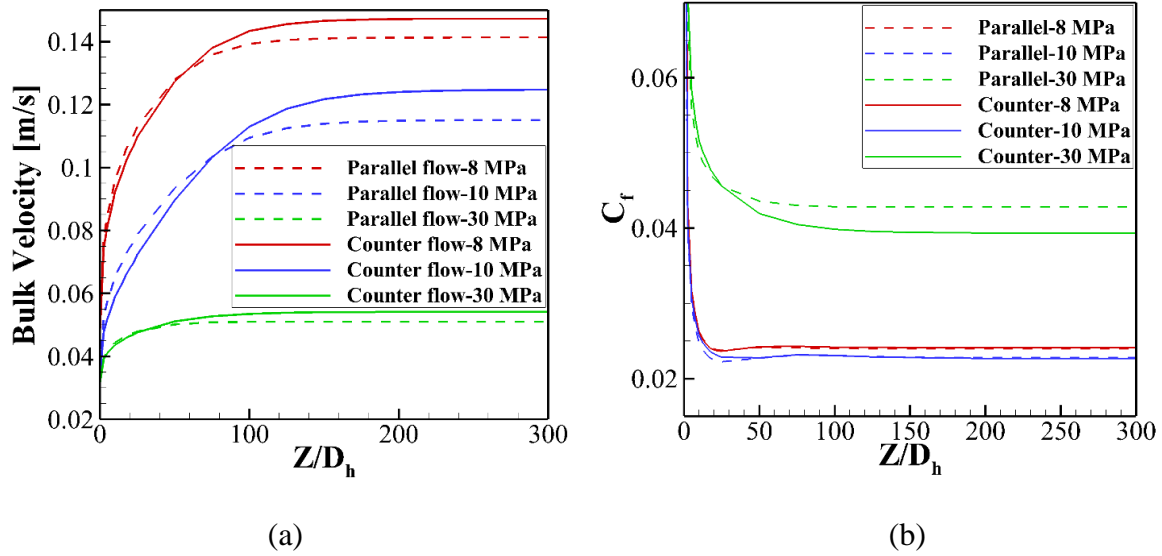


Figure 3. 8. Cold ($s\text{CO}_2$) micro-channel: Variation of (a) Bulk velocity, (b) Friction coefficient for parallel and counter-flow arrangements

Variation of the friction coefficient along the dimensionless length of the cold micro-channel is presented in Figure 3. 8b for the inlet CO_2 pressure in the 8 to 30 MPa range. Since, as shown in Figure 3. 8a, values of bulk velocity for the parallel- and counter-flow arrangements are very close to each other, values of the friction coefficient shown in Figure 3. 8b are approximately the same. The friction coefficient rapidly decreases in the entrance region and reaches constant value of 0.024 at $Z/D_h \approx 150$ because beyond that axial location the flow no longer accelerates, bulk fluid velocity is constant, and wall heat flux is approximately zero, as shown in Figure 3. 5, Figure 3. 6 and Figure 3. 8a. These results show that far from the CP, where changes in fluid properties are gradual and monotonic, the flow of $s\text{CO}_2$ closely resembles the flow of a “regular” gas or liquid.

As discussed earlier, large changes in thermo-physical properties of CO_2 around the CP make the prediction of flow and heat transfer characteristics in that region difficult. Thus, accurate correlations for predicting the friction factor and heat transfer coefficient in the proximity of the critical point and along the pseudo-critical line have not been developed.

Correlations found in the literature are not sufficiently accurate to predict thermo-hydraulic performance in these regions and researchers depend on experiments or numerical predictions [52].

3.5.3.2 Friction coefficient for the liquid sodium

Thermo-hydraulic characteristics of flow of liquid sodium in a smooth rectangular micro-channel geometry were also investigated. Due to its high thermal conductivity (average $k=90$ W/m-K) and small Prandtl number ($Pr=0.0112$), thermo-hydraulic characteristics of the liquid sodium flowing through a channel are significantly different compared to other fluids; as discussed earlier, high thermal conductivity results in a much thicker thermal boundary layer, compared to the velocity boundary layer. Since development of a thermal boundary layer occurs in the presence of a much thinner velocity boundary layer, heat transfer is dominated by the conduction even in a fully developed turbulent flow region [59]. Because thermo-physical properties of liquid sodium do not change with pressure and are only weakly dependent on temperature, the flow develops after about ten hydraulic diameters, after which the bulk flow velocity is constant. Variation of the bulk flow velocity and temperature with dimensionless channel length is presented in Figure 3. 9a for the inlet temperature of 366 K, laminar flow, and inlet Reynolds number of 100, corresponding to the inlet velocity u_{inlet} of 0.1879 m/s. As the results show, flow development is virtually independent of pressure. The bulk temperature of the liquid sodium is changing from 366 to 355 K and from 366 to 350 K for the counter-flow and parallel flow arrangement, respectively. Velocity contours for the fully developed flow presented in Figure 3. 9b shows maximum flow velocity ($u/u_{inlet} = 2$) at the center of the micro-channel, moderate flow velocities over the large portion of the micro-channel cross sectional area, and very low velocities in the corners and near channel walls.

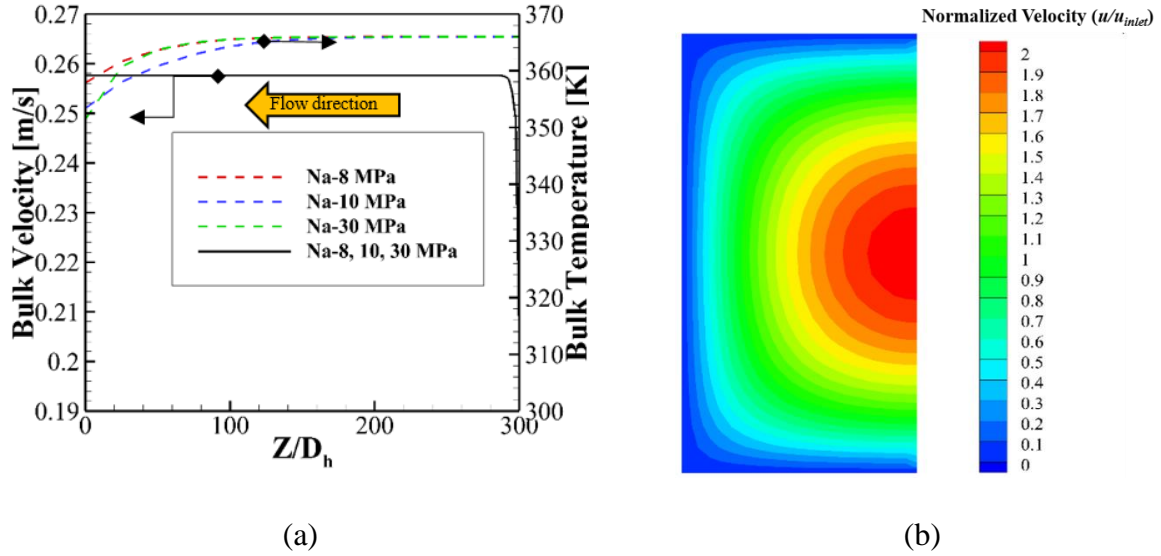


Figure 3. 9. Hot (liquid sodium) micro-channel: (a) Bulk temperature and velocity variation along the duct, (b) Normalized velocity contours at $Z/D_h=200$ in a fully-developed flow for the counter-flow arrangement

Variation of the friction coefficient along the channel length is shown in Figure 3. 10 for the parallel- and counter-flow configurations. As the results show, the predicted value of the friction coefficient does not change with pressure, regardless of the flow arrangement. The flow arrangement, however, does have a small effect on the predicted value of the friction coefficient; with the parallel-flow arrangement resulting in a slightly higher value of C_f , which may be explained by the difference in heat exchanged between the two micro-channels and its effect on liquid sodium properties. For the fully developed flow, the predicted values of the friction factor for liquid sodium and water are 0.078 and 0.076, respectively which is in a very good agreement with the literature [53].

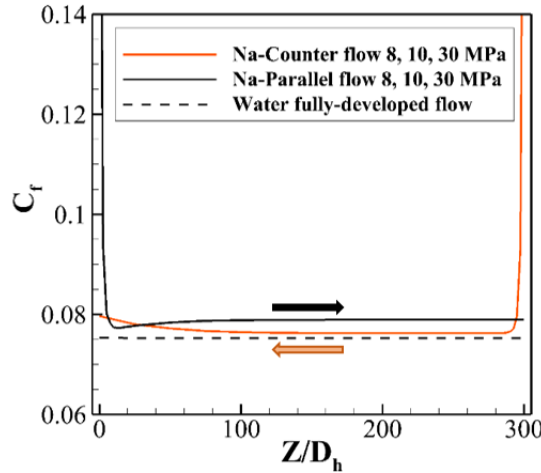


Figure 3. 10. Variation of friction coefficient along the channel length: liquid sodium

3.5.3.3 Local wall shear stress and velocity gradient for supercritical CO₂

The wall shear stress τ_w is one of the parameters used to calculate friction coefficient which plays a significant role in determining pressure drop in the laminar flow. As Eqns. 2.14 shows, wall shear stress is directly related to the local velocity gradient at the wall and fluid viscosity. Since the velocity profile does not change in the hydrodynamically fully-developed flow region, for constant viscosity the local wall shear stress is constant. However, as presented in Figure 3. 7, pressure and temperature have a significant effect on sCO₂ viscosity, especially in the vicinity of the CP and along the pseudo-critical line. Thus, even in the fully-developed flow region the local wall shear stress varies due to changes in fluid viscosity.

The effect of viscosity on local values of velocity gradient at the wall and wall shear stress was determined and results are presented for the X-Y cross-section of the cold micro-channel in the fully-developed flow region ($Z/D_h=200$) along the A-B line (point A is located on the channel symmetry line (corresponding to $X/D_h=0$), while point B is located in the channel corner (corresponding to $X/D_h=0.5$), as shown in Figure 3. 11.

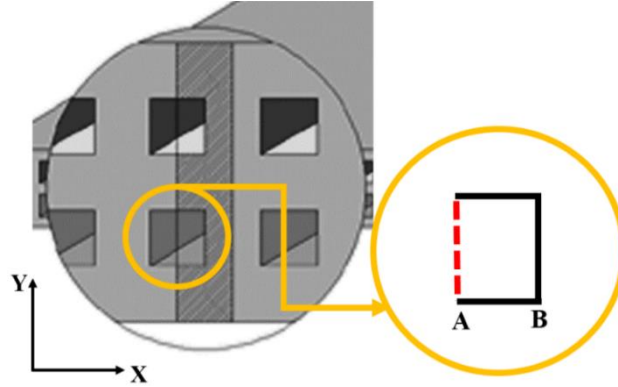


Figure 3. 11. X-Y cross-section at $Z/D_h=200$ for the local shear stress analysis

The results show that viscosity varies with pressure but remains constant along the A-B line, i.e., from the channel symmetry line to the corner. The values of viscosity presented in Table 3. 4 are based on the local wall temperature. Table 3. 4 also summarizes numerical values of the local wall temperature, bulk fluid temperature, wall shear stress, and velocity gradient determined at the channel centerline for the investigated values of fluid temperatures and pressures, and flow arrangement.

Variation in the local wall velocity gradient along the A-B line is presented in Figure 3. 12 for the fully developed flow ($Z/D_h = 200$) and inlet pressures of 8, 10, and 30 MPa. The dotted lines correspond to the parallel-flow arrangement, while the solid lines denote the counter-flow arrangement. As the results show, pressure has a significant effect on the wall velocity gradient; the local velocity gradient at the wall increases as pressure is decreased and approaches critical pressure. Velocity gradient is negligible in the channel corner ($X/D_h = 0.5$) and is the highest at the channel centerline ($X/D_h = 0$).

Table 3. 4. Bulk fluid temperature, local wall temperature, viscosity, velocity gradient, and shear stress as functions of pressure for the parallel- and counter-flow arrangements

Parallel Flow					
			Center Line		Eqn. 2.14
P_i [MPa]	T_w [K]	T_b [K]	$\mu \times 10^3$ [Pa.s]	τ_w [Pa]	$(du/dy)_{y=0} = \tau_w/\mu$ [1/s]
8	359.49	359.44	0.020158	0.0496916	2465
10	356.32	356.054	0.021897	0.043906	2005
30	356.06	356.057	0.062203	0.0554083	891
Counter Flow					
			Center Line		Eqn. 2.14
P_i [MPa]	T_w [K]	T_b [K]	$\mu \times 10^3$ [Pa.s]	τ_w [Pa]	$(du/dy)_{y=0} = \tau_w/\mu$ [1/s]
8	365.99	365.85	0.0203	0.0521185	2568
10	365.89	365.18	0.021784	0.0471841	2166
30	365.98	365.92	0.057185	0.0540162	945

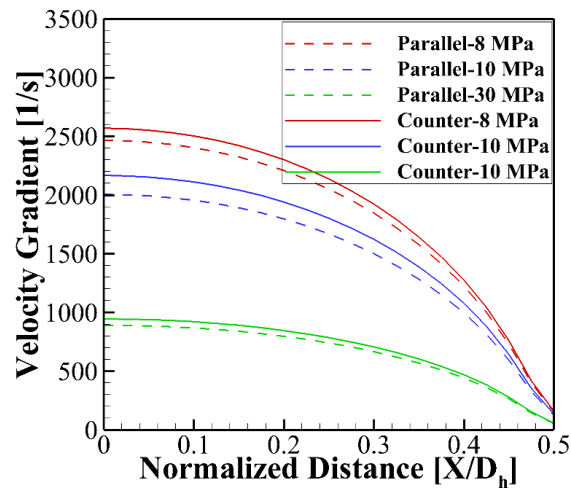


Figure 3. 12. Cold (sCO₂) micro-channel: Variation of local wall velocity gradient along the A-B line with pressure for the Parallel-flow and Counter-flow

3.5.4 Thermal analysis

3.5.4.1 Supercritical CO₂

The axial variation of the peripherally-averaged Nusselt number in the cold micro-channel predicted for operating pressures of 8, 10, and 30 MPa and parallel- and counter-current flow arrangements is presented in Figure 3. 13. It has to be noted that for the fully developed laminar flow, the value of the Nusselt number is strongly dependent on the shape of channel cross-section.

The results obtained for the parallel- and counter-flow arrangements presented in Figure 3. 13 are very similar and show that Nu number in the inlet region depends on the fluid (sCO₂) pressure. As shown in Figure 3. 7, for the pressure of 30 MPa (significantly higher than P_{cr}) thermal conductivity decreases monotonically with temperature. Due to the decrease in thermal conductivity and increase in boundary layer thickness, the local Nu number monotonically decreases in the entrance region of the cold channel reaching the fully developed value of 2.938 for the parallel-flow configuration, and 3.146 for the counter-flow configuration. For the parallel-flow configuration Nu number decreases near the channel exit due to axial conduction in channel walls.

For the operating pressures of 8 and 10 MPa, close to P_{cr} , the axial variation of local Nusselt number in the entrance region of the cold channel is significantly different. The local value of Nu number sharply decreases in the entrance region and reaches minimum at $Z/D_h=10$ to 20. As the flow progresses downstream, Nu number increases and reaches a fully developed value at $Z/D_h \geq 100$ to 150. This variation in Nu number may be explained by the variation in thermal conductivity with temperature and pressure shown in Figure 3. 7. For the operating pressures of 8 and 10 MPa and bulk fluid temperature in the 300 to 310 K range (close to the

inlet temperature to the cold duct), thermal conductivity is approximately constant. For the operating pressure of 8 MPa, an increase in fluid bulk temperature beyond 310 K causes a sharp drop in thermal conductivity and, hence a decrease in heat transfer. The decrease in thermal conductivity is more gradual for higher operating pressure of 10 MPa. As flow progresses downstream, bulk velocity increases resulting in an increase in heat transfer. As discussed earlier, the bulk flow velocity, bulk fluid temperature, and wall heat flux reach constant values at $Z/D_h \geq 100$ to 150 resulting in constant value of Nu number.

The effect of axial heat conduction is small in the counter-flow arrangement due to high temperature difference at the cold end ($Z/D_h = 0$) shown in Figure 3. 6a.

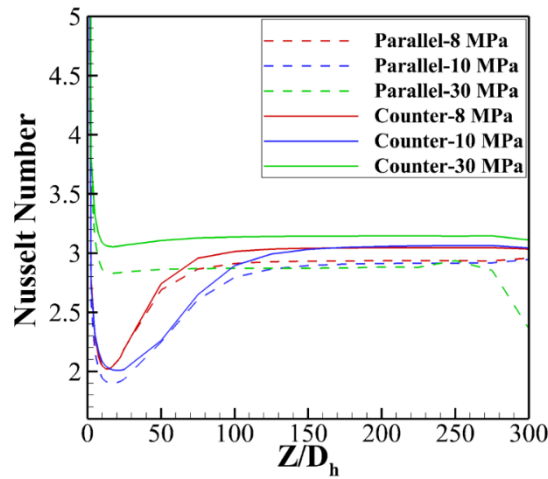


Figure 3. 13. Cold (sCO₂) micro-channel: Axial variation of Nusselt number over a range of pressure

3.5.4.2 Liquid sodium

The predicted temperature contours in the liquid sodium flowing through a hot micro-channel, sCO₂ flowing through a cold micro-channel, and in the channel walls are presented in Figure 3. 14a and Figure 3. 14b at $Z/D_h=125$ for the parallel- and counter-flow configurations and operating pressure of 10 MPa. Since the ratio of thermal conductivity of

the micro-channel walls (steel) and the working fluid (liquid sodium) is very small, temperatures of the channel wall and working fluid are the same at the solid-fluid interface.

As the results show, for the values of fluid temperature and pressure used in the analysis and the selected axial location, the difference in bulk fluid temperature (ΔT_b) between the hot and cold micro-channels is approximately 5 K for the parallel-flow configuration, and 11 K for the counter-flow configuration. The corresponding peripherally-averaged wall temperatures are 356.18 and 365.12 K, respectively as presented in Figure 3. 5a and Figure 3. 6a. The results also show that ΔT_b is larger for the counter-flow configuration, compared to parallel-flow, and decreases as Z/D_h increases. For $Z/D_h > 200$, the difference in bulk temperatures vanishes, resulting in very low values of wall heat flux and heat transfer between the hot and cold micro-channels.

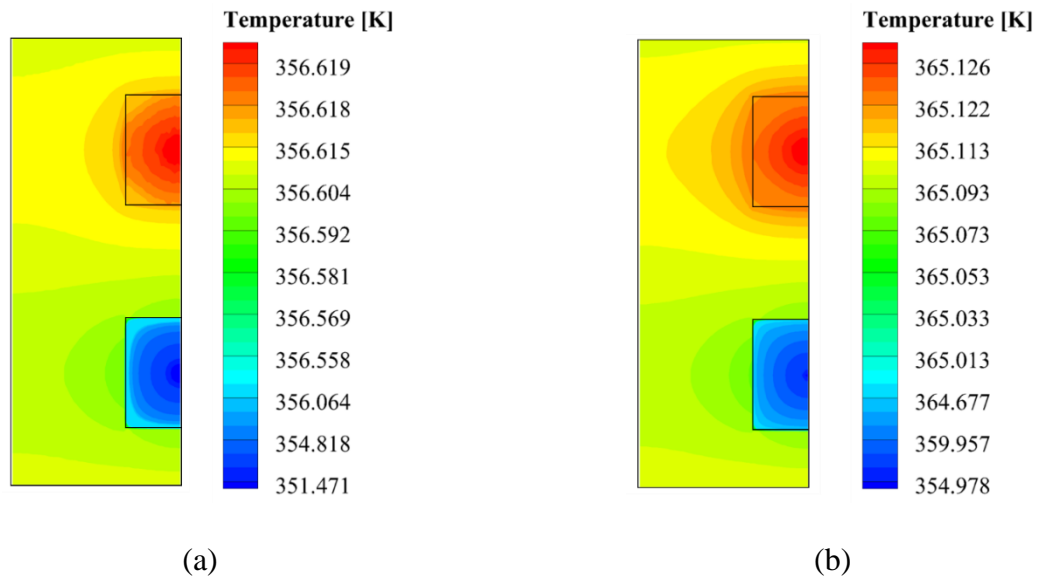


Figure 3. 14. Temperature contours for two micro-channel configurations at a $Z/D_h=125$ and 10 MPa, (a) Parallel flow, (b) Counter-flow

Axial variation of the local Nusselt number along the hot (liquid sodium) micro-channel for the parallel- and counter-flow arrangements and operating pressures in the cold

(sCO₂) channel of 8, 10, and 30 MPa is presented in Figure 3. 15. For both flow arrangements, the entrance length is very short and heat transfer becomes fully developed for values of $Z/D_h \geq 10$. For the parallel- and counter-flow arrangements the predicted values of Nusselt number in the fully developed region are 3.1062 and 3.069, respectively which is in an excellent agreement with the value of 3.096 given by Shah and London [53].

The axial variation of the Nu number in the hot micro-channel is virtually unaffected by the operating pressure since the local wall heat flux is approximately independent of pressure, except in the entrance region as shown in Figure 3. 15. Therefore, variation of thermo-physical properties of sCO₂ (cold fluid) has a small effect on heat transfer between the cold and hot micro-channels, except for pressures close to the critical pressure. For the counter-flow arrangement, the value of Nu number at the cold end (exit of the hot micro-channel, $Z/D_h = 0$) increases because the entrance effects in the cold micro-channel increase heat transfer between the two channels.

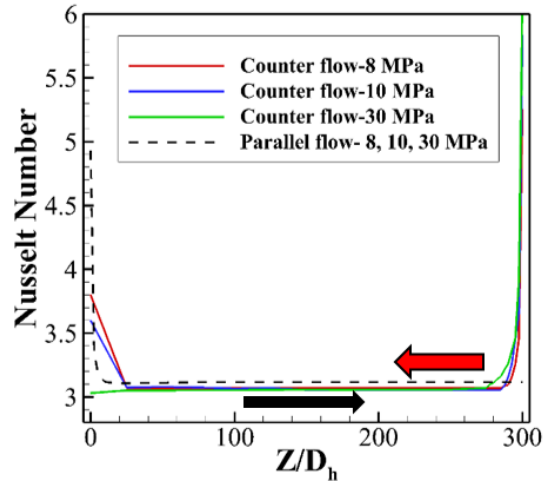


Figure 3. 15. Axial variation of Nusselt number for the liquid sodium in parallel- and counter-flow arrangements for operating pressures of 8, 10, and 30 MPa

3.5.4.3 Local heat transfer coefficient and temperature gradient for supercritical CO₂

To study the details of heat transfer, the local values of convection heat transfer coefficient h , wall heat flux $(q'')_{y=}$, and wall temperature gradient $(dT/dy)_{y=0}$ were determined. The wall temperature gradient was determined from Eqn. 3.13 using predicted value of the wall heat flux, while the local heat transfer coefficient was calculated from Eqn. 2.11. Numerical values of the local wall temperature, bulk fluid temperature, thermal conductivity, wall heat flux, and temperature gradient determined at the cold channel centerline for the values of fluid temperatures and pressures and flow arrangements used in the analysis are summarized in Table 3. 5.

Table 3. 5. Bulk fluid temperature, local wall temperature, wall temperature gradient, wall heat flux, and heat transfer coefficient as functions of pressure for the parallel- and counter-flow arrangements

Parallel Flow						
			Center Line		Eqn. 2.13	Eqn. 2.11
P_i [MPa]	T_w [K]	T_b [K]	k_f [W/mK]	$q''_{y=0}$ [W/m ²]	$(dT/dy)_{y=0} =$ q''/k [K/m]	$h = q''/(T_w -$ $T_{bulk})$ [W/m ² K]
8	359.49	359.440	0.028	17.6	627	335
10	356.32	356.054	0.032	99.8	3,118	381
30	356.06	356.057	0.081	1.8	22	950
Counter Flow						
			Center Line		Eqn. 2.13	Eqn. 2.11
P_i [MPa]	T_w [K]	T_b [K]	k_f [W/mK]	$q''_{y=0}$ [W/m ²]	$(dT/dy)_{y=0} =$ q''/k [K/m]	$h = q''/(T_w -$ $T_{bulk})$ [W/m ² K]
8	365.99	365.85	0.028	44.1	1,575	335
10	365.89	365.18	0.032	278.0	8,688	386
30	365.98	365.92	0.076	54.8	722	952

For the values of inlet fluid temperature and pressure used in the analysis, thermal conductivity k_f increases as pressure is increased above the critical pressure as shown in Figure 3. 7. However, the value of k_f remains constant from the channel centerline to the corner since wall temperature is virtually constant due to high thermal conductivity of the channel walls.

Variation in local values of the wall heat flux, wall temperature gradient, and convection heat transfer coefficient, along the bottom wall of the cold channel from the centerline to the corner, (i.e., from point A to B shown in Figure 3. 11) for the fully developed flow ($Z/D_h=200$) is presented in Figure 3. 16 for operating pressures of 8, 10, and 30 MPa, and parallel- and counter-flow arrangements. Variation in these quantities with X/D_h is similar: local values decrease from the maximum at the channel centerline to the minimum in the corner. As the results show, the wall temperature gradient, convection heat transfer coefficient, and wall heat flux are affected by the working pressure. This can be explained by the effect of pressure on thermo-physical properties of the working fluid ($s\text{CO}_2$), especially in the vicinity of CP. Also, all of these quantities are affected by the flow arrangement. However, for the analyzed geometry and operating conditions, the effect of flow arrangement (parallel- or counter-flow) is smaller compared to the effect of operating pressure.

Variation of the wall heat flux with X/D_h and operating pressure is presented in Figure 3. 16a for the parallel- and counter-flow arrangements. Due to the effect of pressure on thermal conductivity and, thus on temperature gradient (Eqn. 3.13), variation of the wall heat flux with pressure is not monotonic. For the analyzed range of pressures, wall heat flux is higher for the intermediate pressure of 10 MPa compared to the highest and lowest pressures of 30 and 8 MPa. As presented in Table 3. 5, for the operating pressure of 30 MPa the wall temperature

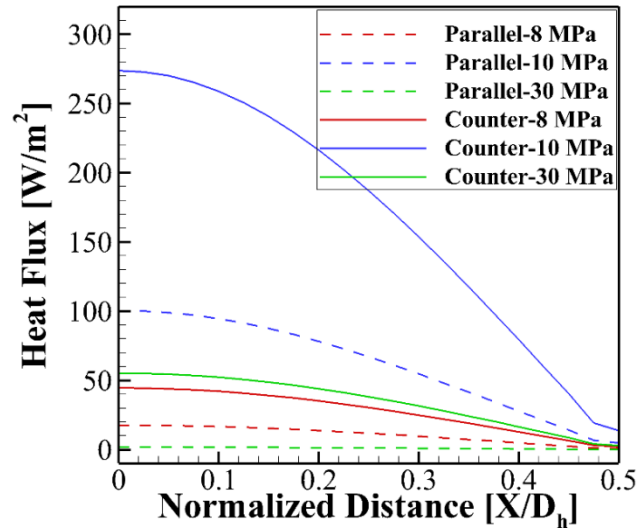
gradient is small resulting in low wall heat flux. However, for the pressure of 10 MPa, wall temperature gradient is very high, resulting in high wall heat flux.

Variation of the wall temperature gradient with X/D_h and operating pressure are presented in Figure 3. 16b for the parallel- and counter-flow arrangements. The local wall temperature gradient is negligible in the corner and increases toward the channel centerline, reaching the maximum value at the centerline. Small values of the wall temperature gradient in the corner result in very low values of the wall heat flux and local convection heat transfer coefficient at that location.

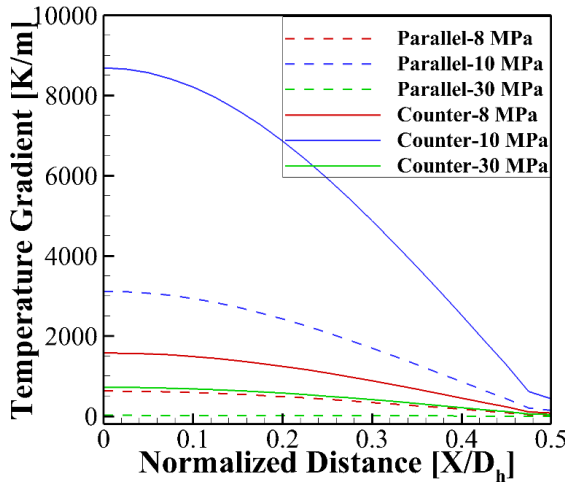
Similar to the wall heat flux and for the same reasons, variation of the wall temperature gradient with operating pressure is not monotonic; for the analyzed range of pressures wall temperature gradient is larger for the intermediate operating pressure of 10 MPa compared to the lowest and highest pressures (8 and 30 MPa, respectively).

Since the convection heat transfer coefficient h is calculated from the predicted value of wall heat flux using Eqn. 3.11, its value is also affected by the operating pressure. Variation of the local heat transfer coefficient with X/D_h , operating pressure, and flow arrangement is presented in Figure 3. 16c. Similar to the wall heat flux and wall temperature gradient, the value of h is the highest at the channel centerline and lowest in the corner. Since the wall temperature gradient is negligible in the corner, the values of h and wall heat flux at that location are very low. The local heat transfer coefficient increases monotonically with the increase in pressure, with the lowest value corresponding to the lowest analyzed pressure (8 MPa), and the highest value corresponding to the highest analyzed pressure (30 MPa). As the results show, the heat transfer coefficient at 8 MPa is lower compared to 10 MPa which is in agreement with experimental results obtained by Hsieh, J.C. et al. [69].

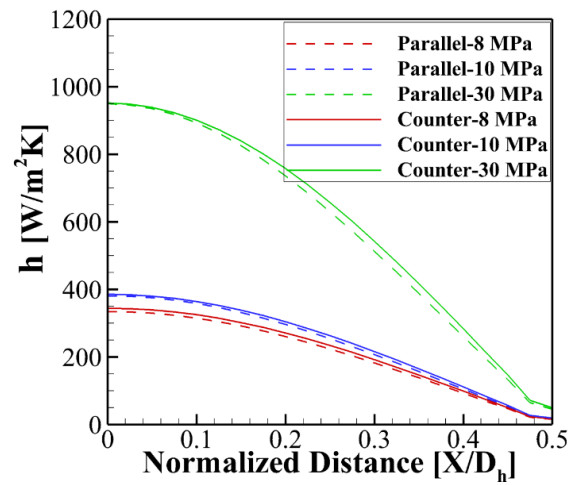
Although thermo-hydraulic characteristics of the parallel- and counter-flow arrangements are similar, for the values of inlet temperature and pressure used in the analysis, the wall heat flux for the counter-flow arrangement is considerably higher compared to the parallel flow arrangement.



(a)



(b)



(c)

Figure 3. 16. Cold (sCO₂) micro-channel: Variation of local (a) heat flux (b) wall temperature gradient (c) heat transfer coefficient along the A- B line over a range of pressure and parallel- and counter-flow arrangements

CHAPTER 4: VALIDATION OF NUMERICAL MODEL

4.1 Overview

The physical model, model assumptions and boundary conditions for the advanced micro-channel geometries (semi-circular and circular cross section) are described in this section. As mentioned in Section 1.7 of Chapter 1, two new micro-channel designs and arrangements (topologies): staggered semi-circle and circular double banking were investigated in this study as potential candidates for a more efficient PCHE design. The numerical model results, such as the friction coefficient and Nusselt number, obtained for these micro-channel geometries and topologies were verified by comparing them to the values reported in the literature [53]. The details of CFD simulations and predicted thermal and hydraulic performance of the PCHEs employing these micro-channel geometries are presented in Chapters 6 and 7. The objective of the analysis described in this section is to validate CFD results for the friction coefficient and Nusselt number obtained for a $s\text{CO}_2$ as the cold side working fluid in the semi-circular and circular micro-channel geometries.

4.2 Physical model

3D numerical analysis of straight micro-channels of semi-circular and circular geometry (cross-section) was performed using $s\text{CO}_2$ as the cold and hot working fluid to study the friction coefficient and Nusselt number in the hot and cold channels of a PCHE recuperator used in a $s\text{CO}_2$ Brayton cycle. For the IHX application, circular micro-channel geometry was investigated where liquid sodium and $s\text{CO}_2$ were used as the hot and cold working fluids, respectively.

The PCHE model with a semi-circular geometry was selected from the In Hum Kim (2012) work [70, 71] as the Base Model (BM). This geometry was developed by HEATRIC

and used as high temperature recuperator (HTR) in a Helium test loop by In Hum Kim (2012) [71].

Figure 4. 1 shows schematic of the semi-circular micro-channel geometry selected as a BM. The channel diameter and cross-section dimensions (width \times height) of the selected geometry are 1.51 mm and 2.62 mm \times 2.92 mm, respectively. In the CFD simulations, a pair of the hot and cold channels were modeled since both the hot and cold channels are repeated periodically with a periodic length (spacing, or pitch) of 2.92 mm, as presented in Figure 4. 1. The use of periodic boundary condition is equivalent to solving the problem with an infinite number of the hot and cold channel arrays [70]. Table 4. 1 lists details of the BM size and geometry. This geometry was also considered in a transient thermal analysis of the PCHE using air as the working fluid performed by Pra et. al [17].

Optimization of a PCHE with the objective to decrease its size and increase compactness depends on parameters such as the micro-channel diameter, spacing, and the number of micro-channels. The heat transfer performance of a PCHE increases for small micro-channel diameters and reduces the overall size of the heat exchanger, but pressure drop increases due to increased frictional losses [8]. For a fixed total mass flow rate, a smaller number of micro-channels results in an increase in the mass flow rate of working fluid through individual channels and, consequently, in higher Reynolds number, convection heat transfer coefficient, and pressure drop. Therefore, a trade-off between heat transfer and pressure drop needs to be considered when selecting channel diameter. For the laminar flow regime, pressure losses are lower compared to the transitional and turbulent flows, resulting in lower pumping power. Also, since transitional Re number for the investigated BM geometry is not known, a low value of Reynolds number was selected to ensure the flow regime is indeed laminar. Pra

et. al [17] used $Re=1000$ on the cold side of a PCHE recuperator in their experiments. Since the geometry used in this study is identical to the geometry used by Pra, the same Reynolds number, i.e., $Re=1000$ was selected for the cold channel geometries studied in this work.

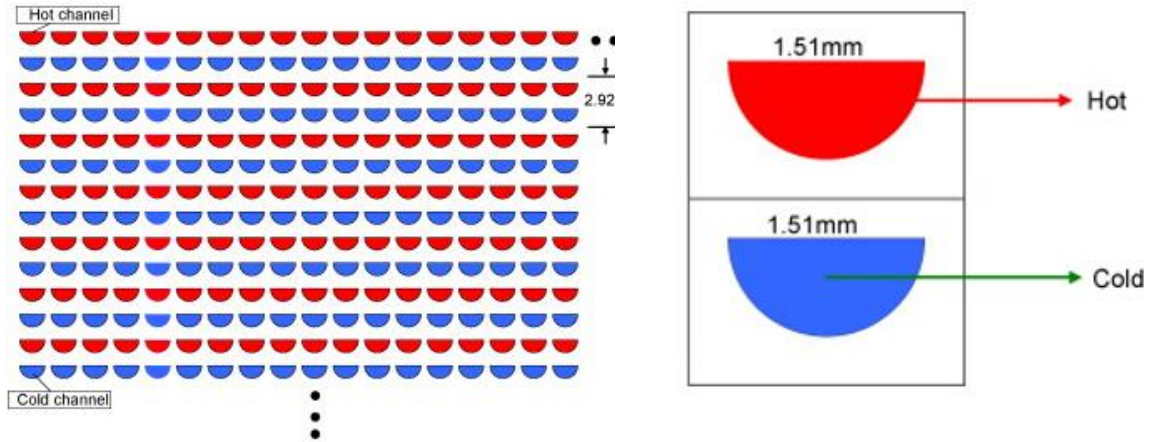


Figure 4. 1. Schematic of a semi-circle channel cross section selected as a Base model from the literature [70, 71]

The circular staggered double-etched (SDE) geometry was modeled using the same micro-channel diameter (1.51 mm) as used for the BM. Figure 4. 2 shows the PCHE cross section employing a circular micro-channel geometry.

A schematic of the semi-circular micro-channel geometry in a staggered double-etched (SDE) pattern for the sCO_2 - sCO_2 application (recuperator or other PCHE heat exchanger used in a sCO_2 Brayton cycle) is presented in Figure 4. 3. As Figure 4. 2 and Figure 4. 3 show, these micro-channel geometries can be manufactured by etching semi-circular channel shapes on both sides of the plate, i.e., by double etching. A shim plate placed between the etched plates is needed for the micro-channel geometry shown in Figure 4. 3.

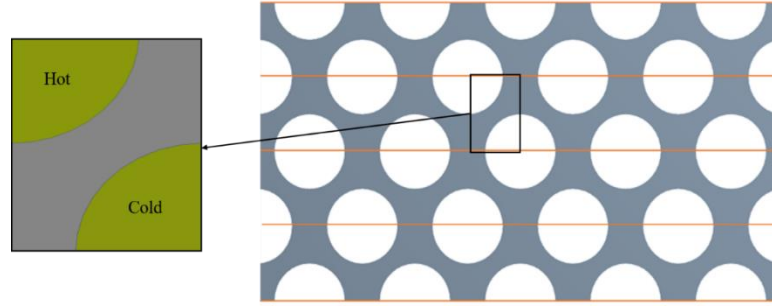


Figure 4. 2. Schematic of a circular micro-channel cross section geometry

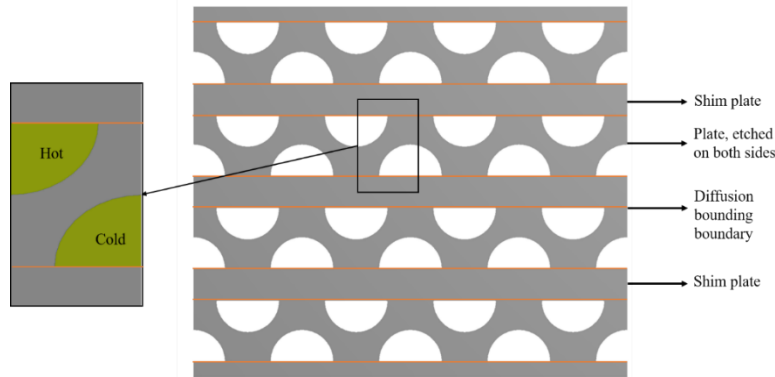
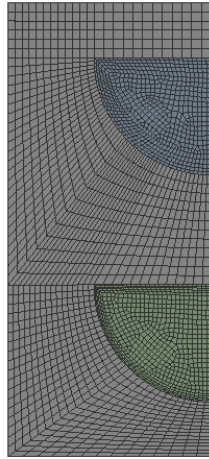


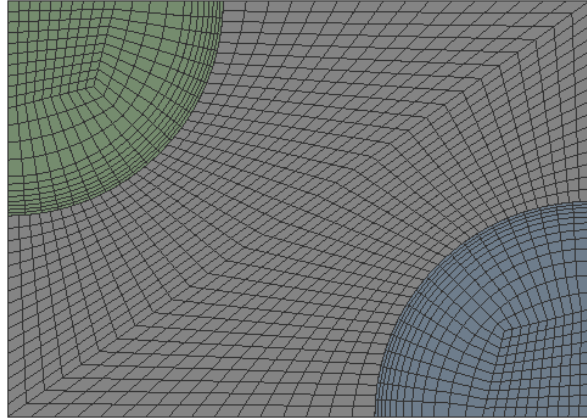
Figure 4. 3. The schematic of semi-circular staggered double-etched cross section geometry and topology

Table 4. 2 lists boundary conditions for the studied geometries. The cross-section area of solid wall in Base model, circular channel, and semi-circular staggered double-etched geometries were assumed to be identical. Figure 4. 4 shows the computational (discretization) grid for both geometries. The mesh sensitivity check was performed for $s\text{CO}_2$ as a working fluid with constant thermo-physical properties at 25.1 MPa, $T_{\text{in}}=620.93$ K and $\text{Re}=1000$ for both the Base model and circular SDE geometry. The flow regime was assumed to be laminar for both the hot and cold channels. The Ansys meshing module was used to generate a fully-structured grid with hexahedral elements for the whole computational domain. Fully structured meshing elements were generated since this model is highly space-efficient, has better convergence, and higher resolution compared to the unstructured grids. The details of the mesh independence study were presented in Chapter 2.

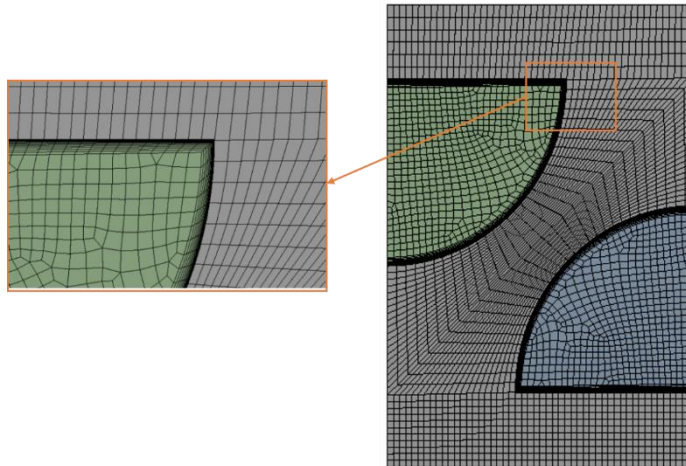
The minimal number of grid elements used for the Base model and circular channel model were 900,000 and 620,000, respectively to minimize the error for the predicted values of C_f , Re and Nu .



Base model



Circular SDE channel geometry



Semi-circular SDE geometry

Figure 4. 4. Computational grid for the Base model, circular and semi-circular staggered double-etched micro-channel geometries

Table 4. 1. Dimensions of the micro-channel and surrounding walls for analyzed geometries

Parameter	Semi-circular (Base model, BM)	Circular SDE model	Semi-circular SDE model
Channel diameter (mm)	1.51	1.51	1.51
Hydraulic diameter (mm)	0.922	1.51	0.922
Channel fin thickness (mm)	0.707	0.67	0.45146
Plate thickness (mm)	1.46	1.46	1.46
Channel length (mm)	365	500	765
Cross-section area of solid wall (mm ²)	5.86	5.86	5.86

Table 4. 2. The Boundary conditions for studied models

Boundary	BM	Circular SDE	Semi-circle SDE
Inlet	Velocity inlet	Velocity inlet	Velocity inlet
Outlet	Pressure outlet	Pressure outlet	Pressure outlet
Top wall	Periodic	Symmetry	Periodic
Bottom wall	Periodic	Symmetry	Periodic
Side walls	Adiabatic/symmetry	Symmetry	Symmetry
Front wall	Adiabatic	Adiabatic	Adiabatic
Back wall	Adiabatic	Adiabatic	Adiabatic

Alloy 617 was used as a material of construction with density of 8,369 kg/m³, specific heat of 417 J/kg.K and thermal conductivity of 21 W/m.K. The values of peripherally-averaged Nusselt number and $C_f Re$ obtained in numerical analysis for both the semi-circular model

(Base model) and circular channel geometry,, and sCO₂ as a working fluid were compared to the values reported in Shah and London [53].

4.3 Semi-circular (Base model) and semi-circular staggered double-etched geometry –

Validation of results

The results concerning thermohydraulic performance of the analyzed geometries obtained in this study (Nusselt number Nu and $C_f.Re$) were compared to the analytical solution from the literature. Table 4. 3 lists the results from this study obtained by assuming constant and temperature- and pressure-dependent properties of sCO₂, and temperature-independent properties of liquid sodium.

The $C_f.Re$ and Nusselt number values of 15.767 and 4.089, respectively were reported by Shah and London [53] for a semi-circular geometry and fully-developed laminar flow. The results of this study demonstrate excellent agreement with the analytical solution [53] . The value of Nu number reported in [1] corresponds to the constant wall heat flux in the axial direction with constant peripheral wall temperature and fully-developed laminar flow.

The Nusselt number reported by Shah and London [53] corresponding to constant wall temperature in peripheral and axial directions is 3.36. The predicted value of Nusselt number of 3.38 obtained in this study for the fully developed flow on the hot side with liquid sodium as a working fluid is in excellent agreement with the value of Nusselt number reported by Shah and London for the B.C. of constant wall temperature in the peripheral and axial directions.

Table 4. 3. The $C_f.Re$ and Nusselt number values obtained in this study for semi-circular geometry. The error was calculated with respect to values reported by Shah and London [53].

Model	$C_f.Re$	Nu	$C_f.Re$ Error%	Nu Error%
Semi-circular (constant sCO ₂ properties)	15.67	4.098	0.57	0.2
Semi-circular (pressure and temperature- dependent sCO ₂ properties)	15.67	4.21	0.57	2.9
Semi-circular (liquid sodium Pr=0.005) constant properties	15.71	3.38	0.3	0.3

4.4 Circular channel geometry -Validation of results

A 3D numerical analysis of a forced laminar convection heat transfer in a PCHE with a circular micro-channel geometry, sCO₂ as the cold working fluid and liquid sodium as the hot working fluid was performed. The Reynolds number values for the cold and hot working fluids are 1000 and 146, respectively. Table 4. 4 lists the results for $C_f.Re$ and average Nusselt number obtained in this study for sCO₂ as a working fluid by assuming constant and temperature- and pressure-dependent thermo-physical properties, and liquid sodium with constant properties. The values for $C_f.Re$ and average Nusselt number of 16 and 4.364, respectively were reported by Shah and London [53] for the fully-developed laminar flow and circular channel geometry. The comparison with the results obtained in this study shows an excellent agreement.

Table 4. 4. The $C_f.Re$ and Nusselt number values obtained in this study for a circular geometry

Model	$C_f.Re$	Nu	$C_f.Re$ Error%	Nu Error%
Circular (constant sCO ₂ properties)	15.987	4.43	0.06	1.6
Circular (pressure and temperature- dependent sCO ₂ properties)	15.987	4.52	0.57	3.6
Circular (liquid sodium Pr=0.005 constant properties)	15.987	4.29	0.06	1.6

CHAPTER 5: FINITE ELEMENT ANALYSIS - BOUNDARY CONDITIONS FOR STRESS CALCULATIONS

5.1 Overview

PCHEs often operate under harsh conditions, high operating temperatures and pressures. Therefore, they are subject to high mechanical and thermal stresses due to large pressure difference between the hot and cold fluids and high temperature gradients. In this section, the results of an analysis performed to investigate applicability of the Finite Element Method (FEM) for predicting stresses in a micro-channel PCHE geometry are presented and discussed. A section of a PCHE, representing a PCHE core, including a pair of hot and cold semi-circular micro-channels was selected for structural assessment for conditions corresponding to the steady-state operation of a heat exchanger. ANSYS-mechanical module was used to calculate 3D stress distribution including thermal and mechanical stresses in a PCHE section selected for the analysis. Temperature distribution corresponding to the simultaneously developing flow and conjugate heat transfer, determined by performing a CFD analysis for the prescribed boundary conditions was mapped to the structural domain. Stainless steel (SS316L) with temperature-dependent mechanical properties was chosen as the material of construction. The stress analysis was performed using the 2D and 3D approaches. The 2D stress field was determined by using the plane strain and generalized plane strain models of the PCHE core located in the middle section of the PCHE, and at the locations close to the PCHE inlet and exit. A sensitivity analysis was performed to determine the appropriate boundary conditions of the novel PCHE topology in the mechanical integrity evaluation.

In general, the diffusion bonded PCHE channels are categorized as high pressure containing vessels. Therefore, the design-by-rule methodology described in the ASME Boiler and Pressure Vessel Code (BPVC) section VIII Division 2 [72] is adopted for the mechanical

stress calculation and PCHE design. As mentioned earlier, the design-by-rule method assumes no thermal strain in the micro-channel axial (flow) direction and no stress concentration at the channel corners, thus rendering insufficient design criteria. However, the design-by-rule method can be used for the intermediate-pressure applications [73] to design a PCHE with the straight and zig-zag semi-circular channels. The design-by-rule methodology may not be sufficient for mechanical design of the high pressure PCHEs and complex geometries such as airfoil fin and S-shape configurations. The design-by-analysis, the tool recommended by BPVC, is an alternative method especially for the elastic-plastic behavior. Thus, the accurate stress and strain modeling is performed to satisfy the design criteria. The design-by-rule methodology has been chosen for the PCHE design by many researchers to date even though it involves some design issues [73].

As no general methodology has been recommended for the design-by-analysis of high-pressure PCHEs, one of the aims of this work was to introduce a suitable FE model allowing for accurate predictions of thermal and mechanical stresses for the high-pressure PCHEs. A 3D stress distribution including thermal and mechanical stresses in a PCHE section selected for the analysis was compared to the commonly used 2-D Plane Strain model at different locations. The 2D Generalized Plane strain model was introduced as an alternative to the 3D stress modeling of high pressure straight and zig-zag PCHEs, and the results of these simulations were compared.

Also, using the average temperature of the solid domain as the reference temperature for thermal stress analysis may result in inaccurate values of thermal stress at some locations of the PCHE core. Thus, a suitable reference temperature was recommended in this study for thermal stress analysis.

5.2 System description

Figure 5. 1 shows the schematic of a closed-loop $s\text{CO}_2$ Brayton cycle with recompression integrated with the Concentrated Solar Power (CSP). The turbine inlet pressure higher than 20 MPa and the turbine inlet temperature higher than 700°C significantly increase thermal efficiency of the $s\text{CO}_2$ Brayton cycle. In the $s\text{CO}_2$ loop, heat provided by the solar tower is transferred to the $s\text{CO}_2$ via an intermediate heat exchanger (IHx), shown in Figure 5. 1. In the $s\text{CO}_2$ Brayton cycle, the high and low temperature recuperators (HTR and LTR), shown in Figure 5. 1, are employed to exchange heat between the hot and cold $s\text{CO}_2$. PCHEs are recommended for the HTR and LTR in a $s\text{CO}_2$ Brayton cycle due to their high-pressure containment capability. Two semi-circular cross section micro-channels, representative of the PCHE heat transfer core geometry, were chosen for thermo-hydraulic and structural analyses.

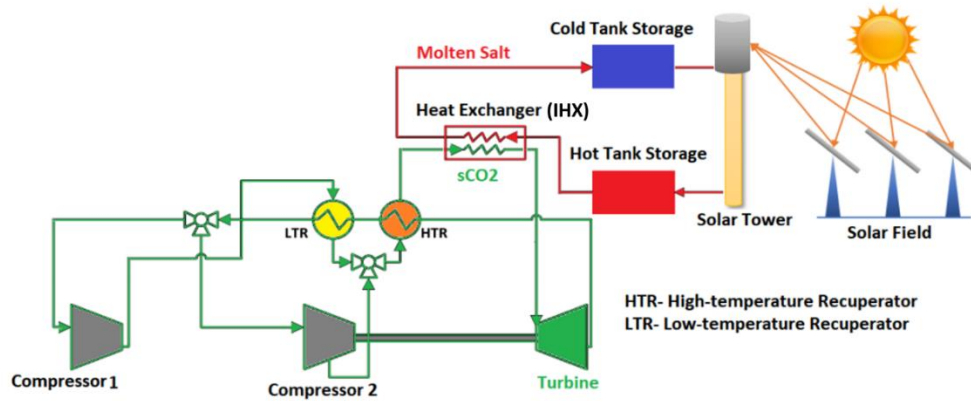


Figure 5. 1. The schematic of $s\text{CO}_2$ Brayton cycle integrated with CSP [74]

5.2.1 Thermal analysis

Schematic of a micro-channel arrangement and configuration is presented in Figure 5. 2a. Table 5. 1 lists dimensions of computational domain used to model the PCHE unit selected for this study [30]. The operating pressure, hot and cold fluid inlet temperatures, and boundary conditions are listed in Table 5. 2.

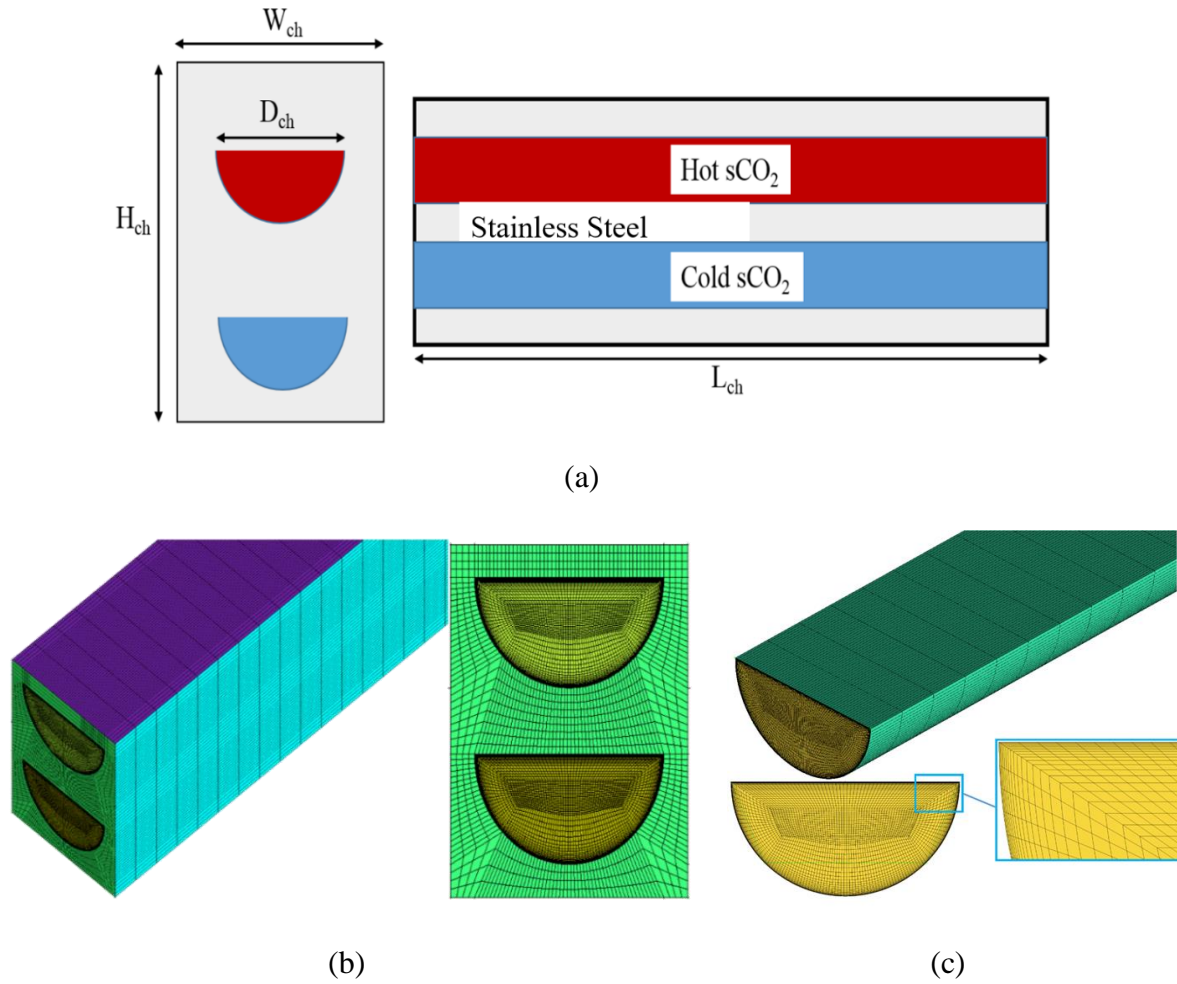


Figure 5. 2. (a) Schematic of the micro-channel arrangement, (b) computational domain, (c) discretization grid

Table 5. 1. The domain parameters

Variable	Values (mm)
D_{ch}	2
H_{ch}	3.2
W_{ch}	2.5
L_{ch}	200

Table 5. 2. Boundary conditions for pressure and temperature used in thermal analysis

Boundary	B.C.	Hot side	Cold side
Inlet	Velocity inlet	6.118 (m/s)	1.518 (m/s)
	Temperature	730 (K)	500 (K)
Outlet	Pressure outlet	9 MPa	22.5 MPa
Bottom /Top wall	Periodic	-	-
Side walls	Adiabatic	-	-
Back /Front wall	Adiabatic	-	-

5.2.2 Numerical modeling and validation

ANSYS-FLUENT was used to model a 3D steady state developing flow and conjugate heat transfer in the PCHE model selected for the analysis. The k- ϵ turbulence model with enhanced wall treatment function was chosen to resolve the Reynolds shear stress. The y-plus value of one ($y^+ = 1$) was used to evaluate the first cell height, equation (5.1).

$$y^+ = \frac{y \sqrt{\frac{\tau_w}{\rho}}}{\nu} \quad (5.1)$$

Where τ_w , ν , ρ , and y are the wall shear stress, kinematic viscosity, density, and the first cell height, respectively. ANSYS-ICEM CFD was used to generate a fully-structured mesh domain using O-grid approach, see Figure 5. 2b and Figure 5. 2c. The periodic B.C. was used for the top/bottom walls and adiabatic B.C for other walls. Stainless steel 316L (SS316L) was selected as the solid material with temperature-dependent thermal conductivity presented in Table 5. 3. Thermo-physical properties of sCO₂ were obtained by coupling FLUENT to NIST REFPROP database.

Table 5. 3. The temperature-dependent thermo-physical and mechanical properties of SS316L

Temperature (°C)	Thermal Conductivity (W/m.K)	Coefficient of Thermal Expansion ($\mu/\text{°C}$)	Elasticity Module (GPa)	Poisson's ratio
100	16.2	16.5	194	0.3
200	17.5	17.3	185	0.3
300	18.8	17.6	177	0.3
400	20.1	18	169	0.3
500	21.4	18	160	0.3

To validate the turbulence model results, the values of average Nusselt number (equation (5.2)) and friction coefficient (equation (5.3)) obtained in the analysis of pure convection for the channel subjected to the constant wall heat flux boundary condition were compared to the well-known Dittus-Boelter and Gnielinski correlations shown in Equation (5.4) and equation (5.5), respectively and to numerical results from reference [30]. The validated turbulence model and numerical grid were used in the selected PCHE model for thermo-hydraulic analysis.

$$Nu = \frac{hD_h}{k_f} \quad (5.2)$$

$$C_f = \frac{\tau_w}{\frac{1}{2}\rho u^2} \quad (5.3)$$

Where h , D_h , k_f , u are the heat transfer coefficient (HTC), hydraulic diameter, thermal conductivity of a fluid, and the bulk velocity, respectively.

$$Nu = 0.023 Re^{0.8} Pr^{0.4} \quad (5.4)$$

$$Nu = \frac{(C_f / 2)(Re - 1000)Pr}{1 + 12.7(C_f / 2)^{0.5}(Pr^{\frac{2}{3}} - 1)} \quad (5.5)$$

$$C_f = \frac{1}{4}(0.79 \ln Re - 1.64)^{-2}$$

Numerical results obtained from the CFD analysis were compared to the corresponding values obtained from Equations (5.4) and (5.5) and are listed in Table 5. 4.

Table 5. 4. The Nusselt number and friction coefficient comparison

Correlation	Friction coefficient	Nusselt number	Friction coefficient Error%	Nusselt Error%
Dittus-Boelter	-	104	-	3.39
Gnielinski	0.00717	107.95	-	2.27
CFD	0.00725	110.65	1.11	-

Table 5. 5 shows comparison of the Nusselt number and fiction coefficient values obtained by the CFD analysis to the published values from reference [30]. The obtained numerical results show excellent agreement with the literature [30].

Table 5. 5. The Nusselt number and friction coefficient comparison with literature for sCO₂

	Hot Channel		Cold Channel	
	C _f	Nu	C _f	Nu
CFD	0.0062	44.39	0.0065	54.10
Reference [75]	0.0060	43.90	0.0066	52.20
Error%	3.30%	1.10%	1.50%	3.60%

5.2.3 Temperature field

Temperature distribution in the solid domain (channel walls) was obtained by performing a conjugate heat transfer analysis. The steady-state heat conduction equation was solved to determine temperature in the 3D model of the channel. The resulting temperature field was used to calculate thermal stresses in the solid domain. Figure 5. 3a illustrates the predicted temperature distribution (temperature contours) in the 3D computational domain.

The temperature is changing linearly along the channel (in the flow direction) from the cold inlet side to the hot inlet side except in the entrance regions where entrance effects dominate. Due to large temperature difference between the hot and cold ends, it is necessary to evaluate thermal stresses at different locations along the channel. Figure 5. 3b shows variation of the average temperature in the solid domain along the channel length, i.e., in the flow direction. Except near the channel inlet and exit, temperature variation is linear, as expected for the boundary condition of the constant wall heat flux.

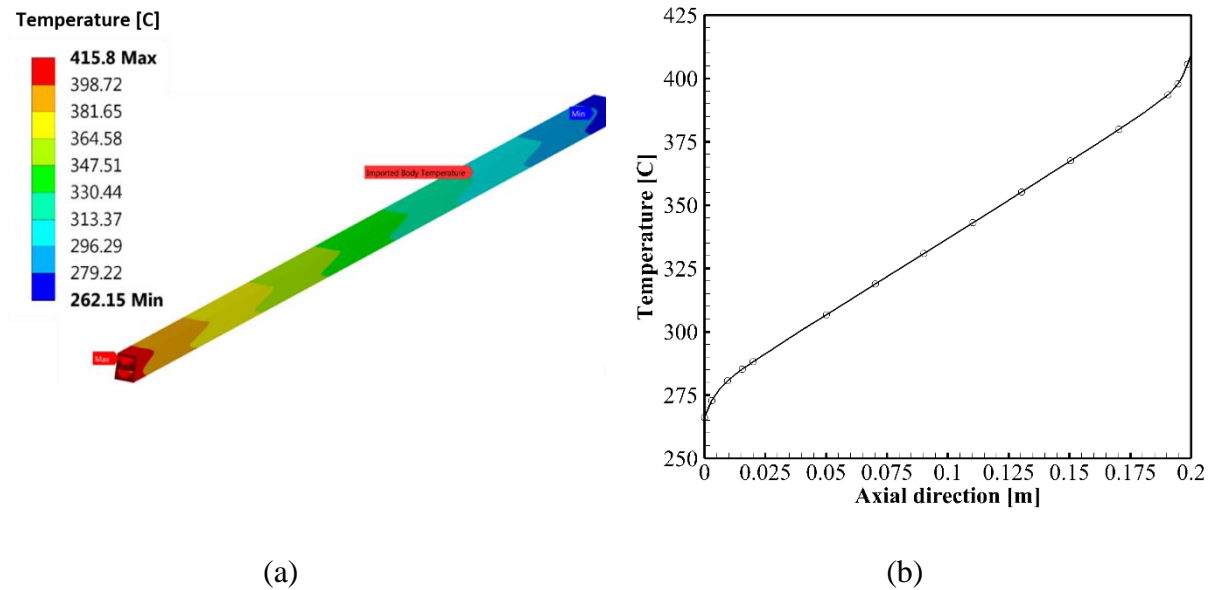


Figure 5. 3. (a) 3D temperature contour, (b) temperature distribution along the channel

To study variation of thermal stresses along the channel, three channel cross sections corresponding to axial locations of $Z=0.025$ m, $Z=0.1$ m (mid plane), and $Z=0.175$ m, were selected. Figure 5. 4 shows temperature contours in channel walls at the selected cross sections. It is noted that the average wall temperature difference (ΔT) between the hot and cold channels is almost 6°C . The 3D temperature distribution obtained in the CFD analysis was imported as a thermal load into the Ansys-mechanical module and used in the 3D stress analysis.

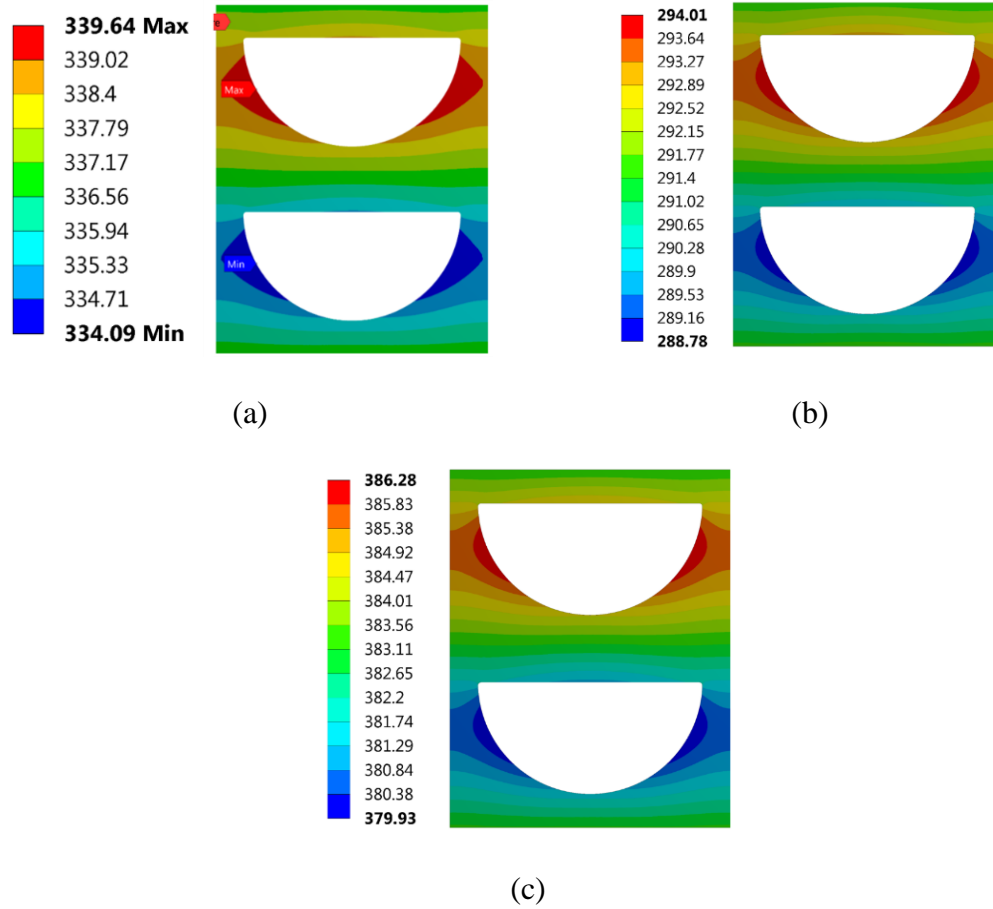


Figure 5. 4. Temperature (°C) contours (a) mid-plane, (b) Z=0.025 m, (c) Z=0.175 m.

5.3 Structural analysis

In the stress analysis, both mechanical and thermal stresses were calculated using ANSYS-mechanical. The ANSYS mechanical uses a FE method (FEM) to solve the Hook's equation in a linear elastic analysis. In this analysis, the mechanical properties of the solid material were considered temperature-dependent. The values of modulus of elasticity (E), coefficient of thermal expansion, and Poisson's ratio used in the analysis are listed in Table 5.

3. The equivalent tensile stress (von-Mises stress (Equation (5.6)) and normal stresses (axial direction stress) are reported for different models. It is assumed that the solid domain is monolithic and there are no distinguished boundaries in the diffusion bonding areas. The objective of this study was to identify and select a suitable FEM approach for 2D simulations

and use it for accurate prediction of stress integrity of a straight channel PCHE operating at high temperature and pressure.

The stress intensity and equivalent tensile stress (von-Mises stress) were calculated using Equations (5.6) and (5.7).

$$\sigma_I = \max(|\sigma_1 - \sigma_2|, |\sigma_2 - \sigma_3|, |\sigma_3 - \sigma_1|) \quad (5.6)$$

$$\sigma_e = \left[\frac{(\sigma_1 - \sigma_2)^2 + (\sigma_2 - \sigma_3)^2 + (\sigma_3 - \sigma_1)^2}{2} \right]^{1/2} \quad (5.7)$$

5.3.1 Finite Element modeling

In the FE modeling of stresses, the representative model of a PCHE includes one hot and one cold channel as shown in Figure 5. 5a. In the 2D models, thermal stresses were calculated based on the temperature distribution obtained from the conjugate heat transfer analysis instead of assuming uniform peripheral distribution of the micro-channel wall temperature. This is because using uniform value would introduce an error in predicted stress values and increase difference between the 2D and 3D predictions.

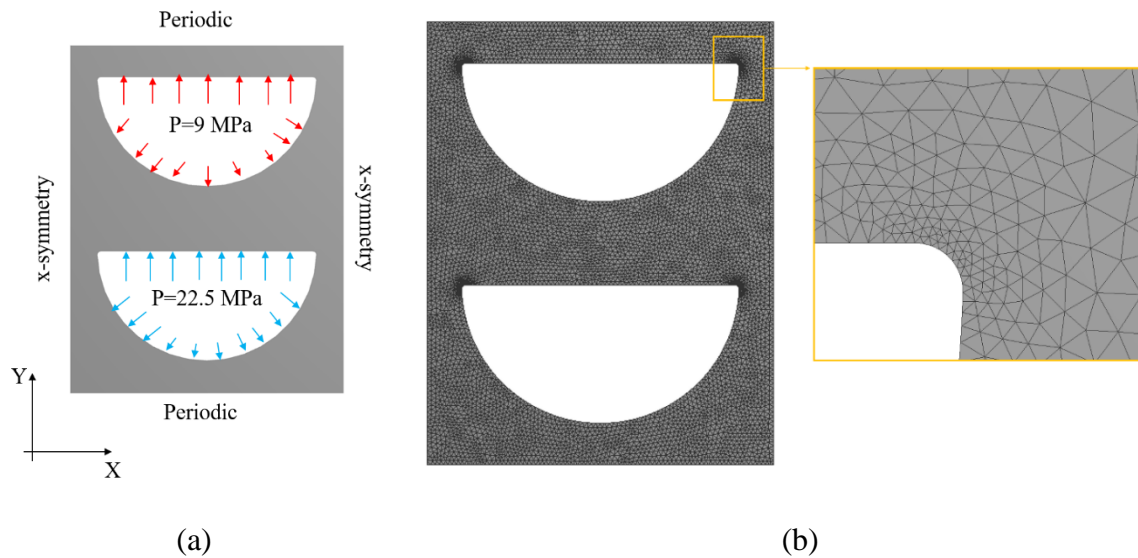


Figure 5. 5. FE model (a) geometry and B. Cs, (b) grid.

The boundary conditions for the 3D and 2D stress models are shown in Figure 5. 5. The periodic boundary condition was applied to the top and bottom walls, as presented in Figure 5. 5a. The FE discretization grid is illustrated in Figure 5. 5b. In the 3D model, no constraint was adopted for the front and back walls, so the model was allowed to deform in the axial direction. The pressure loads applied on the channel wall, see Table 5. 2 for operating pressures, impose forces in the normal direction (perpendicular to the axial direction), causing deformations in the x and y directions. Thus, the strain in the axial direction (z-direction) is due to the thermal expansion. The pressure drop along micro-channel length is small compared to the operating pressure, thus, in this study, the effect of pressure drop on the stress calculation was neglected.

Reference temperature plays important role in the thermal stress calculations. As mentioned earlier, assuming the average solid temperature as the reference temperature may result in inaccurate thermal stress values in the PCHE core. The periodic boundary conditions on the top and bottom walls and symmetry boundary conditions on the side wall place displacement constraints on the model, thus the choice of reference temperature affects thermal stresses. However, if no boundary conditions are imposed on the top, bottom, and side walls, the choice of reference temperature does not affect the calculated values of thermal stresses.

Based on the analyses performed in this study, it is recommended reference temperature be set to the minimum solid wall temperature (262.15 °C in this case) located at the cold end of the PCHE core, where thermal stresses are the lowest. It should be noted that the maximum values of thermal stresses occur at locations close to the PCHE headers and they can be calculated using 3D stress models. The results of thermal stress analysis performed in this

study show that assuming the minimum solid temperature at the cold end provides realistic values of stresses obtained in a 2D model when compared to the 3D model.

As sharp channel corners are blunted during the diffusion bonding process, it has been assumed they are rounded to the fillet radius of 0.02 mm to avoid unrealistically high values at the channel corners. The values of fillet radius have not been reported in literature. A mesh independency analysis was performed to study the effect of number of finite elements in the channel corner on the predicted stress values. The results show that a minimum of 9 triangular elements at the channel corner is needed to make stress values at the channel corner independent of the number of elements. The channel corners are the only regions of the PCHE core where plastic deformation occurs; thus, the use of a linear elastic approach would result in high stress concentration values. Lee and Lee [18] showed that the channel corners experience very high stress concentration if no fillet is assumed at the channel corners. They performed several stress analyses to determine the stress values at the channel corners using a linear elastic model and a non-elastic model. Their results showed that the stress values in channel corners are reduced using the non-elastic model compared to the values obtained by the linear elastic model. The stress values along the micro-channel periphery, excluding the channel corners, stayed unchanged for both linear elastic and the non-elastic models. Thus, in this study, the stress values at the channel corner were not considered in the optimization analysis due to the local plastic deformation at these locations.

5.3.2 Generalized Plane Strain

The diffusion bonded PCHEs are commonly assumed to be pressure-containing vessels and, generally, mechanical design of PCHEs with straight and zigzag channel is performed using the design-by-rule method under ASME BPVC criteria. It should be mentioned that the

design-by-rule methodology overestimates the stress values for PCHEs. The design-by-analysis is a suitable approach for the design and optimization of a PCHE geometry where stress values are not allowed to exceed the design maximum allowed stress values. A simplified stress analysis is generally considered for designing a PCHE, however, this analysis is not conservative. In the design-by-analysis approach, FE analysis is used to calculate stress integrity of the PCHE models. To design a PCHE core, 2D models are generally employed. The 2D plane strain model is commonly considered for stress assessment in the PCHE core. However, the 2D plane strain method overestimates stress values since axial dimension of the model is too short. The plane strain model assumes zero strain along the channel length, while in reality the strain value along the channels is not zero.

It was shown in this study that the 2D Generalized plane strain model is a suitable model for the 2D stress analysis when a small strain is assumed along the channel length. A finite deformation in the axial direction of the channel assumed in the generalized plane strain model provides realistic results when compared to the 2D plane strain model.

The kinematic equations of the generalized plane strain problem are identical to those of the 2D plane strain or plane stress problems, as follows [76]:

$$\begin{Bmatrix} \varepsilon_{xx} \\ \varepsilon_{yy} \\ \gamma_{xy} \end{Bmatrix} = \begin{Bmatrix} \frac{\partial u}{\partial x} \\ \frac{\partial v}{\partial y} \\ \frac{\partial v}{\partial x} + \frac{\partial u}{\partial y} \end{Bmatrix} \quad (5.8)$$

The displacements in the x and y directions are denoted as u and v .

The stress equilibrium equations for the 2D generalized plane strain in the x-y plane are the following [76]:

$$\begin{aligned}\frac{\partial \sigma_{xx}}{\partial x} + \frac{\partial \sigma_{xy}}{\partial y} + f_x &= 0 \\ \frac{\partial \sigma_{yy}}{\partial y} + \frac{\partial \sigma_{xy}}{\partial x} + f_y &= 0\end{aligned}\tag{5.9}$$

Where f is the body force.

The stress-strain relationship can be written as [76]:

$$\begin{Bmatrix} \sigma_{xx} \\ \sigma_{yy} \\ \sigma_{zz} \\ \tau_{xy} \end{Bmatrix} = C_{ij} \begin{Bmatrix} \varepsilon_{xx} \\ \varepsilon_{yy} \\ \varepsilon_{zz} \\ \gamma_{xy} \end{Bmatrix} - \begin{Bmatrix} \alpha_x \\ \alpha_y \\ \alpha_z \\ 0 \end{Bmatrix} \Delta T\tag{5.10}$$

Where the C_{ij} , $i, j=1, 2, 3$, α , and ΔT are the stiffness matrix, the coefficient of thermal expansion and temperature gradient in the solid.

For the generalized plane strain, a constant strain is assumed in the z direction:

$$\varepsilon_{zz} = \varepsilon_{zz}^0\tag{5.11}$$

Thus, the reduced 2D stress-strain relation including ε_{zz}^0 for the generalized plane strain can be rewritten as:

$$\begin{aligned}\begin{Bmatrix} \sigma_{xx} \\ \sigma_{yy} \\ \tau_{xy} \end{Bmatrix} &= C_{ij} \begin{Bmatrix} \varepsilon_{xx} \\ \varepsilon_{yy} \\ \gamma_{xy} \end{Bmatrix} - \begin{Bmatrix} \alpha_x \\ \alpha_y \\ 0 \end{Bmatrix} \Delta T + \begin{Bmatrix} C_{13} \\ C_{23} \\ 0 \end{Bmatrix} (\varepsilon_{zz}^0 - \alpha_z \Delta T) \\ \sigma_{zz} &= [C_{13} \ C_{23} \ 0] \begin{Bmatrix} \varepsilon_{xx} \\ \varepsilon_{yy} \\ \gamma_{xy} \end{Bmatrix} - \begin{Bmatrix} \alpha_x \\ \alpha_y \\ 0 \end{Bmatrix} \Delta T + C_{33} (\varepsilon_{zz}^0 - \alpha_z \Delta T)\end{aligned}\tag{5.12}$$

Where $i=1, 2$ and $j=1, 2$ [76].

5.3 Stress field for the generalized plane strain model

Figure 5. 6a shows a 3D thermal stress field related to the temperature field shown in Figure 5. 3a. In the stress calculation, the boundary conditions applied to the side walls in the

3D model are the same as those used in the 2D FE models. The 3D stress results show that the maximum stress values occur at the channel corners due to stress concentration at these locations. As discussed earlier, due to high stresses, it is expected that channel corners will experience plastic deformation. As shown in Figure 5. 6, the peak stresses occurring at sharp channel corners are significantly higher compared to the stresses along the channel periphery.

The 3D stress field was obtained by performing a 3D stress analysis. The von-Mises stress values, shown as constant stress contours, determined by the 3D stress model are compared to the stress values obtained from other stress models. The results presented in Figure 5. 6c show that the 2D generalized plane strain model provides comparable results when compared to the 3D mid-plane, while the 2D plane strain model overestimates stresses compared to the 3D mid-plane stress model, as presented in Figure 5. 6b. Since the stress contours presented in Figure 5. 6a-d were obtained by performing stress analyses using 2D and 3D models, a contour legend compatible to all contours is not available, instead stress values at specific locations are shown in the figure.

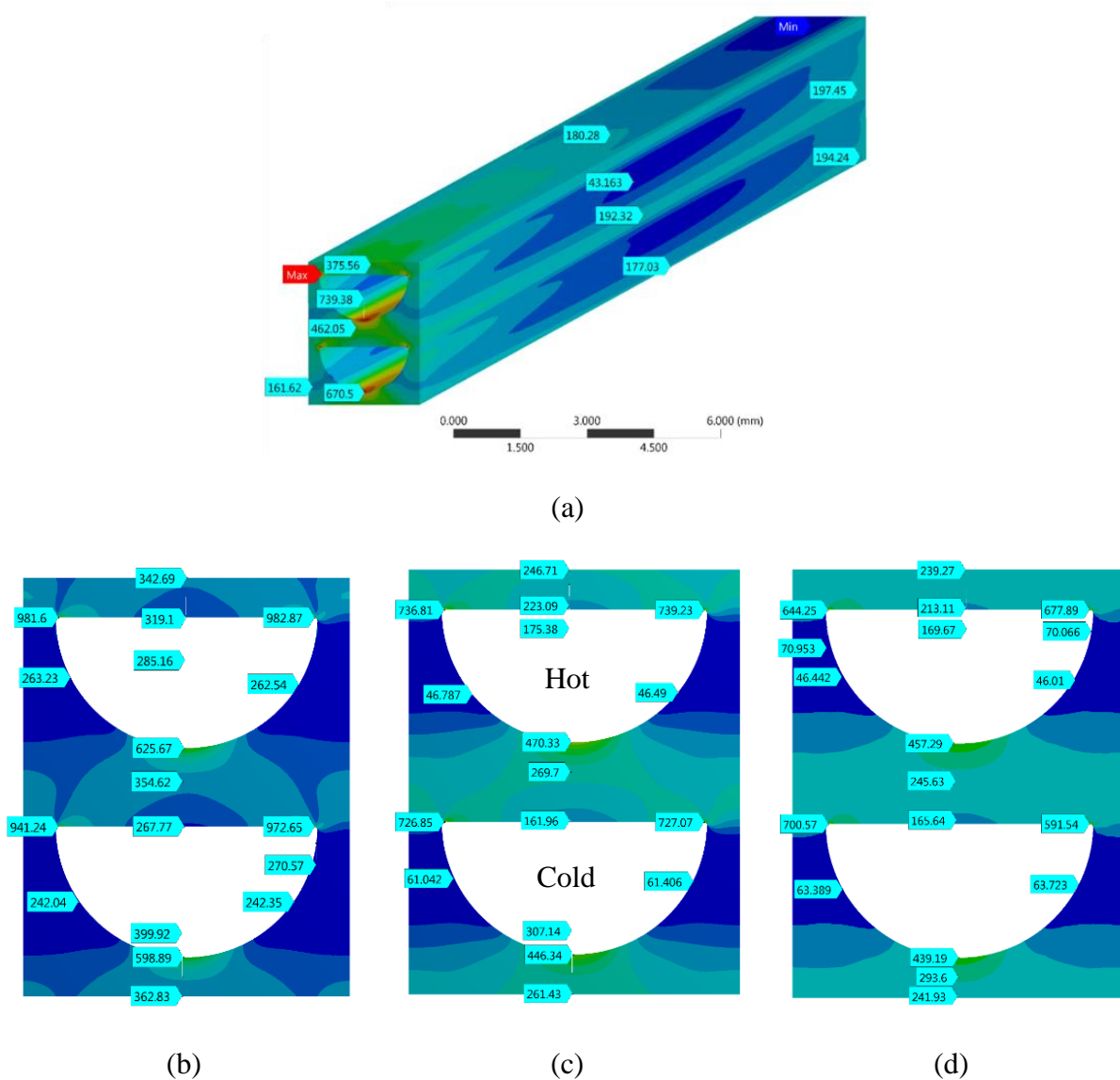


Figure 5. 6. Thermal stress field (a) 3D model, (b) 2D plane strain, (c) 2D generalized plane strain, (d) 3D mid-plane

The predicted values of total (thermal and mechanical) stress shown in Figure 5. 7 were compared to the mechanical stresses predicted using a 2D generalized plane strain. As the results show, the maximum value of the stress is in the corner of the hot channel and is mostly due to the thermal stress. Temperature distribution shown in Figure 5. 4a was used in the 2D plane strain and 2D generalized plane strain models to predict thermal stresses. It should be noted that the hot and cold channels are the top and bottom channels, respectively. The

maximum value of mechanical stress is in sharp corners of the cold channel due to the high fluid pressure (22.5 MPa) exerted along periphery of the cold channel. Thermal stress values are high between the hot and cold channels due to the high temperature gradient in that region. The maximum and minimum values of thermal stress predicted by the 2D generalized plane strain model are 470 MPa and 161 MPa along the hot and cold channels located in between the hot and cold channels, as presented in Figure 5. 6c. The calculated 3D thermal stress values at the same locations are 457 MPa and 165 MPa, respectively, see Figure 5. 6d. The results predicted by the 2D generalized plane strain model are comparable to the 3D mid-plane thermal stress values. Thermal stresses predicted by the 2D plane strain model at the same locations are 625 MPa and 267 MPa and indicate that the 2D plane strain model overestimates thermal stresses. Thus, the 2D generalized plane strain model was selected as a suitable model for predicting stress values for the high pressure PCHE core geometry.

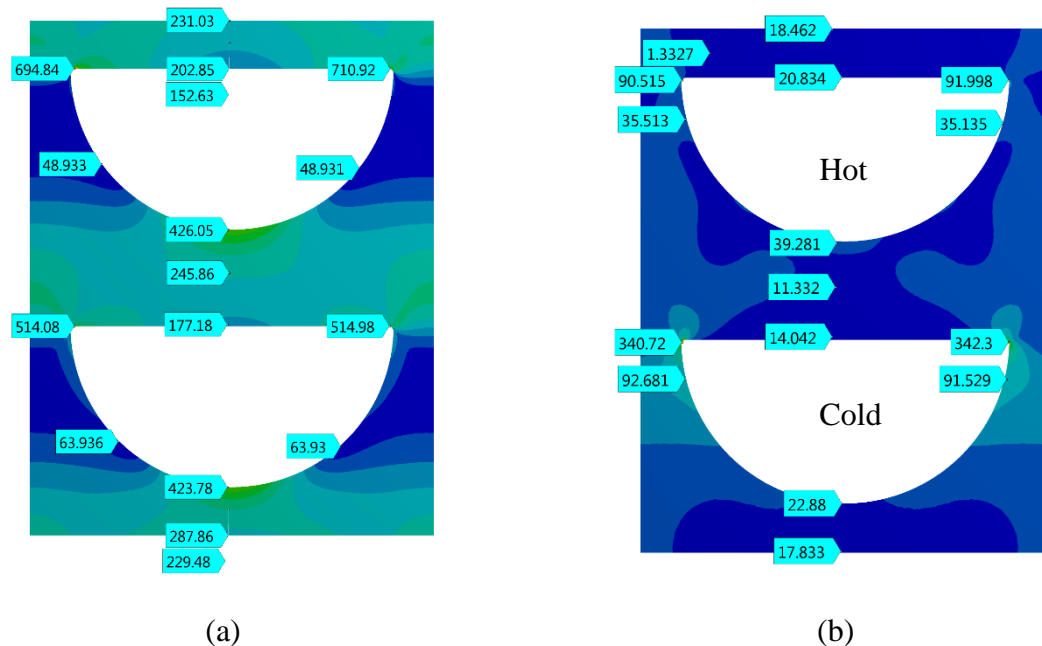


Figure 5. 7. 2D generalized plane strain (a) Total stress, (b) Mechanical stress only

The values of the normal stress component of thermal stress (z-component: along the channel length) obtained by the 2D generalized plane strain model were compared to the 2D plain strain and 3D model results at mid-plane. The comparison of results shows that the stress values predicted by the 2D generalized plane stress model are realistic. The axial direction component (z-component: along the channel length) of thermal stress obtained by the 2D generalized plane strain model is shown in Figure 5. 8, where the results obtained by the 2D plane strain model and 3D model at the mid plane for the same boundary conditions are compared. As expected, the values of the normal stress component (in the axial direction) obtained by the 2D plane strain model are higher compared to those obtained by the 2D generalized plane strain model and the 3-D model at the mid plane. The values of normal stress component obtained by the 2D generalized plane strain model are comparable to those obtained by the 3D analysis at the mid plane.

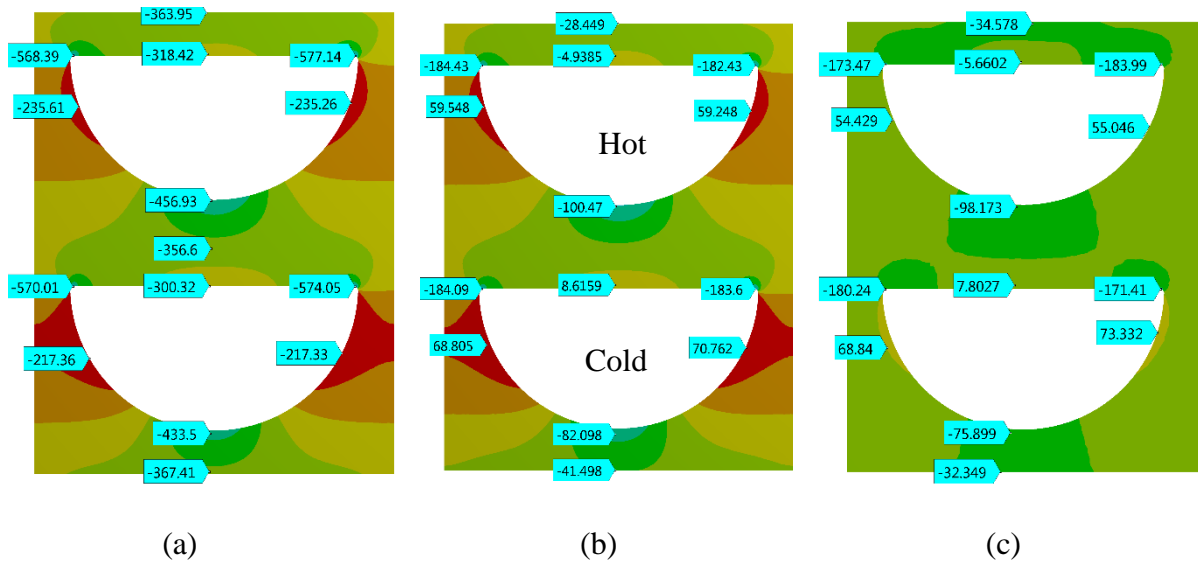


Figure 5. 8. Axial direction thermal stress component contour, periodic BC (a) Plane strain, (b) 2D generalized plane strain, (c) 3-D mid plane

5.3.1 Thermal stress: 2D generalized plane strain versus 3D stress at different locations

The thermal stress fields corresponding to the temperature distributions presented in Figure 5. 4 b and Figure 5. 4c are shown in Figure 5. 9a and Figure 5. 9b. The values of thermal stresses are changing in the axial direction since the temperature is changing linearly from the cold inlet to the hot inlet (except in the entrance regions), as presented in Figure 5. 3a and Figure 5. 3b. The 2D generalized plane strain model was used to calculate the thermal stress values at locations close to the cold ($z=0.025$ m) and hot inlets ($z=0.175$ m) and the results were compared to the values of thermal stresses predicted by the 3D model at the same locations. Figure 5. 9a shows the values of thermal stress at $z=0.025$ m obtained by the 2D generalized plane stress and 3D stress models, while the results obtained for the hot inlet ($z=0.175$ m) are presented in Figure 5. 10.

At $z=0.025$ m the values of thermal stresses obtained by the generalized plane strain are comparable to the 3D stress. The maximum stress values occur at the corners and are comparable to the 3D results. The difference in thermal stress distribution at some locations along the wall periphery can be explained by the effect of thermal expansion in the axial direction, see Figure 5. 6a. The thermal stress values between the hot and cold micro-channels predicted by the generalized plane strain model are higher compared to the 3D model. Thermal expansion at the hot inlet is higher compared to the cold inlet and the axial expansion direction is in the negative z direction, see Figure 5. 8b. This can explain the non-uniform thermal stress distribution at $z=0.025$ m and $z=0.175$ m locations. Due to entrance region effects, as mentioned earlier, temperature distribution is non-linear at the hot and cold inlets as presented in Figure 5. 3b.

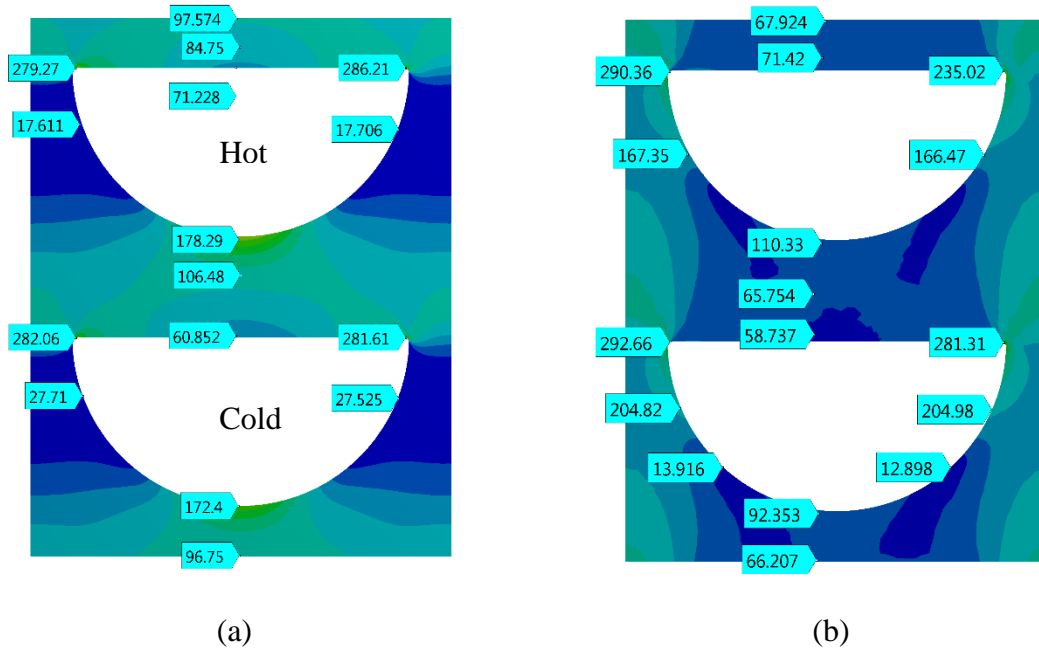


Figure 5. 9. Thermal stress contour at cold inlet ($z=0.025$ m) (a) 2D Generalized plane strain, (b) 3D models

The thermal stress values predicted at a location close to the hot inlet for the 2D generalized plane strain and 3D models are shown in Figure 5. 10. The thermal stress values for both models are comparable. The thermal stress values between the hot and cold channels obtained by the 2D generalized plane strain are almost identical to the 3D model; however, at some locations along the semi-circular wall periphery the values of thermal stress differ from the 3D model results. This difference is caused by thermal strain in the z direction where temperature variation is non-linear. The values of thermal stresses for the generalized plane strain and 3D models are identical at the locations away from the channel inlets and exit as presented in Figure 5. 6. The colors of stress contours presented in Figure 5. 10b are different compared to Figure 5. 10a because presented contours were obtained by using different stress models and a compatible color legend is not available. The scale used for Figure 5. 10b is the same scale used for the 3D stress model for total stress, while the color legend for Figure 5. 10a corresponds to the scale used in the 2D generalized plain strain for total stress.

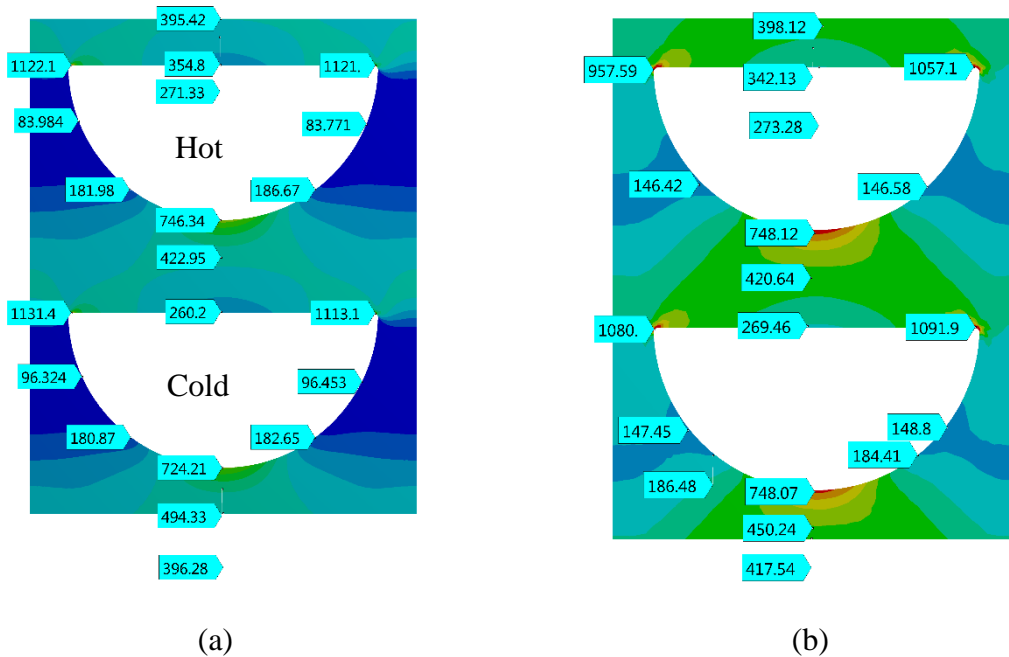


Figure 5. 10. Thermal stress contours (a) 2D Generalized plane strain, (b) at hot inlet ($z=0.175$ m) in 3D models

The maximum and minimum values of thermal stress predicted in the walls of hot and cold micro-channels at $z=0.175$ m using the 2D generalized plane strain are 746 MPa and 260 MPa and are virtually identical to the values of 748 MPa and 269 MPa, respectively obtained at the same locations by the 3D stress model, as presented in Figure 5. 10.

5.4 The effect of mechanical boundary conditions on thermal and mechanical stresses

5.4.1 Physical model

Since there are no experimental data available for stress intensity in an individual PCHE channel, the Finite Element Method (FEM) was used in this work to numerically determine stress distribution in the models of PCHE core. The results of the FEM analysis performed by Lee and Lee [18] were used as a benchmark for comparison with the results obtained in this work.

Lee and Lee [18] performed a FEM analysis to investigate structural integrity of an intermediate PCHE with semi-circular channel geometry used for a Sodium-Cooled Fast

Reactor (SFR) coupled to a sCO₂ Brayton cycle. Ansys-Mechanical was utilized to perform FEM simulations and calculate stress field in a PCHE core. Both thermal and mechanical stresses were calculated for a different number of channel rows and columns in the PCHE core. The Na-CO₂ cycle in SFR operates with very high pressure difference between the cold and hot side (0.1 vs 20 MPa) and at high temperature. To calculate the thermal stress field within the PCHE model, wall temperatures, determined by the CFD analysis, were specified along the periphery of channel walls and a steady-state heat conduction equation subject to the boundary conditions of the first kind (known temperature) was solved for temperature distribution between the hot and cold micro-channels.

Studied geometries and boundary conditions used in calculation of the mechanical and thermal stresses are shown in Figure 5. 11. A weak spring boundary condition was applied to the model to prevent the rigid body motion. Table 5. 6 lists geometry specifications and the solid material used for the stress integrity assessment.

Table 5. 6. The domain parameters

Parameters	Values (mm)
Channel diameter	2
Plate thickness	2
Pitch	3
Solid material	Stainless-Steel 316

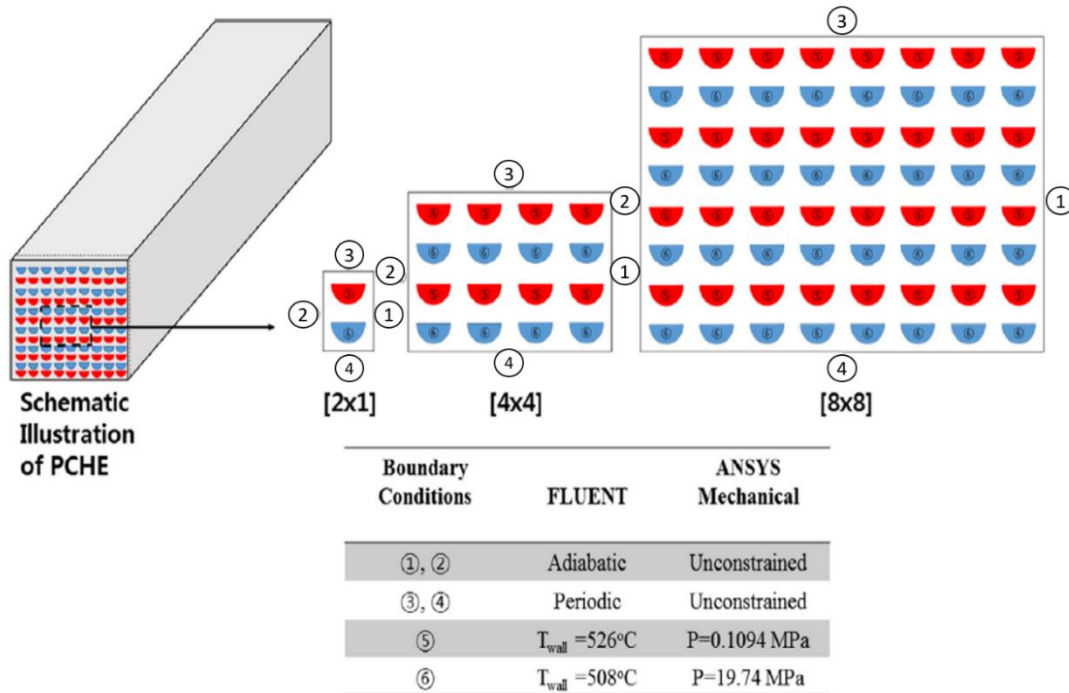


Figure 5. 11. Schematic of studied geometries by Lee and Lee [18] and boundary conditions

Material properties of stainless steel 316 as reported in Lee and Lee [18] are listed in Table 5. 7. The values of thermal conductivity and density of stainless steel of 17.25 W/m.K and 7850 kg/m³, respectively were used in the analysis.

Table 5. 7. Material properties of stainless steel 316 [18]

Temperature (C)	Modulus of elasticity (GPa)	Thermal expansion coefficient (1/K)
482.2	162.0	20.2×10^{-6}
510.0	160.0	20.4×10^{-6}
537.8	157.2	20.5×10^{-6}
565.6	155.1	20.7×10^{-6}

Since the channel corners are assumed to be rounded as the result of the diffusion bonding process, a fillet of 0.01 mm in the channel corners was used in the simulations [18].

5.4.2 Grid independence study

A 4×4 PCHE model, shown in Figure 5. 11, used in the Lee and Lee [18] work was selected for mesh independence study and the model validation. A 100,000 triangular elements with the element size of 0.2 mm were used for the structural analysis of the selected 4×4 PCHE model. The results of the grid independence study show that the total stress values along the channel periphery do not change with the number of grid elements, however the values of stresses predicted at the channel corners are sensitive to the grid fineness. In a similar study performed for the same PCHE geometry, Bennet [77] showed that the stress intensity along the channel periphery is insensitive to the grid size and the number of nodes but the stress in the channel corner is extremely sensitive to these parameters. Therefore, the effect of number of grid elements on total stress intensity for different fillet radii was studied. Figure 5. 12 shows the variation of maximum stress intensity at the channel corner obtained for different number of grid elements and fillet size. The results show ten triangular grid elements in the channel corner are sufficient to ensure the predicted stress values are independent of the grid size.

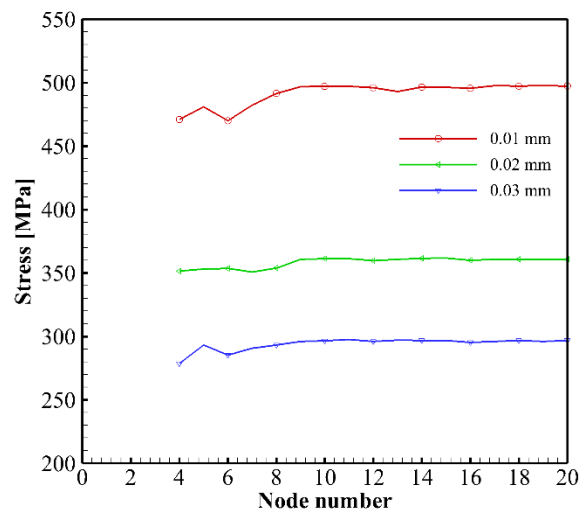


Figure 5. 12. Maximum stress intensity value at the channel corner for different number of grid elements and fillet size

Figure 5. 13 shows the triangular grid elements used in validation of the numerical model in FEM simulation for the 4×4 PCHE core. A grid refinement was carried out along the channel periphery to increase the grid resolution.

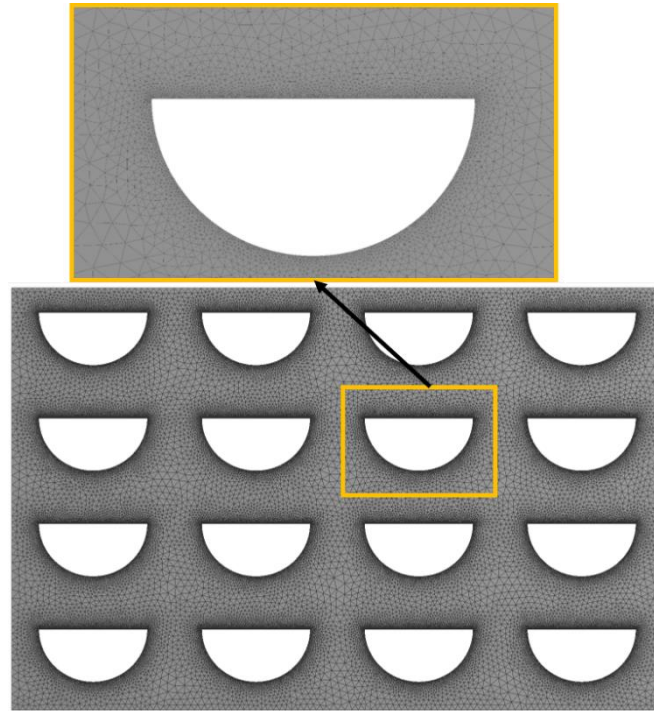


Figure 5. 13. Numerical grid used for the 4×4 PCHE core simulation

5.4.3 Validation of the numerical model

Temperature distribution in a solid domain of the 4x4 PCHE model was determined using the steady-state thermal analysis performed by the Ansys-steady-state thermal module. The temperature contours in the 4×4 PCHE model corresponding to the boundary conditions presented in Figure 5. 11 is shown in Figure 5. 14. For the results presented in the figure, the maximum hot micro-channel temperature is 526 °C, while the minimum cold micro-channel temperature is 508 °C. The maximum temperature difference of 9 °C occurs between the hot and cold micro-channels.

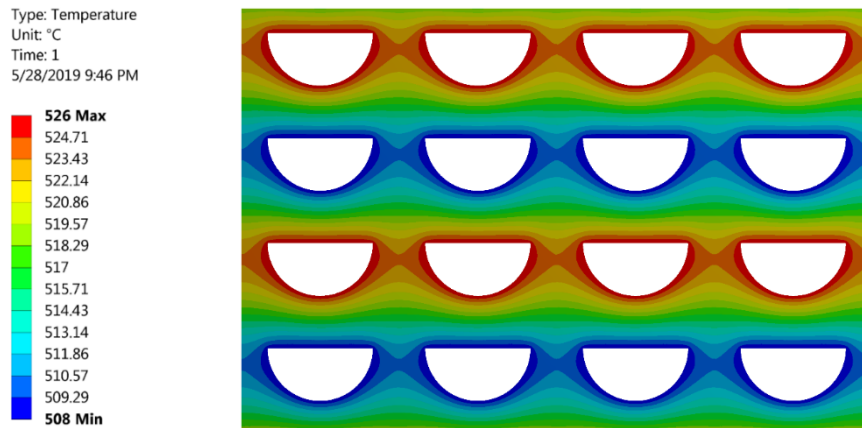


Figure 5. 14. The temperature contours in 4×4 PCHE model

The temperature distribution shown in Figure 5. 14 was used to obtain thermal stresses in channel walls. Since the top and bottom wall boundaries are considered linear periodic, the number of hot and cold channel rows does not play a role in temperature distribution within the PCHE core.

A linear isotropic elasticity model was used in the calculation of thermal and mechanical stresses and the obtained results were compared to those reported in Lee and Lee [18]. Figure 5. 15 show the stress intensity distribution along the periphery of the hot and cold micro-channels for the 4×4 PCHE model. The results show that due to stress concentration, stress intensity is significantly higher at the channel corners (locations B and D) compared to the periphery of the micro-channel wall. The maximum stress intensity value of 520 MPa predicted in the current study at Point B is higher compared to the maximum values of stress intensity of 450 MPa reported by Lee and Lee [18]. For the rest of the wall channel periphery the agreement is excellent. This discrepancy in stress intensity at the channel corners was noted in the study performed by Bennet [77] and may be attributed to the different number of grid elements used in the analysis by Lee and Lee [18]. The number of grid elements at the channel corner used by Lee and Lee was, however, not mentioned in their report. The results presented

in Section 5.3 and Figure 5. 7 showed that the reference temperature is a likely reason this difference.

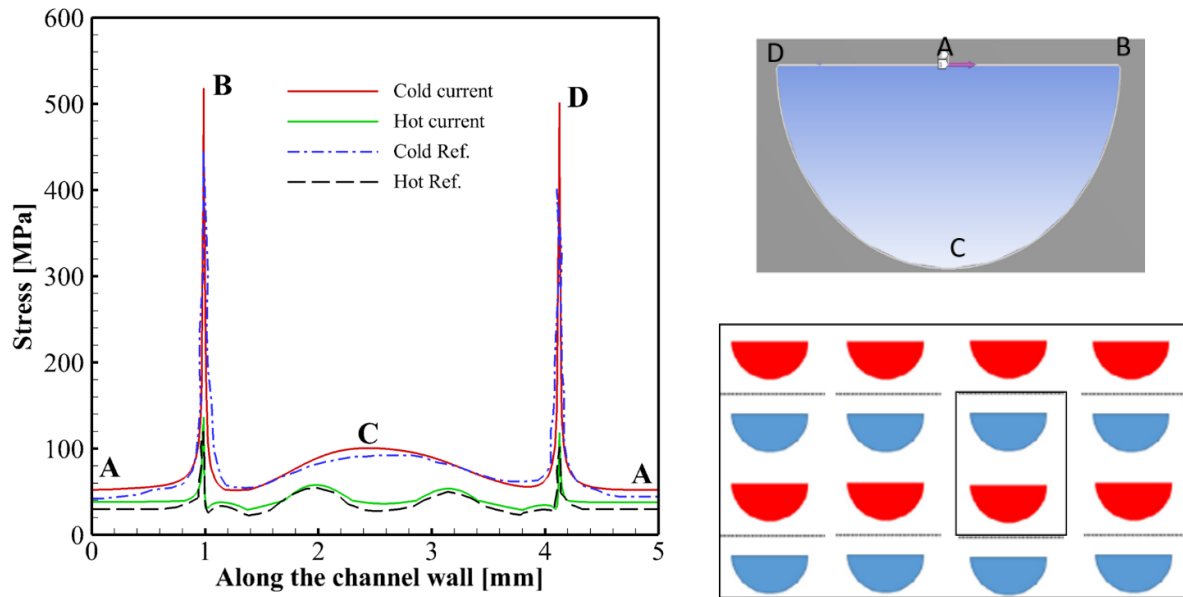
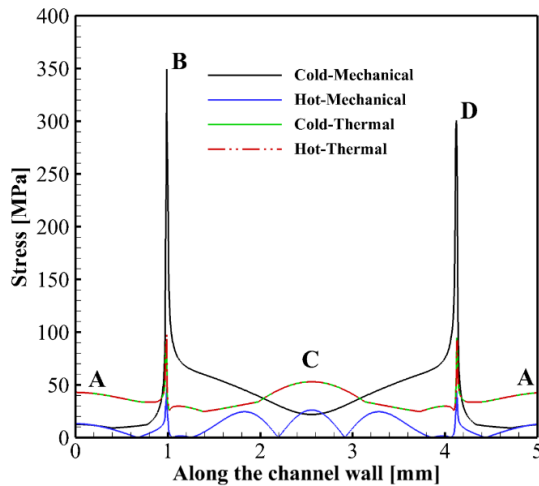


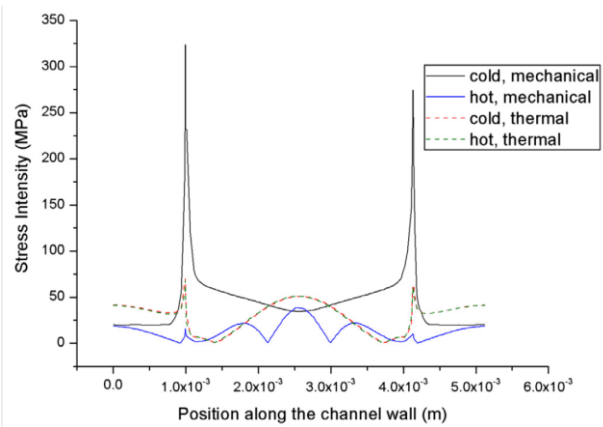
Figure 5. 15. The stress intensity along the hot and cold wall periphery compared to values reported in Lee and Lee [18]

The mechanical and thermal stresses obtained in the current study shown in Figure 5. 16a are compared to those reported in Lee and Lee. Figure 5. 16b shows the variation of mechanical and thermal stresses for the hot and cold channels obtained by Lee and Lee [18]. The mechanical and thermal stress intensity values reported by Lee and Lee [18] were digitized from Figure 5. 16b and compared to the values obtained in the current study, presented in Figure 5. 16c-e. the results presented in Figure 5. 16b by Lee and Lee [18] show the thermal stress in the hot and cold channels walls are identical. Also, the mechanical stress intensity in the hot channel walls is lower compared to the cold channel walls due to low pressure of working fluid in this channel. Using this figure, Lee and Lee showed that the total stress intensity is mostly contributed by the mechanical loads than the thermal loads. The results presented in Figure 5. 16b-c show that the mechanical stress intensity obtained in the current

study is in excellent agreement with the results reported by Lee and Lee [18]. The maximum stress intensity at Point B of 350 MPa was obtained in this study, while Lee and Lee [18] reported the maximum mechanical stress intensity of 330 MPa at the same location. The results presented in Figure 5. 16e show that the thermal stress intensity value of 98 MPa predicted at point B in this study is higher compared to that of 70 MPa reported by Lee and Lee [18] at the same location. This difference may be attributed to the reference temperature value (average temperature between the hot and cold channel) used by Lee and Lee to calculate thermal stresses [18], while the minimum temperature at the cold inlet was used as a reference temperature in this study. As discussed earlier in Section 5.3, using the minimum temperature in the 3D geometry of PCHE core gives realistic predictions of thermal stresses.

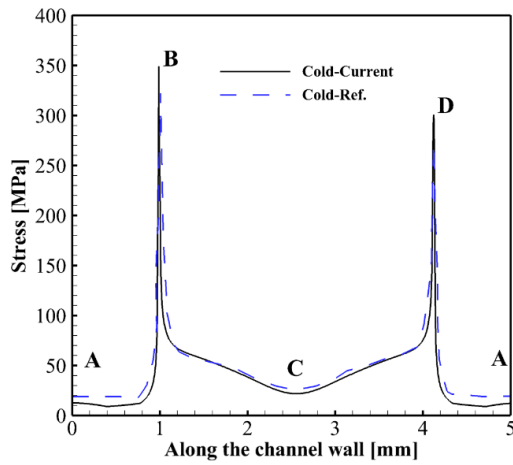


(a) Current study

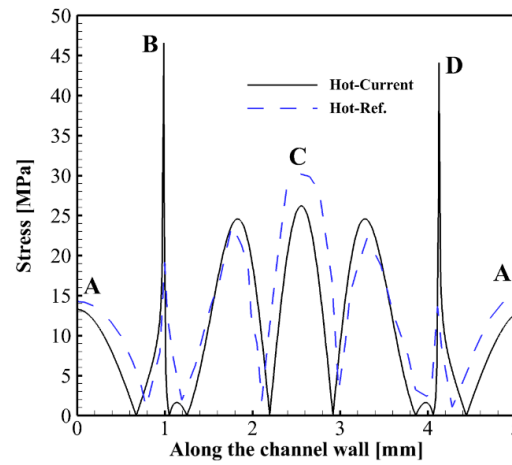


(b) Literature [18]

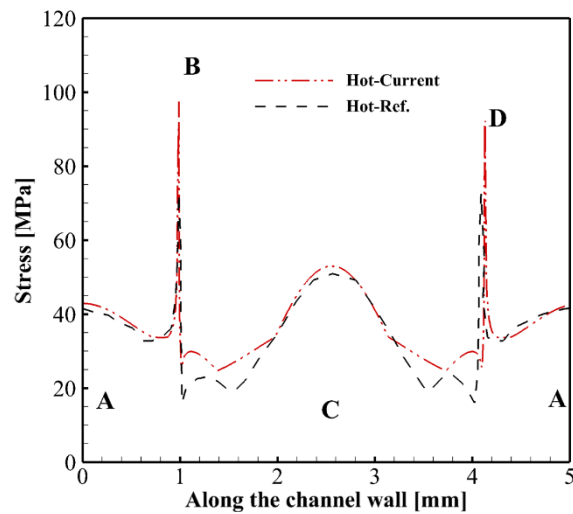
Figure 5. 16. (a) mechanical stresses (b) mechanical stress



(c) Mechanical stress, cold channel



(d) Mechanical stress, hot channel



(e) Thermal stress

Figure 5.16. Continued, (c) mechanical stress cold channel (d) mechanical stress hot channel, (e) thermal stress for hot and cold channel compared to values reported in Lee and Lee [18]

5.4.4 Stress field for different models with different boundary conditions

This section describes the analysis and the results obtained by using the 2D plane strain model combined with a linear isotropic elasticity model to investigate the effect of boundary

conditions on the predicted values of stress intensity and equivalent stress (von-Mises stress) in PCHE models presented in Figure 5. 11.

The 2×1 PCHE, 8×1 PCHE, and 4×4 PCHE models were analyzed by applying periodic, zero y-displacement, and zero x and y- displacement boundary conditions imposed to the top and bottom of the PCHE model (boundaries of computational domain). The x-symmetry boundary conditions were used for the 2×1 PCHE and 8×1 PCHE models while the zero x-displacement and unconstrained boundary conditions were applied to the 4×4 PCHE model. The obtained results concerning stress intensity and equivalent stress are presented and are compared at different micro-channel wall locations for both the hot and cold channels. Figure 5. 17 shows the physical models and B.C.s used in the boundary conditions sensitivity study.

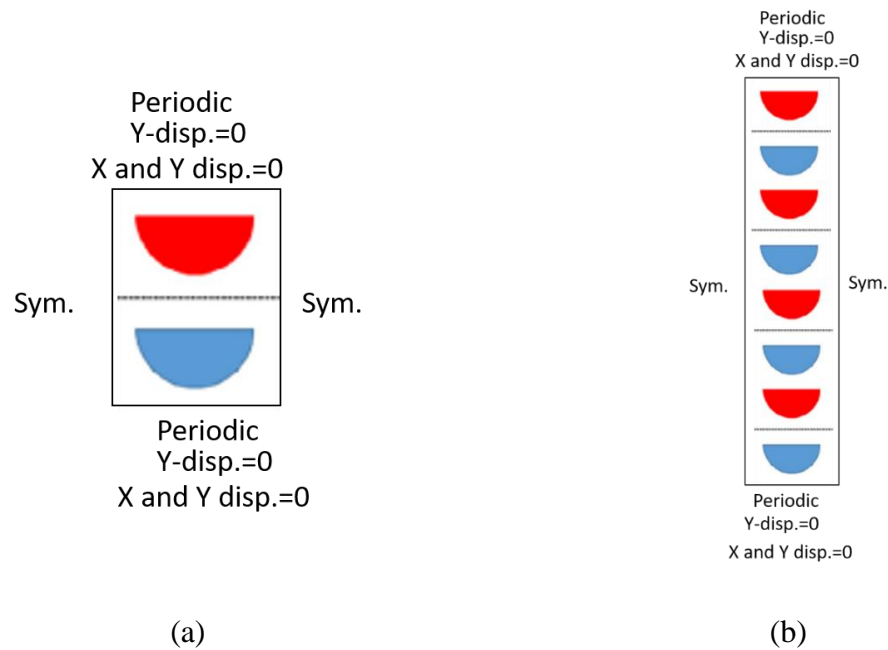


Figure 5. 17. Schematics of the PCHE models used in the boundary conditions sensitivity analysis (a) 2×1 , (b) 8×1 PCHEs

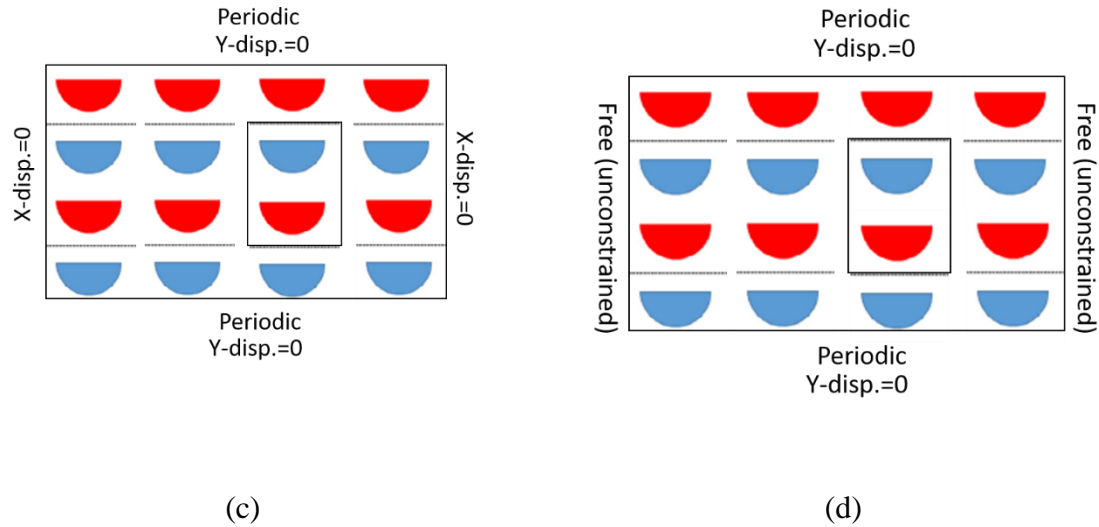


Figure 5.17. Continued, Schematics of the PCHE models used in the boundary conditions sensitivity analysis (c-d) 4x4 PCHE

Figure 5. 18 shows locations of points A, B, C and D located along the hot/cold channel periphery used for the stress analysis. As the figure shows, points B and D are located at the channel corners. The predicted stress values are plotted from point A to D and back to A location in the clockwise direction.

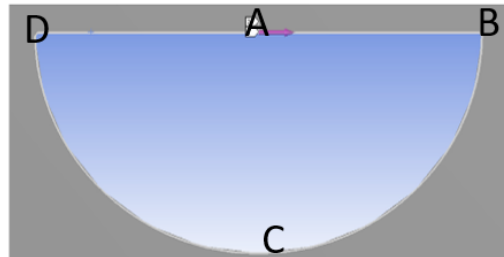


Figure 5. 18. The location where stress is reported

Figure 5. 19 shows the stress intensity distribution along the hot and cold micro-channel walls from point A to D and back to A. The results show that the stress intensity values in the cold channel wall for the periodic B.C. are higher compared to the y-displacement=zero and x and y-displacement=zero. The periodic boundary condition imposes a constraint which results in reaction forces acting on the top and bottom boundaries and creating periodic stress field

within the PCHE model. Thus, the periodic boundary condition may not be a suitable boundary condition for the PCHE core, and the analysis of boundary conditions was expanded to include other options.

The results concerning the predicted stress intensity and equivalent stress values associated with a range of boundary conditions imposed on the top, bottom, and side walls of the investigated PCHE model are summarized in Table 5. 8 and Table 5. 9. The results show that for the periodic boundary conditions the stress intensity and von-Mises stress values predicted at Points A-D and shown in Figure 5. 19 are identical for the 2x1 and 8x1 PCHE geometries except at the channel corner (Points B and D). Also, for the periodic B.C.s, the mechanical stress intensity is higher compared to the B.C.s of zero y-displacement and zero x-and-y-displacement.

The results presented in Figure 5. 19 also show that the values of stress and their variation along the micro-channel periphery for both the zero y-displacement and zero x-and-y-displacement are virtually identical for the studied PCHE geometries, with maximum values occurring at the channel corners.

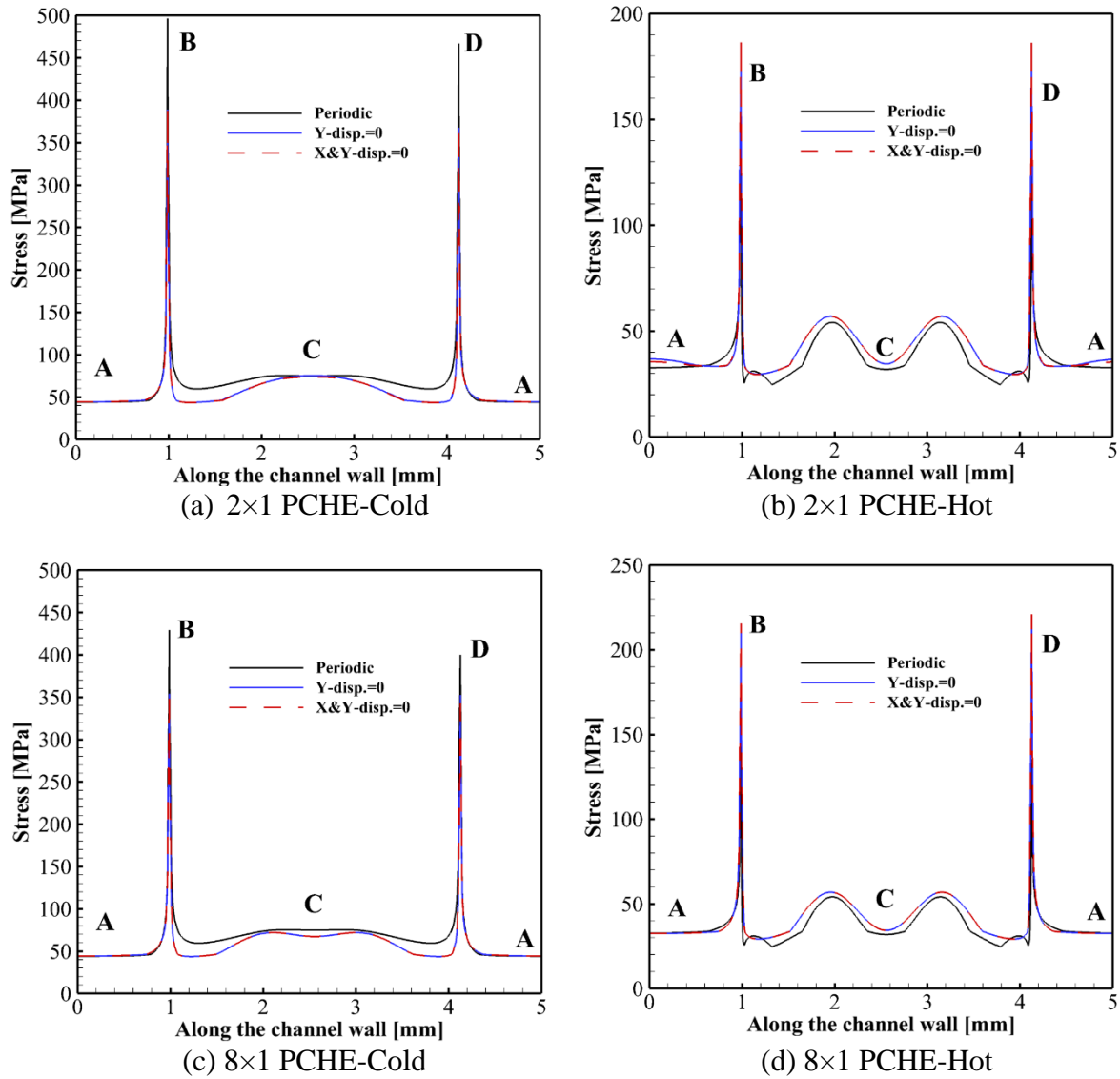


Figure 5. 19. Stress intensity distribution along the channel hot/cold wall for 2×1 PCHE and 8×1 PCHE

Table 5. 8. Stress intensity for studied locations A to D

2x1	Periodic		Y displacement=0		X and Y displacement=0	
Point	Cold	Hot	Cold	Hot	Cold	Hot
A	44.077	32.724	44.254	36.915	44.256	35.558
B	496.36	134.82	388.95	185.82	389.06	187.59
C	74.998	31.95	75.58	34.523	73.849	34.528
D	466.81	125.9	367.37	185.91	367.48	187.67
8x1	Periodic		Y displacement=0		X and Y displacement=0	
Point	Cold	Hot	Cold	Hot	Cold	Hot
A	44.078	32.724	44.241	32.561	44.241	32.561
B	429.35	144.04	353.8	215.58	353.82	215.57
C	75.005	31.95	67.475	34.354	67.476	34.353
D	400.15	135.49	352.37	220.92	352.38	220.91

Table 5. 9. The equivalent stress for studied locations A to D

2x1	Periodic		Y displacement=0		X and Y displacement=0	
Point	Cold	Hot	Cold	Hot	Cold	Hot
A	41.347	31.319	41.709	35.847	41.712	34.949
B	441.5	117.42	344.63	163.73	344.73	165.32
C	67.034	29.719	67.49	34.279	66.137	34.281
D	416.37	109.65	325.87	163.8	325.97	165.39
8x1	Periodic		Y displacement=0		X and Y displacement=0	
Point	Cold	Hot	Cold	Hot	Cold	Hot
A	41.348	31.319	41.682	30.972	41.682	30.972
B	384.28	125.47	314.65	190.94	314.66	190.92
C	67.04	29.72	61.239	34.17	61.24	34.169
D	438.4	118.03	313.77	195.45	313.78	195.44

Figure 5. 20 compares the total stress intensity along the channel wall from Point A to D and back to A for the 8x1 PCHE model (geometry) predicted in the current study to the results of total stress intensity for the 8x8 PCHE geometry reported by Lee and Lee [18]. The results of this study show that the values of total stress intensity are different for the 8x1 PCHE

and 8x8 PCHE geometries. The total stress intensity for the 8x8 PCHE geometry at Point C reported by Lee and Lee is higher compared to the results obtained in this study because boundary conditions at the top/bottom wall were assumed unconstrained. So, 8x1 PCHE gives unrealistic stress results.

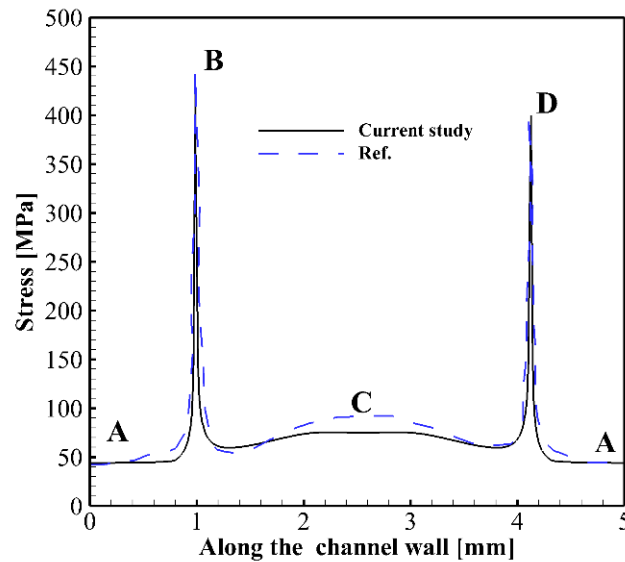


Figure 5. 20. Total stress intensity along the channel wall for 8x1 PCHE in current study and 8x8 PCHE from Lee and Lee

Lee and Lee [18] showed that the 4x4 PCHE and 8x8 PCHE models provide more realistic stress results compared to the 2x1 PCHE geometry and stated that total stress intensity results for both the 4x4 PCHE and the 8x8 PCHE geometries are identical [18].

The analysis of stress results reported by Lee and Lee [18] shows that the 4x4 PCHE model provides realistic stress results and can be considered as a suitable geometry for the PCHE core. Thus, the 4x4 PCHE geometry was selected to study the effect of boundary conditions on stress intensity.

As shown in Figure 5. 17 (c and d), zero x-displacement and unconstrained side walls were selected to investigate the effect of side wall boundary conditions on the stress intensity values in the 4x4 PCHE model (geometry). The mechanical boundary conditions imposed on

the top and bottom walls were changed from periodic to zero y-displacement. The zero x and y-displacement boundary conditions were not studied for the 4×4 PCHE model since stress values for both zero x and zero y-displacement are identical.

Figure 5. 21 shows the predicted stress intensity distribution along periphery of the hot and cold channel walls from point A to D and back to A for different applied B.C.s. In the zero x-displacement case, the results show that the predicted stress intensity values in the cold channel wall for periodic B.C.s applied on the top/bottom walls are higher compared to the zero y-displacement due to constraint imposed by periodic B.C. to create periodic stress field within the geometry. The stress intensity values at the corners using periodic B.C.s are significantly higher compared to the stress values for B.C. of zero y-displacement. The stress intensity values on the hot wall for both periodic and zero y-displacement B.C.s are identical. For the x-unconstrained B.C. case, both the periodic and zero y-displacement=zero B.C.s provide similar stress intensity values and distribution along the micro-channel walls. However, the stress intensity values in both the hot and cold channels are higher compared to those in the zero x-displacement case. The stress intensity and equivalent stress values for the studied locations along the channel walls for the 4x4 PCHE model are listed in Table 5. 10.

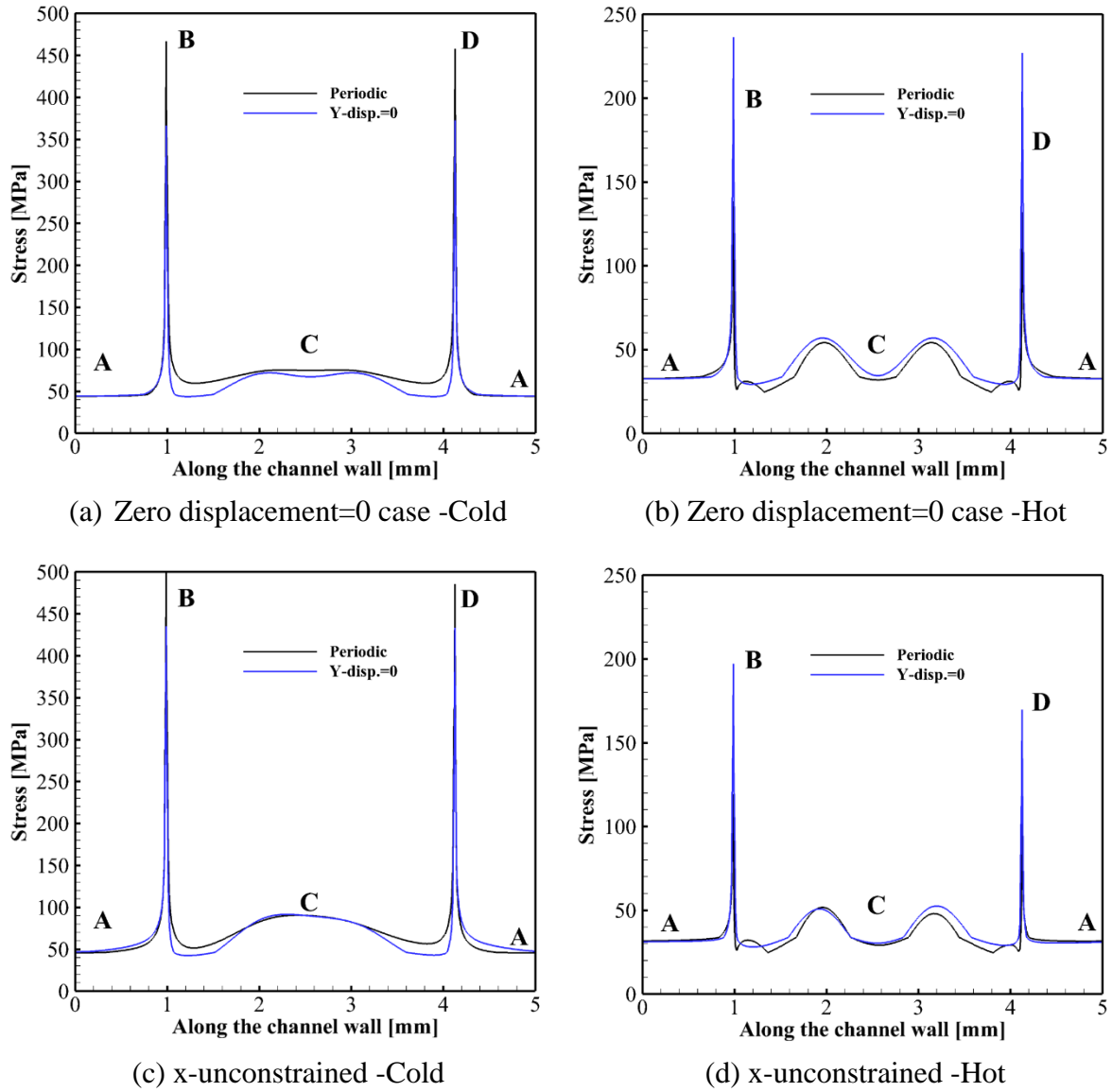


Figure 5. 21. Stress intensity distribution along the channel hot/cold wall in 4x4 PCHE model

Table 5. 10. Stress intensity and equivalent stress for locations A to D for the 4×4 PCHE model

Zero x-displacement	Periodic				Zero y displacement			
Point	Stress intensity		von Mises		Stress intensity		von Mises	
	Cold	Hot	Cold	Hot	Cold	Hot	Cold	Hot
A	44.078	32.724	41.348	31.319	44.248	32.559	41.695	30.969
B	466.54	138.41	408.07	114.56	372.49	236.33	325.3	200.2
C	75.007	31.954	67.041	29.727	67.421	34.42	61.198	34.212
D	457.45	131.83	415.86	120.83	366.73	226.76	330.84	208.58
x-unconstrained	Periodic				Zero y-displacement			
Point	Stress intensity		von Mises		Stress intensity		von Mises	
A	45.757	31.718	44.974	29.271	47.118	31.187	28.288	46.841
B	499.41	119.14	446.15	103.62	434.91	197.02	173.66	387.44
C	90.112	29.26	79.133	25.437	89.748	30.396	26.97	78.836
D	485.37	102.52	433.11	88.819	433.21	169.65	148.33	385.8

Based on the studied boundary conditions applied to the 4x4 PCHE geometry, the 4×4 PCHE geometry was selected as a suitable geometry for the PCHE core. However, the boundary conditions for the top/bottom and right/left walls need to be investigated for the specific PCHE model.

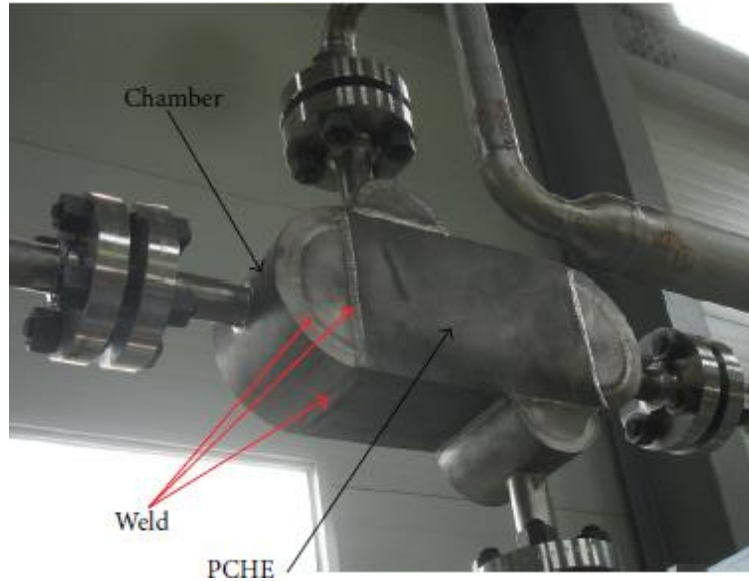
5.5 Effective and realistic boundary conditions for the PCHE core

Lee and Lee [18] performed FE analyses to investigate the effect of the number of hot/cold micro-channels on the stress intensity within a PCHE core. They assumed there are no mechanical boundary conditions applied to the sides of the PCHE model and allowed the

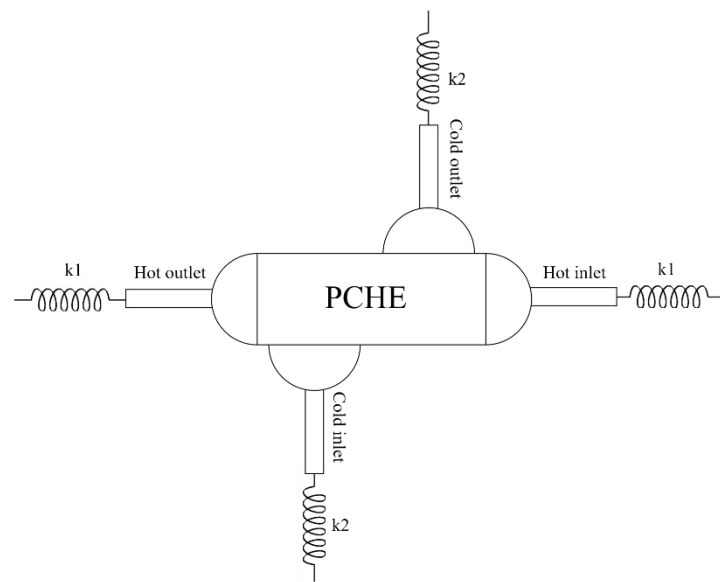
PCHE geometry to expand in all directions. They assumed the internal mechanical constraints account for the stress field inside the PCHE core.

Although it is true that in real situation a PCHE is not constrained, reaction forces are created at the pipe joints/headers that intensify the internal mechanical constraints. Thus, assuming no mechanical boundary conditions on the PCHE sides is not realistic. Also, with no mechanical boundary conditions applied on the PCHE sides, thermal expansion of the PCHE model will be underestimated because in operation a PCHE is subject to the reaction forces from the connecting pipes due to thermal expansion. Thus, a combination of the boundary conditions for a 2D PCHE core model which would realistically represent a PCHE core attached to headers needs to be devised.

A semi-constrained boundary condition using spring element is presented in this section. The reaction forces exerted on the PCHE model due to thermal expansion of the model from the pipes/headers attached to the PCHE were simulated by the spring elements having specific stiffness. Figure 5. 22a shows a typical 3D PCHE lab-scale prototype [78]. The PCHE prototype is attached to the pipes, carrying the hot and cold fluids, via headers. The pipe size, thickness, and stiffness are dependent upon the working fluid pressures. Since no pipes are attached to the PCHE sides, it can be assumed that the PCHE core can expand in these directions without constraints. However, pipes and headers limit PCHE expansion in other directions. Figure 5. 22b illustrates the spring elements attached to the PCHE model to constrain its expansion at locations where PCHE is connected to the outside pipes and headers.



(a)



(b)

Figure 5. 22. (a) 3D PCHE lab-scale prototype [78], (b) schematic of PCHE and spring elements

Since the PCHE core was modeled as 2D, thermal expansion in the flow direction (axial direction in the hot flow) is assumed to be limited. The 2D generalized plane strain model was

used to simulate the stress field assuming a limited expansion occurs in the axial direction (see Section 5.2 for details concerning a 2D generalized plane strain model).

The objective of this study is to determine stress field including thermal stresses within the PCHE core. Thus, the stress field in the proximity of the spring elements was not considered in the design of the PCHE core.

5.5.1 Mechanical boundary conditions on top/bottom walls

As shown above, periodic B.C.s applied to a PCHE result in higher stress values in the core compared to the B.C. of zero y-displacement applied to the top/bottom. Therefore, the effect of different boundary conditions on the stress field using a spring element was investigated. The results of 3 cases including different boundary conditions applied to the top/bottom walls of the PCHE model studied in this work are described in this section.

Figure 5. 23 shows a schematic of the staggered double-etched pattern for a semi-circular channel topology model which includes spring elements applied at the top/bottom walls. Springs are attached to the PCHE walls on one side and are fixed on the other side. It should be mentioned that the boundary conditions on the right/left walls should be separately studied, as discussed in Section 5.5.4. Based on the results of Lee and Lee [18] and Song et. al. [78] investigation of the spring elements as boundary conditions for a PCHE core performed in this study for Cases 1, 2, and 3, was conducted in combination with unconstrained boundary conditions on the left/right walls. The paths in the channel fins and shim plate used to show stress distribution within the walls of PCHE core are presented in Figure 5. 23d. The stress values in the middle of PCHE model away from the boundaries are used in this study as representative of the PCHE core. The stresses in the PCHE core close to the boundaries are

considered not representative of the PCHE core since they are affected by the boundary conditions.

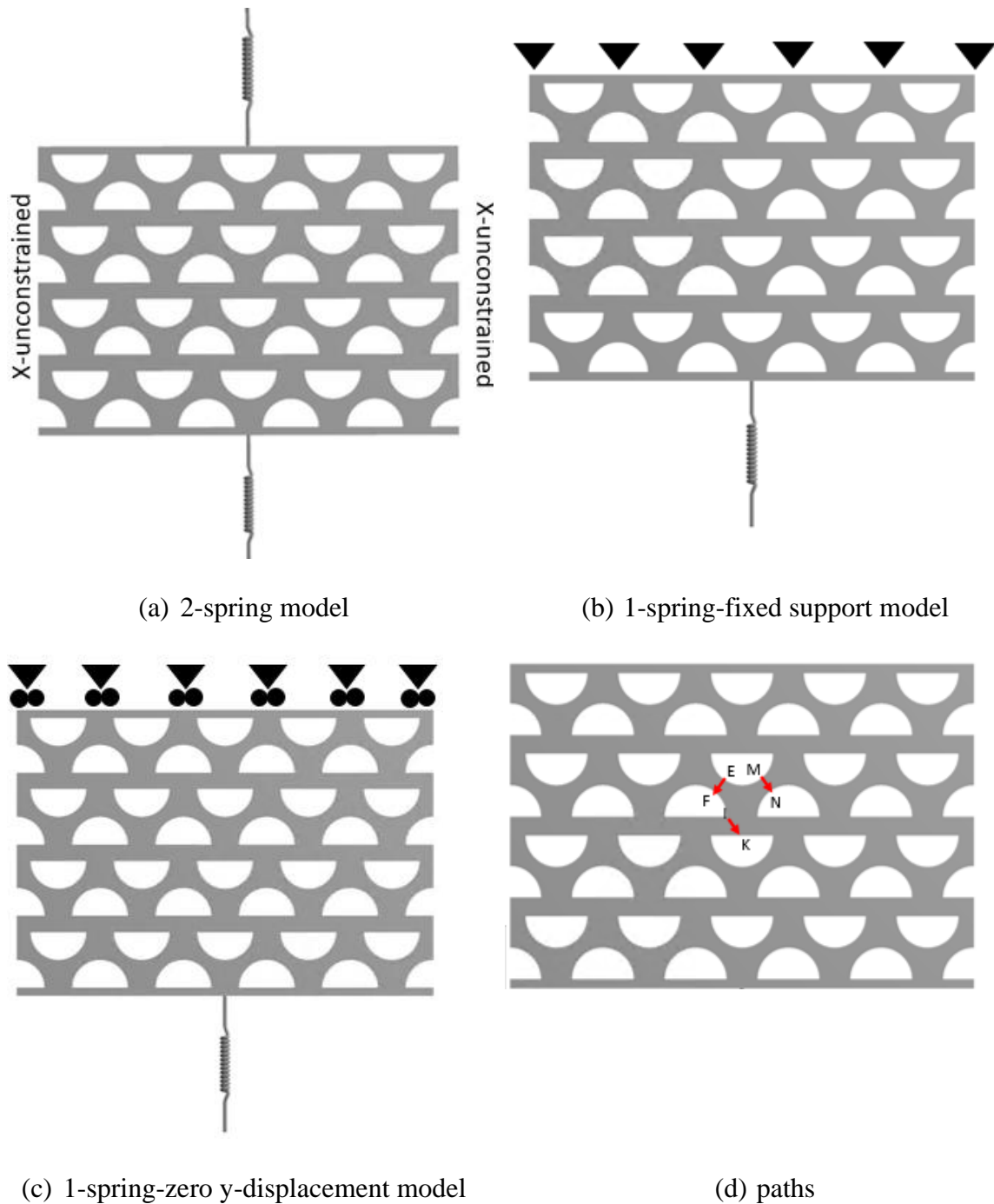


Figure 5. 23. (a) 2-spring model, (b) 1-spring-fixed model, (c) 1-spring-zero y-displacement model, (d) paths

5.5.2 Temperature field

ANSYS-FLUENT was used to determine temperature distribution within the solid and fluid domains of the studied PCHE model in a 3D steady-state conjugate heat transfer analysis. Figure 5. 24 shows the cross-section of the CFD model used in the analysis, while Table 5. 2 lists boundary conditions used in the analysis. sCO₂ was used on both the hot and cold sides as the working fluid. Alloy 617 was selected as the solid material with constant thermo-physical and mechanical properties at 360 °C. Table 5. 11 lists thermal and mechanical properties of Alloy 617. Thermo-physical properties of sCO₂ were obtained by coupling FLUENT to NIST REFPROP database. The details of CFD simulation can be found in section 5.2.2.

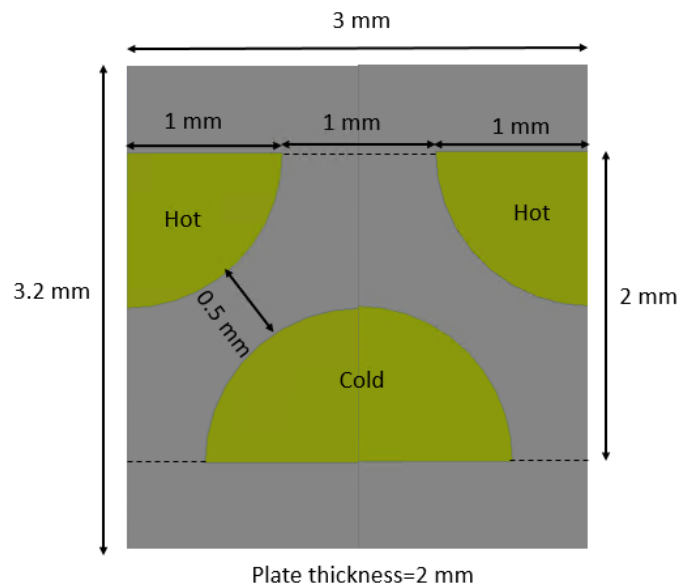


Figure 5. 24. Cross-section of the CFD model

Table 5. 11. Thermal and mechanical properties of Alloy 617 at 360 °C

Property	Value	Unit
Density	8,360	kg/m ³
Specific heat capacity	417	J/kg-K
Thermal conductivity	21	W/m-K
Coef. of thermal expansion	13.1E-06	1/C
Elastic modulus	194	GPa
Passion ratio	0.3	-

To reduce the computation time, half of the model was simulated by invoking symmetry. The right/left walls and top/bottom walls are subject to the symmetry and periodic BCs, respectively. Figure 5. 25a shows temperature distribution in the mid-plane where, for this numerical example, the average temperature is 336.45 °C. The local wall temperature distribution along perimeters of the hot and cold channel walls is illustrated in Figure 5. 25b. Point A is the channel corner for both the hot and cold sides. The minimum and maximum temperatures for this example are 333.1 °C and 339.36 °C, respectively which occur at Point C of the cold and hot channel walls. The hot and cold wall temperature difference for the presented case is 6 °C.

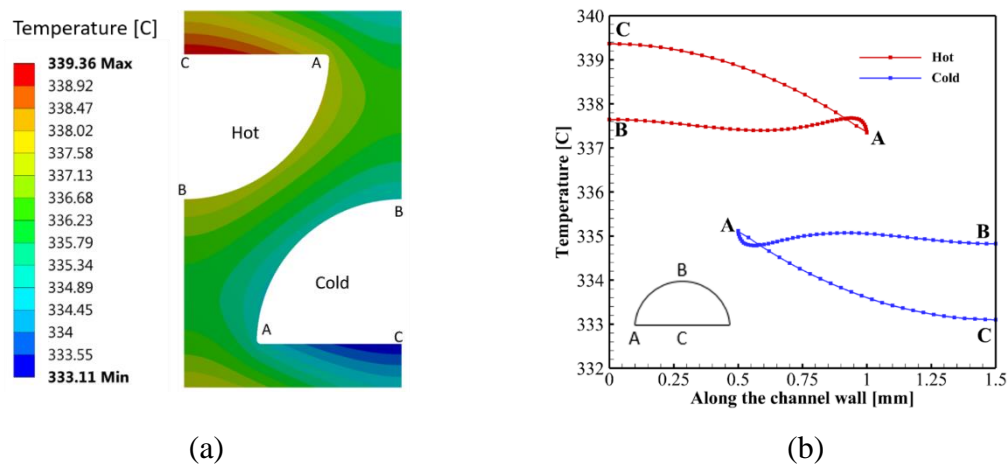


Figure 5. 25. (a) mid-plane solid temperature distribution, (b) hot and cold local wall channel temperature

5.5.3 Stress field

Song et al. [78] suggested four spring elements for the 3D laboratory scale PCHE shown schematically in Figure 5. 26 with each spring element representing the attached pipe stiffness. Based on the information provided on Figure 5. 26, the hard spring having stiffness of 82,925.3 N/mm was applied to the hot inlet (1st inflow), while a soft spring having stiffness of 194.2 N/mm was applied to the hot outlet (1st outflow). A hard and soft spring element limit thermal expansion of the 3D model in the axial direction. The 2D generalized plane strain was used as a suitable choice for a 2D simulation of the constrained thermal expansion in the axial direction. The values of spring elements of 277.6 N/mm and 2395.6 N/mm were applied at the top and bottom walls, corresponding to the locations of the 2nd inlet and 2nd outlet presented in Figure 5. 26 [78].

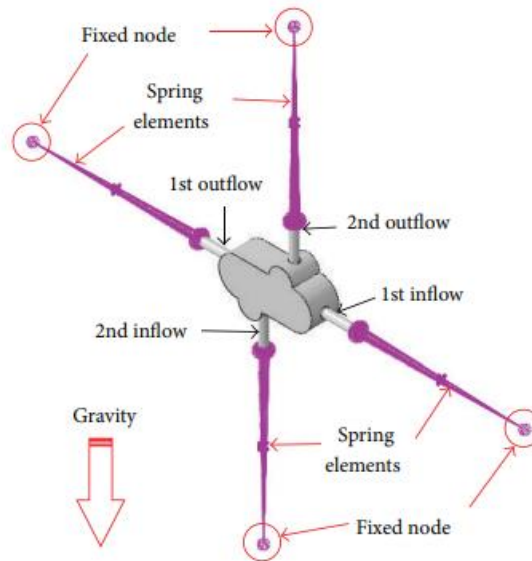
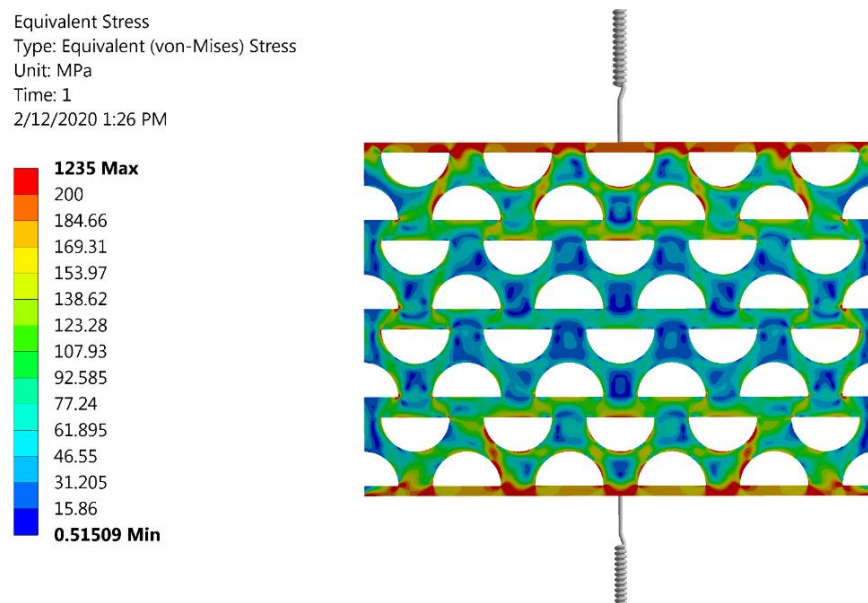


Figure 5. 26. The schematic of 3D lab-scale PCHE by Song [78]

This section describes results of the analysis performed concerning the effect of spring elements used as B.C.s. The analysis was performed using spring stiffness values reported by

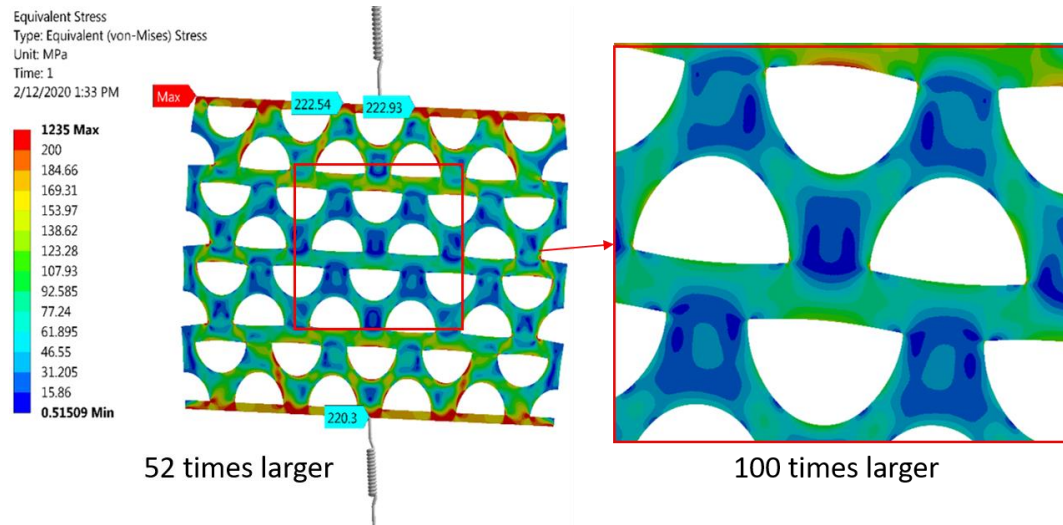
Song [78]. The obtained stress results were also compared to the stress values obtained for boundary conditions presented in Figure 5. 23.

Case 1 results: Figure 5. 27a shows stress field for the 2-spring element B.C. with spring stiffness corresponding to the hard and soft spring elements used by Song [78] described earlier. Figure 5. 27b and Figure 5. 27c show stress contours 100 time larger compared to the original stress contours and total deformation of the geometry under these boundary conditions, respectively.

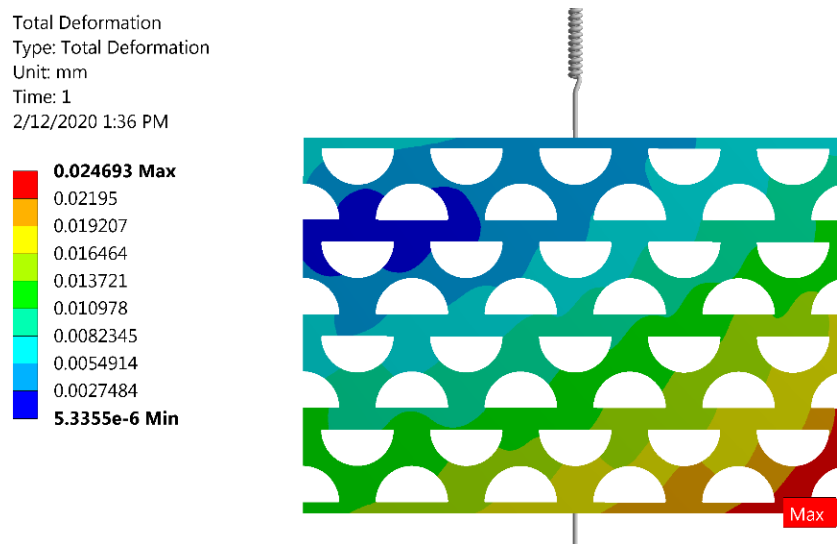


(a) Stress field using Song [78] B.C.s

Figure 5. 27. Case 1: (a) stress field corresponding to Song's B.C.s



(b) Stress field, scaled to 100 times larger



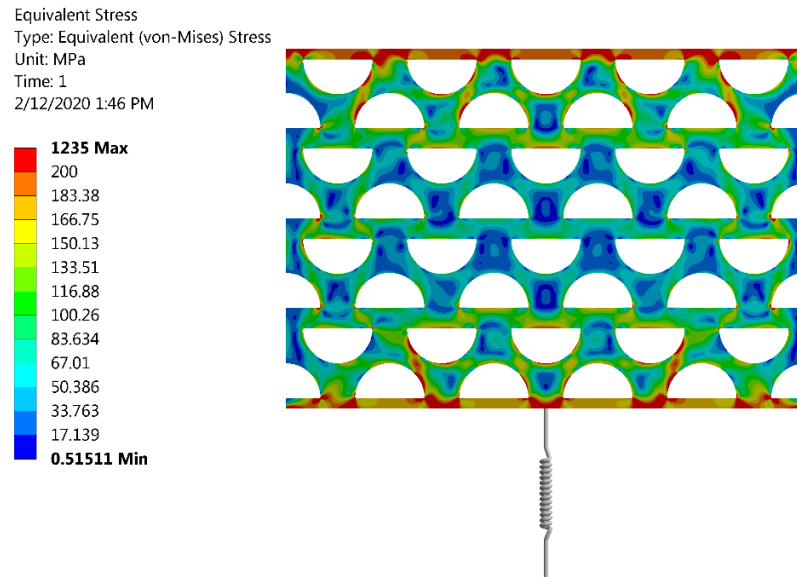
(c) Total deformation

Figure 5.27. Continued, (b) stress field corresponding to Song's B.C.s, (c) total deformation

The results presented in Figure 5. 27a-b show that the maximum value of equivalent stress is 222 MPa and it occurs in the proximity of the top wall spring element. The stress values in the middle of the model range between 0.5 and 128 MPa. Since the stress calculation scheme is isotropic linear elastic, the values of equivalent stress reached 350 MPa at the

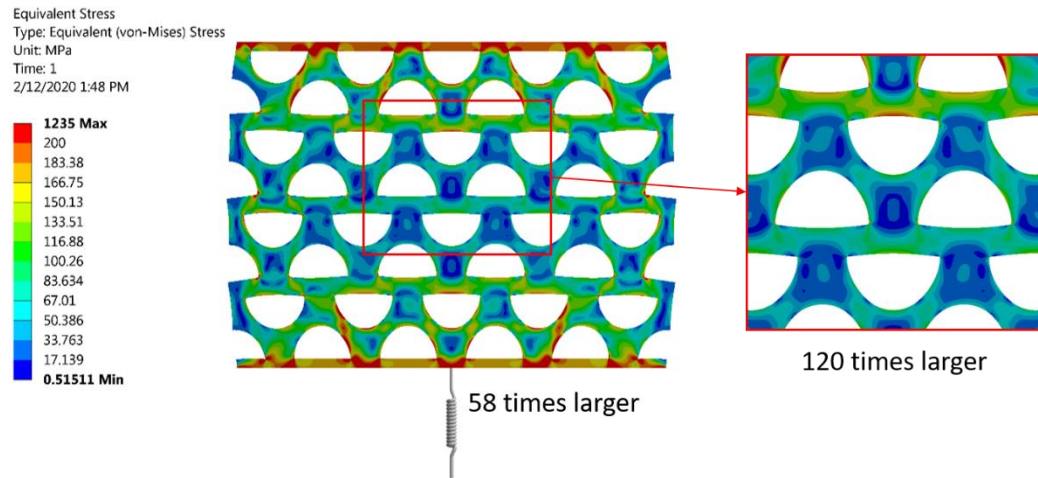
channel corners. The spring elements allow thermal expansion of the model in the y-direction (along the spring elements). Since thermal expansion and the displacement due to pressure forces are not identical, the total expansion (total deformation) occurs at the model corner as presented in Figure 5. 27c. The results show that the channel deformations caused by thermal expansion and pressure force using 2-spring B.C. element provides a realistic stress field. As mentioned earlier, the channel corners may experience plastic deformation under high pressure and temperature conditions.

Case 2 results: Figure 5. 28a-c shows stress field corresponding to 1-spring element-fixed support B.C (a fix support and soft spring element (194.2 N/mm)), shown in Figure 5. 21b. Figure 5. 28d shows the total deformation of the model subject to the spring boundary conditions (spring attached to the bottom).

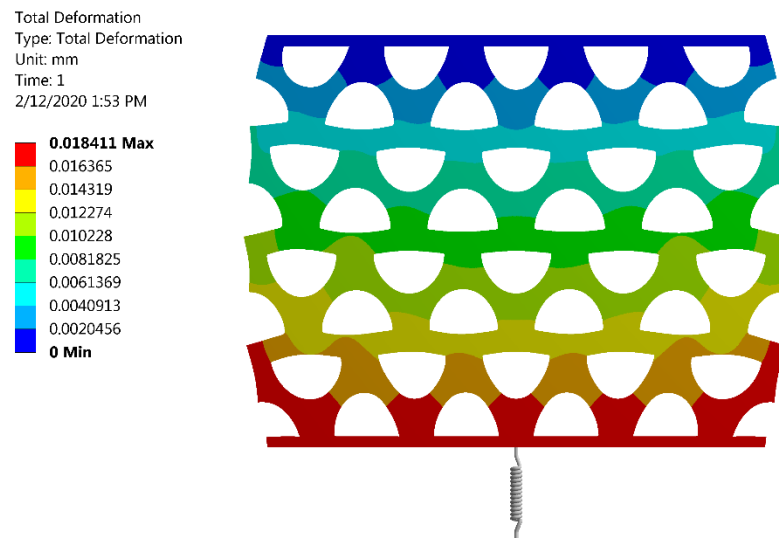


(a) Stress field

Figure 5. 28. Case 2: (a) stress field corresponding to 1-spring-fixed support B.C.s,



(b) Stress field, scaled to 120 times larger



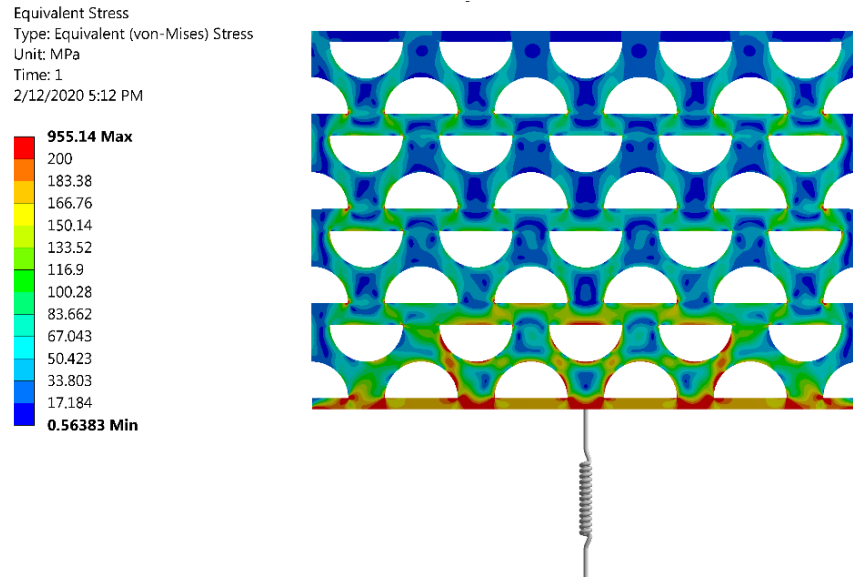
(c) Total deformation (120 times larger)

Figure 5.28. Continued, Case 2: (b) stress field corresponding to 1-spring-fixed support B.C.s, (c) total deformation

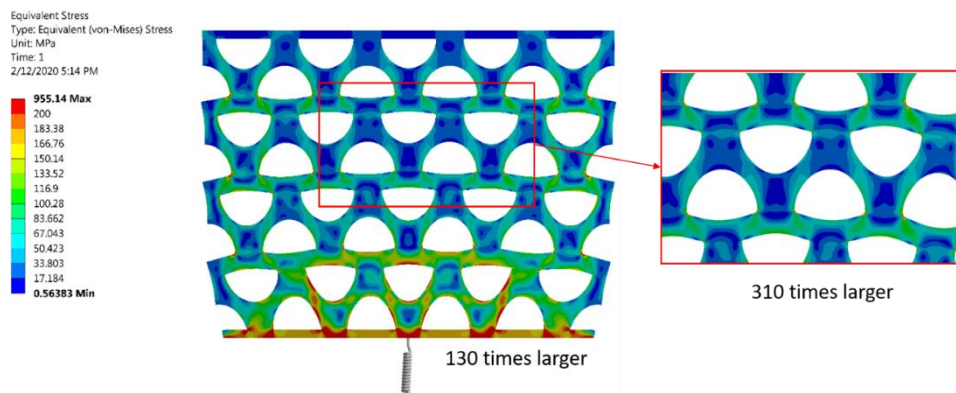
The results show that the stress field corresponding to 1-spring-fixed support B.C.s is identical to the 2-spring model used by Song [78]. The maximum value of equivalent stress is 222 MPa and occurs at the proximity of the top wall spring element. The stress values in the

middle of the model range between 0.5 and 128 MPa. Since the stress calculation scheme is isentropic linear elastic, the values of equivalent stress reached 350 MPa at the channel corners.

Case 3 results: Figure 5. 29a-c shows the stress field corresponding to 1-spring element-zero y-displacement B.C. shown in Figure 5. 23c. Figure 5. 29c shows the total deformation of the model under spring boundary conditions described above.

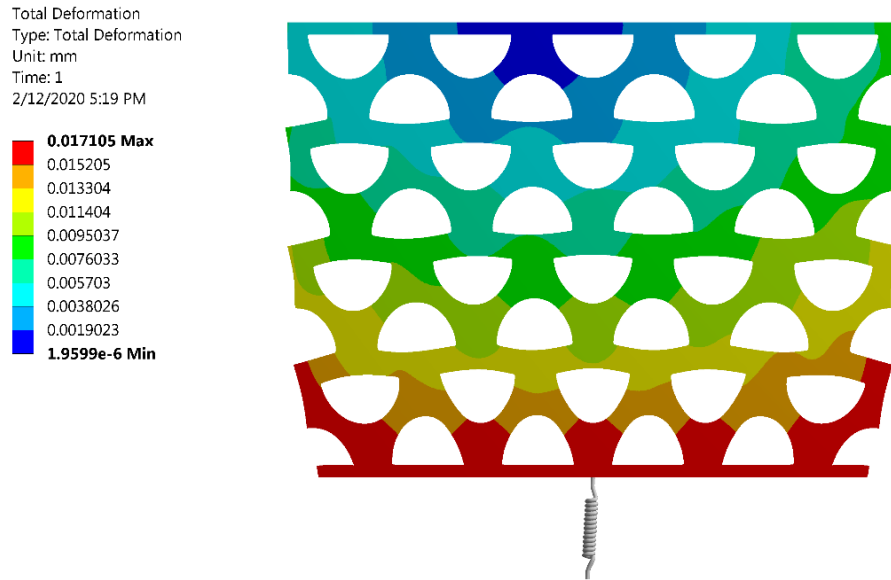


(a) Stress field



(b) Stress field, scaled to 130 times larger

Figure 5. 29. Case 3: (a-b) stress field for 1-spring- zero y-displacement B.C.s



(c) Total deformation (130 times larger)

Figure 5.29. Continued, (c) total deformation

The results obtained for Case 3 show that the zero y displacement B.C. provides lower stress compared to Case 1 and Case 2 due to restraining one displacement component. However, the stress values at the channel corners increase due to the imposed constraints and resulting channel deformation. The results show that the zero y-displacement may not be a suitable B.C. for the top/bottom boundaries.

Figure 5. 30a-c shows stress distribution predicted for Cases 1, 2, and 3 along different paths shown in Figure 5. 23d. The M-N and E-F paths represent channel fin in the PCHE model. The stress distribution along these two paths is identical due to symmetry. The results show that the predicted stress values in channel fin along the E-F and M-N paths for Cases 1 and 2 are virtually identical and reach maximum value in the middle of the fin. For Case 3 (spring and the zero y-displacement B.C.) the predicted stress is almost constant (approximately 40 MPa). along the E-F and M-N paths, indicating that Case 3 results in unrealistic stress distribution in the channel fin.

The results presented in Figure 5.30c show that for the zero y-displacement B.C., the equivalent stress reaches the maximum value of 450 MPa in the channel corner on the shim plate, point I. For the same location, the maximum stress corresponding to Cases 1 and 2 (2-spring element and 1-spring-fix support boundary condition) is lower, 350 MPa. Also, stress values in the shim plate and channel fin predicted for Case 3 (zero y-displacement) are lower compared to Cases 1 and 2. Therefore, the zero y-displacement (Case 3) was not selected as a boundary condition for further studies.

Song et al. [78] used two soft springs for the top and bottom walls and hard and soft spring elements in the axial direction while side walls were assumed unconstrained. To enable a comparison, two soft spring elements were chosen for the top and bottom walls in the current study, but the side wall boundary conditions need to be studied.

A combination of the spring element for the side walls and 2-spring element for the top/bottom walls was investigated, and the results are presented in the following section. Also, the effect of spring stiffness on the stress field should be investigated, as described in Section 5.5.4.

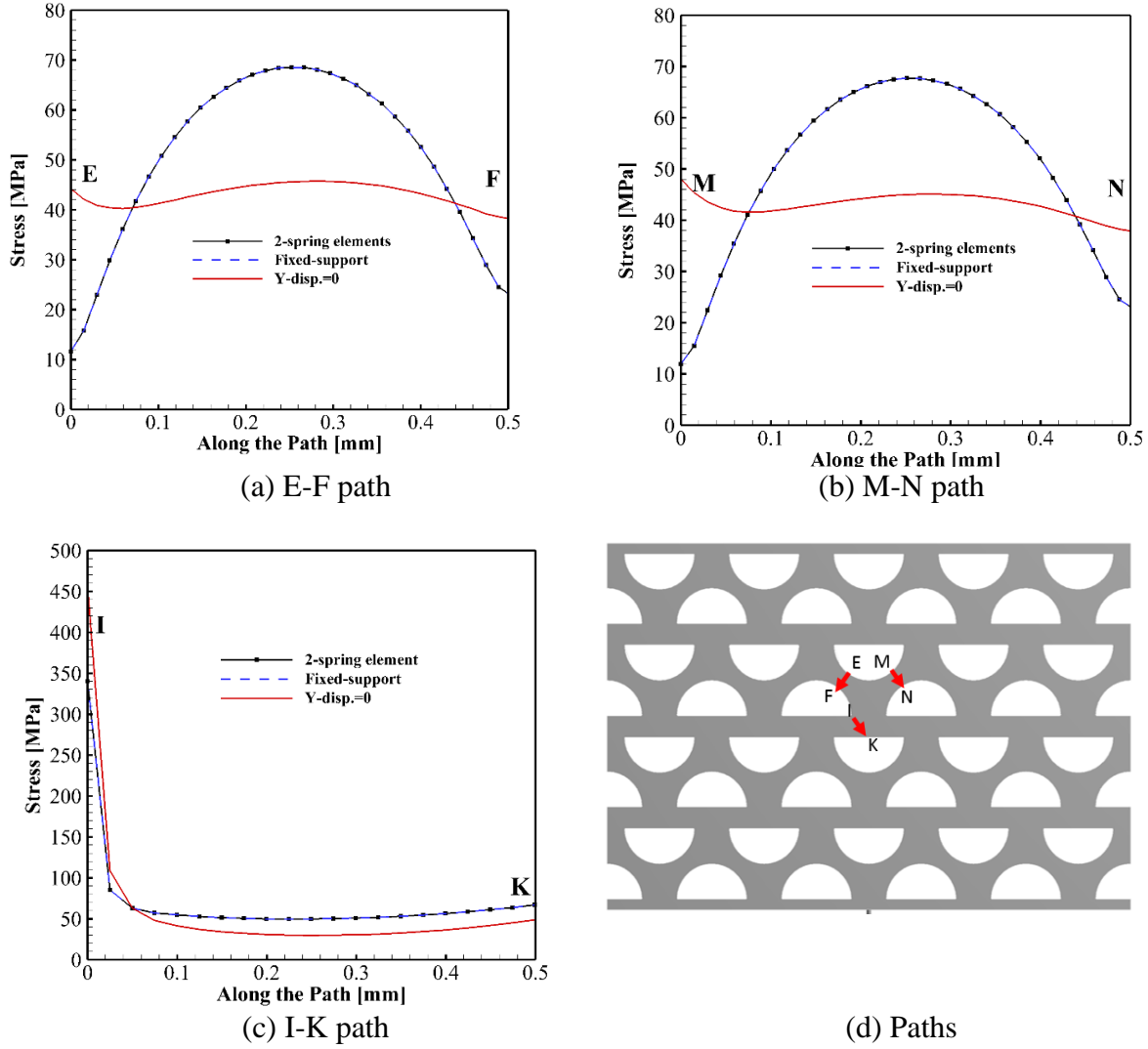


Figure 5. 30. (a-c) stress distribution along the paths (d) paths

5.5.4 The effect of the right/left wall B.C.s and spring stiffness on stress distribution

As mentioned earlier, Song [78] simulated a 3D lab-scale PCHE using spring elements as boundary conditions. Since the analyzed PCHE is not connected to the pipes on the right/left side, the right/left walls boundary were assumed unconstrained. Also, Lee and Lee [18] assumed the side walls of the 2D PCHE model are free to expand, thus unconstrained boundary conditions were assumed for the right/left walls. Based on the information provided by Song [78] for a 3D lab-scale PCHE and results obtained in this study (Section 5.5.2), the assumption of unconstrained right/left walls is realistic. However, an investigation should be performed to

explore the effect of different boundary conditions imposed on the right/left walls on the predicted stress field.

FE simulations were performed in this study for different right/left wall B.C.s and the resulting stress distribution in the channel fin and shim plate (along the E-F and I-K paths, presented in Figure 5. 30d, is presented in Figure 5. 31a-b.

The following B.C. imposed on the right/left walls were considered for the stress analysis:

Case 4: 2-spring on top/bottom walls and x-symmetry on side walls

Case 5: 2-spring on top/bottom walls and 2-spring on side walls.

In the physical model for Cases 4 and 5, the top/bottom wall B.C.s are constrained by spring elements having spring stiffness of 2000 N/mm (2k N/mm). Figure 5. 31a-b shows stress distribution along the I-K and E-F paths corresponding to the channel fin and shim plate for Cases 4 5 and also for Case 1. The results presented in Figure 5. 31a-b show that constraints in B.C.s used in Case 4 and Case 5 imposed on the right and left walls create an additional constraint on the 4×4 PCHE model and overestimates predicted stress values in the PCHE core. These B.C.s limit deformations in the x direction, thus reaction forces acting in the x-direction result in higher stresses inside computational domain compared to the unconstrained core. Figure 5. 31b shows that the stress values corresponding to Case 5 predicted at the channel corner reach 1200 MPa, which makes the results unrealistic.

The spring stiffness values in the 0.002k N/mm (2 N/mm) and 80k N/mm (80,000 N/mm) range were selected to investigate the effect of this parameter on the resulting stress field in the PCHE model. The stress distribution predicted in the channel fin along E-F path for different boundary conditions are presented in Figure 5. 31c. It was assumed that the spring

stiffness for both spring elements is identical. The results presented in Figure 5. 31c show that stress values predicted for low values of spring stiffness are identical to the unconstrained B.C., which is expected result. Increasing spring stiffness increases stress in the channel walls. The fixed-support B.C. provides unrealistically high stresses in the PCHE core since deformation is limited. Since the spring stiffness depends on the pipe stiffness, it was assumed that the pipe stiffness is identical at both the inlet and outlet of the PCHE. Thus, the assumption of using identical spring stiffness at both sides of the model is realistic.

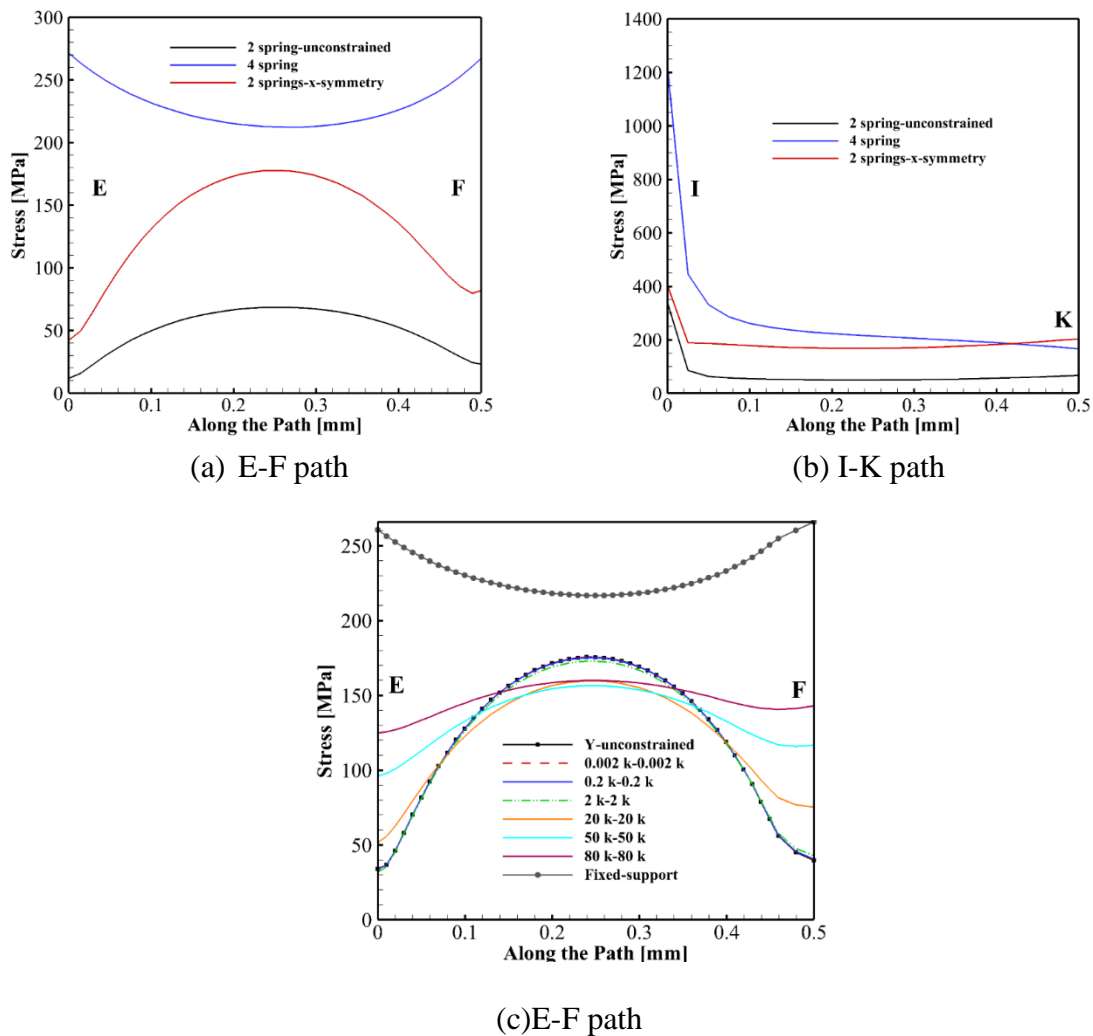


Figure 5. 31. The equivalent stress distribution on (a) F-E path (b) I-K path for different right/left wall B.C.s, (c) F-E path over a range of spring stiffness

In summary, a 2-spring element model provides reasonable stress field in the 4×4 PCHE model shown in Figure 5. 23a. The results of the current study and Lee and Lee [18] and Song [78] concerning B.C.s imposed on the right and left walls of the model show that the unconstrained B.C.s are realistic for these walls. Thus, the B.C.s used in Case 1, presented in Figure 5. 23a, were used for the design and optimization of the staggered double-etched and double banking patterns for semi-circular channels (Chapter 6) and for the staggered double-banking circular geometry (Chapter 7).

CHAPTER 6: ADVANCED MICRO-CHANNEL GEOMETRY AND TOPOLOGY- DOUBLE-ETCHED STAGGERED GEOMETRY

6.1 Overview

Optimization of an advanced PCHE topology employing staggered double-etched micro-channel geometry is described in this section. The PCHE topology was optimized using ANSYS software with the objective to increase heat transfer performance by developing a PCHE with larger specific heat transfer area and reducing PCHE weight and cost by better utilization of the metal. A multi-objective optimization with Non-dominated Sorting Genetic Algorithm II (NSGA-II) using Response Surface Approximation (RSA) as a surrogate model was employed to optimize the PCHE geometry. The channel fin thickness, the channel pitch, and shim plate thickness were the parameters used in the optimization. Alloy 617 with temperature-dependent thermo-physical properties of material was used in the CFD and stress analyses. The 3D CFD simulations were performed for both the optimized topology and the Base Model, and the obtained results concerning thermal and hydraulic performance were compared. The effectiveness-NTU method was used to investigate the effect of studied parameters on the PCHE thermal performance. The sequence of calculations and analyses performed in Chapter 6 are presented in Figure 6. 1. The section number corresponding to each step of the analysis is shown in the flowchart boxes.

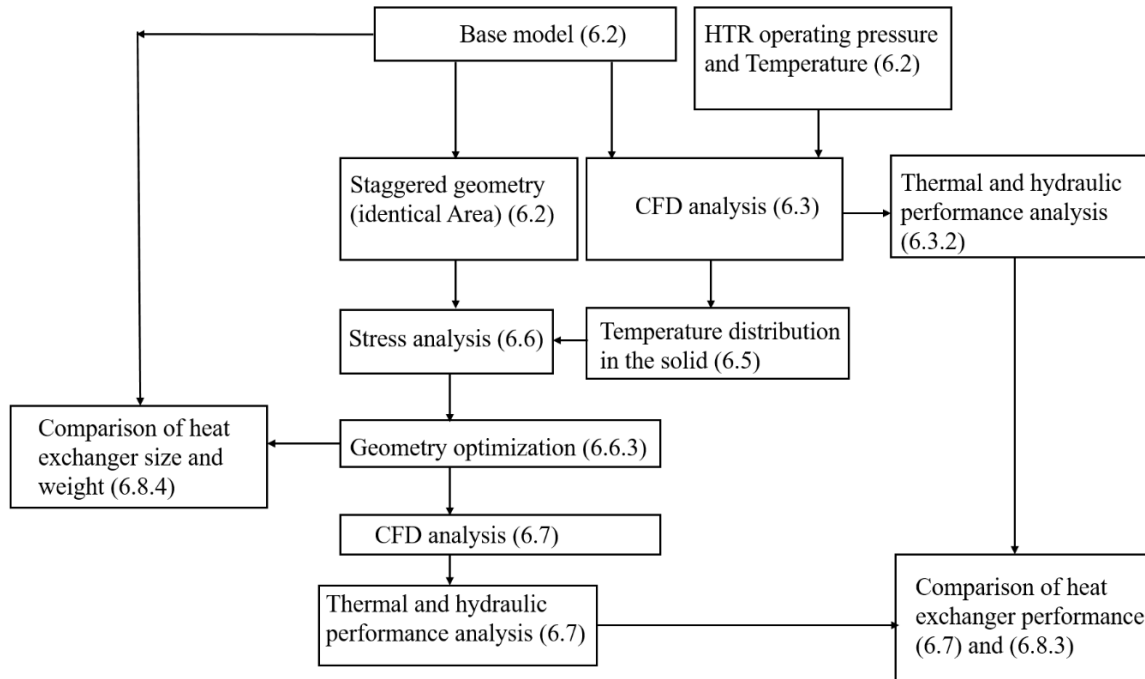


Figure 6. 1. The flowchart of calculations and analyses performed in Chapter 6

6.2 System description, operating pressure and temperature

Supercritical CO₂ (sCO₂) Brayton power cycle has attracted attention for the next generation of Sodium Fast Reactors (SFRs) coupled to the power cycles and the Concentrated Solar (CSP) power plants. A sCO₂ Brayton cycle offers efficiency equivalent to the steam-cycle efficiency while avoiding a potentially violent Na/H₂O reaction. A sCO₂ Brayton cycle is a simple, compact, and highly efficient power cycle, however, large variations in thermo-physical properties of sCO₂ in the proximity of CP and along the pseudo-critical line make the design and optimization of the power cycle and the equipment challenging. Floyd et al. [8] numerically studied the sCO₂ recompression Brayton cycles in the off-design mode and optimized power cycles for the next generation (Gen IV) of French ASTRID (1500 MW_{th}) SFR. The system includes two 750 MW_{th} loops with a sCO₂ recompression Brayton cycle coupled to the SFR operating with the core temperature in the 395 °C-545 °C range. The sCO₂

recompression power cycle operating with the turbine inlet temperature (TIT) of 515 °C and pressure (TIP) of 25 MPa can achieve net thermodynamic efficiency of 42-43%. Figure 6. 2 shows arrangement of the highly recuperated sCO₂ recompression Brayton cycle. The Intermediate Heat Exchanger (IHx) and the high- and low-temperature recuperators (HTR and LTR) are used to transfer heat from the heat source (liquid sodium from SFR) to sCO₂ (working fluid) and recuperate it at supercritical conditions in a Brayton cycle.

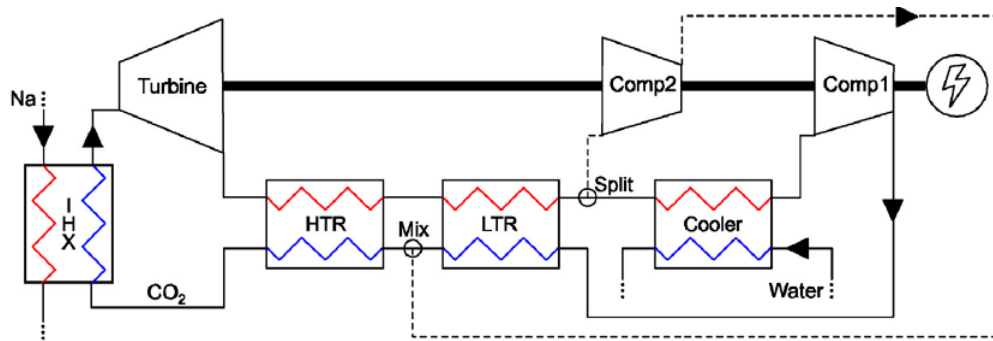


Figure 6. 2. The sCO₂ recompression Brayton cycle arrangement

Figure 6. 3 shows the optimized sCO₂ Brayton cycle designed and optimized by Floyd et al. [8] including the primary and secondary liquid sodium (Na) loops and integrated recompression sCO₂ Brayton cycle. The TIT and TIP values of 515 °C and 25 MPa, respectively used in the analysis of a 759 MW_{th} sCO₂ Brayton cycle give the net efficiency of 42.2%.

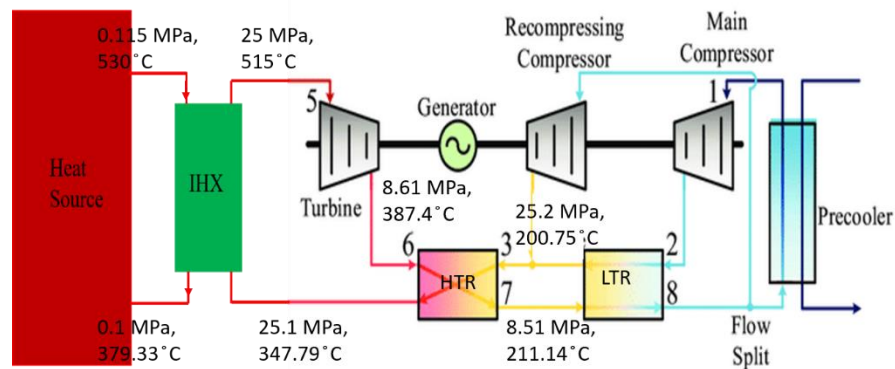


Figure 6. 3. The optimized sCO₂ Brayton cycle with recompression [8]

The operating temperature and pressure determined by Floyd [8] for the HTR operating in the optimized sCO₂ cycle were used in this study to design an advanced PCHE that would operate in the optimized sCO₂ cycle. Figure 6. 4 summarizes operating conditions (temperature and pressure) for the HTR.

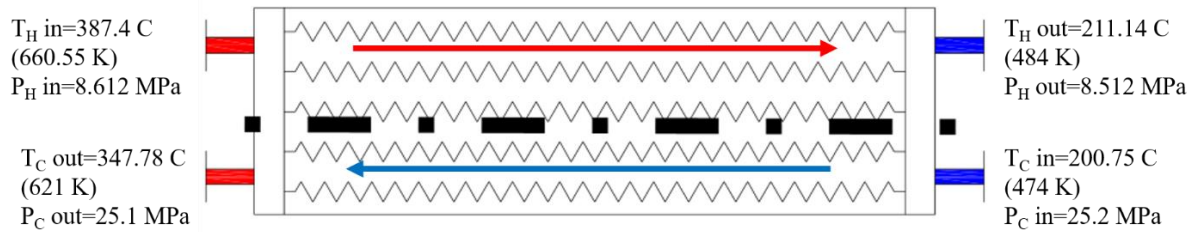


Figure 6. 4. The operating temperature and pressure determined by Floyd et al. [8] for HTR

As explained in Chapter 7, the operating conditions (temperature and pressure) determined by Floyd [8] for the IHX operating in the optimized sCO₂ cycle were used to design an advanced PCHE employing circular staggered micro-channel geometry and topology.

Since a large amount of recuperation is used in a sCO₂ Brayton cycle, the size and efficiency of heat exchangers are important parameters in the design and optimization of the cycle. Floyd et al. [8] considered advanced heat exchangers such as PCHEs for the sCO₂ cycle design.

The values of PCHE channel diameter, channel width, and the plate thickness used by Hun Kim (2009) [70] and (2012) [71] were selected for the analysis. Thus, the channel diameter and length of 1.51 mm and 765 mm, respectively were used in the analysis. The detailed information of the PCHE Base Model (BM) used in this study is listed in Table 4.1, while schematic of the BM is shown in Figure 4.1 (Chapter 4). Numerical analysis of the PCHE, its hydraulic and thermal performance, mesh independence study, validation of the numerical model, and details of the CFD analysis are described in Chapter 4.

The semi-circular staggered, double-etched pattern for the $s\text{CO}_2$ - $s\text{CO}_2$ application in a recuperator, presented in Figure 6. 5, was designed and optimized in this work. The results are presented in this section. It has to be noted that the cross-section area of solid wall in the semi-circular SDE geometry is identical to the Base Model described in Section 4.2 (Chapter 4). Dimensions of the micro-channel and surrounding walls for both geometries are listed in Table 4.1 and are presented in Figure 6. 5.

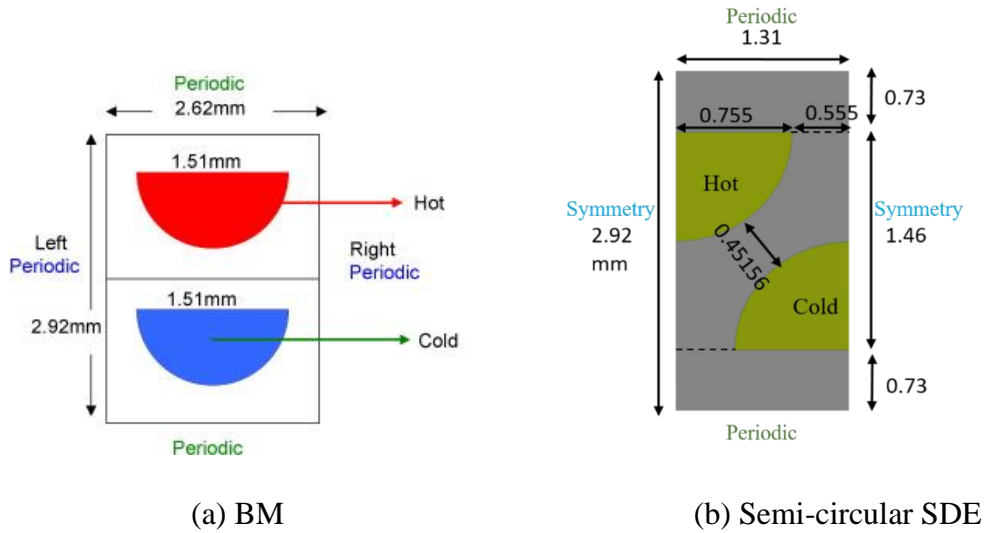


Figure 6. 5. The Base and semi-circular staggered double-etched models

6.3 Thermal and hydraulic performance of studied PCHEs

6.3.1 Boundary conditions for the Base and Staggered double-etched models

Straight channels with semi-circular cross-section geometry were modeled and analyzed in 3D CFD simulations to determine thermal and hydraulic performance of a PCHE operating as a HTR in a $s\text{CO}_2$ Brayton cycle. Table 6. 1 lists boundary conditions used in the 3D CFD simulations. The conservation and energy equations for the 3D steady-state laminar incompressible fluid flow at $\text{Re}=1000$ on the $s\text{CO}_2$ side and Laplace equation for the steady-state heat conduction in solid walls were solved numerically by the Fluent code. The details of

the grid sensitivity analysis and validation were presented in Chapter 4. Fluent was coupled to the NIST REFPROP 9.0 to obtain accurate fluid properties for sCO₂.

Table 6. 1. The Boundary conditions for studied PCHE models

Boundary	BM (semi-circular)	Semi-circular SDE	Hot side	Cold side
Inlet	Velocity (m/s)	Velocity inlet	0.5	0.1074
Inlet	Temperature (K)	Temperature	660.55	474
Outlet	Pressure outlet (MPa)	Pressure outlet	8.612	25.2
Top wall	Periodic	Periodic	-	-
Bottom wall	Periodic	Periodic	-	-
Side walls	Adiabatic/symmetry	Symmetry	-	-
Front/Back walls	Adiabatic	Adiabatic	-	-

6.3.2 CFD results for the Base and Staggered double-etched geometries

The values of peripherally-averaged Nusselt number and friction coefficient (fanning friction factor) C_f obtained in numerical analysis of a semi-circular model (Base Model, BM) and semi-circular staggered double-etched (SDE) geometries for sCO₂ as the hot and cold working fluid are listed in Table 6. 2.

Table 6. 2. Thermal and hydraulic performance of studied PCHEs

	Hot channel (sCO ₂)					Cold channel (sCO ₂)				
Configuration	C_f	Nu	Pressure drop [Pa]	T_{bulk} at outlet [K]	Q [W]	C_f	Nu	Pressure drop [Pa]	T_{bulk} at outlet [K]	Q [W]
BM (semi-circular)	0.007	4.03	309	483.7	6.22	0.0086	4.12	122	624.7	6.40
Semi-circular SDE	0.007	4.13	309	484	6.22	0.0086	4.23	122	626	6.40
Difference%	0.00	2.7	0.00	0.07	0.00	0.00	2.6	0.00	0.20	0.00

The results show that friction coefficient for the semi-circular BM and SDE geometry/topology is the same since both the channel length and thermo-physical properties of sCO₂ did not change, resulting in the same pressure drop for both analyzed geometries. The variation in thermo-physical properties of sCO₂ is negligible since the change in bulk

temperature along the channel length is small. It has to be noted that pressure drop in the hot channel is 3 times higher compared to the cold side (309 vs 122 Pa) since shear stress in the hot channel is significantly higher compared to the cold channel due to higher velocity gradient near the hot channel wall. Thermal and hydraulic performance of the BM is presented and discussed in Section 6.7. The pressure drop difference between the hot and cold channels was also reported in the literature (Kim (2009)) [70].

The heat transfer coefficient for both geometries is approximately the same since the mass flow rate and hydraulic diameters of the BM and SDE geometries are identical. The Nusselt number for the semi-circular channel geometry corresponding to the constant wall heat flux in the axial (flow) direction with constant peripheral wall temperature in the fully developed laminar flow reported in the literature [53] is 4.089. The results obtained in this work show that the Nu number values for the hot and cold channels are 4.03 and 4.12, respectively for the semi-circular BM and 4.13 and 4.23, respectively for the semi-circular SDE model. The Nu number for the SDE geometry is 2.5 percent higher compared to the BM, which can be explained by the increase in overall heat transfer since hydraulic diameter is fixed and thermal conductivity of $s\text{CO}_2$ remained unchanged because of the virtually identical bulk fluid temperature. Thus, the increase in heat transfer and corresponding increases in wall heat flux and Nu number can be attributed to the decrease in channel fin thickness and resulting decrease in thermal resistance. The details of wall heat flux variation are presented in Section 6.7.

6.4 The effect of channel fin thickness on the channel wall temperature

Since the channel wall temperature plays an important role in design and optimization of the PCHE channel topology, the aim of the analysis is to determine the effect of fin thickness

on the channel wall temperature. The steady-state heat conduction equation uses channel wall temperature as the boundary condition to determine temperature distribution in the solid material. The resulting temperature distribution is then used to calculate thermal stresses within the solid domain.

The SDE geometry presented in Figure 6. 5b, was used to study the effect of fin thickness on the wall temperature. Four 3D CFD simulations were performed in this investigation assuming laminar flow regime with $Re=1000$, counter-flow arrangement, water as the working fluid with constant thermo-physical properties, and Alloy 617 as solid material with constant thermal properties. The boundary conditions are listed in Table 6. 1. As shown in Figure 6. 5, the maximum channel fin and shim plate thicknesses are 0.45156 mm and 1.46 mm. The SDE geometry parameters are listed in Table 4.1. A range of channel fin thickness from 0.45156 mm to 0.30 mm was used to calculate thermal resistance and overall heat transfer coefficient U .

Thermal resistance of the SDE geometry was simulated by using the heat conduction model for a hollow cylinder, shown in Figure 6. 6. The inner and outer surfaces of the model are exposed to different fluid temperatures and convection coefficients to simulate the cold and hot channels. Considering a steady-state heat conduction, with no heat generation inside the solid, using the Fourier's law, Eq. 6.1 was used to determine thermal conduction resistance in the fin (channel wall). Thermal resistance to convection heat transfer was calculated using Eq. 6.2. The total thermal resistance was determined from Eqn. 6.3. The inverse of total thermal resistance, UA was calculated using Eq. 6.4.

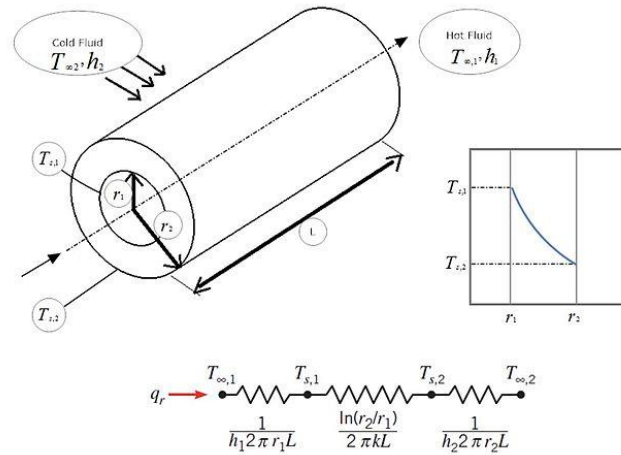


Figure 6. 6. Hollow cylinder with different convection surface boundary conditions [51]

$$R_c = \frac{\ln \left(\frac{r_2}{r_1} \right)}{2\pi k L} \quad (6.1)$$

$$R_h = \frac{1}{h 2\pi r L} \quad (6.2)$$

$$R_t = R_h + R_c + R_h \quad (6.3)$$

$$R_t = \frac{1}{UA} \quad (6.4)$$

Table 6. 3 lists values of the total thermal resistance obtained from Eq. 6.4, resistance to heat conduction in the channel fin (radial conduction in a cylindrical wall) and peripherally-averaged temperature of the hot and cold channel walls.

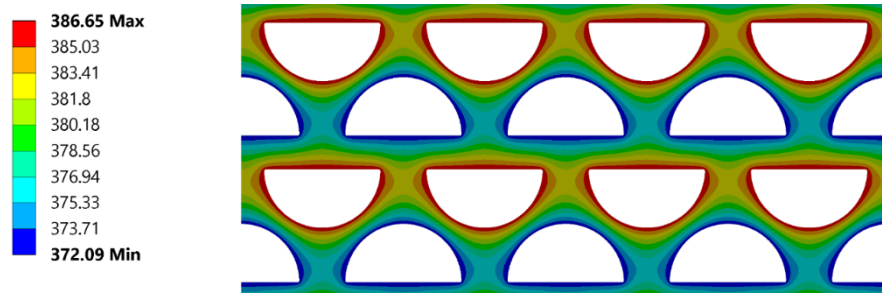
Table 6. 3. Hot and cold channel wall temperature for different fin thickness

Fin thickness (mm)	R_c [K/W]	R_h ($1/h_{cold}A$) [K/W]	R_h ($1/h_{hot}A$) [K/W]	R_t ($1/UA$) [K/W]	Hot wall Temperature (K)	Cold wall Temperature (K)
0.45156	0.0177	0.3311	0.3311	0.680	553.23	563.59
0.40	0.0161	0.3308	0.3308	0.677	552.94	563.82
0.35	0.0144	0.3304	0.3304	0.675	552.70	564.03
0.30	0.0126	0.3299	0.3299	0.672	552.52	564.18

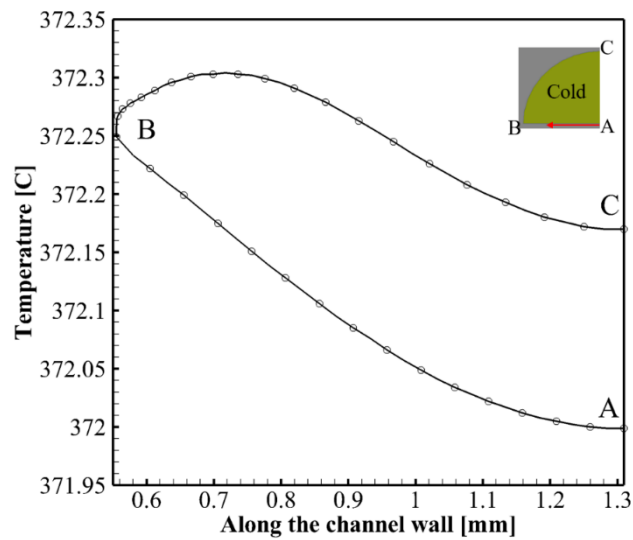
The results show that the cold wall temperature increases linearly as the fin thickness decreases; 0.2°C for each 0.05 mm reduction in fin thickness, while the hot wall temperature follows the opposite trend. The difference in wall temperatures is less than 1°C as fin thickness is decreased from 0.45156 to 0.3 mm . These results show that the effect of fin thickness on the channel wall temperature is small and its effect on temperature distribution in channel walls can be neglected. Thus, temperature distribution obtained for the fin thickness of 0.45156 mm was used in calculation of thermal stresses.

6.5 Temperature distribution in channel walls

To calculate temperature distribution within the solid domain (channel walls), conservation equations for momentum, energy, and mass were solved for the 3D steady-state laminar incompressible fluid flow, while the Laplace equation for the steady-state heat conduction was solved for the channel walls. The geometry of semi-circular SDE micro-channels having fin thickness of 0.45156 mm was analyzed. Detailed information considering the geometry and boundary conditions is presented in Table 6. 4 and Table 6. 5. Temperature contours in channel walls and variation in wall temperature along the cold channel periphery predicted at the hot end are presented in Figure 6. 7. For conservative thermal stress analysis, the wall temperature at the hot end was selected since the maximum wall temperature in the solid domain (386.65°C) happens at the hot end. The maximum and minimum values of local wall temperature on the cold channel wall are 372.3°C and 372°C .



(a)



(b)

Figure 6. 7. (a) temperature contours, (b) cold side channel wall temperature distribution

The results presented in Figure 6. 7b shows that temperature along periphery of the cold channel wall is not uniform, but this variation is small and can be neglected. For the analyzed case, the variation of temperature within the channel walls is, however, significant with the the maximum temperature difference of 14°C occurring between the hot and cold channel walls and the shim plate, as presented in Figure 6. 7a. Thus, thermal stress due to temperature difference is higher in the shim plate and the channel fin compared to the channel walls. For the analyzed operating conditions of the PCHE, temperature gradient in channel walls in the axial (flow) direction is 175.65°C .

6.6 Structural analysis

Thermal and mechanical stresses (von-Mises stresses) and total stress were calculated by using ANSYS-mechanical module under specific loading conditions. The results are presented in this section. As discussed in Chapter 5, the 2D generalized plane strain model provides realistic results and was, thus selected for stress calculations which were performed by employing FEM. The 2-spring boundary condition was selected for stress analysis. The temperature field was used as an input to the ANSYS mechanical module for stress calculations. The boundary conditions for thermal analysis of the PCHE model are described in Section 6.3. To obtain the thermal stress field, temperature distribution obtained by using a 3D CFD analysis, described in Section 6.5, was mapped to the structural model. The total stress corresponding to the thermal and mechanical loadings in the model was obtained and used to investigate the mechanical design methodology in compliance with the ASME standards. As discussed in Chapter 5, the Design-by-Analysis approach was used to determine the optimum PCHE core geometry, such as channel fin thickness and the shim plate thickness. The channel fin and shim plate thicknesses were determined through an optimization method (The Multi Objective Genetic Algorithm) by using thermal and mechanical stress fields. The PCHE core geometry was optimized by using the advanced correlation-based multi-objective evolutionary algorithm (MOEA), which is a part of ANSYS. The ANSYS optimization module includes NSGA-II (Non-dominated Sorting Genetic Algorithms), an advanced MOEA, for optimization. The maximum allowable stresses were used as the maximum stress limit in the optimization of the PCHE core geometry. The following assumptions were used in the stress calculations and optimization of the PCHE geometry:

2D stress calculations were performed using the Generalized plane strain model and Ansys-mechanical module. The predicted values of von-Mises stress were analyzed.

Temperature distribution in channel walls was considered unaffected by changes in channel fin and shim plate thickness, as described in Section 6.4. The minimum temperature in the solid domain (211°C in the analyzed case) was used as the reference temperature.

Alloy 617 with temperature-dependent physical and mechanical properties was used in thermal and mechanical stress calculations. The maximum allowable stress for Alloy 617 of 160 MPa at 250°C was used as the optimization constraint in the optimization of the PCHE geometry.

The linear stress calculation (Hook's law) was used in stress calculations.

The highest stress values predicted at the channel corners would cause plastic deformation at these locations. As discussed previously, plastic deformations were not considered in this work. Thus, the stress values predicted at the channel corner were not considered in the optimization process, i.e., plastic deformations were not included in the PCHE model optimization.

A round fillet of 0.02 mm was used at the channel corners to obtain more realistic values of stresses at these locations. The spring stiffness of 200 N/mm was assumed on the top and bottom of the model as described in Chapter 5, Section 5.5.1.

6.6.1 ANSYS modeling

Figure 6. 8 shows the staggered double-etched (SDE) geometry used in stress calculations and optimization of the PCHE geometry. The details of the geometry are presented in Figure 6. 5. The channel diameter and cross-section area of solid wall in the SDE geometry are identical to those of the BM. The micro-channels were considered to be straight. The micro-

channel fin and shim plate thicknesses were varied to achieve optimization objective subject to the constraint of the maximum allowable stress. The mechanical boundary conditions were presented in Chapter 5, Section 5.5.1, while the channel pressure applied to walls of the hot and cold channels is listed in Table 6. 1. Figure 6. 8b shows locations of the maximum stress values in the channel fin and shim plate obtained for the temperature field in channel walls presented in Figure 6. 7.

The stress analysis includes both thermal and mechanical stress. The details of stress calculations and validation were provided in Chapter 5.

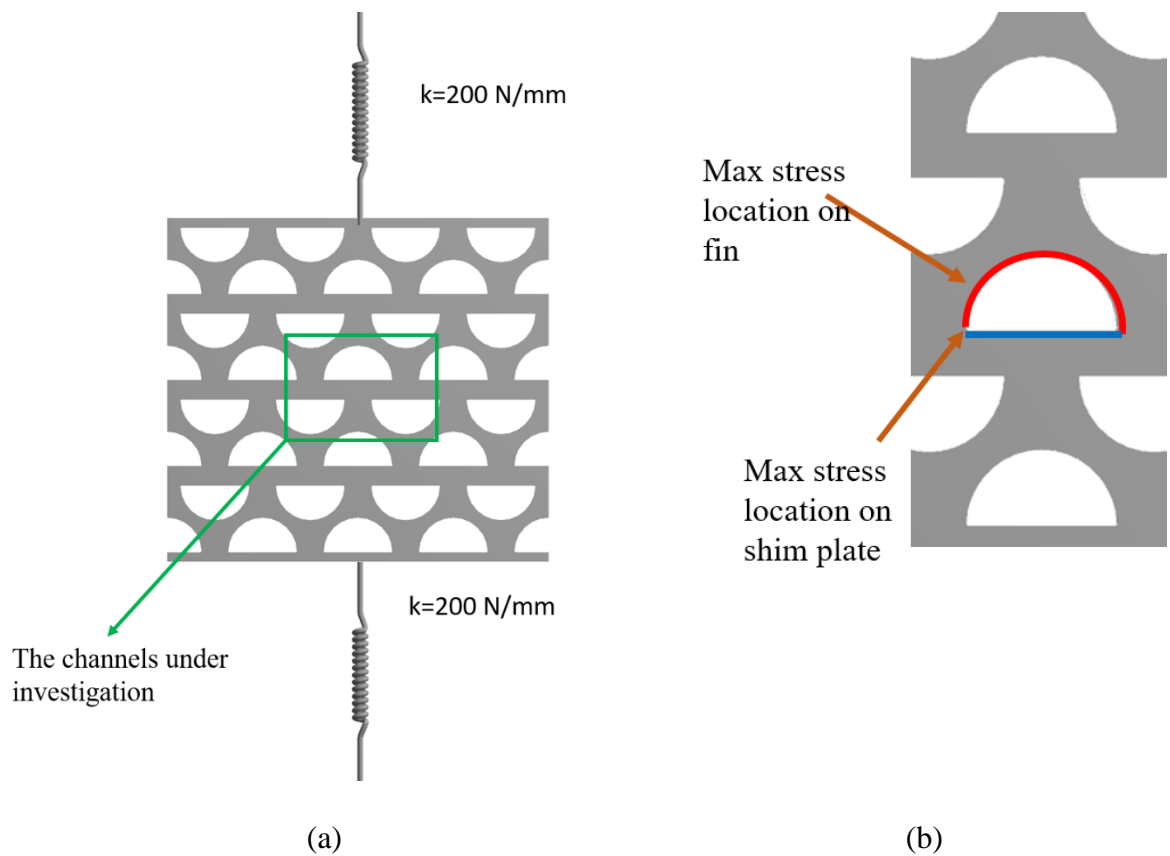


Figure 6. 8. (a) Staggered double-etched geometry used in stress calculation, (b) Locations of the maximum stress

Table 6. 4 lists temperature-dependent physical and mechanical properties of Alloy 617 used in the analysis. The maximum allowable stress for the construction material used for heat

exchanger plates, sheets and strips, and variation of the Yield stress for Alloy 617 for a range of temperature are presented in Figure 6. 9a-b [79, 80]. According to the ASME standard recommendation for the safety factor based on the Yield stress, a safety factor of 1.5 was applied to the maximum allowable stress presented in Figure 6. 9a. Based on the information presented in reference [68], the Yield stress in the 400-600 °C range is 225 MPa for Alloy 617, thus the maximum allowable stress presented in Figure 6. 9a includes a safety factor of 1.5 based on Yield stress ($225\text{MPa}/150\text{MPa} = 1.5$).

Table 6. 4. Physical and mechanical properties of Alloy 617

Temperature (C)	Thermal conductivity (W/m.C)	Coefficient of thermal expansion (1/C)	Poisson's ratio	Elasticity module (Pa)	Density (kg/m ³)
20	13.4	-	0.3	2.11E+11	8360
100	14.7	1.16×10^{-5}	0.3	2.06E+11	8360
200	16.3	1.26×10^{-5}	0.3	2.01E+11	8360
300	17.7	1.31×10^{-5}	0.3	1.94E+11	8360
400	19.3	1.36×10^{-5}	0.3	1.88E+11	8360
500	21	1.39×10^{-5}	0.3	1.81E+11	8360

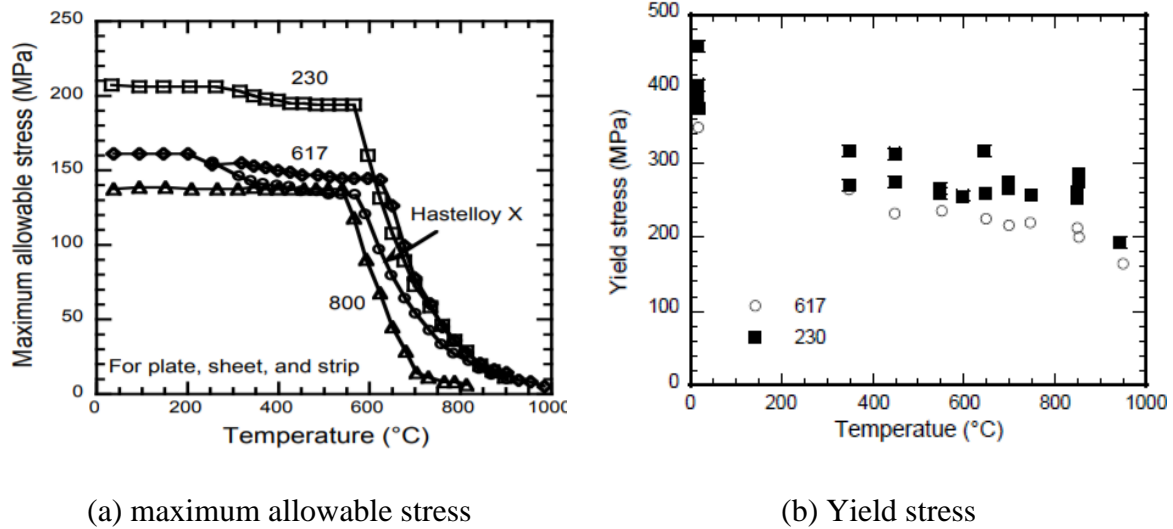


Figure 6. 9. (a) the maximum allowable stress for different high temperature materials [79], mechanical properties of as-received Alloys 617 from the French VHTR program (b) Yield Stress vs. Temperature [80]

6.6.2 Mesh independence study for stress calculation

Figure 6. 10 illustrates mesh configuration used in the stress calculations. A mesh sensitivity study was performed to determine the effect of grid size and number of grid elements on the calculated stress values. Quadratic meshing elements were used within the channel walls and the shim plate. The minimum channel fin thickness and shim plate thickness of 0.15 mm and 0.05 mm were used in the mesh independence study since the desired grid size needs to be generated in the channel fin and shim plate. If the grid size were larger than the channel fin thickness, only one grid element would be generated in the fin. To increase stress resolution, a grid refinement was applied to the channel walls where the maximum stress values are expected to occur.

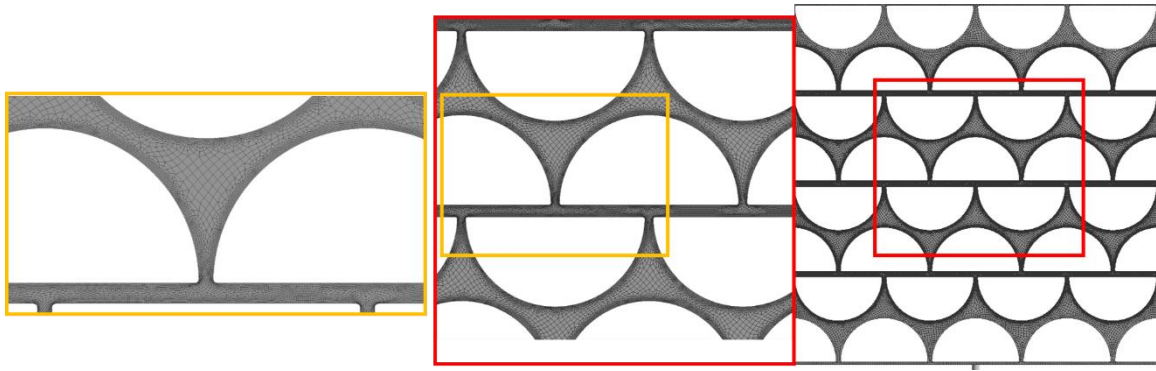


Figure 6. 10. Mesh illustration for stress calculations

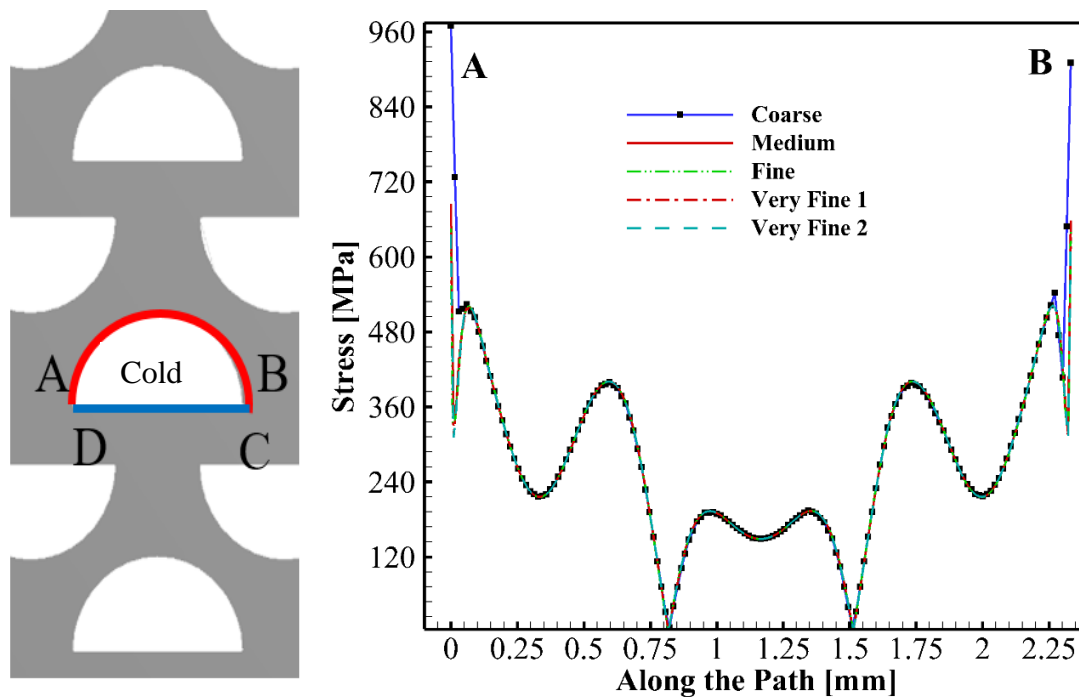


Figure 6. 11. The stress variation along the A-B path

Figure 6. 11 shows values of the von Mises stress predicted along the A-B path. As shown, the stress values reach maximum at channel corners due to stress concentration and are an order of magnitude higher compared to the average stress value. The results show that the grid size (finesness) does not have a significant effect on the stress values along the channel wall but affects stresses at the channel corners, with finer grid resulting in lower stresses, as expected. Table 6. 5 lists the grid size and number of grid elements used in the grid

independence study, where the grid size was varied from a coarse mesh to a very fine mesh. As the results show, the maximum stress values at Point B obtained with a very fine mesh 1 and very fine mesh 2 are the same. The very fine mesh 2 was selected for further stress calculations and optimization of the geometry.

Table 6. 5. The grid size and number of elements used in the grid independence study

Mesh	No. Element	Stress value at corner (MPa) at Point B
Coarse	55,250	910
Medium	104,800	657
Fine	111,380	658
Very Fine #1	143,450	629
Very Fine #2	160,655	629

6.6.3 Optimization of staggered double-etched geometry

In engineering problems, the objective of an optimization is to minimize total cost of the design and maximize its performance. Regarding the PCHE design and optimization, the total cost refers to the material cost, while performance refers to thermal and hydraulic performance of the PCHE. In this work, the non-dominated sorting genetic algorithm (NSGA-II) was used to obtain the optimum channel fin thickness and shim plate thickness. The objective function selected for the optimization requires stress values to be lower compared to the maximum allowable stress, while the design variables included channel fin thickness and shim plate thickness. No physical or correlation-based modeling was used in the optimization, instead the design engineering techniques were applied to develop the objective function and design space for the design variables. In the NSGA-II method, design points play important role in the design optimization, and are used to establish the objective function. In this method,

a mathematical function based on the stress values and design points was constructed and optimum geometries were determined based on the optimization criteria. Using Latin hypercube sampling, 10 design points are generated first in the Design of Experiment (DOE) module and then a mathematical function is generated to develop objective functions' values. The Response Surface Approximation (RSA) model then uses those 10 design points to develop a pool of surrogate design points which provide design space for the MOGA calculation. The MOGA calculation generates 2000 initial samples, 400 samples per iteration, and selects three best candidates in a maximum of 20 iterations. The optimization process includes many statistical and mathematical techniques in order to reduce numerical effort. In summary, the MOGA provides three best candidates meeting optimization criteria.

Table 6. 6 lists the three best candidates determined by the design optimization. The first candidate geometry has the minimum channel fin thickness of 0.2949 mm and shim plate thickness of 0.448 mm. The corresponding equivalent stresses occurring in the channel fin and shim plate are 158.35 and 153.2 MPa, respectively.

Table 6. 6. Three candidate geometries selected in the design optimization

	Candidate 1	Candidate 2	Candidate 3
Fin thickness (mm)	0.295	0.3188	0.3408
Shim plate thickness (mm)	0.448	0.454	0.479
Equivalent Stress - Fin Maximum (MPa)	158.35	140.77	147.91
Equivalent Stress - Shim Maximum (MPa)	153.20	142.88	159.68

For the first candidate geometry, the channel fin thickness was decreased from the initial value of 0.45156 to 0.295 mm. As presented in Table 6. 7, this reduction in fin thickness offers a relative size reduction of the PCHE of 34.67% compared to the staggered design. It should be noted that the staggered channel fin thickness was calculated by assuming cross-section area of solid wall in SDE geometry is identical to the BM.

Table 6. 7. PCHE improvement in optimization design

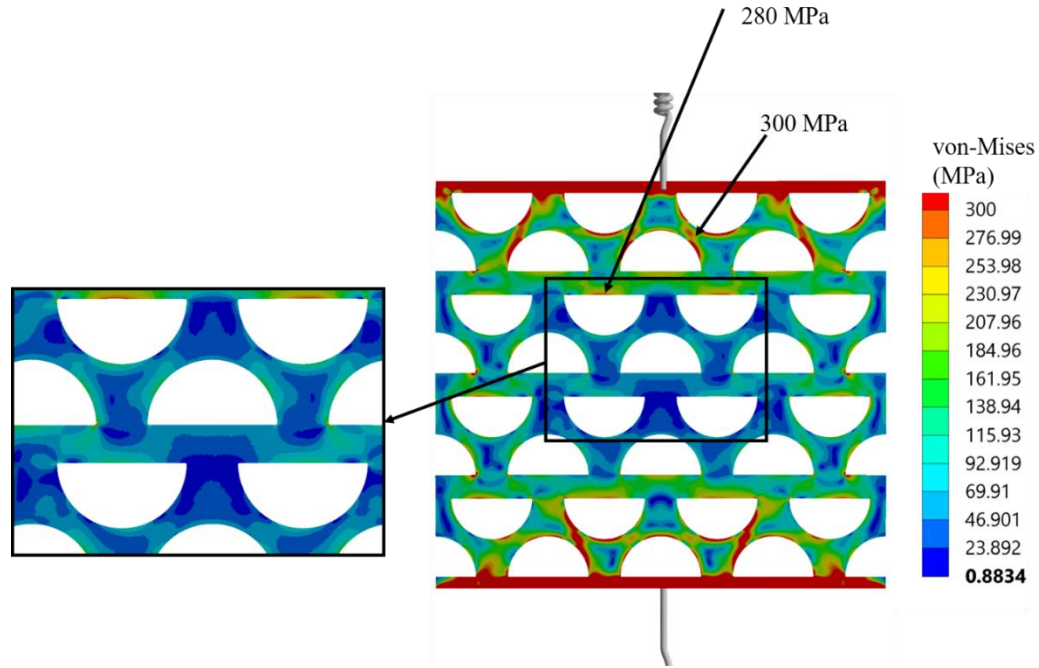
Parameter	Optimized staggered	Staggered	improvement
Channel diameter (mm)	1.51	1.51	-
Hydraulic diameter (mm)	0.922	0.922	-
Channel fin thickness (mm)	0.295	0.45156	-34.67%
Plate thickness (mm)	1.46	1.46	-
Channel length (mm)	765	765	-
Cross-section area of solid wall (mm ²)	2.21	5.8596	-62.28%
Shim plate thickness (mm)	0.448	1.46	-69.31%

For the optimized SDE geometry, a 34.67% reduction of the SDE channel fin thickness corresponds to the reduction of the area of the channel wall from 5.8596 to 2.21 mm². Von Mises stress contours for the optimized geometry (Candidate 1) obtained for the boundary conditions listed in Table 6. 1, are presented in Figure 6. 12a.

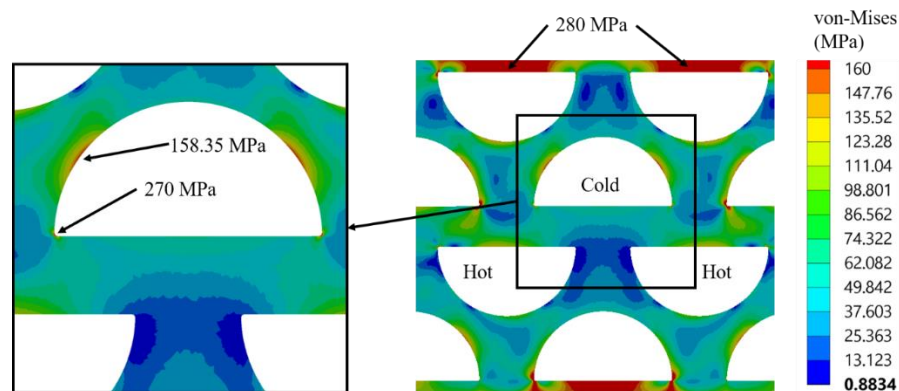
The maximum stress values of 300 MPa occur at the model boundaries where model is attached to the spring elements. The stress values decrease to 280 MPa and continue decreasing

as the distance from the spring-constrained boundary increases (y-direction) and the model is free to expand in the unconstrained horizontal direction. In summary, stress values in the proximity of the spring elements (constraints) are higher compared to the section of the PCHE core in the middle of the model which is less constrained and free to expand in the horizontal direction.

Details of the stress contours within the channel walls for the optimized SDE geometry are presented in Figure 6. 12b. The stress values in the cold channel walls are higher compared to hot channel wall due to the higher pressure of the working fluid in the cold channel compared to the hot channel. As discussed earlier, stress values at the channel corners are higher compared to the channel wall due to stress concentration at those locations. The results show that the maximum stress at the cold channel corner is 270 MPa, while the maximum stress in the channel fin is considerably lower, 158.35 MPa.



(a) Stress contour for the optimized geometry (full PCHE model)



(b) Details of stress contours

Figure 6. 12. Stress contours (a) full PCHE model, (b) details of stress contours for the optimized geometry (channel fin thickness=0.294 mm)

Stress distribution along the A-B and C-D paths for the optimized geometry (Candidate 1) is presented in Figure 6. 13. Due to high pressure in the cold channel (25.2 Ma) compared to the hot channel (8.612 MPa), the forces acting on the walls of the cold channel result in high

stresses at points marked by green crosses in Figure 6. 13. The maximum stress in the shim plate occurs at Points C and Point D located in the proximity of channel corners.

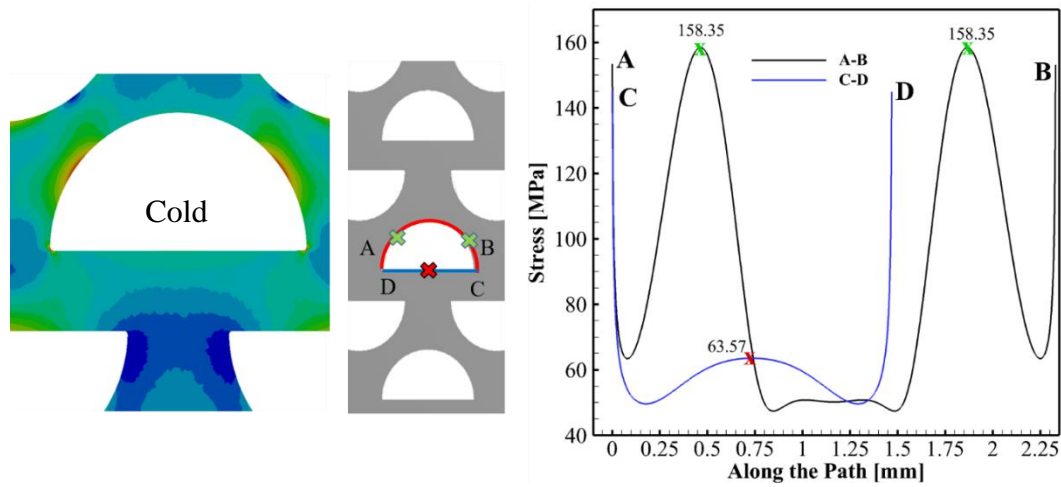


Figure 6. 13. Stress distribution along the A-B and C-D paths of the optimized geometry.

Figure 6. 14a-b shows stresses in the channel fin and shim plate over a range of channel fin and shim plate thicknesses. As the results presented in Figures 6.14 (a) and (b) show, stress in the channel fin is affected by the thickness of the shim plate, while stress in the shim plate is affected by the channel fin thickness. Thus, variation of fin thickness affects stresses in the fin and shim plate. Similarly, variation of shim thickness affects stresses in channel fin. Because of this inter-dependency, fin and shim thicknesses were selected as independent optimization parameters

Figure 6. 14a shows that for small values of shim plate thickness (very thin shim plate) stress values in the channel fin and shim plate are very high, with stresses in the shim plate being significantly higher compared to the channel fin. Based on the presented results we can conclude that for the maximum allowable stress of 150 MPa shim thickness of approximately 0.4 mm is the minimum practical thickness. Figure 6. 15b shows stresses in channel fin and shim plate as functions of channel fin thickness. The results show that for very thin fins (fin thickness less than 0.3 mm) stresses in the fin and shim plate increase rapidly as fin thickness

is decreased, with stress in the fin being significantly higher compared to the stress in the shim plate and increasing more rapidly. Based on these results and maximum allowable stress of 150 MPa, we can conclude that the minimum practical fin thickness is approximately 0.3 mm or slightly lower. As presented in Table 6. 6, the optimum channel fin thickness and shim plate thickness obtained by performing simultaneous optimization of two inter-related parameters are 0.295 mm and 0.488 mm, respectively, which is in a very good agreement with one-dimensional observational analysis of the results

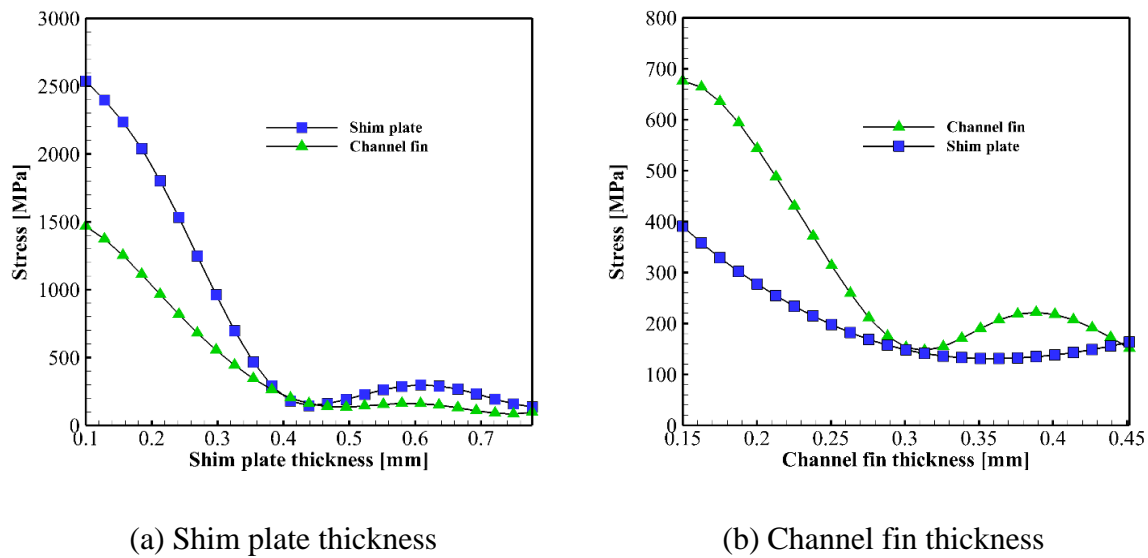


Figure 6. 14. Stresses in channel fin and shim plate over a range of (a) shim plate thickness, (b) channel fin thickness

The effect of fin thickness on stresses in the channel fin and the shim plate was investigated for a fixed shim plate thickness of 0.448 mm in a series of calculations where fin thickness was varied parametrically. Figure 6. 15 shows stresses in the channel fin and shim plate over a range of channel fin thickness. The results show that for the fin thickness of 0.29 mm (slightly thinner compared to the optimum fin thickness value of 0.295 mm) the stress in the fin is 160 MPa, while the stress in the shim plate is lower, 145.33 MPa. The results also

show that the stress in the channel fin decreases as the fin thickness increases, while the stress in the shim plate reaches minimum value of 70 MPa at the fin thickness of 0.33 mm. As discussed earlier, variation of channel fin thickness affects the stress distribution of shim plate. Thus, as the channel fin thickness decreases, stresses in both the shim plate and channel fin increases. The results presented in Figure 6. 15 show that, for the analyzed micro-channel geometry and topology and selected operating conditions, stress in the shim plate cannot be reduced below 70 MPa by increasing the channel fin thickness.

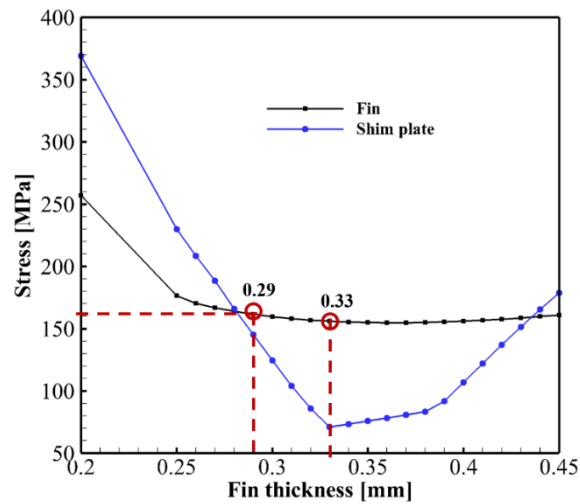


Figure 6. 15. Stresses in the channel fin and shim plate plotted over a range of channel fin thickness for shim plate thickness of 0.448

6.7 Thermal and hydraulic performance of the optimized staggered double-etched (SDE) geometry

Using the channel fin and shim plate thickness obtained in the design optimization for Candidate 1 geometry, a 3D model having the same length as the staggered double-etched geometry (Base model, BM) was developed for the 3D CFD simulation. The boundary conditions and operating pressure and temperatures were identical for both the BM and SDE geometries. Table 6. 1 lists boundary conditions used in the 3D CFD simulations. Thermal and hydraulic performance of a PCHE employing optimized SDE geometry and sCO₂ as the

working fluid in the hot and cold channels of a HTR recuperator operating in a sCO₂ Brayton cycle was obtained and analyzed. The conservation of momentum and energy equations for the 3D steady-state laminar incompressible fluid flow for Re=1000 on the cold side (the Reynolds number on the hot side was calculated in accordance with the mass flow rate on the cold side) and Laplace equation for the steady-state heat conduction in solid walls were solved numerically by the Fluent code. As stated earlier, Fluent was coupled to the NIST REFPROP 9.0 to obtain accurate fluid properties for sCO₂.

The values of peripherally-averaged Nusselt number Nu and friction coefficient C_f obtained in numerical analysis of the BM and optimized SDE geometries and sCO₂ as the working fluid on the hot and cold sides are listed in Table 6. 8.

Table 6. 8. Thermal and hydraulic performance of the Base model (BM) and optimized staggered double-etched (SDE) geometries

	Hot Side (sCO ₂)					Cold Side (sCO ₂)				
Configuration	C_f	Nu	Pressure drop [Pa]	T_{bulk} at outlet [K]	Q [W]	C_f	Nu	Pressure drop [Pa]	T_{bulk} at outlet [K]	Q [W]
BM	0.007	4.03	309	483.65	6.22	0.0086	4.12	122	624.72	6.40
Optimized SDE	0.007	4.26	309	483.55	6.24	0.0086	4.37	122	625.7	6.44
Difference%	0.00	5.71	0.00	0.02	0.32	0.00	6.07	0.00	0.16	0.62

Thermal and hydraulic performance of the BM and optimized SDE models are virtually identical since the flow regime, hydraulic diameter and channel length are identical. Also, the bulk fluid and channel wall temperatures at any location in the fully-developed flow region are identical for both models, resulting in identical thermo-physical properties of sCO₂ for both geometries.

The heat transfer rate Q for both geometries is virtually the same since the mass flow rate and hydraulic diameters are identical for both geometries. The Nusselt number in the

optimized SDE geometry is approximately 6 percent higher compared to the Base model. Since the flow regime is laminar, and the channel diameter is fixed, the increase in Nu number is due to the increase in wall heat flux. As discussed earlier, the increase in wall heat flux is caused by lower thermal resistance to heat conduction due to thinner channel fin and shim plate.

Figure 6. 16 shows the variation of wall heat flux along the length of cold and hot channels for both geometries. The results show that the increase in the Nu number value is similar for the hot and cold channels. The Nu number values for the hot and cold channels are 4.03 and 4.12 for the BM and 4.26 and 4.37 for the optimized SDE model.

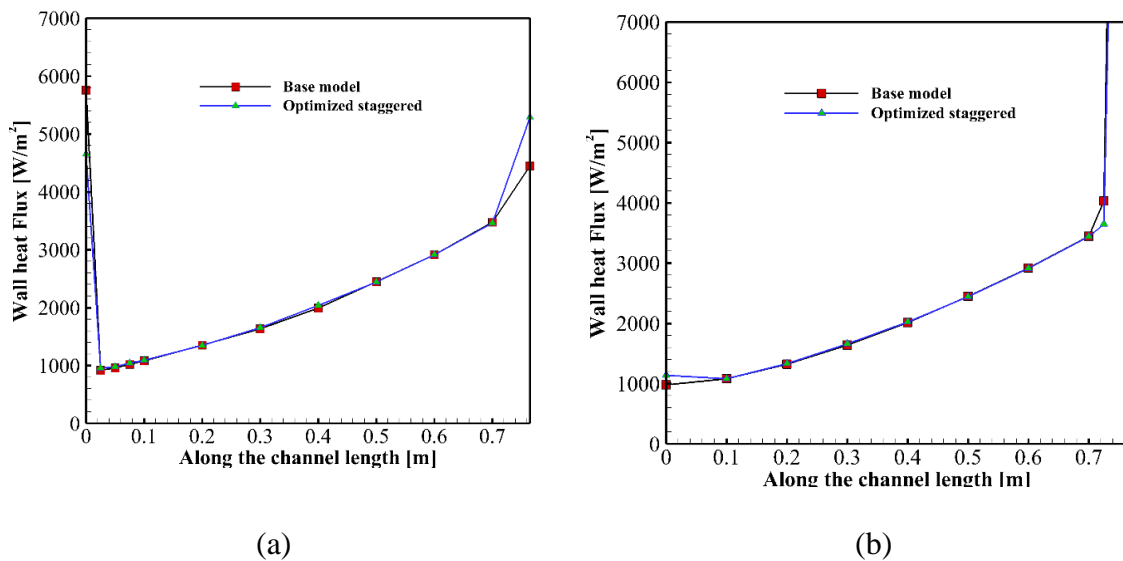


Figure 6. 16. The wall heat flux (a) cold side, (b) hot side, for both geometries

Figure 6. 17 shows variation of the bulk temperature along the length of the cold and hot channels for both geometries. The results show that the difference between bulk fluid temperatures in the hot and cold channels, referred to as a pitch temperature difference, or pitch, in the figure is not constant and varies (increases) along the channel length. As discussed before, the increase in the heat transfer performance of the optimized PCHE channel geometry

and topology is due to the increase in overall heat transfer coefficient U . Details concerning calculation of U and obtained values are presented in Section 6.8 below.

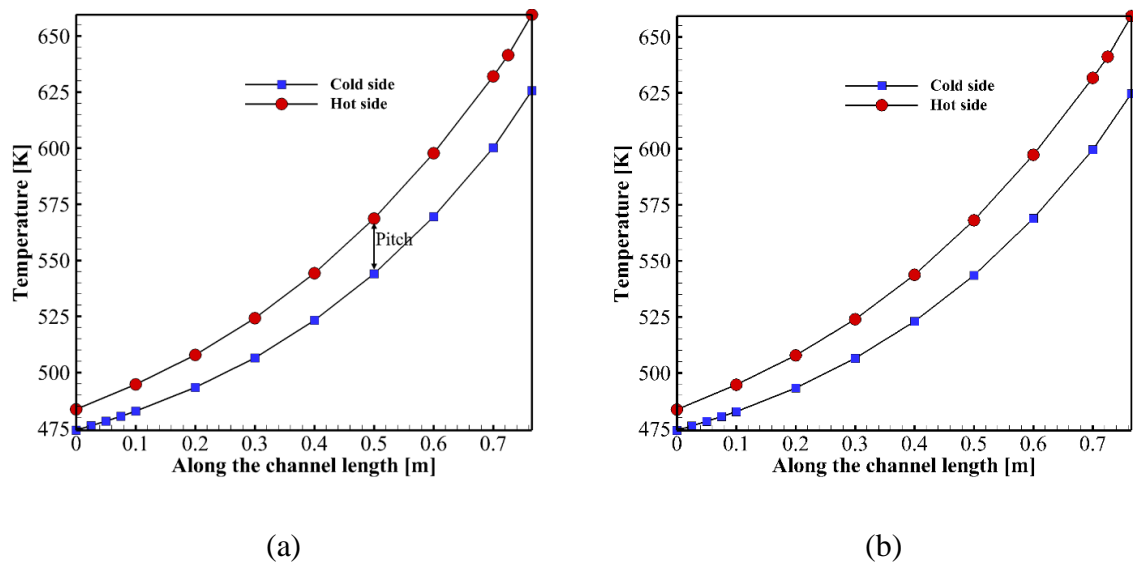


Figure 6. 17. Variation of bulk temperature along the channel for (a) Optimized geometry, (b) Base model

6.8 Overall heat transfer coefficient (U)

The overall heat transfer coefficient U was calculated by the two methods: LMTD and Integration method to compare the results and select the accurate approach for calculating dimensionless size of the heat exchanger by the e-NTU method to be used for comparison of performance of the BM and optimized SDE geometries.

6.8.1 LMTD method

The log-mean temperature difference (LMTD) method is a popular approach for the heat exchanger thermal design. The LMTD formulation can be found in Chapter 1, Equations (1.1) - (1.3). Using Equation (1.1) and LMTD method, the overall heat transfer coefficient U can be obtained. Table 6. 9 lists the overall heat transfer coefficient U for the Base Model and optimized staggered geometry obtained using the LMTD method. The bulk temperature at hot and cold inlet and outlet can be found in Figure 6. 17.

Table 6. 9. The overall heat transfer coefficient U by LMTD method

	Q_{avg} [W]	$T_{hi}-T_{co}$ [K]	$T_{ho}-T_{ci}$ [K]	ΔT_{LMTD} [K]	UA_{LMTD} [W/K]	U [W/m ² K]	NTU
Base model (BM)	6.313	35.83	9.65	19.95	0.316	106.52	8.92
Optimized SDE	6.34	34.85	9.55	19.54	0.324	109.23	9.15

The results presented in Table 6. 9 show that the value of the overall heat transfer coefficient U for the optimized SDE geometry (109.23 W/m²K) is higher compared to the Base model (106.52 W/m²K), which is in agreement with the results and explanation given in Section 6.7. Since the heat capacity rate C and heat transfer area A_s used in Equation (1.6) are identical for both geometries, but the value of U is higher for the optimized SDE geometry, the value of NTU for the optimized SDE geometry is higher compared to the BM.

The LMTD method is, however, subject to errors since variation of thermo-physical properties with temperature is neglected in the analysis. As shown in Figure 6. 17, variation of the bulk fluid temperatures in the hot and cold channels with channel length is not linear and so is the difference between the two. Therefore, neglecting dependence of thermo-physical properties on temperature, or using the average bulk fluid temperature would result in errors in the calculated values of U and NTU. As reported in the literature [81], the LMTD method is not the suitable method for performance analysis of heat exchangers operating with large temperature variations. According to Utamura et al. [81], the integration approach should be used instead of LMDT for heat exchangers (including PCHE) subject to large temperature differences.

6.8.2 Integration method

In the Integration method, the local heat transfer coefficient is calculated using average cross-sectional physical properties determined at several locations along the channel length

and then an integration of these local heat transfer coefficient values is performed along the channel length in the direction of the flow. The overall heat transfer coefficient is calculated by:

$$\bar{U} = \frac{1}{A_0} \int_0^{Q_0} U_A dA \quad (6.5)$$

Where Q_0 is the total heat transfer, A_0 is total heat transfer area. The heat flux and NTU are then calculated by using Equations (6.3) and (6.4).

$$dU_A = \frac{dQ}{dA(T_w - T_b)} \quad (6.6)$$

$$dq'' = \frac{dQ}{dA} \quad (6.7)$$

$$NTU = \frac{\bar{U}A}{C_{\min}} \quad (6.8)$$

Where U_A is the local overall heat transfer at any section, while T_w and T_b are peripherally-averaged wall and bulk temperatures at any section. The fully developed flow region (0.1-0.7 m) was used in this analysis. Table 6. 10 lists the overall heat transfer coefficient obtained using the Integration method. The overall heat transfer coefficient calculated using the LMTD method is approximately 11 percent higher (see Table 6. 9) compared to the Integration method because the effect of variation of thermo-physical properties of sCO_2 with temperature and pressure was included in the Integration method.

Table 6. 10. Overall heat transfer coefficient obtained by using the Integration method

	$h_{ave} \text{ Hot}$ [W/m ² K]	$h_{avg} \text{ Cold}$ [W/m ² K]	UA [W/K]	U [W/m ² K]
BM	174.85	220.3	0.2892	97.29
Optimized SDE	176.15	221.89	0.291	98.11

Variations of the wall heat flux and overall heat transfer coefficient obtained using the Integration method are presented in Figure 6. 18 as functions of the channel length.

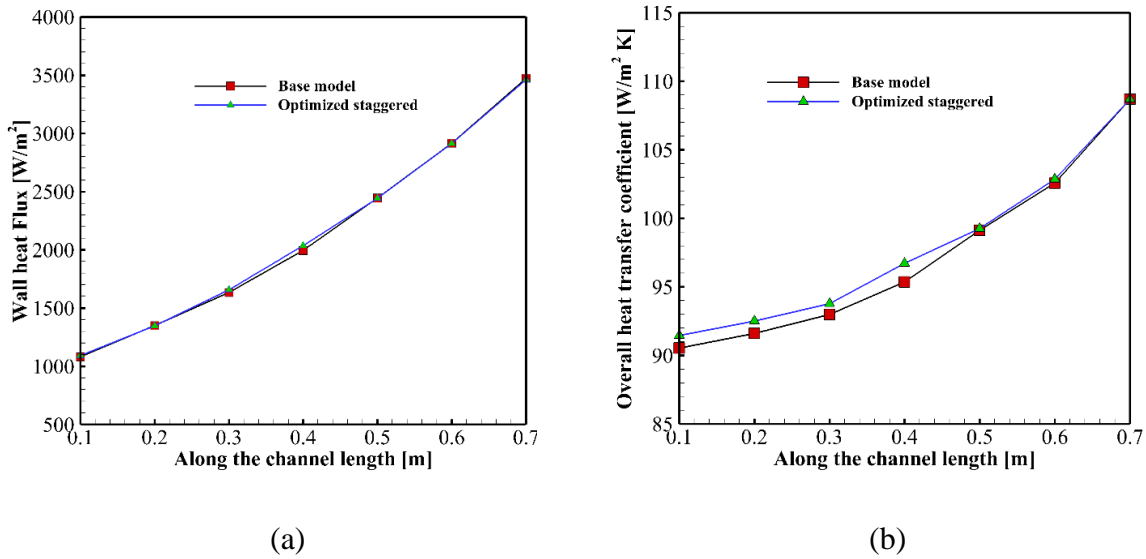


Figure 6. 18. The variation of (a) the wall heat flux cold side, (b) overall heat transfer coefficient

6.8.3 Effectiveness-NTU (ϵ -NTU) method

As discussed in Chapter 1, the ϵ -NTU method is a well-known approach for calculating the heat exchanger thermal duty and other performance parameters at steady-state operating conditions. Equations (1.6) - (1.8) were used to calculate the ϵ and NTU for the analyzed heat exchanger. Thermal and hydraulic performance of the optimized staggered double-etched PCHE designed used for the HTR application were determined using the ϵ -NTU method. The overall heat transfer coefficient was calculated using Equation (1.4), while values of NTU and ϵ were obtained using Equations (1.6) and (1.8), where U was calculated using the Integration method.

C_{\min} and U are critical parameters for determining thermal duty Q of a heat exchanger and dimensionless heat transfer size of a heat exchanger NTU. For the fixed heat transfer area

A_s of a heat exchanger, the minimum thermal capacity rate C_{\min} and U determine thermal duty of the heat exchanger. The minimum thermal capacity rate may C_{\min} be increased by either increasing the mass flow rate or specific heat of the working fluid. Since the increase in mass flow rate causes increase in pressure drop, thermo-physical properties of the working fluid play an important role.

As discussed earlier, $s\text{CO}_2$ is a promising working fluid that can be used to increase efficiency of a power cycle. Since the value of specific heat increases significantly in the proximity of the critical point and along the pseudo-critical line, thermal capacity rate can be increased using $s\text{CO}_2$ in this region. Also, as previously discussed, a decrease of the micro-channel fin thickness in a PCHE will increase the overall heat transfer coefficient, resulting in an increase in thermal duty of the heat exchanger. Table 6. 11 lists the values of NTU and effectiveness calculated for the optimized SDE micro-channel geometry. The results show that the values of effectiveness and NTU are higher for the optimized SDE geometry compared to the BM geometry. For the laminar flow regime and fixed hydraulic diameter, the results show that the fin thickness does not have a significant effect on the overall heat transfer performance. However, for the temperatures, pressures and Reynolds number used in this study, the NTU value obtained for the optimized SDE geometry is higher compared to the Base model.

Table 6. 11. The NTU and effectiveness calculated for the optimized staggered double-etched (SDE) and Base model (BM)

	C_{\min} [W/K]	$h_{\text{avg Hot}}$ [W/m ² K]	$h_{\text{avg Cold}}$ [W/m ² K]	UA [W/K]	U [W/m ² K]	Effectiveness	NTU
BM	0.03546	174.85	220.30	0.2892	97.29	0.9482	8.15
Optimized SDE	0.03546	176.15	221.89	0.291	98.11	0.9488	8.20

The effectiveness of the BM and optimized SDE geometries are nearly identical since the mass flow rate, bulk temperature, and working fluids are the same.

6.8.4 Summary

The results of the optimization of the geometry and topology of the analyzed PCHE are summarized in Table 6. 11 and Table 6. 12. As the results presented in Table 6. 11 show, optimized SDE geometry results in a small improvement in parameters such as overall heat transfer coefficient U , and heat exchanger effectiveness e and number of heat transfer units NTU , showing that the optimized geometry does not have a significant effect on heat transfer. However, as presented in Table 6. 12 and Table 6. 13, the optimized SDE geometry has a very significant effect on the PCHE size and cost, and compactness.

The optimized SDE geometry reduces the total weight of the heat exchanger by 62.5% (Table 6. 12). The volumetric heat transfer rate (Q/V) increased by the approximately the same amount (62.3%) as shown in Table 6. 13. Both of these parameters play a very important role in determining the PCHE cost. Since PCHEs are manufactured from expensive super alloys and stainless steels [73], the cost of the optimized SDE PCHE is significantly lower compared to the conventional PCHE. As reported by Kim (2009) [70], the weight of the PCHE unit employing 1280 by 1280 hot and cold channels is 48 kg. In comparison, the weight of the PCHE employing optimized SDE geometry would be 18 kg, i.e., 30 kg less due to 62.5% reduction of the PCHE volume. Dimensions and weights of the conventional and optimized SDE geometries are compared in Table 6. 12. The relative difference with respect to the BM design was calculated using $\frac{\Phi - \Phi_{ref}}{\Phi_{ref}} \times 100$ where Φ is any parameter of interest.

Table 6. 12. PCHE unit weight and dimensions for BM and optimized SDE geometries

	Unit width (mm)	Unit height (mm)	Unit length (mm)	Unit cross-section area of solid wall (m ²)	No. plates in Unit	Unit Volume (m ³)	Unit weight (kg)
BM	104.8	93.44	765	7.50×10^{-3}	64	5.74×10^{-3}	48
Optimized SDE	84.224	60.8	765	2.83×10^{-3}	32	2.16×10^{-3}	18
Diff. %	-19.63	-34.93	-	-62.28	-50	-62.28	-62.5

The front view of the BM and optimized SDE geometries is presented in Figure 6. 19. The figure shows that the number plates including the shim plates has decreased by 50 percent for the same heat transfer area A_s . Expressed differently, opacity of the SDE geometry is significantly higher compared to the BM design. Opacity is defined as the ratio of the cross sectional area available for flow to the overall frontal area of the heat exchanger. Higher opacity is preferred since it indicates better utilization of the material of construction.

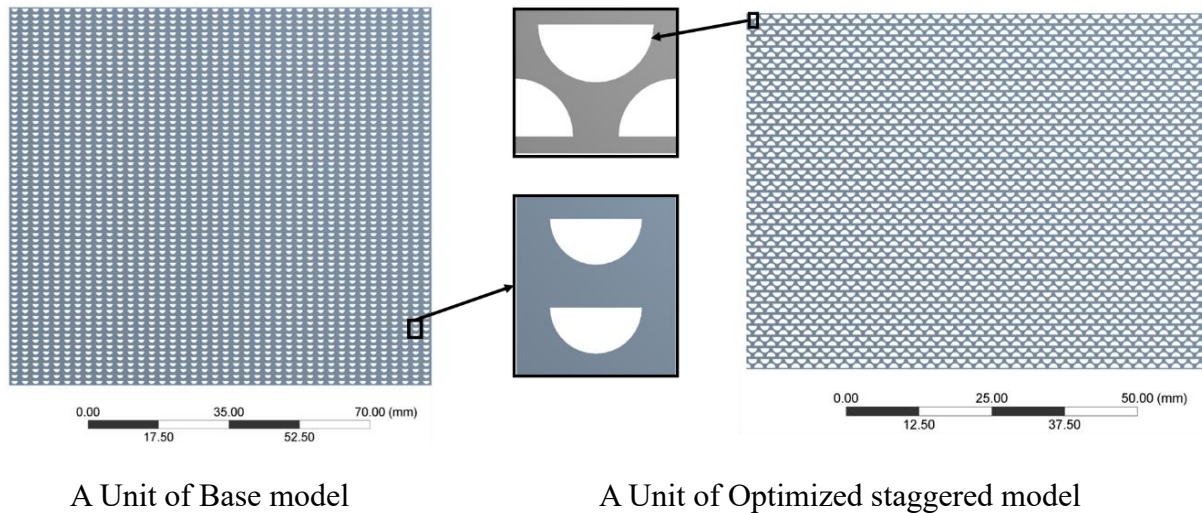


Figure 6. 19. An illustration of both Base model and the optimized staggered geometries

Table 6. 13 compares values of the total (Q) and volumetric heat transfer rate Q/V , heat transfer area A , heat exchanger volume V and heat exchanger compactness A/V for the BM and the optimized SDE geometry. Since, as discussed earlier, optimization of the geometry has a very small effect on heat transfer, the total heat transfer Q is virtually the same for both geometries since the total heat transfer area, mass flow rate, flow regime, and hydraulic diameters are the same. However, due to the significantly smaller (62.5%) volume of the optimized geometry, the volumetric heat transfer rate Q/V was also reduced by 62.5%, resulting in the volumetric heat transfer enhancement of 2.65. The volume enhancement is defined as the ratio of the BM volume to the optimized SDE volume, meaning the BM volume is 2.65 larger compared to the optimized SDE geometry volume. As a result, the compactness A/V of the optimized design is significantly higher compared to the BM, allowing for a 165% higher heat transfer per unit volume. Expressed differently, for the same heat exchanger volume (mass of metal used for the construction), the optimized geometry can transfer 2.65 times more heat compared to the BM geometry. In summary, the optimized SDE topology is significantly smaller in size, lighter, more economical to manufacture, and has higher thermal duty compared to the BM geometry.

Table 6. 13. Heat transfer per volume and the heat exchanger compactness for Base model (BM) and optimized staggered double-etched (SDE) geometries

	A (m ²), cross- section area of solid wall for a pair of H _{ot/cold} Cell	Q (W), Heat for a pair of Hot/ cold Cell	V (m ³), Volu me Hot/C old unit	Q/V (W/m ³)	A (m ²) /V (m ³) reducti on %	Volume enhance ment (V _{base} /V _{op timized})	Heat enhance ment for constant volume %	Compact ness (A/V) (m ² /m ³)
BM	5.86×10 ⁻⁶	6.22	5.74× 10 ⁻³	1.40×10 ⁶	62.28	2.65	165	1,325
Optimi zed SDE	2.21×10 ⁻⁶	6.23	2.16× 10 ⁻³	3.71×10 ⁶				3,514

CHAPTER 7: ADVANCED MICRO-CHANNEL GEOMETRY AND TOPOLOGY- STAGGERED DOUBLE-BANKING CIRCULAR GEOMETRY

7.1 Overview

An advanced circular staggered double-etched PCHE geometry to be used for IHX in a sCO₂ Brayton cycle coupled to a SFR was designed and optimized using ANSYS software. The analysis and the results are presented in this section. The advanced circular double-etched PCHE geometry provides enhanced heat transfer performance, reduced weight and larger specific heat transfer area compared to the conventional semi-circular PCHE geometries. For the IHX application, sCO₂ and liquid sodium are used as working fluids. The operating conditions used in the analysis are representative of an IHX for a 650 MW Brayton cycle with recompression previously described in Chapter 6.

A multi-objective optimization algorithm employing NSGA-II and Response Surface Approximation (RSA) as a surrogate model was used for the design and optimization of the advanced PCHE geometry. Similar to the semi-circular staggered double-etched (SDE) geometry and topology described in Chapter 6, the channel fin thickness and pitch were the parameters used in optimization. Alloys 617 and 230 were used as materials of construction. Temperature-dependent thermo-physical properties were used for the CFD and stress analyses. Heat transfer performance and details of the fluid flow and heat transfer of the optimized PCHE were analyzed. The results of 3D CFD simulations obtained for the optimized topology and the Base model (BM) were compared. The effectiveness-NTU method was used to investigate the effect of studied parameters on thermal performance of the PCHE.

7.2 System description, operating pressure and temperature

The schematic of a sCO₂ recompression Brayton cycle with recuperation coupled to an SFR is shown in Figure 7. 1. IHX is used to transfer heat from the primary loop to the power

cycle using liquid sodium as a hot working fluid in the primary loop and sCO₂ as a cold working fluid in the power cycle (sCO₂ Brayton cycle). The turbine inlet temperature (TIT) of 515 °C and pressure (TIP) of 25 MPa in the sCO₂ Brayton cycle generate 650 MW net power with the net efficiency of 42-43% [8].

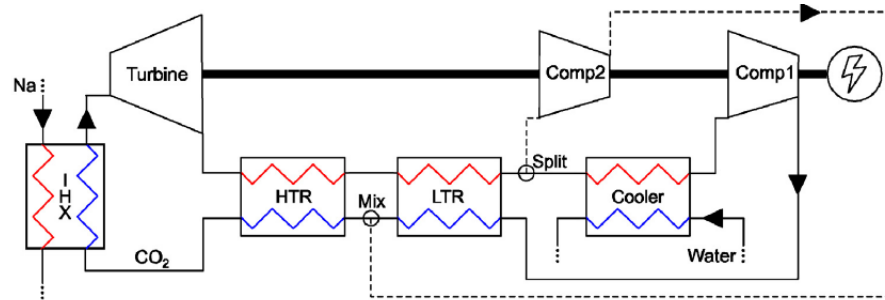
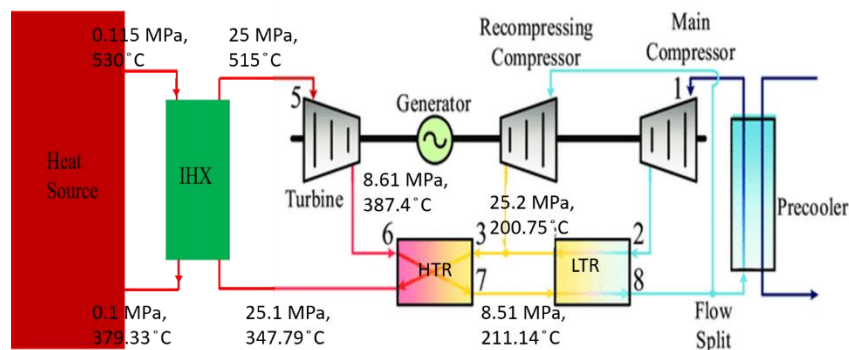


Figure 7. 1. The sCO₂ recompression Brayton cycle arrangement [8]

As described in Chapter 6, Floyd et al. [8] optimized a sCO₂ Brayton cycle based on the ASTRID N2 specification. Figure 7. 2 illustrates the optimized sCO₂ Brayton cycle designed and optimized by Floyd et al. [8] including the primary liquid Na loop coupled to a recompression sCO₂ Brayton cycle via IHX.



analysis are presented in Figure 7. 3. The pressure in the hot channel (liquid sodium) is very low, 0.115 MPa, since vapor pressure of liquid metals is very low. Since operating pressure in a cold channel, where supercritical conditions for CO₂ are maintained pressure difference between the hot and cold channels is high. As presented later in this chapter, this high pressure difference causes high mechanical stresses in PCHE walls.

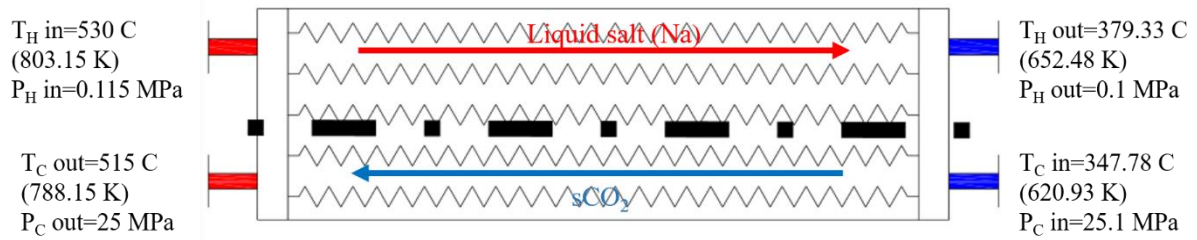
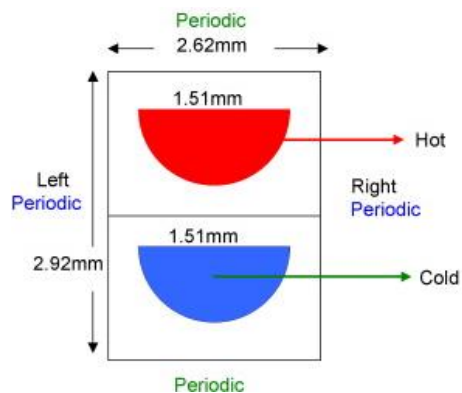


Figure 7. 3. The operating temperature and pressure determined by Floyd et al.[8] for HTR

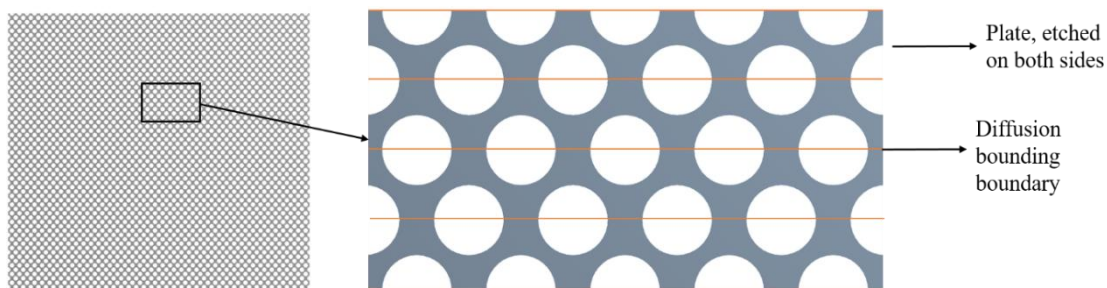
PCHEs are advanced heat exchangers and are considered for the IHX application in a sCO₂ Brayton cycle coupled to an SFR or CSP plant. Floyd et al. [8] optimized a sCO₂ Brayton cycle based on ASTRID N2 specifications and considered PCHE for high temperature heat exchanger application. The PCHE geometry used by Floyd [8] employed zigzag microchannels with semi-circular cross-section. The micro-channel semi-circular geometry presented in Figure 7. 4a, was considered as the BM geometry in this work. The PCHE channel diameter, channel width, and plate thickness were chosen from In Hun Kim (2012) and (2009) [70, 71]. The detailed information concerning the BM geometry, model schematic, details of the CFD analysis, and validation of the numerical model are described in Chapter 4.

Since the length of the IHX micro-channels used in the BM is unknown, the LMTD method was used in this study to estimate it. The circular staggered double-etched (SDE) geometry presented in Figure 7. 4b was developed and optimized as described in this section. The plates are etched on both sides to form semi-circular channels and stacked to create circular channel geometry of the PCHE core using a diffusion bounding process. The cross-section area

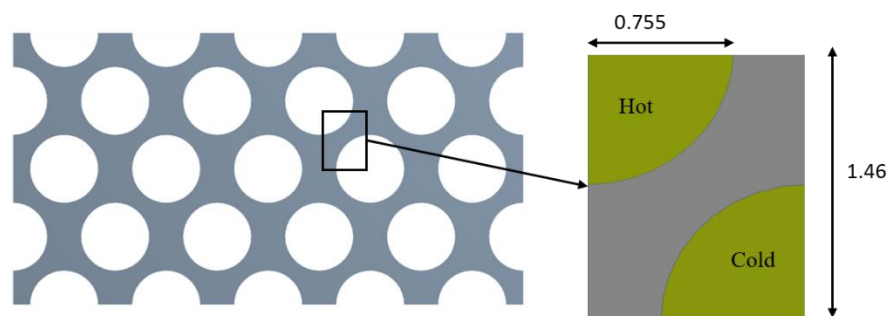
of solid wall in the circular SDE geometry was assumed to be identical to the BM geometry. Dimensions of the micro-channel and surrounding walls for both geometries are listed in Table 4.1 and are also presented in Figure 7. 4a, c.



(a) Base model (BM)



(b) Circular staggered double-etched (SDE) model



(c) A section of the circular SDE micro-channel geometry

Figure 7. 4. The Base and circular staggered double-etched geometry

7.3 Thermal and hydraulic performance of studied PCHEs

Thermal and hydraulic performance of the conventional PCHE (Base model, BM) and circular SDE micro-channel geometries was determined. As discussed earlier, sCO_2 and liquid sodium were employed as the hot and cold working fluids for the IHX application. The operating pressures and temperatures are listed in

Table 7. 1. Thermo-physical properties of liquid sodium (hot fluid) were considered as temperature-dependent. The specific heat of liquid sodium of $1,380 \text{ J/kg.K}$ was used, while other thermo-physical physical properties were calculated using Equations (2.5)-(2.7).

Fluent was coupled to the NIST REFPROP 9.0 to obtain accurate fluid properties for the sCO_2 . 3D CFD simulations were performed to obtain thermal and hydraulic performance of the analyzed PCHE. Boundary conditions used for the BM are listed in

Table 7. 1. The details of the BM geometry are presented in Section 6.3 of Chapter 6. The conservation of momentum and energy equations for the 3D steady-state laminar incompressible fluid flow with $\text{Re}=1000$ on the sCO_2 (cold) side and Laplace equation for the steady-state heat conduction in solid walls were solved numerically by the Fluent code.

As mentioned earlier, the cross-section area of solid wall, channel diameter and plate thickness of the circular SDE geometry were assumed to be the same as for the BM. However, for the same heat transfer rate, channel lengths associated with the BM and the circular SDE geometries are different since thermal and hydraulic performance of micro-channels based on these geometries is different. To enable a comparison, it was assumed that the outlet hot and cold temperatures are identical in both geometries.

Since hydraulic diameter of the circular SDE geometry is larger compared to that of the BM geometry, the two scenarios were considered in thermal analysis of the circular SDE geometry to account for this difference.

1. **1st Scenario.** Re number for the Base Model and circular SDE geometry is assumed to be the same. This assumption was applied to the hot and cold sides (channels). For this scenario and the analyzed PCHE geometry and operating conditions, the inlet Reynolds number on the hot side (liquid sodium) is 146, while the inlet Reynolds number on the cold (sCO₂) side is 1,000. Under this scenario, velocity u of the hot and cold working fluids is lower for the circular SDE geometry compared to the BM since hydraulic diameter D_h of the circular SDE geometry is larger compared to the BM geometry ($u = Re\mu/D_h$). The mass flow rate for the circular SDE geometry is higher compared to the BM geometry since the mass flow m is proportional to the flow area ($m = Re\pi D_h \mu/4$). For the analyzed PCHE geometry and operating conditions, the mass flow rate of the hot fluid (liquid sodium) through a single hot micro-channel is 3.928×10^{-5} kg/s, while the mass flow rate of the cold fluid (sCO₂) through a single cold micro-channel is 3.908×10^{-5} kg/s.
2. **2nd Scenario.** Velocity of the hot and cold working fluids in the BM and circular SDE geometries is assumed to be the same. For this scenario, the mass flow rate and Reynolds number for the circular SDE geometry is higher compared to the BM geometry, since both parameters are proportional to the hydraulic diameter of the micro-channel. For the analyzed PCHE geometry and operating conditions, the mass flow rate of the hot fluid (liquid sodium) through a single hot micro-channel is 6.43×10^{-5} kg/s, while the mass flow rate of the cold fluid (sCO₂) through a single cold micro-

channel is 6.4×10^{-5} kg/s. The hot side and cold side Reynolds numbers corresponding to these flows are 254 and 1,630, respectively.

Since the 1st and 2nd Scenarios result in different operating conditions, the analysis of hydraulic and thermal performance of a PCHE was performed for both scenarios to determine difference in performance.

7.3.1 Boundary conditions for the BM and circular SDE geometries for the 1st scenario

Boundary conditions for the Base model and circular SDE geometry and calculation procedure for determining unknown length of the micro-channels in the IHX analyzed in this work are presented in this section. The channel length was determined by using the LMDT method and also by performing 3D CFD simulation of the channel performance.

Table 7. 1 lists boundary conditions for the Base model. The velocity magnitudes at the hot and cold inlets were calculated using Re number values of 1,000 and 146 at the cold and hot sides, respectively. Thermo-physical properties of sCO₂ at the cold channel inlet were obtained from the NIST REFPROP database at 25.1 MPa and inlet temperature of 620.93 K. The mass flow rate (Re number) at the hot inlet was calculated by using conservation of energy and thermo-physical properties of liquid sodium at the hot inlet temperature of 803.15 K. Since, as discussed earlier, length of the IHX channels in the Base model is unknown, the LMTD method, Equation (1.1) was used assuming temperature-independent properties of working fluids. The channel length was also determined by using a 3D CFD simulation with temperature-dependent properties of both sCO₂ and liquid sodium. The inlet and outlet temperatures of the cold and hot working fluids used in the IHX design are presented in Figure 7. 3. Table 7. 2 The average convection heat transfer coefficients on the hot and cold sides, temperature difference ΔT between the hot and cold inlet and outlet, average overall heat

transfer coefficient U and heat transfer value Q determined by the LMDT method for the Base model are listed in Table 7. 2.

Table 7. 1. Boundary conditions for the Base model

Boundary	Base model	Hot side	Cold side
Inlet	Velocity (m/s)	0.0434	0.16912
	Temperature (K)	803.15	620.93
Outlet	Pressure outlet (MPa)	0.115	25.1
Top/Bottom wall	Periodic	-	-
Right/left walls	Adiabatic/symmetry	-	-
Front/Back walls	Adiabatic	-	-

Table 7. 2. Details of channel length calculations for the BM (LMDT method, hot and cold fluids)

Base model	$h_{\text{avg hot}}$ (W/m ² K)	$h_{\text{avg cold}}$ (W/m ² K)	$C_{p\text{cold}}$ (J/kgK)	$Q(W)$	ΔT_{hot} (K)	ΔT_{cold} (K)	ΔT_{LMTD}	$U(W/m^2 \cdot K)$	$L(m)$
	235,600	217.63	1250	6.68	15	31.0 7	22.06	217.42	0.36

Table 7. 3 lists boundary conditions for the circular SDE geometry. Since symmetry applies on the top and bottom walls, as presented in Figure 7. 4c, one quarter of the model was used for 3D CFD simulations. The details of the mesh independence study, grid size, CFD validation, and CFD simulation setting can be found in Section 4.4 of Chapter 4.

Table 7. 3. Boundary conditions for the circular staggered double-etched model, 1st scenario

Boundary	Circular staggered model	Hot side	Cold side
Inlet	Velocity (m/s)	0.0265	0.103
	Temperature (K)	803.15	620.93
Outlet	Pressure outlet (MPa)	0.115	25.1
Top/bottom wall	Symmetry	-	-
Side walls	Adiabatic/symmetry	-	-
Front/Back walls	Adiabatic	-	-

For the circular SDE geometry, the LMDT method gives the channel (IHX) length of 0.46 m, while the 3D CFD simulation predicts a longer length of 0.50 m. Table 7. 4 lists results obtained by the LMTD analysis for the circular staggered geometry.

Table 7. 4. Details of channel length calculations for circular staggered geometry (LMDT method, hot (liquid sodium) and cold (sCO₂) fluids)

Circular SDE	h avg hot [W/m ² K]	h avg cold [W/m ² K]	Cp cold [J/kgK]	Q[W]	ΔT hot [K]	ΔT cold [K]	ΔT_{LMTD} [K]	U[W/m ² .K]	L[m]
	193,400	170	1,250	6.68	15	31.07	22.06	169.85	0.46

The results presented in Table 7. 2 and Table 7. 4 show the heat transfer coefficient on the cold working fluid side in the circular SDE model is lower compared to that of liquid sodium on the hot side since the channel hydraulic diameter is larger in the BM. The mass flow rate on the hot and cold working fluid sides for both models can be found in Section 7.3. Table 7. 5 lists details of the PCHE geometry for the Base model and circular SDE geometries.

Table 7. 5. Details of the PCHE geometries used in this study

Parameter	Base model	Circular SDE
Channel diameter (mm)	1.51	1.51
Hydraulic diameter (mm)	0.922	1.51
Channel fin thickness (mm)	0.707	0.67
Plate thickness (mm)	1.46	1.46
Channel length (mm)	360	500
Cross-section area of solid wall (mm ²)	5.86	5.86

7.3.2 Thermal and hydraulic performance of the Base and circular SDE geometries for the 1st scenario

Table 7. 6 lists values of the peripherally-averaged Nusselt number Nu and friction coefficient C_f obtained by the CFD analysis of the simultaneously developing flow and conjugate heat transfer in the semi-circular (Base model) and circular SDE geometries presented in Table 7. 5 for sCO₂ as the cold side working fluid and liquid sodium as the hot side working fluid and boundary conditions presented in Table 7. 3.

Table 7. 6. Thermal and hydraulic performance of studied PCHEs

	Cold channel-sCO ₂					
Configuration	Mass flow rate [kg/s]	C _f	Nu	Pressure drop [Pa]	T _{bulk} at outlet [K]	Q [W]
Base model, Re=1000	3.20×10 ⁻⁵	0.0238	4.21	102.56	790.4	6.79
Circular SDE, 1 st scenario. Re = 1000.	3.91×10 ⁻⁵	0.0243	4.52	33.15	789.5	8.19
Diff%	22.13	2.1	7.36	-67.68	-0.11	20.62
	Hot channel-liquid sodium					
Configuration	Mass flow rate [kg/s]	C _f	Nu	Pressure drop [Pa]	T _{bulk} at outlet [K]	Q [W]
Base model, Re=146	3.21×10 ⁻⁵	0.1128	3.48	142.68	650.3	6.8
Circular SDE, 1 st scenario. Re = 146	3.93×10 ⁻⁵	0.1158	4.49	45.95	652.6	8.2
Diff%	22.1	2.66	29.02	-67.8	0.35	20.59

The most important advantages of the circular staggered double-etched geometry compared to the semi-circular geometry (Base model) are higher heat transfer coefficient and lower pressure drop, and lower stresses since channel corners are eliminated.

The results show increase in heat transfer rate Q by 20.6% in the circular staggered model compared to the Base model because of the higher the mass flow rate in the circular staggered model.

The results presented in Table 7. 5 show the Nu number in the hot channel for the circular staggered geometry is 29% higher compared to the BM geometry since regions of low

heat transfer in the channel corners have been eliminated. On the cold side, Nu number for the circular SDE geometry is by 7 percent higher compared to the BM geometry due to the higher convection heat transfer coefficient resulting from larger hydraulic diameter of the circular SDE channel geometry compared to the BM geometry (see Table 7. 5).

Variation of Nu and wall heat flux along length of the hot and cold channels for the BM geometry is presented in Figure 7. 5a–b. The results presented in Figure 7. 5a show that for the fully developed flow in the cold channel, Nu number is approaching 4.08. For the fully developed flow in the hot channel, Nu number is approaching 3.38. As the flow progresses downstream, Nu number increases to 4.99 at the channel exit due to axial conduction.

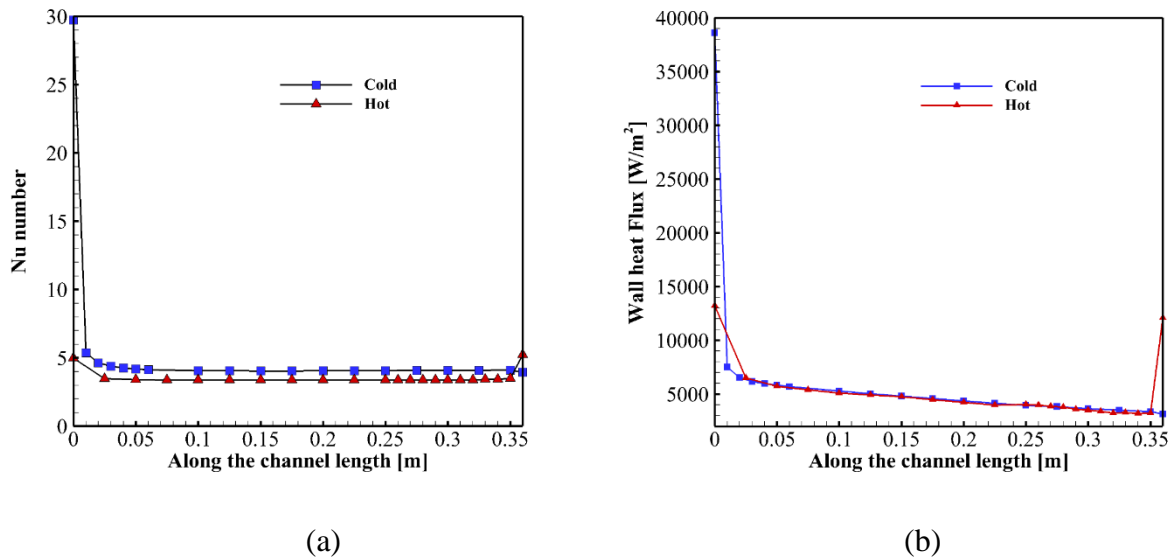


Figure 7. 5. Variation of (a) Nusselt number, (b) wall heat flux, along the channel length for the Base model

Figure 7. 5b shows variation of the wall heat flux along channel length and the effect of axial conduction in the hot channel. As discussed in earlier chapters, thermal conductivity of the liquid sodium (62 W/m.K) is much higher compared to the solid metal channel walls (21 W/mK), resulting in more pronounced contribution of the axial conduction heat transfer. Also, in the studied temperature range, liquid sodium has a very low Pr number ($\text{Pr}=0.0051$),

compared to sCO_2 ($\text{Pr}=0.8$), thus thermal boundary layer is much thicker compared to the hydraulic boundary layer and thermal resistance is distributed over the channel cross section instead being concentrated near the wall.

Variation of Nu, and wall heat flux along length of the hot and cold channels for the circular staggered model is presented in Figure 7. 6a-b. The results show that the value of Nu number for the fully developed flow in the cold channel is approaching 4.36, while the value of Nu for the fully developed flow in the hot channel is approaching 4.42, i.e., in the fully developed region of the flow the value of Nu number in the hot and cold channels is almost the same. The results presented in Figure 7. 5 and Figure 7. 6 show that the effect of axial conduction in the circular staggered model is identical to the Base model (semi-circular channel) since the channel diameter, the ratio of channel fin to the plate thickness, and the ratio of thermal conductivity of solid fin to working fluids for both models are identical for both geometries.

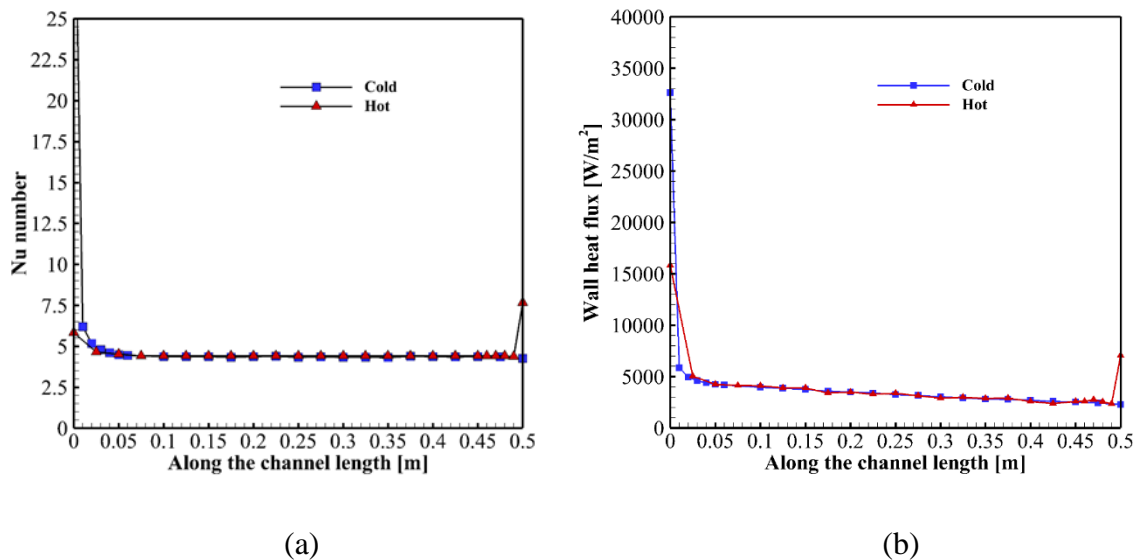


Figure 7. 6. Variation of (a) Nusselt number, (b) wall heat flux, along the channel length for the circular staggered doubled-etched geometry

The results shown in Figure 7. 6 show that values of wall heat flux in the hot and cold channels are identical except in the entrance region due to developing thermal boundary layer at the channel entrance. Since wall heat fluxes in the fully developed region are almost identical, the Nu numbers in that region are very close, as discussed above and presented in Figure 7. 5a.

Variation of the local wall heat flux along periphery of the hot and cold channel walls at $Z/D_h=110$ for the Base model and circular staggered geometry is presented in Figure 7. 7a-c. For the Base model and the cold channel, the wall heat flux in the channel corner (point B in Figure 7. 7a) is zero due to zero fluid velocity at that location. As a result, the convection heat transfer coefficient at that location is also zero. The wall heat flux increases away from the corner and reaches maximum value at the channel midspan (Point A). Variation of wall heat flux along periphery of the hot channel presented in Figure 7. 7b shows the local wall heat flux is not zero in the channel corner. As discussed earlier, due to high thermal conductivity of the hot fluid (liquid sodium), the heat transfer mode in this region is conduction. The convection heat transfer is zero in the channel corner since fluid velocity is zero. The average wall heat fluxes in the cold and hot channels at $Z/D = 150$ are 5,330 and 5,233 W/m², respectively.

Variation of the local wall heat flux along periphery of the circular channel is uniform, as presented in Figure 7. 7c. The average values for the hot and cold channels are virtually identical and equal to 3,503 W/m². The heat flux in the circular staggered geometry is lower compared to semi-circular channel since the heat transfer area for the circular staggered model is larger compared to the semi-circular geometry (Base model).

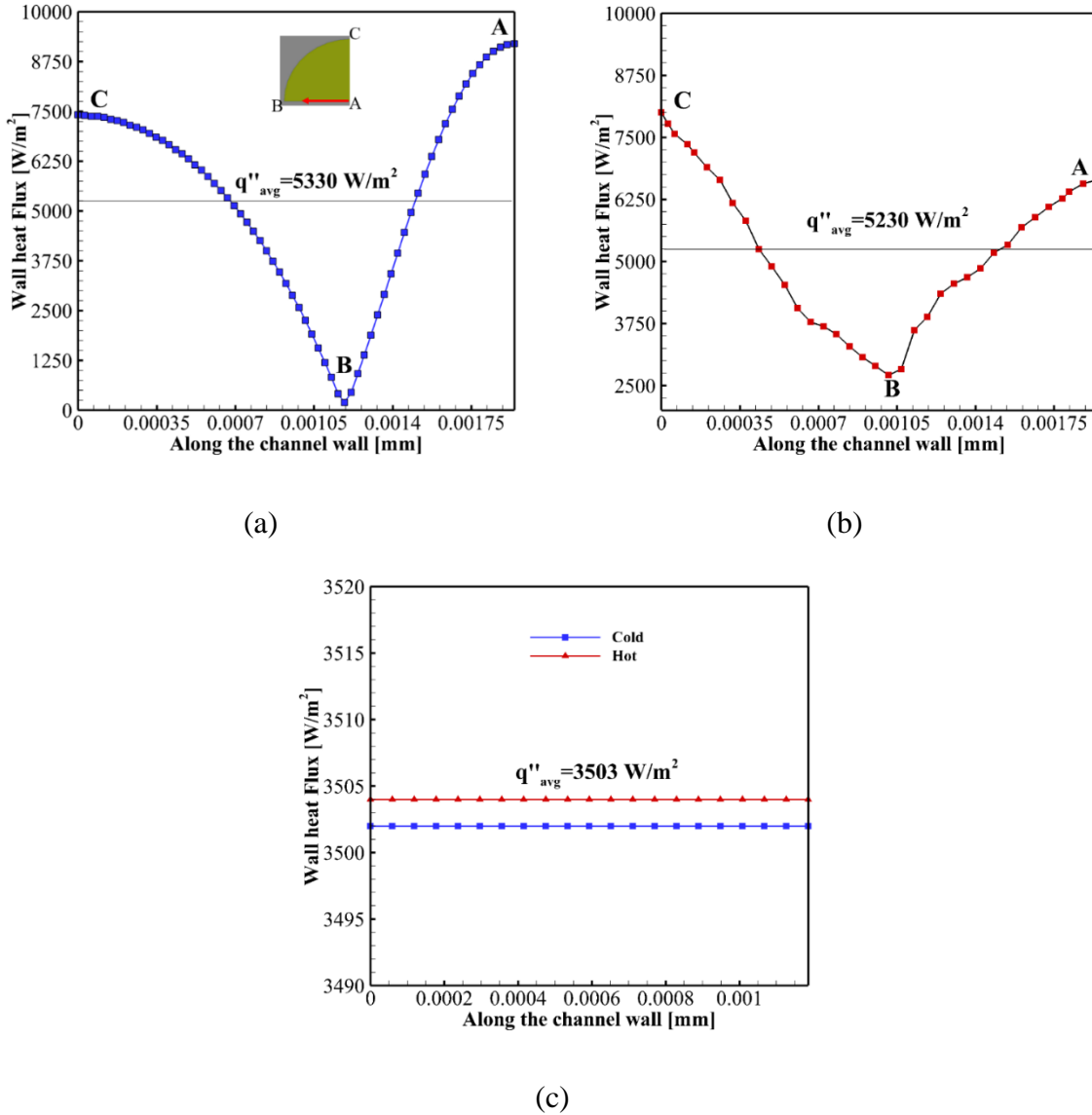


Figure 7. 7. Variation of local wall heat flux at $Z/D_h=110$ (a) Base model cold side, (b) Base model hot side, (c) circular staggered model, hot and cold sides

Variation of the friction coefficient along channel length is presented in Figure 7. 8. As the results show, friction coefficient C_f in the hot channel is higher compared to the cold channel for both geometries because of the higher wall shear stress and higher density of the hot working fluid (liquid sodium) compared to the cold fluid (sCO₂). Also, friction coefficient for the hot and cold channels in the BM geometry is higher compared to the circular staggered geometry because the average wall shear stress is higher in the Base model.

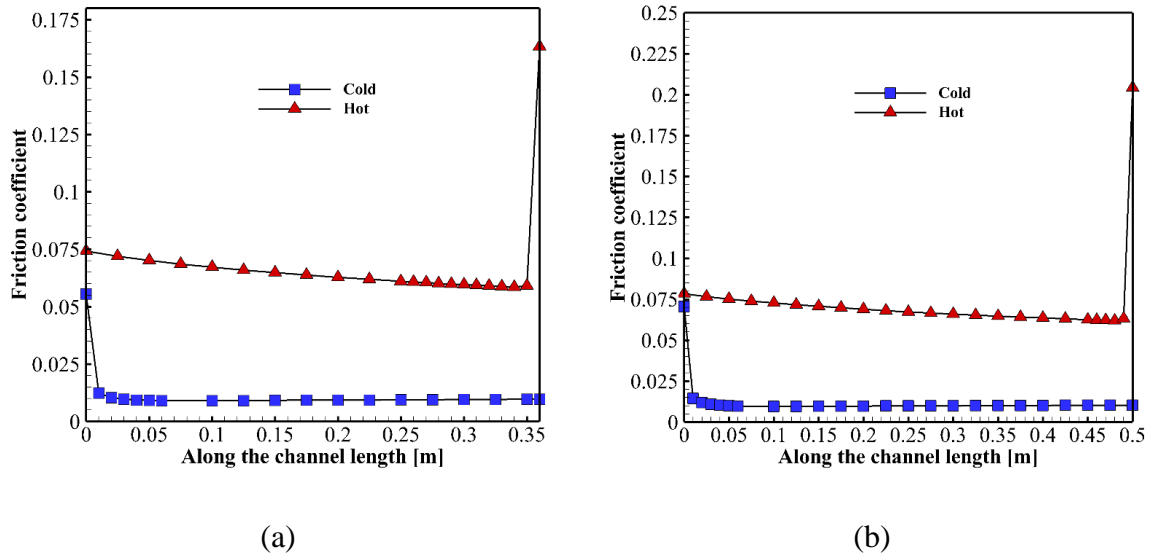


Figure 7. 8. Friction coefficient along the channel length, (a) The Base model, (b) the circular staggered model

Variation of the wall shear stress along length of the hot and cold channels for both geometries is presented in Figure 7. 9a. Wall shear stress for the circular geometry is lower compared to the BM geometry due to larger hydraulic diameter (channel size) and different shape of the micro-channel. In a circular channel geometry there are no corners, thus high wall shear stresses in this region of the flow are eliminated. Thus, as the results presented in Table 7. 6 show, pressure drop in the circular staggered geometry is significantly (67.7%) lower compared to the semi-circular channel for both the hot and cold channels.

The average values of density in the cold channel (sCO_2) and liquid sodium in the hot channel for both models are 185.34 kg/m^3 and 841.24 kg/m^3 , respectively. Variation of density along the channel length is identical for both the BM and circular staggered geometries, as presented in Figure 7. 9b. The average values of dynamic viscosity in the cold channel (sCO_2) and liquid sodium in the hot channel for both models are $3.51 \times 10^{-5} \text{ Pa.s}$ and $24.8 \times 10^{-5} \text{ Pa.s}$, respectively, as presented in Figure 7. 9c. Fluid density and viscosity affect wall shear stress, as discussed in Chapter 3[1, 25].

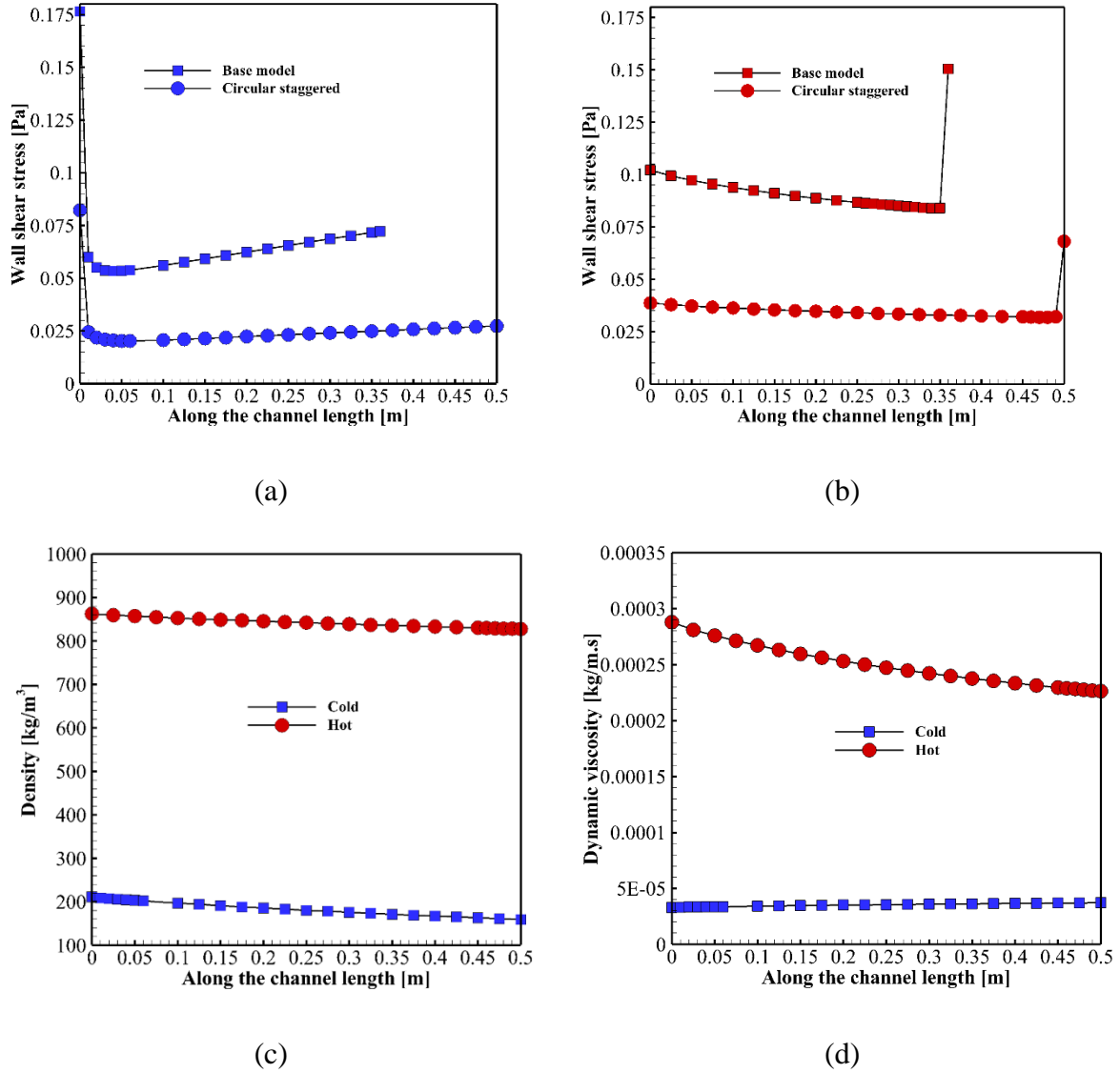


Figure 7. 9. Variation of (a) wall shear stress, Left: sCO₂ channel, Right: liquid sodium channel (b) dynamic viscosity, (c) density, along the channel length in the Base model and the circular SDE geometry

7.4 Temperature distribution in channel walls

To obtain temperature distribution in the channel walls, the equations describing a 3D steady-state laminar incompressible fluid flow within the hot and cold micro-channels and Laplace equation for the steady-state heat conduction in channel walls were solved numerically for the circular SDE geometry. Computational domain for the 3D CFD simulation is shown in Figure 7. 4c while Table 7. 5 lists details of the circular staggered geometry. Table 7. 3

summarizes boundary conditions used in the 3D CFD simulations. The circular SDE geometry with fin thickness of 0.67 mm was used in the calculations.

The predicted solid temperature contours at the mid-plane section are presented in Figure 7. 10. Temperature distribution along the channel periphery is uniform since for the circular channel geometry the wall heat flux is uniform along the channel periphery, as presented in Figure 7. 7c. The values of peripherally-averaged wall temperature for the hot and cold channels in the mid-plane are 468.26 °C and 467.86 °C, respectively. For the analyzed case, temperature difference between the hot and cold walls is 0.4 °C. The minimum predicted temperature in the 3D solid domain is 375.45 °C and is located in the cold channel wall at the channel inlet. The mid-plane section was selected for design and optimization of the IHX since the results of stress analysis performed by the 2D Generalized plane strain model, described in Chapter 5, show that the total stress values predicted at the mid-plane section are compatible with the total stress values obtained in the 3D stress analysis for the same B.Cs.

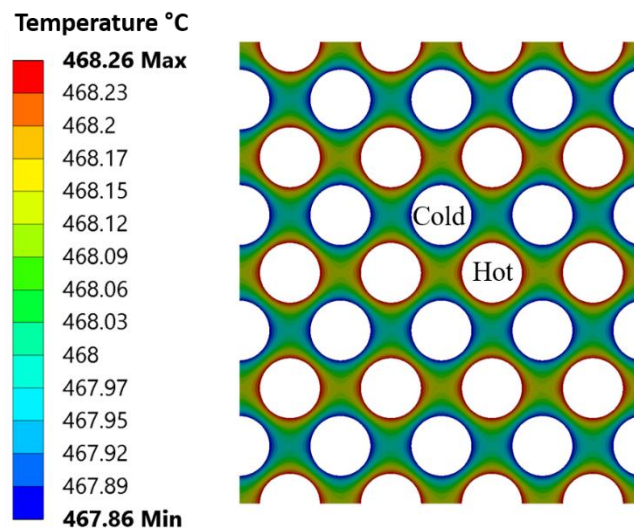


Figure 7. 10. Contour of solid domain temperature at mid-plane section

7.5 Potential candidate materials for IHX

The selection of suitable construction materials for an IHX is primarily based on the maximum allowable stresses and the safety rules established by The International Boiler and Pressure Vessel Code (BPVC) of the American Society of Mechanical Engineers (ASME). Section II, part D of the ASME BPVC provides guideline for the new material approval. For the high temperature application, section III is followed by section II for nuclear application materials. The criteria of the maximum allowable stress are established in section II, part D of the ASME BPVC. ASME, Section VIII, Division 1 states that for tensile strength, the ASME code requires a safety factor of 3.5 for non-bolting and 4 or 5 for bolting applications. In addition, if the product form is a welded tube or pipe, a joint efficiency factor (R_Y), a factor that expresses the ratio of the strength of a welded or brazed joint to the strength of the base material [72], of 0.85 is typically applied.

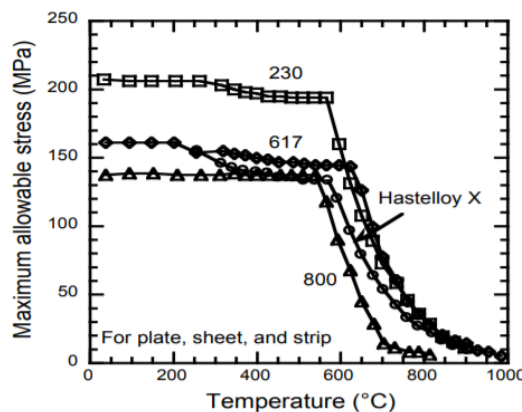
The ASME standard Section VIII, Division 1 states that the for the yield strength (S_Y), a $2/3$ multiplier is applied. For some cases, the safety efficiency factor is also multiplied ($2/3 R_Y S_Y$). The BPVC VIII-2 Appendix 3 recommends a safety factor SF of 1.5 based on the yield strength ($S_Y / 1.5$) or SF=4 based on the tensile strength value at the operating temperature.

Alloys 617 and 230 are potential candidates for the high temperature applications, such as IHX. Figure 7. 11a shows the maximum allowable stress for Alloys 617 and 230 over a range of operating temperatures. Based on the information provided in [79, 82], the Yield stress in the temperature range 400 to 600 C is 225 MPa for Alloy 617 and 300 MPa for Alloy 230. According to the ASME standard recommendation for the safety factor based on the Yield stress, a safety factor of 1.5 was applied to obtain the maximum allowable stress values presented in Figure 7. 11a. Additional information concerning the yield stress and ultimate

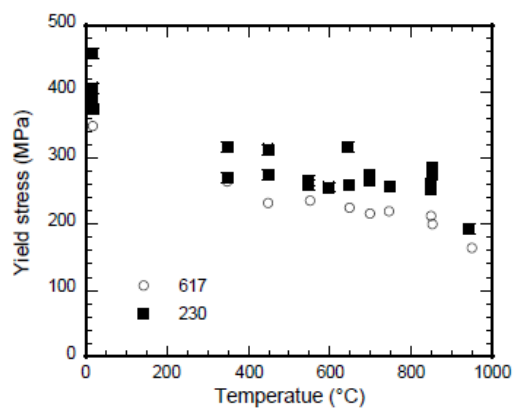
tensile stress for Alloys 617 and 230 is presented in Figure 7. 11b-c. According to [82], Alloys 617 and 230 are approved for high temperature applications below 600°C for non-nuclear service. As presented in Figure 7. 11a, the maximum allowable stress values for Alloys 617 and 230 at 500°C are 150 and 200 MPa, respectively. The allowable design stress for Alloy 617 is listed in Table 1B of Section III, Part D of ASME BPVC. The data show that the yield stress of Alloy 617 decreases for temperature higher than 400°C and remains relatively constant for temperatures in the 400 to 800°C range.

The recently developed Alloy 230 is another candidate for the high temperature applications. The mechanical properties (coefficient of thermal expansion and Young's modulus) of Alloy 230 are similar to Alloy 617, while its thermal stability and oxidation resistance are comparable to Alloy 617 [82]. The allowable design stresses for Alloy 230 are listed in Table 1B of Section III, Part D of ASME BPVC.

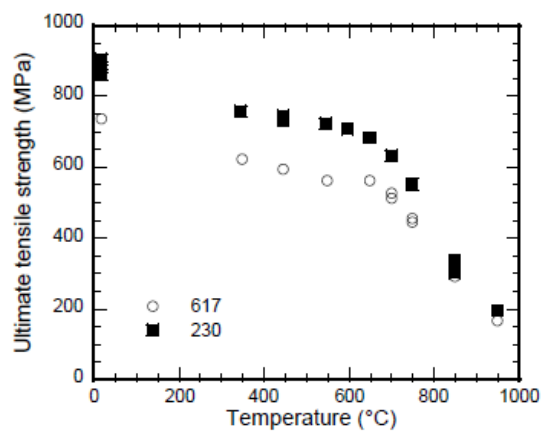
Table 7. 7 lists physical and mechanical properties of Alloys 617 and 230 over a range of operating temperatures used for the structural analysis in this work.



(a)



(b)



(c)

Figure 7. 11. Variation of (a) maximum allowable stress [79], mechanical properties of as-received Alloys 617 and 230 from the French VHTR program (b) Yield Stress vs. Temperature and (c) UTS vs. Temperature [19, 80]

Table 7. 7. Physical and mechanical properties of Alloys 617 and 230

Temperature (°C)	Thermal conductivity (W/m.°C)	Coefficient of thermal expansion (1/°C)	Poisson's ratio	Elasticity module (GPa)	Density (kg/m ³)
Alloy 617					
20	13.4	-	0.3	211	8360
100	14.7	1.16×10^{-5}	0.3	206	8360
200	16.3	1.26×10^{-5}	0.3	201	8360
300	17.7	1.31×10^{-5}	0.3	194	8360
400	19.3	1.36×10^{-5}	0.3	188	8360
500	21	1.39×10^{-5}	0.3	181	8360
Alloy 230					
20	8.9	1.27×10^{-5}	0.31	211	9050
100	10.4	1.30×10^{-5}	0.31	207	9050
200	12.4	1.33×10^{-5}	0.32	202	9050
300	14.4	1.37×10^{-5}	0.32	196	9050
400	16.4	1.40×10^{-5}	0.33	190	9050
500	18.4	1.44×10^{-5}	0.33	184	9050

7.6 Structural analysis

The generalized plane strain model in the ANSYS-mechanical module was used to perform a 2D analysis of thermal and mechanical stresses for the IHX. Thermal and mechanical stresses were calculated using FEM and applying boundary conditions listed in Table 7. 3, as explained in Section 5.21 of Chapter 5. Temperature distribution within the solid domain (channel walls) shown in Figure 7. 10 was used for the stress analysis. The Multi Objective Genetic Algorithm was applied to optimize channel geometry and topology for the IHX. The details of MOGA and optimization process were provided in Section 6.6 of Chapter 6. The maximum allowable stress was used as stress limit in the optimization process.

The following assumptions were considered in stress calculation and optimization of the geometry:

- Pressure forces are imposed uniformly along the channel wall periphery.
- 2D linear elastic stress analysis was employed in all stress calculations.
- The predicted Von-Mises stresses were used in the analysis.
- The effect of fin thickness on temperature distribution in the solid domain is negligible, as presented in Chapter 6.
- The maximum allowable stresses for Alloys 617 and 230 at 500 °C, and 150 and 200 MPa were used as the maximum stress values in the optimization process.
- Plastic deformation was not considered in the solid domain, thus was not included in the optimization process.
- The spring stiffness of 200 N/mm was assumed on the top and bottom walls of the model, as explained in Section 5.5 of Chapter 5.
- The maximum allowable stress values of 150 MPa and 200 MPa were assumed for Alloy 617 and Alloy 230, respectively, in the temperature range of 450-600 °C (see Figure 7. 11a).

7.6.1 ANSYS modeling

The circular SDE geometry used in the stress calculation and optimization is presented in Figure 7. 12. The details of the geometry dimensions are given in Figure 7. 4c. As mentioned before, the circular staggered geometry has identical cross-section area of solid wall and channel diameter as the semi-circular geometry (BM). The fin thickness was varied during the optimization process until the predicted stress at that location reached the maximum allowable stress value. The values of equivalent stress in the hot and cold channel walls were used as optimization constraints. The locations of reported stress values are indicated by the green and red circles in Figure 7. 12b, with red circle corresponding to the hot channel and green circle

corresponding to the cold channel. Both thermal and mechanical stresses were determined and used in the optimization procedure. The details concerning stress calculation and validation of results are presented in Chapter 5. As presented in Chapter 6, Quadratic grid elements were used in the FEM analysis.

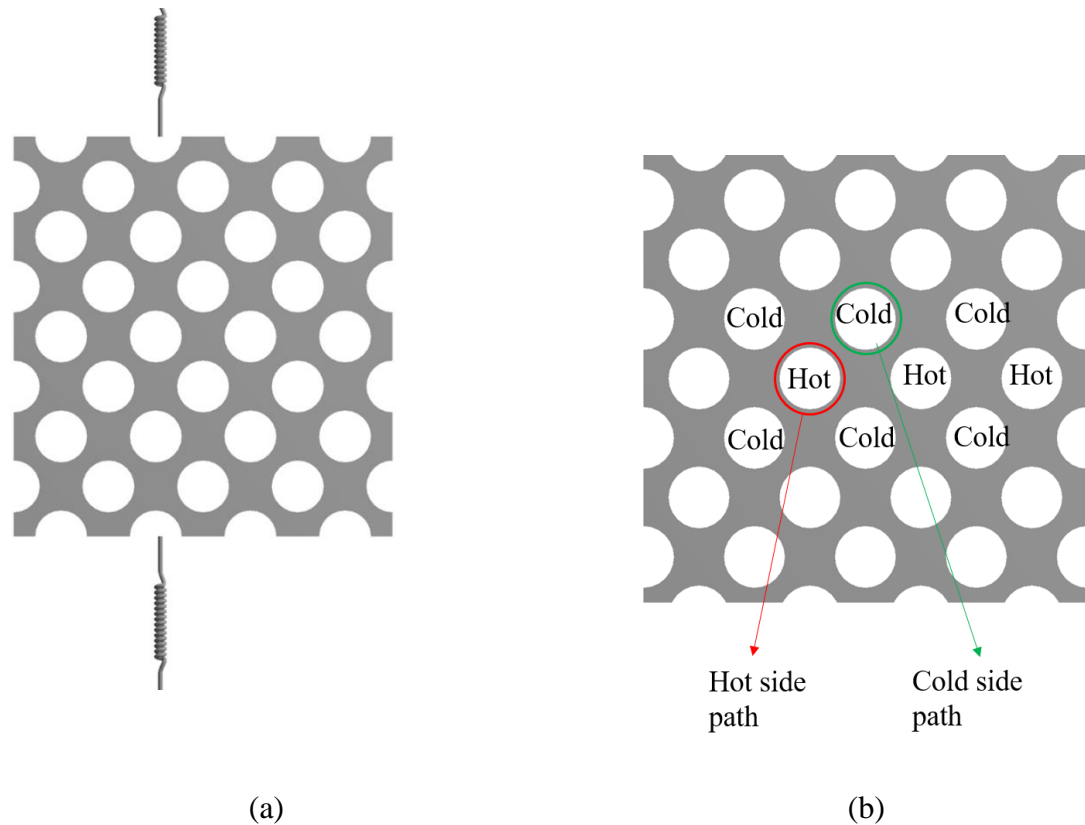


Figure 7. 12. (a) the circular staggered double-etched geometry used in stress calculation, (b) the locations (hot side and cold side paths) where stresses in channel walls are reported

Since circular channels have no corners, there is no stress concentration in these channels. The minimum and maximum fin thicknesses for the channel walls of 0.2 mm and 0.67 mm were used, respectively.

7.6.2 Stress calculation and optimization of the circular staggered double-etched geometry

Heat exchanger size and weight are important criteria in design of the heat exchangers because heat exchangers are one of the most expensive components in power generation

systems and industry in general. The high-temperature heat exchangers are generally manufactured by using expensive high-temperature alloys and stainless steels. The optimization of high-temperature heat exchangers results in a significant reduction of the heat exchanger weight and total cost. Optimization of the heat exchanger size includes its thermal and hydraulic performance.

Similar to the optimization of the semi-circular staggered, double-etched channel geometry described in Chapter 6, the non-dominated sorting genetic algorithm (NSGA-II) was used in optimization of the circular channel geometry. The objective functions and design parameters used in the optimization were maximum allowable stress and channel fin thickness, respectively. As described in Chapter 6, the design optimization process provides a list of candidates for the optimal geometry. The first three candidates obtained in optimization of the circular geometry are listed in Table 7. 8. The first candidate has the minimum channel fin thickness of 0.428 mm. The corresponding maximum equivalent stresses on the hot and the cold sides are 129 MPa and 149.94 MPa, respectively as shown in Table 7. 8.

Table 7. 8. First three candidates for optimal geometry in the design optimization

	Candidate 1	Candidate 2	Candidate 3
Fin thickness (mm)	0.428	0.456	0.484
Hot side Maximum Equivalent Stress (MPa)	129	126	124
Cold side Maximum Equivalent Stress (MPa)	149.94	146.66	144.3

As presented in Table 7. 9, a decrease in channel fin thickness from the maximum value of 0.67 mm to 0.428 mm results in a 34.13% reduction in the cross-section area of solid wall and PCHE size.

Table 7. 9. Reduction of PCHE size in optimization design for Alloy 617

Parameter	Optimized circular staggered	Circular staggered	Improvement
Channel diameter (mm)	1.51	1.51	-
Hydraulic diameter (mm)	1.51	1.51	-
Channel fin thickness (mm)	0.428	0.67	-36.13%
Plate thickness (mm)	1.46	1.46	-
Channel length (mm)	500	500	-
Cross-section area of solid wall (mm ²)	3.86	5.86	-34.13%

The cross-section area of solid wall in the optimized circular SDE geometry was reduced from 5.86 to 3.86 mm²- an improvement of 34.13%.

Stress contours obtained for the optimized circular SDE geometry are shown in Figure 7. 13. The results show the highest stress values occur in the cold channel walls in proximity of the spring boundary condition which restricts expansion of the PCHE model.

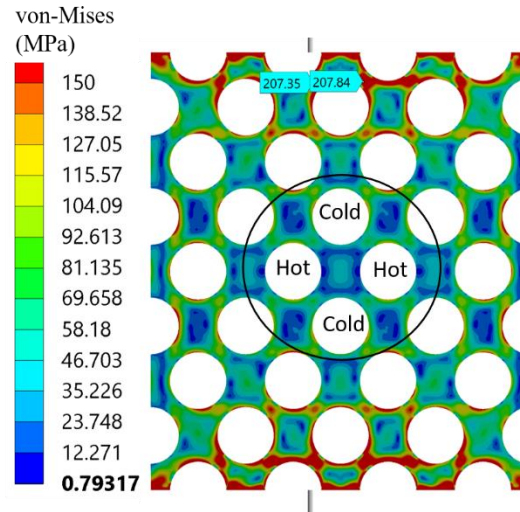


Figure 7. 13. The stress contours for the optimized geometry (channel fin thickness=0.428 mm)

Unlike the semi-circular channel geometries, there is no stress concentration in the circular channel, thus the total stress values are significantly lower. As a result, there is a potential for a significant reduction of the PCHE size. However, for IHX, the temperature and pressure differences between the hot and cold channels are significantly higher compared to the HTR application. These larger differences limit the size reduction that could be achieved for IHX.

As discussed earlier, the stress predicted in the cold channel wall reaches maximum value of 149.94 MPa, while stress values predicted in the proximity of spring elements (imposed constraints) are higher due to constrained displacement at the model boundaries. The stress distribution along the hot channel (hot path shown in Figure 7. 12b) for the optimized geometry (Candidate 1) is presented in Figure 7. 14. The maximum stress value of 129 MPa occurs at Point D because the model expansion is constrained in the vertical direction by the springs, while it is free to expand in the horizontal direction. The stress value of 10 MPa occurs in the hot channel wall at Point A, and is identical to Points B and C.

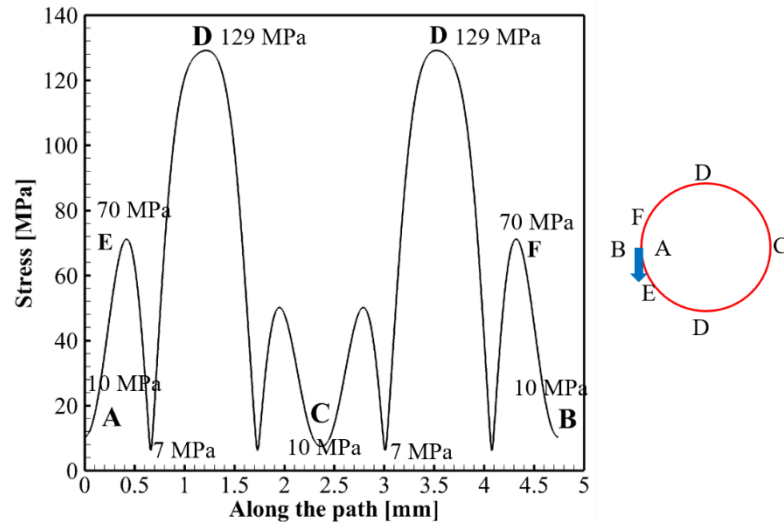


Figure 7. 14. The stress distribution along the hot path.

The minimum stress in the hot channel is almost zero because the pressure forces exerted on the hot channel walls are almost zero. Figure 7. 15 shows stress distribution along the cold path. The maximum stress values of 149.95 MPa occurring at points D correspond to the maximum stress values for the optimized geometry (Candidate 1). The stress value at Point D in the cold path is higher compared to the Point D in the hot path since the pressure in the cold channels is much higher compared to the hot channels. The minimum stress value in the cold channel wall is 15 MPa as shown in Figure 7. 15. Since stress distribution along the hot and cold paths is repeated periodically between Point A and Point C, for the circular channel geometry, the minimum and maximum stress values occur at the same locations.

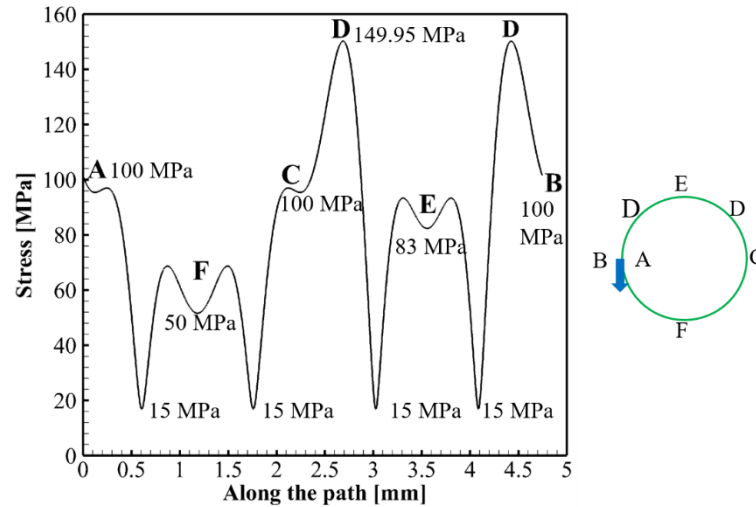


Figure 7. 15. The stress distribution along the cold path.

Figure 7. 16 shows the maximum total stress in the fin of the hot and cold channel walls over a range of fin thicknesses. The results show that the maximum total stress values in the cold channel wall decrease monotonically as the channel fin thickness increases, while the maximum total stress values in the hot channel wall decreases to a minimum value of 123 MPa at fin thickness 0.532 mm. The maximum total stress value of 270 MPa occurs in the cold channel wall for the minimum analyzed fin thickness of 0.2 mm. As shown in Figure 7. 16, for the optimal fin thickness of 0.428 the total stress is 149.94 MPa in the cold channel wall, while the total stress in the hot channel wall is lower, 129 MPa. The minimum total stress of 122.88 MPa occurs in the hot channel wall at channel fin thickness of 0.533 mm.

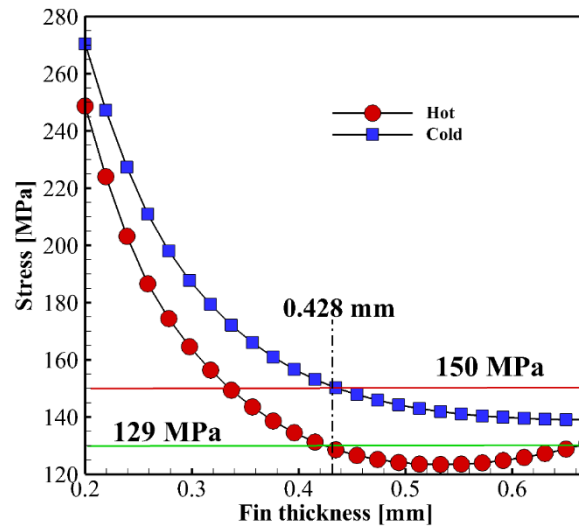


Figure 7. 16. Variation of maximum total stress over a range of channel fin thickness

Figure 7. 17 shows variation of the maximum von-Mises stress occurring in the fins of the cold and hot channel walls. The y-axis and x-axis represent the maximum stress values in the hot and cold channel walls, respectively. Fin thickness is indicated by the number next to the blue square symbol. Since the maximum allowed stress value is 150 MPa, the channel fin thickness larger than 0.435 mm meet requirement of the maximum allowable stress.

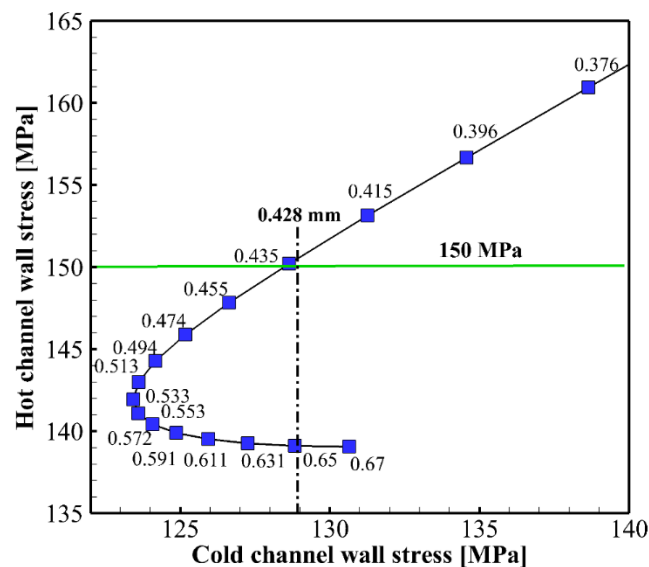


Figure 7. 17. Hot and cold channel walls maximum stress values over a range of channel fin thickness

7.7 Thermal and hydraulic performance of the optimized geometry, 1st scenario

A 3D CFD simulation was performed to determine thermal and hydraulic performance of the optimized circular staggered geometry. Channel lengths of the optimized circular staggered geometry and circular staggered geometry are identical (500 mm). The boundary conditions and operating pressure and temperatures are also identical for both geometries. The boundary conditions used in the 3D CFD simulations are listed in Table 7. 3. The conservation equations for momentum and energy for a 3D steady-state laminar incompressible fluid flow and Laplace equation for the steady-state heat conduction in solid channel walls for the 1st scenario described in Section 7.3, were numerically solved using the Fluent code.

The values of peripherally-averaged Nu and C_f obtained by CFD analysis of the optimized circular staggered geometry and circular staggered geometry for the hot and cold channels are listed in Table 7. 10.

Table 7. 10. Thermal and hydraulic performance of the optimized circular staggered geometry and circular staggered geometry, 1st scenario, Re=1000 for the cold side inlet

	Cold channel (sCO ₂)					Hot channel (Na)				
Configuration	C_f	Nu	Pressure drop [Pa]	T_{bulk} at outlet [K]	Q [W]	C_f	Nu	Pressure drop [Pa]	T_{bulk} at outlet [K]	Q [W]
Circular SDE	0.0243	4.52	33.15	789.5	8.19	0.1158	4.49	45.95	652.6	8.2
Optimized circular SDE	0.0243	4.52	33	789.23	8.22	0.116	4.51	46	650.9	8.24
Difference%	0.00	0	0.00	0.45	0.03	0.17	0.45	0.11	0.25	0.49

The results show that thermal and hydraulic performance of the optimized circular staggered geometry and circular staggered geometry is virtually identical for operating conditions corresponding to the 1st scenario. The small difference between the values of Nu number and pressure drop in the hot channel is due to numerical error. Since the flow regime is laminar, mass flow rate and hydraulic diameters are identical for both geometries, change in

bulk temperature along the channels is small and variation in thermophysical properties is negligible, hydraulic and thermal performance of both geometries is identical. However, as it will be discussed in more detail later, optimized geometry is more compact resulting in a smaller heat exchanger size, better utilization of metal, and lower cost.

Variation of the peripherally-averaged wall heat flux along the length of hot and cold channels for both geometries is presented in Figure 7. 18. The results show that the average wall heat flux for the hot and cold sides of the circular SDE geometry is $3,451 \text{ W/m}^2$ which is virtually identical to that of the optimized circular SDE geometry ($3,464 \text{ W/m}^2$).

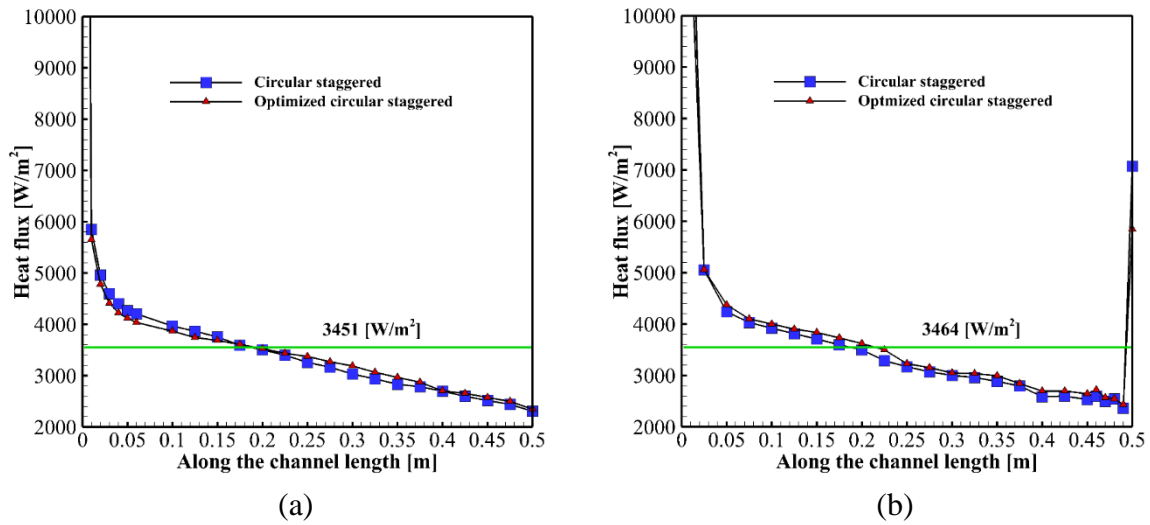


Figure 7. 18. The peripherally-averaged wall heat flux (a) cold channel, (b) hot channel, for both geometries, 1st scenario

The results presented in Table 7. 10 also show that the bulk fluid temperature at the cold and hot channel outlets for both geometries is virtually the same. Therefore, as shown in Section 7.8 below, the increase in heat transfer performance of a heat PCHE exchanger employing optimized geometry is due to higher value of the overall heat transfer coefficient U .

7.8 IHX thermal performance

7.8.1 Overall heat transfer coefficient (U)

Similar to Chapter 6, the overall heat transfer coefficient U was calculated using Integration method, Equation (6.1) presented in Section 6.8.2. The average convection heat transfer coefficients $h_{\text{avg,Hot}}$ and $h_{\text{avg,Cold}}$ for the hot and cold channels were calculated using values of the local heat transfer coefficient along the channel length. Table 7. 11 lists values of the overall heat transfer coefficient obtained using Integration Method for the Base model, circular staggered, and optimized circular staggered geometries. The values of overall heat transfer coefficient U for the optimized circular staggered and circular staggered geometries are approximately the same ($169.58 \text{ W/m}^2\text{K}$) and ($169.17 \text{ W/m}^2\text{K}$), respectively, but smaller compared to the Base Model ($258.09 \text{ W/m}^2\text{K}$).

Table 7. 11. Heat transfer coefficient for studied geometries

	$h_{\text{avg Hot}}$ [W/m ² K]	$h_{\text{avg Cold}}$ [W/m ² K]	UA [W/K]	U [W/m ² K]
Optimized circular SDE	198,114	170.31	0.4024	169.58
Circular SDE	198,243	170.24	0.4017	169.17
BM	246,391	260.63	0.3618	258.09

Also, thermal resistance to convection for the optimized circular staggered and circular staggered geometries is identical since the average heat transfer coefficients are the same. Thermal resistance to convection in the semi-circular channel (Base model) is smaller since for the same mass flow rate of the working fluid, convection heat transfer coefficient is higher for smaller semi-circular channels compared to larger circular channels. The total thermal resistance ($R_t=1/UA$), Equation (6.4), for the optimized circular staggered, and the circular staggered geometries is identical and is higher compared to the Base model. However, thermal

resistance to conduction (R_t), Equation (6.3), is higher for the Base model (0.0139 K/W) compared to the optimized circular staggered geometry (0.0068 K/W) and the circular staggered geometry (0.0096 K/W) since it depends on the channel fin thickness.

The overall heat transfer coefficient U for the Base model (semi-circular channels) is higher compared to the circular staggered geometries because the overall heat transfer coefficient U , Equation (6.5), is a function of the convection heat transfer coefficient h and thermal resistance to conduction which depends on the channel fin thickness, Equation (6.4). Since, as shown in Figure 7. 11, the value of the convection heat transfer coefficient in the cold channel is much lower compared to the convection heat transfer coefficient in the hot channel, and resistance to conduction is very low, the cold side convection heat transfer coefficient is a dominant factor determining value of the overall heat transfer coefficient.

The convection and overall heat transfer coefficients for the circular staggered and optimized circular staggered channels are lower compared to the Base model since the hydraulic diameter for both hot and cold channels in the BM is smaller compared to the circular staggered geometry for the same fluid flow. The average Nu number is unchanged in the fully developed laminar flow, but the heat transfer coefficient changes with respect to the hydraulic diameter of the channel ($h=Nu.k/D_h$).

7.8.2 Effectiveness-NTU (ϵ -NTU) method

Thermal performance of the optimized circular staggered double-etched PCHE designed for the IHX application, predicted by using the ϵ - NTU method, is presented in this section. The overall heat transfer coefficient was calculated using Equation (6.5) while NTU and ϵ were obtained using Equations (6.8) and (1.8).

Table 7. 12 lists values of NTU and effectiveness ε calculated for the optimized circular staggered geometry. The results show that the values of effectiveness ε and NTU obtained for the optimized circular staggered geometry are virtually the same as for the circular staggered geometry. As explained in Chapter 6, for the laminar flow regime and the same hydraulic diameter, thermal resistance of the channel fin does not have a significant effect on the overall heat transfer performance. In other words, under conditions stated above, fin thickness has a negligible effect on heat transfer between the hot and cold channels.

For the values of temperature, pressure, and Reynolds number used in this study, the NTU value obtained for the optimized circular staggered double-etched geometry is smaller compared to the Base model, while values of ε and NTU for both circular geometries are approximately the same, but somewhat smaller compared to the BM geometry. Since the quantity NTU represents dimensionless size of a heat exchanger, a smaller value of NTU corresponds to a smaller and more compact heat exchanger. Although a more detailed analysis is needed to determine the actual heat exchanger size, it can be concluded that circular staggered geometry is more compact compared to the BM geometry. Also, values of ε presented in Table 7. 12 show that effectiveness of the optimized circular geometry is only slightly lower compared to the effectiveness of a larger BM geometry.

Table 7. 12. NTU and effectiveness of the optimized circular staggered double-etched, circular staggered, and Base model geometry

	Hydraulic diameter	C_{min} [J/K.s]	h_{avg} Hot [W/m ² K]	h_{avg} Cold [W/m ² K]	U [W/m ² K]	effectiveness	NTU
Optimized circular SDE	1.51E-03	0.0488	198,114	170.318	169.71	0.9376	8.2431
Circular SDE	1.51E-03	0.0488	198,243	170.240	169.43	0.9281	8.2304
BM	9.22E-04	0.040	246,391	260.637	259.05	0.9433	9.0515

The optimized circular staggered, and circular staggered geometries are compared in Table 7. 13. The results show that the total weight of a PCHE employing optimized circular staggered geometry is by 34% lower compared to the non-optimized geometry due to the more compact design (smaller frontal area). The weights of PCHEs employing optimized and non-optimized circular geometries were also compared to the weight of a PCHE unit employing 1280 by 1280 hot and cold channels similar to PCHE configuration described by Kim [70]. As presented in Table 7. 13 the weight of a PCHE employing circular staggered geometry is 31.35 kg, while the weight of a PCHE employing optimized circular geometry is much lower, only 20.65 kg. As discussed earlier, this represents a weight and size reduction of 34% compared to the circular staggered geometry. The relative difference was calculated using $\frac{\Phi - \Phi_{ref}}{\Phi_{ref}} \times 100$ where Φ is any parameter of interest. The circular staggered model was used as the reference case in this comparison. The frontal view of the optimized circular SDE geometry is presented in Figure 7. 19.

Table 7. 13. PCHE unit weight and dimensions of the circular staggered and optimized circular staggered geometries

	Unit width (mm)	Unit height (mm)	Unit length (mm)	Unit cross-section area of solid wall (m ²)	No. plates in Unit	Unit volume (m ³)	Unit weight (kg)
Circular SDE	129.4	93.44	500	0.0075	64	0.00375	31.35
Optimized SDE	101.96	93.44	500	0.00494	64	0.00247	20.65
Diff. %	-21.2	0	0	-34.13	0	-34.13	-34.13

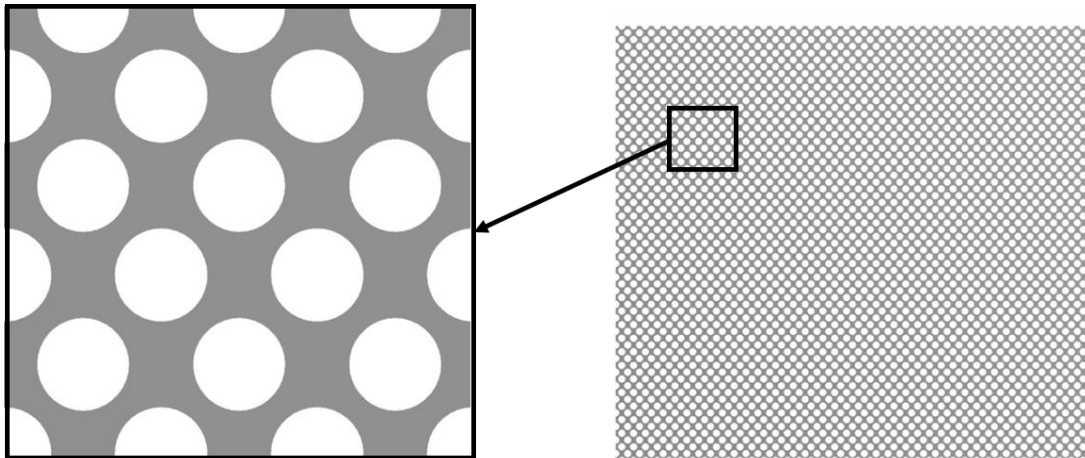


Figure 7. 19. The frontal view in the optimized circular SDE staggered geometry

Table 7. 14 compares values of the total (Q) and volumetric heat transfer rate (Q/V), heat transfer area (A_s), heat exchanger volume (V) and heat exchanger compactness (A_s/V) for the BM and the optimized circular staggered geometry. Since, as discussed earlier, optimization of the geometry has a very small effect on heat transfer, the total heat transfer rate Q is virtually the same for both geometries since the total heat transfer area, mass flow rate, flow regime, and hydraulic diameters are the same. However, due to the 34% smaller volume

of the optimized geometry, the volumetric heat transfer rate Q/V increased by 52%, resulting in the volumetric heat transfer enhancement of 1.52. The volume enhancement is defined as the ratio of the circular staggered volume to the optimized SDE volume, meaning heat exchanger volume associated with the circular staggered geometry is 1.52 times larger compared to the volume of the optimized circular staggered geometry. As a result, compactness A/V of the optimized design is significantly higher compared to the circular staggered, allowing for a 52% higher heat transfer per unit volume. Expressed differently, for the same heat exchanger volume (mass of metal used for the construction), the optimized geometry can transfer 1.52 times more heat compared to the circular staggered geometry. In summary, the optimized circular staggered topology is smaller in size, lighter, more economical to manufacture, and has higher thermal duty compared to the BM geometry.

Table 7. 14. Heat transfer per volume and the heat exchanger compactness for circular staggered geometries

	A (m ²), cross- section area of solid wall for a pair of Hot/cold Cell	Q (W), Heat for a pair of Hot/cold Cell	V (m ³), Volume Hot/Cold unit	Q/V (W/m ³)	A (m ²) /V (m ³) reduction %	Volume enhancement (V _{circular staggered} /V _{optimized circular staggered})	Heat enhancement for constant volume %	Compact ness (A/V) (m ² /m ³)
Circular SDE	5.86×10 ⁻⁶	8.195	3.75×10 ⁻³	2.80×10 ⁶	0.0075008	1.52	52	809.4
Optimized circular SDE	3.86×10 ⁻⁶	8.23	2.47×10 ⁻³	4.26×10 ⁶	0.0049408			1,228.8
Diff. %	-34	0.43	-34	52	-34			52

7.9 Optimized circular staggered geometry for Alloy 230

The tensile strength of Alloy 230 is superior compared to Alloy 617 for higher temperature conditions [82]. Since for operating temperatures lower than 750-800°C, Alloy 230 has higher yield and maximum allowable stress compared to Alloy 617, it is potentially better material for design of an IHX. Also, Alloys 230 and 617 have identical mechanical properties such as modulus of Elasticity and the coefficient of thermal expansion. However, etchability and diffusion bounding process of plates made of Alloy 230 have not been thoroughly investigated.

Optimization of an IHX constructed of Alloy 230 is described in this section. The operating conditions (temperature and pressure) of the IHX correspond to 650 MW recompression Brayton cycle [8]. The optimization process for Alloy 230 is virtually identical to the optimization process for Alloy 617 - MOGA was employed to optimize the channel fin thickness. The operating conditions (pressure and temperature) and thermo-physical properties of Alloy 230 are listed in Table 7. 3 and Table 7. 7. The assumptions used in structural analysis and optimization are described in Section 7.6.

Since thermo-physical and mechanical properties of Alloy 230 and Alloy 617 are identical [82], temperature distribution and resulting stress fields in the solid material (channel walls) are identical.

Since the cross-section of the circular SDE geometry is identical to the Base model, it was considered as the primary (starting) geometry for the fin thickness optimization. The grid size and discretization elements were the same as used for Alloy 617. The same assumptions and optimization criteria used in the optimization process for Alloy 617 were selected for optimization for Alloy 230. For example, the channel fin thickness was varied until the

criterion of the maximum allowable stress was met. Since the maximum allowable stress in Alloy 230 is higher compared to Alloy 617, fin thickness, channel wall geometry, and IHX size were smaller compared to Alloy 617. As stated earlier, the assumptions used in design and optimization were the same as used for Alloy 617, see Sections 7.6 and 6.6.3 in Chapter 6. The maximum allowable stress for Alloy 230 at 500 °C of 200 MPa and yield stress base safety factor (SF) of 1.5, were used was used in the optimization process.

Table 7. 15 lists three candidates for the optimal design using Alloy 230. The first candidate has the minimum channel fin thickness of 0.275 mm. The equivalent stresses in the hot and cold channel walls are 173.48 MPa and 198.78 MPa, respectively.

Table 7. 15. Three candidates for the design optimization using Alloy 230

	Candidate 1	Candidate 2	Candidate 3
Fin thickness (mm)	0.275	0.2761	0.2764
Hot channel Maximum Equivalent Stress (MPa)	173.48	173.25	173.1
Cold channel Maximum Equivalent Stress (MPa)	198.78	198.53	198.37

As presented in Table 7. 5, the channel fin thickness for the circular staggered geometry is 0.67 mm. The first candidate for the circular staggered geometry using Alloy 230 has the channel fin thickness of 0.275 mm (see Table 7. 15). Comparison of the optimized circular staggered geometries for Alloys 617 and 230, presented in Table 7. 16, shows a 37.41% reduction of the IHX cross-section area of solid wall for Alloy 230.

Table 7. 16. Comparison of optimized circular geometries for Alloys 617 and 230

Parameter	Optimized circular staggered, Alloy 617	Optimized circular staggered, Alloy 230	Improvement (%)
Channel diameter (mm)	1.51	1.51	-
Hydraulic diameter (mm)	1.51	1.51	-
Channel fin thickness (mm)	0.428	0.275	-
Plate thickness (mm)	1.46	1.46	-
Channel length (mm)	500	500	-
Cross-section area of solid wall (mm ²)	3.86	2.4158	37.41%

Figure 7. 20 shows the maximum total stress in the fin of the hot and cold channel walls over a range of fin thickness for Alloys 617 and 230 as materials of construction. As explained in Section 7.5, mechanical properties of Alloy 617 and Alloy 230 are identical, thus for the same boundary conditions, stress distribution in channel walls is identical for both alloys. As the results presented in Figure 7. 20 show, the maximum total stress decreases as the fin thickness increases. For both alloys the maximum total stress value of 265 MPa occurs in the cold channel wall for the minimum fin thickness of 0.2 mm. For the optimal value of fin thickness of 0.275 mm, the total stress in the cold and hot channel walls is 198.78 MPa and 173.48 MPa, respectively (less than maximum allowable stress of 200 MPa for Alloy 230). The minimum

total stress of 122.88 MPa occurs in the hot channel wall for the channel fin thickness of 0.533 mm.

For comparison, for Alloy 617 the maximum allowable stress of 150 MPa is reached at the optimal fin thickness of 0.428 mm in the cold channel (see Figure 7. 16), thus using Alloy 230 allows reduction of the heat exchanger (IHX) size.

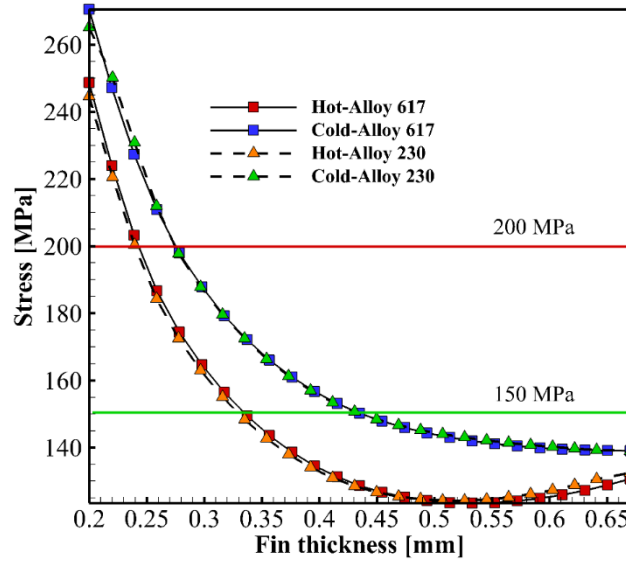


Figure 7. 20. The variation of maximum total stress over a range of channel fin thickness using Alloy 617 and Alloy 230 as solid materials

As presented in Table 7. 17, for Alloy 230 the optimized IHX topology is smaller and lighter compared to Alloy 617. For the analyzed operating pressures and temperatures and optimized circular staggered geometry, the results listed in Table 7. 17 show the use of Alloy 230 results in 37% reduction of frontal area and volume, and 60% increase in heat transfer enhancement. These improvements correspond to the volume enhancement of 1.6 and 60% reduction in weight, compared to Alloy 617.

Table 7. 17.Comparison of the IHX size for Alloys 617 and 230 - optimized circular staggered geometries

	A (m ²), cross- section area of solid wall in a pair of Hot/cold channels	Q (W), Heat for a pair of Hot/cold channels	No. Hot/Cold channels in a unit	A (m ²), Area unit	V (m ³), Volume Hot/Cold unit	
Optimized SDE, Alloy 617	3.86×10^{-6}	8.23	1280	0.00494	0.00247	
Optimized SDE, Alloy 230	2.4158×10^{-6}	8.23	1280	0.00309	0.00154	
Diff. %	-37	0.00	0.00	-37	-37	
	Q/V (W/m ³)	A (m ²) or V (m ³) reduction %	Volume enhancement	Heat enhancement for constant volume %	As/V (m ² /m ³)	Unit weight (kg)
Optimized SDE, Alloy 617	4,264,939	0.0049408	1.60	60	1,228.8	20.64
Optimized SDE, Alloy 230	6,813,478	0.003092			1,963	13.99
Diff. %	60	-37			60	-32

7.10 Thermal and hydraulic performance of studied IHX, 2nd scenario

7.10.1 Geometry and boundary conditions

As presented in Section 7.3, for the 2nd scenario, velocity of the hot and cold working fluids in the BM and circular SDE geometries is assumed to be the same. For this scenario, the mass flow rate and Reynolds number for the circular SDE geometry is higher compared to the BM geometry, since both parameters are proportional of the hydraulic diameter of the micro-

channel. For the analyzed PCHE geometry and operating conditions, the hot side and cold side Reynolds numbers are 254 and 1,630, respectively.

Boundary conditions used for the CFD analysis of the 2nd scenario are presented in Table 7. 18 and are identical to those used for the Base model. The analysis was performed for the optimized circular SDE geometry, liquid sodium and sCO₂ as the hot and cold working fluids, and Alloy 617 as the material of construction. Thermo-physical properties of liquid sodium and sCO₂ were presented in Section 7.3. The inlet mass flow rates and corresponding Re numbers at the hot and cold inlets presented in Section 7.3 and above are summarized in Table 7. 18. Dimensions of the optimized circular staggered geometry used in the analysis are given in Table 7. 9.

Table 7. 18. Boundary conditions and mass flows of working fluids for the 2nd scenario

Boundary	Optimized circular staggered geometry	Hot side	Cold side
Inlet	Velocity inlet (m/s)	0.043	0.1691
	Re number	254	1630
	Mass flow rate (kg/s)	3.928×10^{-5}	3.908×10^{-5}
	Temperature (K)	803.15	620.9
Outlet	Pressure outlet (MPa)	0.115	25.1
Top/bottom wall	Symmetry	-	-
Side walls	Adiabatic/symmetry	-	-
Front/Back walls	Adiabatic	-	-

The grid element size and configuration, numerical setup, and Fluent code setup are the same as for the optimized circular staggered geometry.

7.10.2 Thermal and hydraulic performance, 2nd scenario

3D CFD simulations were performed to obtain thermal and hydraulic performance of the IHX employing optimized circular staggered geometry and Alloy 617 as a material of

construction. The details of the CFD simulation, numerical setup, grid element size, and information on the Fluent code setup can be found in Section 7.3. Table 7. 19 compares numerical results of the peripherally-averaged Nu number, friction coefficient, pressure drop, bulk temperature at the channel exit, and heat transfer value in the cold and hot channels for the 1st and 2nd scenario.

Table 7. 19. Thermal and hydraulic performance for studied scenarios

Cold channel-sCO ₂						
Configuration	Mass flow rate [kg/s]	C _f	Nu	Pressure drop [Pa]	T _{bulk} at outlet [K]	Q [W]
Circular SDE, 1 st scenario Re = 1000.	3.91×10 ⁻⁵	0.0243	4.52	33	789.23	8.22
Circular SDE, 2 nd scenario Re = 1630.	6.40×10 ⁻⁵	0.0146	4.54	56	778.43	12.61
Diff%	63.79	-39.92	0.44	69.70	1.37	53.41
Hot channel-liquid sodium						
Configuration	Mass flow rate [kg/s]	C _f	Nu	Pressure drop [Pa]	T _{bulk} at outlet [K]	Q [W]
Circular SDE, 1 st scenario Re = 146	3.93×10 ⁻⁵	0.116	4.51	46	650.94	8.24
Circular SDE, 2 nd scenario Re = 254	6.43×10 ⁻⁵	0.0704	4.53	75	660.67	12.68
Diff%	63.81	-39.31	0.5	63.04	1.49	53

The results presented in Table 7. 19 show that the heat transfer rate Q in the 2nd scenario is 53 percent higher compared to the 1st scenario since the mass flow rate in the 2nd scenario is 63 percent higher compared to the 1st scenario. As discussed earlier, mass flow rate was determined from the Reynolds number, channel geometry, and thermo-physical properties of the working fluid. Since the heat transfer rate is proportional to the mass flow rate and bulk fluid temperature difference between the channel inlet and outlet, changes in mass flow rate and heat transfer rate are not proportional.

Based on the energy balance for the hot and cold channels, for the constant rate of heat transfer, an increase in mass flow rate results in a decrease in bulk temperature of the working fluids. Thus, for the 2nd scenario, bulk temperature at the cold channel exit decreased due to the higher mass flow rate.

Heat transfer performance corresponding to the 1st and 2nd scenarios is presented in Table 7. 20. The Nu number remained unchanged since the flow regime in both scenarios is laminar. However, as presented in Table 7. 20, convection heat transfer coefficient in the 2nd scenario is slightly (0.5 to 2%) higher compared to the 1st scenario due to higher Re number, thus resulting in approximately 2 percent higher value of the overall heat transfer coefficient U and conductance UA .

In summary, there is very little difference in heat transfer performance between the 1st and 2nd scenario. However, the choice of a scenario has a significant effect on the mass flow rate and heat transfer rate.

Table 7. 20. The overall heat transfer coefficient for studied scenarios

	$h_{\text{avg}}^{\text{Hot}}$ [W/m ² K]	$h_{\text{avg}}^{\text{Cold}}$ [W/m ² K]	UA [W/K]	U [W/m ² K]
1 st scenario, Re=1000	198,114	170.318	0.4024	169.584
2 nd scenario, Re=1630	199,169	173.792	0.41	173.156
Diff. %	0.5	2	2	2.11

Variation of friction coefficient C_f and shear stress along the channel length for the investigated scenarios is compared in Figure 7. 21. The higher mass flow rate in the hot and cold channels results in higher wall shear stress and lower friction coefficient. In the fully developed laminar flow with constant thermo-physical properties, friction coefficient decreases with an increase in Re number (for example, for a circular tube $C_f=16/\text{Re}$). The results for C_f presented in Table 7. 19 collaborate theoretical results showing approximately 40% lower values of friction coefficient for both the cold and hot channels for the 2nd scenario compared to the 1st scenario. The results presented in Figure 7. 21c-d show that the wall shear stress for the 2nd scenario is higher compared to the 1st scenario due to higher mass flow rate. The wall shear stress was calculated using Equation (2.24).

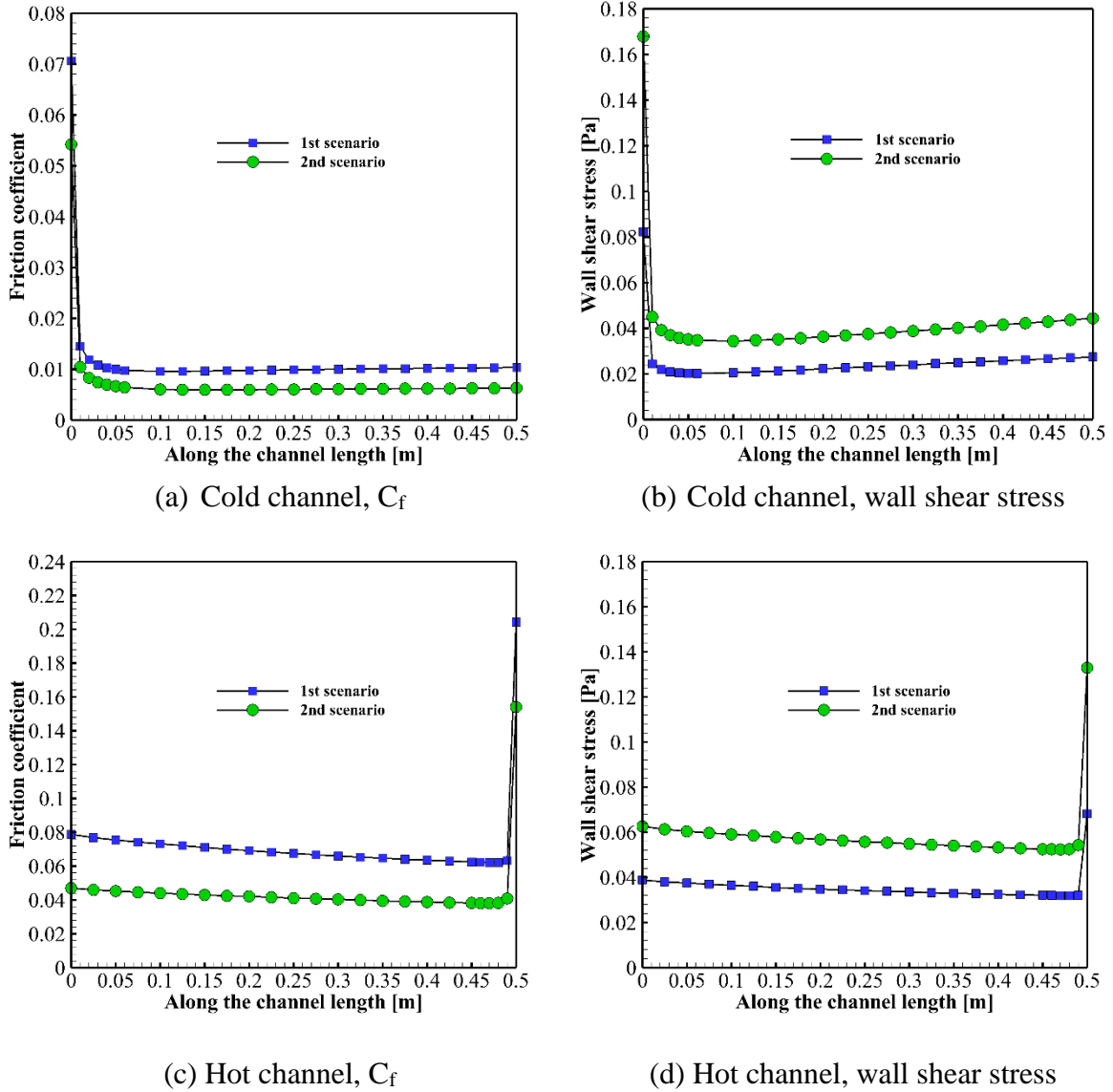


Figure 7. 21. Friction coefficient C_f and wall shear stress for both scenarios

7.10.3 Heat exchanger thermal duty and effectiveness

Thermal performance of the optimized circular staggered geometry for the 2nd scenario was determined using the ε – NTU method. The overall heat transfer coefficient U was calculated using Equation (1.4) while NTU and ε were obtained using Equations (1.6) and (1.8).

The effectiveness, NTU and other heat transfer performance values obtained for the optimized circular staggered geometry for the 1st and 2nd scenarios are compared in Table 7.

21. The results show that the heat transfer per unit volume Q/V , and thermal performance of optimized circular staggered geometry obtained for the 2nd scenario are 53% higher compared to the 1st scenario. As discussed earlier and presented in Table 7.20, the overall heat transfer coefficient U increased slightly due to higher Re number, mass flow rate and bulk velocity while NTU decreased by 37.7 percent since the minimum capacity rate C_{min} increased due to the higher mass flow rate. The effectiveness ε decreased due to higher mass flow rate associated with the 2nd scenario.

Table 7. 21. Heat transfer performance of a heat exchanger for investigated scenarios

	Q/V [W/m ³]	C_{min} [J/K.s]	h_{avg} Hot [W/m ² K]	h_{avg} Cold [W/m ² K]	U [W/m ² K]	effectiveness	NTU
1 st scenario, $Re=1000$	4.26×10^6	0.0488	198,114	170.31	169.58	0.9376	8.2431
2 nd scenario, $Re=1630$	6.55×10^6	0.0799	199,169	173.79	173.15	0.8778	5.1349
Diff. %	53	63.79	0.5	2.0	2.11	6.37	-37.7

Table 7. 22 compares bulk temperature at the hot and cold channel inlets and exits for both scenarios and ΔT_{LMTD} calculated by using Equation (1.3). The LMTD method was described in Section 1.6 of Chapter 1. The inlet fluid temperatures for the hot and cold channels were presented in Table 7. 3 and Table 7. 18 for the 1st scenario and 2nd scenario, respectively.

Table 7. 22. The bulk temperature at the hot and cold channel inlet and exit

	T_{ho} [K]	T_{co} [K]	ΔT_1	ΔT_2	ΔT_{LMTD}	Q [W]	$\frac{Q_{max}}{[W]}$
1 st scenario, Re=1000	650.94	789.32	13.83	28.01	20.09	8.22	8.8
2 nd scenario, Re=1630	660.67	778.44	24.71	37.74	30.77	12.61	14.39
Diff. %	1.5	1.4	78	34	53	53	63

In summary, the results show that for the same geometry, the mass flow rate of the working fluids, heat transfer rate Q , ΔT_{LMTD} , and minimum capacity rate ratio C_{min} for the 2nd scenario are higher compared to the 1st scenario, resulting in lower effectiveness ε and NTU values. The lower value of ε , determined from Equation (1.8), can be explained by higher values of quantities Q_{max} and Q .

CHAPTER 8: CONCLUSIONS AND RECOMMENDATIONS FOR FUTURE RESEARCH

8.1 Overview

This chapter provides an overview of the contributions of this research study to the relevant literature and recommendations for future research work.

8.2 Research contributions

The main contributions of this research work are the following:

8.2.1 The effect of large variation of thermo-physical properties of sCO₂ and liquid sodium on thermal and hydraulic performance of microchannel PCHE

Simultaneously developing flow and conjugate heat transfer for sCO₂ and liquid sodium as working fluids were analyzed in 3D micro-channel geometries to study thermal and hydraulic performance of the micro-channel PCHE used in a sCO₂ Brayton cycle. The conservation equations for a 3D steady-state incompressible laminar flow were solved numerically for different micro-channel geometries to determine the effect of operating conditions and thermo-physical properties of different working fluids, covering a wide Prandtl number range, on thermal performance of a PCHE heat exchanger.

The results show that fluid flow and heat transfer parameters such as friction coefficient and heat transfer coefficient are affected by the variation of thermo-physical properties of sCO₂ in the region near the critical point (CP) and along the pseudo-critical line. These effects propagate from the cold (sCO₂) micro-channel to the hot (liquid sodium) micro-channel affecting heat exchange between the two channels. For the operating conditions away from the CP, where variation in thermo-physical properties of sCO₂ with pressure and temperature is more gradual, thermo-hydraulic performance of the investigated micro-channel geometries resembles performance associated with “regular” fluids.

The peripherally-averaged Nu number for liquid sodium in a fully developed flow for semi-circular PCHE is smaller compared to that of the sCO₂. The heat flux is increased in the axial direction due to the combined effect of the molecular thermal conduction as well as axial conduction in liquid sodium in the simultaneously developing conjugate heat transfer along the channel. Since liquid sodium has a very low Prandtl number compared to that of sCO₂ at temperatures and pressures studies in this work, thermal boundary layer is much thicker compared to the hydraulic boundary layer and thermal resistance is distributed over the channel cross section instead being concentrated near the wall.

The heat transfer coefficient in the channel is very high for liquid sodium compared to “regular fluids” such as water and air since, for the analyzed channel geometries and operating conditions, the bulk fluid temperature is approaching wall temperature.

8.2.2 Design and optimization of advanced double-etched micro-channel PCHE geometries

Two novel advanced micro-channel PCHE topologies, semi-circular staggered doubled-etched (SDE) and circular staggered double etched geometries, were designed and optimized for use in the High Temperature Recuperator (HTR) and Intermediate Heat Exchanger (IHx) in a recompression sCO₂ Brayton cycle. A multi-objective optimization, MOGA, with NSGA-II using Response Surface Approximation (RSA) as a surrogate model was used to design and optimize two advanced PCHE geometries developed in this work. The channel fin thickness and shim plate thickness were geometric parameters used in the optimization.

The results show that the effect of channel fin thickness on wall temperature is small. However, a significant reduction of the channel fin thickness increases the value of the overall heat transfer coefficient U. The Nu number does not change in the fully-developed flow since

the flow regime is laminar. However, a decrease of the micro-channel fin thickness in a PCHE will increase the overall heat transfer coefficient, resulting in an increase in thermal duty of the heat exchanger.

For the temperatures, pressures and Reynolds number values used in the HTR design and optimization, the results show that the values of effectiveness ε and NTU for the optimized semi-circular SDE geometry increased compared to the conventional semi-circular geometry. However, for the values of temperature, pressure and Reynolds number used in the IHX design and optimization, the conventional geometry (semi-circular channel) has higher effectiveness and NTU since the overall heat transfer coefficient is higher in the semi-circular channels.

The results show that thermal duty and compactness factor of the optimized HTR and IHX SDE and micro-channel topology have significantly improved compared to the conventional semi-circular micro-channel geometry, resulting in higher heat transfer per unit volume. The optimized SDE topologies are significantly smaller in size and lighter, more economical to manufacture, and also have higher thermal duty compared to the conventional semi-circular microchannel topology.

The comparison of two materials of construction; Alloy 617 and Alloy 230 shows that for the same operating conditions (pressure and temperature), the size, weight and production cost of a heat exchanger constructed of Alloy 230 are smaller compared to Alloy 617. This is because the maximum allowable stress for Alloy 230 is higher compared to Alloy 617. However, etchability and diffusion bonding process of plates made of Alloy 230 has not been thoroughly investigated.

8.3 Challenges associated with the design and optimization

Some of the main challenges involved in the design and optimization of advanced geometries are the following:

- Understanding of the simultaneously developing flow and conjugate heat transfer in a microchannel geometry using sCO₂ as the working fluid for operating conditions near the CP.
- Computational approach and numerical modeling for sCO₂ for the operating pressure and temperature near the CP, and numerical convergence at the solid-fluid interface in the hot channel for liquid sodium.
- The conjugate heat transfer analysis in a micro-channel using liquid sodium as a hot working fluid.
- Thermal stress analysis and Finite Element Method (FEM) for the advanced geometries along with the choice of realistic boundary conditions for the structural analysis.
- Understanding of the multi-objective genetic algorithm for design and optimization of advanced microchannel geometries.

8.4 Recommendations for future research

This study focused on numerical analysis of the local and overall flow and heat transfer in 3D advanced staggered double-etched micro-channel geometries for the laminar flow regime and constant value of Reynolds number. It is recommended to extend the analysis to higher Re numbers corresponding to the turbulent flow regime on the sCO₂ side.

Design and optimization of an IHX employing a double-etched circular geometry on the hot (liquid sodium) side with a single-etched semi-circular geometry on the cold (sCO₂) side is recommended. Since dynamic viscosity of liquid sodium is high, larger cross-sectional

area of the circular micro-channel geometry and smooth geometry (no corners) will help reduce or eliminate channel fouling and clogging in the long run. Using the semi-circular micro-channel on the cold side will result in a higher value of the convection heat transfer coefficient and, consequently, higher overall heat transfer coefficient. Therefore, higher effectiveness and NTU of the optimized semi-circular geometry integrated with the circular double-etched geometry will result in higher thermal duty of a heat exchanger.

Another suggestion for future work includes a geometry where the airfoil fins are etched on one side of the plate and straight semi-circular channels are etched on the other side. A shim plate would be needed for diffusion bounding to create a PCHE stack. Since pressure drop is significantly higher in the PCHE channels in turbulent flow compared to laminar flow, the airfoil fin channel can reduce the pressure drop in the PCHE channels for high Re numbers. Also, the airfoil fin PCHE channel can be constructed using 3D printing technology. However, the mechanical integrity of the airfoil channel PCHE configuration should be thoroughly investigated because of smaller diffusion bounding surface area. Although the straight micro-channel PCHE provides lower cost, the airfoil PCHE configuration provides superior thermal and hydraulic performance compared to the straight micro-channel PCHE for high Re numbers.

REFERENCES

1. Khalesi, J. and N. Sarunac, *Numerical analysis of flow and conjugate heat transfer for supercritical CO₂ and liquid sodium in square microchannels*. International Journal of Heat and Mass Transfer, 2019. **132**: p. 1187-1199.
2. Lemmon, E., et al., *NIST standard reference database 23: Reference fluid thermodynamic and transport Properties-REFPROP, Version 10.0*, national institute of standards and technology. Standard Reference Data Program, Gaithersburg, 2018.
3. Dostal, V., M.J. Driscoll, and P. Hejzlar, *A supercritical carbon dioxide cycle for next generation nuclear reactors*. 2004, Massachusetts Institute of Technology, Department of Nuclear Engineering
4. Reznicek, E.P., *Design and Simulation of Supercritical Carbon Dioxide Recompression Brayton Cycles with Regenerators for Recuperation*. 2019, Colorado School of Mines.
5. Feher, E.G., *The supercritical thermodynamic power cycle*. Energy conversion, 1968. **8**(2): p. 85-90.
6. Angelino, G., *Carbon dioxide condensation cycles for power production*. 1968.
7. Kim, Y., C. Kim, and D. Favrat, *Transcritical or supercritical CO₂ cycles using both low-and high-temperature heat sources*. Energy, 2012. **43**(1): p. 402-415.
8. Floyd, J., et al., *A numerical investigation of the sCO₂ recompression cycle off-design behaviour, coupled to a sodium cooled fast reactor, for seasonal variation in the heat sink temperature*. Nuclear Engineering and Design, 2013. **260**: p. 78-92.
9. Kim, W., et al., *A mathematical correlation for predicting the thermal performance of cross, parallel, and counterflow PCHEs*. International Journal of Heat and Mass Transfer, 2017. **106**: p. 1294-1302.
10. Cui, X., et al., *Numerical study on novel airfoil fins for printed circuit heat exchanger using supercritical CO₂*. International Journal of Heat and Mass Transfer, 2018. **121**: p. 354-366.
11. Chu, W.-x., et al., *Experimental investigation on SCO₂-water heat transfer characteristics in a printed circuit heat exchanger with straight channels*. International Journal of Heat and Mass Transfer, 2017. **113**: p. 184-194.
12. Moore, R. and T. Conboy, *Metal corrosion in a supercritical carbon dioxide-liquid sodium power cycle*. Sandia National Laboratory Report SAND2012-0184, 2012.

13. Kim, S.G., et al., *CFD aided approach to design printed circuit heat exchangers for supercritical CO₂ Brayton cycle application*. Annals of Nuclear Energy, 2016. **92**: p. 175-185.
14. Takeda, T., et al., *Feasibility study on the applicability of a diffusion-welded compact intermediate heat exchanger to next-generation high temperature gas-cooled reactor*. Nuclear engineering and design, 1997. **168**(1-3): p. 11-21.
15. Aneesh, A., et al., *Effects of wavy channel configurations on thermal-hydraulic characteristics of Printed Circuit Heat Exchanger (PCHE)*. International Journal of Heat and Mass Transfer, 2018. **118**: p. 304-315.
16. Hesselgreaves, J.E., R. Law, and D. Reay, *Compact heat exchangers: selection, design and operation*. 2016: Butterworth-Heinemann.
17. Pra, F., et al., *Promising designs of compact heat exchangers for modular HTRs using the Brayton cycle*. Nuclear Engineering and Design, 2008. **238**(11): p. 3160-3173.
18. Lee, Y. and J.I. Lee, *Structural assessment of intermediate printed circuit heat exchanger for sodium-cooled fast reactor with supercritical CO₂ cycle*. Annals of Nuclear Energy, 2014. **73**: p. 84-95.
19. Natesan, K., A. Moiseyev, and S. Majumdar, *Preliminary issues associated with the next generation nuclear plant intermediate heat exchanger design*. Journal of nuclear materials, 2009. **392**(2): p. 307-315.
20. Zhao, Z., et al., *Experimental and numerical investigation of thermal-hydraulic performance of supercritical nitrogen in airfoil fin printed circuit heat exchanger*. Applied Thermal Engineering, 2020. **168**: p. 114829.
21. Ren, Z., et al., *Investigation on local convection heat transfer of supercritical CO₂ during cooling in horizontal semicircular channels of printed circuit heat exchanger*. Applied Thermal Engineering, 2019. **157**: p. 113697.
22. Bone, V., et al., *Methodology to develop off-design models of heat exchangers with non-ideal fluids*. Applied Thermal Engineering, 2018. **145**: p. 716-734.
23. Wen, Z.-X., et al., *Numerical study on heat transfer behavior of wavy channel supercritical CO₂ printed circuit heat exchangers with different amplitude and wavelength parameters*. International Journal of Heat and Mass Transfer, 2020. **147**: p. 118922.

24. Zhang, H., et al., *Studies on the thermal-hydraulic performance of zigzag channel with supercritical pressure CO₂*. The Journal of Supercritical Fluids, 2019. **148**: p. 104-115.
25. Khalesi, J., N. Sarunac, and Z. Razzaghpanah, *Supercritical CO₂ conjugate heat transfer and flow analysis in a rectangular microchannel subject to uniformly heated substrate wall*. Thermal Science and Engineering Progress, 2020: p. 100596.
26. Shi, H.-Y., et al., *Heat transfer and friction of molten salt and supercritical CO₂ flowing in an airfoil channel of a printed circuit heat exchanger*. International Journal of Heat and Mass Transfer, 2020. **150**: p. 119006.
27. Marchionni, M., et al., *Numerical modelling and transient analysis of a printed circuit heat exchanger used as recuperator for supercritical CO₂ heat to power conversion systems*. Applied Thermal Engineering, 2019. **161**: p. 114190.
28. Guo, J. and X. Huai, *Performance analysis of printed circuit heat exchanger for supercritical carbon dioxide*. Journal of Heat Transfer, 2017. **139**(6).
29. Li, H., et al., *based modeling on the turbulent convection heat transfer of supercritical CO₂ in the printed circuit heat exchangers for the supercritical CO₂ Brayton cycle*. International journal of heat and mass transfer, 2016. **98**: p. 204-218.
30. Meshram, A., et al., *Modeling and analysis of a printed circuit heat exchanger for supercritical CO₂ power cycle applications*. Applied Thermal Engineering, 2016. **109**: p. 861-870.
31. Baik, Y.-J., et al., *Heat transfer performance of wavy-channeled PCHEs and the effects of waviness factors*. International Journal of Heat and Mass Transfer, 2017. **114**: p. 809-815.
32. Saeed, M. and M.-H. Kim, *Thermal and hydraulic performance of SCO₂ PCHE with different fin configurations*. Applied thermal engineering, 2017. **127**: p. 975-985.
33. Chu, W.-x., et al., *Study on hydraulic and thermal performance of printed circuit heat transfer surface with distributed airfoil fins*. Applied Thermal Engineering, 2017. **114**: p. 1309-1318.
34. Chen, F., et al., *Comprehensive performance comparison of airfoil fin PCHEs with NACA 00XX series airfoil*. Nuclear Engineering and Design, 2017. **315**: p. 42-50.
35. Chu, W.-X., et al., *Thermo-hydraulic performance of printed circuit heat exchanger with different cambered airfoil fins*. Heat Transfer Engineering, 2020. **41**(8): p. 708-722.

36. Li, X.L., et al., *Numerical Analysis of Slotted Airfoil Fins for Printed Circuit Heat Exchanger in S-CO₂ Brayton Cycle*. Journal of Nuclear Engineering and Radiation Science, 2019. **5**(4).
37. Cheng, K., et al., *Experimental investigation of thermal-hydraulic characteristics of a printed circuit heat exchanger used as a pre-cooler for the supercritical CO₂ Brayton cycle*. Applied Thermal Engineering, 2020: p. 115116.
38. Zhou, J., et al., *Test platform and experimental test on 100 kW class Printed Circuit Heat Exchanger for Supercritical CO₂ Brayton Cycle*. International Journal of Heat and Mass Transfer, 2020. **148**: p. 118540.
39. Aakre, S. and M.H. Anderson, *Molten salt to supercritical CO₂ diffusion-bonded heat exchanger testing to support component certification for advanced nuclear power systems*. 2019, University of Wisconsin-Madison.
40. Pidaparti, S.R., M.H. Anderson, and D. Ranjan, *Experimental investigation of thermal-hydraulic performance of discontinuous fin printed circuit heat exchangers for supercritical CO₂ power cycles*. Experimental Thermal and Fluid Science, 2019. **106**: p. 119-129.
41. Bae, S.J., et al., *Condensation heat transfer and multi-phase pressure drop of CO₂ near the critical point in a printed circuit heat exchanger*. International Journal of Heat and Mass Transfer, 2019. **129**: p. 1206-1221.
42. Jajja, S.A., K.R. Zada, and B.M. Fronk, *Experimental investigation of supercritical carbon dioxide in horizontal microchannels with non-uniform heat flux boundary conditions*. International Journal of Heat and Mass Transfer, 2019. **130**: p. 304-319.
43. Baek, S., et al., *Development of highly effective cryogenic printed circuit heat exchanger (PCHE) with low axial conduction*. Cryogenics, 2012. **52**(7-9): p. 366-374.
44. Yih, J. and H. Wang, *Experimental characterization of thermal-hydraulic performance of a microchannel heat exchanger for waste heat recovery*. Energy Conversion and Management, 2020. **204**: p. 112309.
45. Deb, K., et al. *A fast elitist non-dominated sorting genetic algorithm for multi-objective optimization: NSGA-II*. in *International conference on parallel problem solving from nature*. 2000. Springer.

46. Goel, T., et al., *Response surface approximation of Pareto optimal front in multi-objective optimization*. Computer methods in applied mechanics and engineering, 2007. **196**(4-6): p. 879-893.
47. Husain, A. and K.-Y. Kim, *Enhanced multi-objective optimization of a microchannel heat sink through evolutionary algorithm coupled with multiple surrogate models*. Applied Thermal Engineering, 2010. **30**(13): p. 1683-1691.
48. Li, P. and K.-Y. Kim, *Multiobjective optimization of staggered elliptical pin-fin arrays*. Numerical Heat Transfer, Part A: Applications, 2008. **53**(4): p. 418-431.
49. Lee, S.-M., K.-Y. Kim, and S.-W. Kim, *Multi-objective optimization of a double-faced type printed circuit heat exchanger*. Applied thermal engineering, 2013. **60**(1-2): p. 44-50.
50. Lee, S.-M. and K.-Y. Kim, *Comparative study on performance of a zigzag printed circuit heat exchanger with various channel shapes and configurations*. Heat and Mass Transfer, 2013. **49**(7): p. 1021-1028.
51. Bergman, T.L., et al., *Fundamentals of heat and mass transfer*. 2011: John Wiley & Sons.
52. Cheng, L., G. Ribatski, and J.R. Thome, *Analysis of supercritical CO₂ cooling in macro- and micro-channels*. International journal of refrigeration, 2008. **31**(8): p. 1301-1316.
53. Shah, R.K. and A.L. London, *Laminar flow forced convection in ducts: a source book for compact heat exchanger analytical data*. 2014: Academic press.
54. Nonino, C., et al., *Conjugate forced convection and heat conduction in circular microchannels*. International Journal of Heat and Fluid Flow, 2009. **30**(5): p. 823-830.
55. Cole, K.D. and B. Çetin, *The effect of axial conduction on heat transfer in a liquid microchannel flow*. International Journal of Heat and Mass Transfer, 2011. **54**(11-12): p. 2542-2549.
56. Koşar, A., *Effect of substrate thickness and material on heat transfer in microchannel heat sinks*. International Journal of Thermal Sciences, 2010. **49**(4): p. 635-642.
57. Morini, G.L., *Scaling effects for liquid flows in microchannels*. Heat Transfer Engineering, 2006. **27**(4): p. 64-73.

58. Maranzana, G., I. Perry, and D. Maillet, *Mini-and micro-channels: influence of axial conduction in the walls*. International journal of heat and mass transfer, 2004. **47**(17-18): p. 3993-4004.
59. Boerema, N., et al., *Liquid sodium versus Hitec as a heat transfer fluid in solar thermal central receiver systems*. Solar Energy, 2012. **86**(9): p. 2293-2305.
60. Shah, R.K. and D.P. Sekulic, *Fundamentals of heat exchanger design*. 2003: John Wiley & Sons.
61. Bhatti, M. and C. Savary. *Heat transfer in the entrance region of a straight channel- Laminar flow with uniform wall temperature*. in asme. 1977.
62. Bhatti, M. and C. Savary, *Heat transfer in the entrance region of a straight channel: laminar flow with uniform wall heat flux*. 1977.
63. ANSYS, *Fluent*. **Release 19.1**.
64. Fink, J. and L. Leibowitz, *Thermodynamic and transport properties of sodium liquid and vapor*. 1995, Argonne National Lab.
65. Lundgren, T., E. Sparrow, and J. Starr, *Pressure drop due to the entrance region in ducts of arbitrary cross section*. 1964.
66. Javanshir, A., *Development and Analysis of a High-efficiency Concentrating Solar Power Tower Plant Concept*. 2018, The University of North Carolina at Charlotte.
67. Wright, S.A., et al., *Operation and analysis of a supercritical CO₂ Brayton cycle*. Sandia Report SAND2010-0171, 2010: p. 1-101.
68. Mylavarapu, S.K., et al., *Thermal hydraulic performance testing of printed circuit heat exchangers in a high-temperature helium test facility*. Applied Thermal Engineering, 2014. **65**(1-2): p. 605-614.
69. Hsieh, J.-C., et al., *Heat Transfer Characteristics of Supercritical Carbon Dioxide in a Horizontal Tube*. Int. Proc. Chem. Bio. Env. Eng., 2015. **82**.
70. Kim, I.H., et al., *Thermal hydraulic performance analysis of the printed circuit heat exchanger using a helium test facility and CFD simulations*. Nuclear Engineering and Design, 2009. **239**(11): p. 2399-2408.
71. Kim, I.H. and H.C. No, *Physical model development and optimal design of PCHE for intermediate heat exchangers in HTGRs*. Nuclear Engineering and Design, 2012. **243**: p. 243-250.

72. American Society of Mechanical Engineers, *ASME Boiler & Pressure Vessel Code: an International Code*. New York, 2015.
73. Sun, X., et al., *Compact Heat Exchanger Design and Testing for Advanced Reactors and Advanced Power Cycles*. 2018, The Ohio State Univ., Columbus, OH (United States).
74. Jarrahbashi, D., et al. *Computational Analysis of Ceramic Heat Exchangers for Supercritical CO₂ Brayton Cycle in CSP Applications at High-Temperatures*. in *Supercrit. CO₂ Power Cycles Symp., Pittsburgh, PA*. 2018.
75. Meshram, A., et al., *Modeling and analysis of a printed circuit heat exchanger for supercritical CO₂ power cycle applications*. 2016. **109**: p. 861-870.
76. Li, S. and S.-H. Lim, *Variational principles for generalized plane strain problems and their applications*. Composites Part A: Applied Science and Manufacturing, 2005. **36**(3): p. 353-365.
77. Bennett, K., *Performance Modeling of Supercritical Carbon Dioxide Zigzag-Channel Printed Circuit Heat Exchangers*. 2019, University of Nevada, Las Vegas.
78. Song, K.-n. and S.-d. Hong, *Structural integrity evaluation of a lab-scale PCHE prototype under the test conditions of HELP*. Science and Technology of Nuclear Installations, 2013. **2013**.
79. Ryu, W. *Korean R&D Program on HT Materials*. in *GIF VHTR Materials and Components, PMB Meeting, South Korea*. 2005.
80. Burlet, H., et al., *French VHTR Near Term High Temperature Alloy Development Program*. Gen IV VHTR Development, Paris, 2005.
81. Utamura, M., K. Nikitin, and Y. Kato, *A generalised mean temperature difference method for thermal design of heat exchangers*. International Journal of Nuclear Energy Science and Technology, 2008. **4**(1): p. 11-31.
82. Mylavarapu, S.K., *Design, fabrication, performance testing, and modeling of diffusion bonded compact heat exchangers in a high-temperature helium test facility*. 2011, The Ohio State University.